The role of TSPO in malignant hallmarks of glioblastoma

Dissertation
zur Erlangung des Doktorgrades
der Biomedizinischen Wissenschaften
(Dr. rer. physiol.)

der
Fakultät für Medizin
der Universität Regensburg

vorgelegt von
Laura-Marie Ammer
aus
Wolfhagen

im Jahr
2023

The role of TSPO in malignant hallmarks of glioblastoma

Dissertation
zur Erlangung des Doktorgrades
der Biomedizinischen Wissenschaften
(Dr. rer. physiol.)

der
Fakultät für Medizin
der Universität Regensburg

vorgelegt von
Laura-Marie Ammer
aus
Wolfhagen

im Jahr
2023

Dekan: Prof. Dr. Dirk Hellwig

Betreuer/in: Prof. Dr. Peter Hau

Tag der mündlichen Prüfung: 18.03.2024

Abstract

Despite continuing efforts to find new therapeutic strategies for glioblastoma, the prognosis of affected patients remains poor. Tumor recurrence is an unfortunate reality, largely due to the malignant nature of glioblastoma including its intrinsic heterogeneity and immunosuppressive microenvironment. The urgent need for innovative therapeutic approaches and new molecular targets has brought attention to the 18 kDa translocator protein, TSPO. This mitochondrial protein is overexpressed in glioblastoma and during neuroinflammation. Functionally, TSPO has been linked to apoptosis, mitochondrial metabolism, and immunomodulation, however its role in glioblastoma remains enigmatic. Intriguingly, dysregulation of these potential TSPO functions drives glioblastoma therapy resistance and tumor progression.

Therefore, we hypothesized that TSPO plays a pivotal role in these malignant traits of glioblastoma. The overarching goal was to gain a functional understanding of TSPO in glioblastoma with a particular focus on its involvement in tumor-intrinsic mechanisms following cytotoxic T cell attacks. This includes tumor cell apoptosis and the secretion of immunomodulatory cytokines in response to T cell effector molecules. Additionally, the impact of TSPO on mitochondrial energy metabolism, which is crucial for glioblastoma growth, was explored. To address this critical research question, BTIC13 patient-derived mesenchymal glioblastoma cells underwent a wide array of molecular and functional analyses, including state of the art genetic loss-of-function approaches, comprehensive examination of apoptosis pathways, multilayer examination of pro-inflammatory cytokine effects, and analysis of mitochondrial respiration.

Key findings of this thesis include the selective upregulation of TSPO in tumor cells in response to direct contact with T cells and following exposure to the pro-inflammatory cytokines IFNγ and TNFα. The death ligand TRAIL has been identified as potential mechanism through which cytotoxic T cells induce extrinsic and intrinsic apoptosis in BTIC13. However, the TRAIL-induced apoptotic response of BTIC13 did not solely depend on TSPO expression but was rather influenced by a multitude of tumor cell-intrinsic mechanisms in monoculture conditions. Additionally, TSPO appeared to play no substantial role in the induction of the immune-modulatory cytokines IL-6 and IL-8 by BTIC13 in response to IFNγ and TNFα stimulation. However, TSPO-deficiency significantly impaired cancer cell migration and elevated maximal mitochondrial respiration and reactive oxygen production.

Taken together, this thesis positions TSPO as a potential marker for effector T cell activity and OXPHOS regulation in glioblastoma. However, concrete conclusions regarding TSPO's potential as a therapeutic target remain elusive at this point. The established methodology and results presented here set the groundwork for unravelling a putatively tightly regulated role of TSPO in glioblastoma and serve as a basis for future experiments.

Zusammenfassung

Trotz der Bemühungen um neue Therapiestrategien für Glioblastoma bleibt die Prognose der betroffenen Patienten nach wie vor düster. Tumorrezidive sind eine bedauerliche Realität, die größtenteils auf die bösartige Natur des Glioblastoms, einschließlich seiner intrinsischen Heterogenität und seiner immunsuppressiven Mikroumgebung, zurückzuführen sind. Der dringende Bedarf an innovativen Therapieansätzen und neuen molekularen Zielen hat die Aufmerksamkeit auf das 18 kDa Translocator Protein TSPO gelenkt. Dieses mitochondriale Protein wird in Glioblastoma und bei der Neuroinflammation übermäßig stark exprimiert. Funktionell wird TSPO vor allem mit der Apoptose, dem mitochondrialen Stoffwechsel und der Immunmodulation in Verbindung gebracht, doch die Funktion im Glioblastom ist noch nicht hinreichend erforscht. Interessanterweise ist die Fehlregulation der potenziellen TSPO-Funktionen maßgeblich an der Therapieresistenz und der Progression des Tumors beteiligt.

Die Grundlage der vorliegenden Arbeit bildete die Hypothese, dass TSPO eine zentrale Rolle bei diesen malignen Eigenschaften des Glioblastoms spielt, und das übergeordnete Ziel war es, ein funktionelles Verständnis von TSPO im Glioblastom zu erlangen. Dabei lag ein besonderer Fokus auf der Beteiligung von TSPO an tumoreigenen Mechanismen nach einem zytotoxischen T-Zell-Angriff wie zum Beispiel der Tumorzell-Apoptose und der Sekretion immunmodulatorischer Zytokine als Reaktion auf T-Zell-Effektor Moleküle. Darüber hinaus wurden die Auswirkungen von TSPO auf den mitochondrialen Energiestoffwechsel untersucht, welcher für das Wachstum des Glioblastoms mit entscheidend ist. Im Rahmen dieser Arbeit wurde die vom Patienten stammende, mesenchymale BTIC13-Glioblastom Zelllinie einer breiten Palette von Analysen unterzogen. Dazu gehörten der genetische Knockdown und Knockout von TSPO in BTIC13, die umfassenden Untersuchungen der Apoptose Wege, die mehrschichtigen Untersuchungen der Auswirkungen von proinflammatorischen Zytokinen und Analysen der mitochondrialen Atmung.

Nach direktem Kontakt mit zytotoxischen T-Zellen oder nach der Stimulation mit den proinflammatorischen Zytokinen IFNγ und TNFα, wurde TSPO selektiv in den Tumorzellen hochreguliert. Der Todesligand TRAIL wurde als potenzieller Mechanismus identifiziert, durch den zytotoxische T-Zellen die extrinsische und intrinsische Apoptose in BTIC13 auslösen. Die Empfindlichkeit gegenüber der TRAIL-induzierten Apoptose von BTIC13 hing jedoch nicht allein von der TSPO-Expression ab, sondern wurde unter Monokulturbedingungen durch eine Vielzahl intrinsischer Resistenzmechanismen der Tumorzellen beeinflusst. Darüber hinaus schien TSPO keine wesentliche Rolle bei IFNγ– und TNFα–stimulierten Induktion und Sekretion der immunmodulatorischen Zytokine IL-6 und IL-8 zu spielen. Knockdown und Knockout

von TSPO in BTIC13 beeinträchtigten die Migration von Krebszellen erheblich und erhöhten die maximale mitochondriale Atmung sowie die Produktion von reaktiven Sauerstoffspezies.

Zusammenfassend positioniert diese Arbeit TSPO als potenziellen Marker für die Aktivität von Effektor-T-Zellen und der OXPHOS Regulation im Glioblastom. Dennoch bleiben konkrete Schlussfolgerungen hinsichtlich des therapeutischen Potenzials von TSPO zum jetzigen Zeitpunkt aus. Die hier vorgestellte Methodik und die Ergebnisse legen jedoch den Grundstein für die Aufklärung einer vermutlich streng regulierten Rolle von TSPO beim Glioblastom und dienen als Grundlage für zukünftige Experimente.

Table of contents

List of Figures

List of Tables

List of Abbreviations

A

7AAD	7-amino-actinomycin D
A	Antimycin A
AC	Astrocytes
ACBP	Acyl-CoA-binding protein
AMPK	AMP-activated protein kinases
ANOVA	Analysis of variance
ANT	Adenine nucleotide translocase
AnxV	Annexin V
Ap1	Activator protein 1
Apaf-1	Apoptotic protease activating factor 1
ARF	ADP ribosylation factor
ATPB	ATP synthase subunit beta

B

Bcl	B-cell lymphoma
BTIC	Brain tumor initiating cells

C

Casp	Caspase
CDK4	Cyclin dependent kinase 4
CDKN2A/B	Cyclin dependent kinase inhibitor 2A/B
cDNA	Complementary deoxyribonucleic acid
cFLIP	Cellular FLICE-like inhibitory protein
CIP	Calf intestinal alkaline phosphatase
cl	Cleaved
CM	Control medium

CNS	Central nervous system
CRAC	Cholesterol recognition amino acid consensus motif
Ctrl	Control

D

dATP	Deoxyadenosine triphosphate
DBI	Diazepam binding inhibitor
DCR	Decoy receptor
DD	Death domain
DISC	Death inducing signaling complex
DNA	Deoxyribonucleic acid
DR	Death receptor

E

ECAR	Extracellular acidification rate
EGFR	Epidermal growth factor
ELISA	Enzyme-linked immunosorbent assay
ERK	Extracellular signal regulated kinase
ETC	Electron transport chain

F

FACS	Fluorescence activated cell sorting
FADD	Fas-associated death domain
FAP-1	Fas-associated phosphatase-1
FasL	Fas ligand
FCCP	Carbonyl cyanide 4-(trifluoromethoxy)phenylhydrazone
FITC	Fluorescein isothiocyanate
FluP	Influenza peptide
FluT sup	Cell culture supernatant of activated FluT cells

FLuT	Flu antigen specific cytotoxic $CD8^+$ T cells

G

gDNA	Guide deoxyribonucleic acid
GPI	Glycosylphosphatidylinositol anchor

H

H_2DCFDA	2',7'-Dichlorodihydrofluorescein diacetate
HLA	Human leukocyte antigen
HRP	Horseradish peroxidase

I

IAP	Inhibitor of apoptosis
IDH	Isocitrate dehydrogenase
IDO	Indoleamine 2,3 dioxygenase
IFN	Interferon
IFNR	Interferon receptor
IL	Interleukin
IMM	Inner mitochondrial membrane
INDEL	Insertion, deletion
iNO	Inducible nitric oxide synthase

K

KD	Knockdown
kDa	Kilo Dalton
KO	Knockout

L

LOH	Loss of heterozygosity

LPS	Lipopolysaccharide

M

MAP	Mitogen activated protein
MDM	Mouse double minute homologue
MDSC	Myeloid derived suppressor cells
MES	Mesenchymal
MGMT	O6-methylguanine DNA methyltransferase
MOMP	Mitochondrial outer membrane permeabilization
MPD	Membrane proximal domain
mPTP	Mitochondrial permeability transition pore
mRNA	Messenger ribonucleic acid
mt	Mutant
MVP	Microvascular proliferation

N

NF1	Neurofibromatosis type 1
NFκB	Nuclear factor κB
NK	Natural killer
NMR	Nuclear magnetic resonance
NOX	NADPH oxidases
NPC	Neural progenitor cell
Ns	Non-significant

O

O	Oligomycin
OCR	Oxygen consumption rate
OMM	Outer mitochondrial membrane
OPC	Oligodendrocyte precursor cell

OPG	Osteoprotegerin
OXPHOS	Oxidative phosphorylation

P

P	Phosphorylated
PBR	Peripheral benzodiazepine receptor
PCD	Programmed cell death
PCR	Polymerase chain reaction
PD-1	Programmed death 1
PDGFRA	Platelet derived growth factor receptor A
PDL-1	Programmed death ligand 1
PE	Phycoerythrin
PET	Positron emission tomography
PI3K	Phosphatidylinositol-3-kinase
PTEN	Phosphatase and tensin homolog

R

R	Rotenone
RAS	Rat sarcoma
RB	Retinoblastoma
RLU	Relative light unit
RNA	Ribonucleic acid
ROS	Reactive oxygen species
RT	Room temperature
RTK	Receptor tyrosine kinase
RT-qPCR	Real time quantitative polymerase chain reaction

S

Scr	Scrambled

SDS PAGE	Sodium dodecyl sulfate polyacrylamide gel electrophoresis
shRNA	Short hairpin ribonucleic acid
SMAC	Second mitochondria derived activator of caspases
SNP	Single nucleotide polymorphism
SP	Specificity protein
StAR	Steroidogenic acute regulatory protein
STAT3	Signal transducer and activator of transcription 3

T

TAM	Tumor-associated macrophages and microglia
TAPE	Threonine, alanine, proline, glutamine domain
TCA	Tricarboxylic acid cycle
TCGA	The Cancer Genome Atlas
TERT	Telomerase reverse transcriptase
TGF-β	Transforming growth factor beta
TME	Tumor microenvironment
TNF	Tumor necrosis factor
TNFR	Tumor necrosis factor receptor
TP53	Tumor protein 53
TRADD	TNFR associated death domain
TRAIL	TNF related apoptosis inducing ligand
Tregs	Regulatory T cells
TSPO	Translocator protein
TTF	Tumor treating fields

V

VDAC1	Voltage dependent anion channel 1

W

WHO	World health organization

1 Introduction

1.1 Glioblastoma

1.1.1 Classification of glioblastoma

Diffuse gliomas represent the most abundant type of malignant brain tumors in adults [1] . They arise from glial cells or its precursor cells and are characterized by diffusely infiltrative growth into the brain parenchyma [2].

Historically, gliomas were classified and graded by the World Health Organization (WHO) based on histological characteristics, however the updated versions from 2016 and 2021 also take molecular features into account [3, 4]. The prognostic grades range from 1 to 4, with grade 1 having the longest survival rate after diagnosis and grade 4 having the worst prognosis. At current state, adult-type diffuse gliomas are broadly divided into three subtypes based on morphological and molecular features (Figure 1):

(1) Oligodendrogliomas are defined by isocitrate dehydrogenase (IDH) mutation and co-deletion of the chromosome arms 1p and 19q [3]. They also often exhibit increased *telomerase reverse transcriptase* (*TERT*) promotor mutations and are graded as WHO grade 2 or 3 based on the absence or presence of the histological feature of anaplasia [3, 5].

(2) Astrocytomas, IDH-mutant are defined by gain-of-function mutations in *IDH1* or *IDH2*. Loss of nuclear ATRX and loss-of-function mutations in tumor suppressor protein *TP53* are also observed in the vast majority of these tumors [5]. They are stratified from WHO grade 2 to 4 depending on the abundance of histopathological criteria and the homozygous deletion in *cyclin-dependent kinase inhibitor 2A/B* (*CDKN2A/B*) which serves as a negative prognostic marker [6, 7].

(3) Glioblastomas, IDH-wildtype lack IDH mutations but show *epidermal growth factor receptor* (*EGFR*) gene amplification or *TERT* promotor mutations and gain of chromosome 7 combined with loss of chromosome 10 [4, 5, 8]. They always correspond to WHO grade 4 and their histological features include prominent cellular and nuclear atypia, frequent mitotic figures, and areas of necrosis and vascular proliferation [3]. However, if they lack necrosis and /or vascular proliferation, they can also be diagnosed by the above-mentioned genetic alterations.

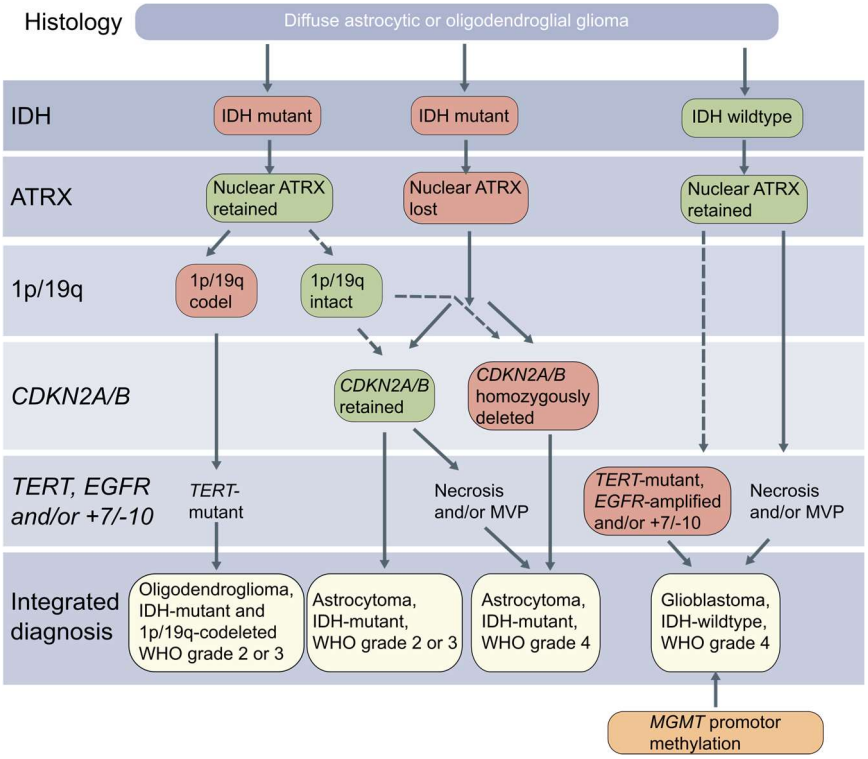

Figure 1. Basic classification of adult diffuse gliomas according to the WHO classification from 2021. Shown is the classification of adult-type diffuse gliomas into Oligodendroglioma, Astrocytoma and Glioblastoma based on diagnostically relevant molecular alterations. Green colored boxes mark intact or retained markers, and red colored boxes mark the loss, mutation, or amplification of markers. Own illustration based on [5]. MVP, microvascular proliferation.

Glioblastomas are the most common type of malignant brain tumors and account for 50.1 % of primary malignant brain tumors [1]. Their high aggressiveness and complexity lead to a particularly poor prognosis. Even with advanced therapies, the median overall survival remains low at 15-17 months and less than 7 % of the patients are alive after 5 years of diagnosis [1, 9, 10].

The current standard of care for glioblastoma after surgery was established 18 years ago in 2005 and amended in 2015 for the last time. It consists of six weeks of daily fractionated radiation therapy combined with concurrent and adjuvant temozolomide [10]. In 2015, tumor treating fields (TTFs) were included to this treatment regimen in patients with good clinical conditions. These devices inhibit the division of rapidly proliferating cells by low-intensity, intermediate frequency (200 kHz) alternating electric fields [11]. This increased the progression-free survival significantly from 4.0 months to 6.7 months and the median overall survival from 16.0 months to 20.9 months [12].

For certain molecular subgroups of glioblastoma also other treatments additionally to standard temozolomide are potentially beneficial. For example, a phase 3 trial has shown that patients with methylated O6-methylguanine DNA methyltransferase (MGMT) promoter in newly diagnosed glioblastoma benefit from Lomustine administration in addition to standard treatment. This improved the median overall survival from 31.4 months to 48.1 months [13].

Overall, however, substantial progress in improving the outcome of therapy is still lacking. Many novel therapeutic strategies such as kinase inhibitors [14, 15], immune therapy [16–18], and proteasome- and transcription factor inhibitors [19–21] have not been successful so far. Nevertheless, global efforts to advance new therapeutic options have led to many promising strategies that are currently investigated in preclinical and clinical trials all over the world (reviewed in [22, 23]).

1.1.2 Heterogeneity of glioblastoma

One reason for treatment failure and the poor patient outcome is the extensive heterogenous nature of glioblastoma. This is reflected in the dynamic and highly variable molecular characteristics between patients (inter-tumoral heterogeneity), but also within individual tumors (intra-tumoral heterogeneity) (reviewed in [24]). Furthermore, the heterogeneity can change and evolve over time and affect various malignant traits such as the expression of pro-tumorigenic genes, modulation of metabolic pathways and evasion of the immune system. In the last years, great efforts have been made to capture the several layers of heterogeneity in glioblastoma.

Classically, glioblastomas have been divided into the primary or secondary type, which not only affect different age groups and vary in prognosis but also harbor distinct molecular profiles [25]. Primary glioblastomas are more prevalent in older patients and develop *de novo*. They account for over 90 % of the cases and are characterized by *EGFR* amplification, inactivation of phosphatase and tensin homolog (PTEN) and loss of heterozygosity (LOH) on chromosome 10q [25]. Secondary glioblastomas are much rarer and develop as secondary neoplasm through the progression from lower grade glial tumors. In general, patients with secondary glioblastoma are younger and their genetic alterations frequently include *TP53* mutations and LOH of 10q [25].

A genetic signature of secondary glioblastoma is the mutation of *IDH1/2*, which occurs in more than 80 % of the cases [26]. However, based on the newest WHO classification from 2021, *IDH1/2* mutation is an exclusion criterion for glioblastoma [4] (Figure 1). Therefore, tumors with a clinical history resembling secondary glioblastoma and high-grade features are now classified as astrocytoma, WHO grade 4.

1.1.2.1 Genetic alterations of glioblastoma

Glioblastoma was one of the first tumors that was part of a large-molecular profiling study conducted by The Cancer Genome Atlas Network (TCGA). By analyzing the genomic, transcriptomic, and epigenetic composition of over 200 glioblastoma cases, they revealed a network of three core pathways that are frequently dysregulated in glioblastoma [27] (Figure 2). These include receptor tyrosine kinase (RTK) signaling, alterations in the retinoblastoma (RB) and p53 tumor suppressor pathways.

Receptor tyrosine kinase/rat sarcoma/phosphatidylinositol-(3)-kinase (RTK/RAS/PI(3)K) signaling was activated in 88 % of the cases due to mutations and amplifications of RTKs (*EGFR*, *ERBB2*, platelet-derived growth factor receptor A (*PDGFRA)* and *MET)* and frequent deletions of the tumor suppressors *PTEN* and *neurofibromatosis type 1* (*NF1*).
RB signaling was altered in 77 % of the cases and the most common aberrations were deletions of *CDKN2A/CDKN2B* (52 % and 57 %) and amplifications of *cyclin-dependent kinase 4* (*CDK4*) (18 %). In 11 % of the samples, *RB1* was homozygous deleted. *P53* signaling was inactivated in 87 % of the cases as a consequence of *ADP ribosylation factor (ARF*) deletions, amplifications of *mouse double minute homologue 2* (*MDM2*) and *MDM4* and mutations of *TP53*.

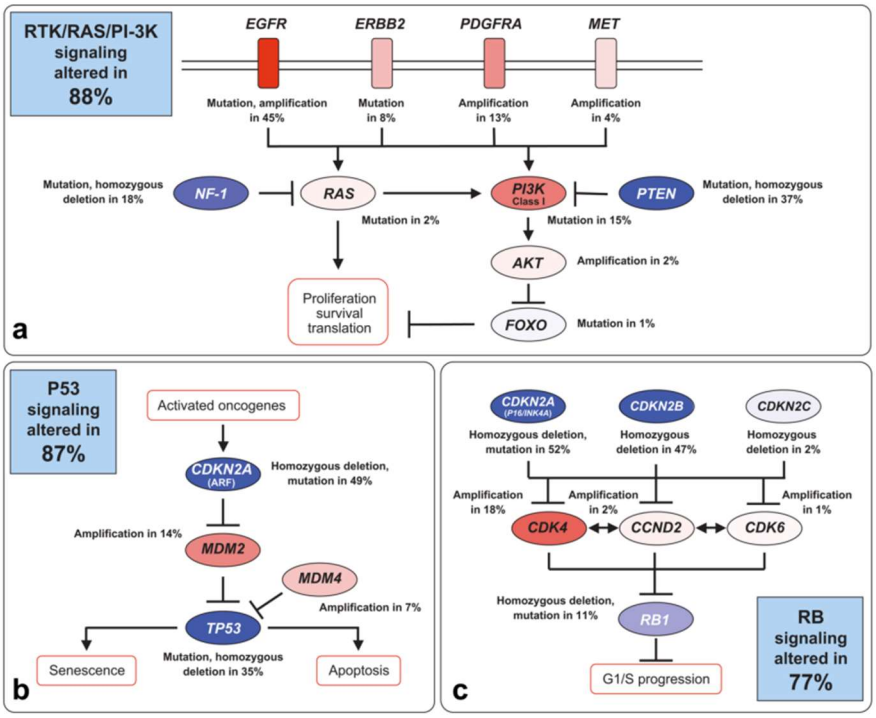

Figure 2. The three core signaling pathways altered in glioblastoma. Shown are the altered pathway components, types of mutation, and the percentage of tumors affected by alterations of the (**a**) RKT/RAS/PI-3K, (**b**) P53 and (**c**) RB signaling pathway. Amplification and activating mutations are highlighted in red. Deletions and loss of function mutations are shown in blue. Original image is from [27] and has been adapted from the reprinted version of [28].

Summarizing, tumorigenesis of glioblastoma is not the result of a single driver gene mutation and most of the samples showed alterations in all three pathways. This allows the tumor to escape from cell cycle checkpoints and apoptotic cues and favors a cooperative pro-survival and proliferative signaling state [27, 28].

1.1.2.2 Transcriptional subtypes of glioblastoma

To understand the diversity of these molecular changes and obtain a more reliable prediction to therapeutic vulnerabilities, glioblastoma has been classified into different transcriptional subtypes. The greater availability of transcriptomic and proteomic data enabled the evolution of these subtypes which provides increasingly detailed insight into the molecular landscape of glioblastoma [29, 30]. A first step was made in 2006 by Phillips and colleagues who identified three subtypes with mesenchymal, proneural and proliferative characteristics based on the expression of marker genes [29]. Using data from The Cancer Genome Atlas (TCGA) project and gene expression profiling, these subtypes were further divided into four clusters namely classical, mesenchymal, neural and proneural, which were tightly associated with genomic abnormalities [30]. Currently however, glioblastoma is classified into three transcriptional subtypes. These include the highly proliferative classical subtype, which is linked to chromosome 7 amplifications and chromosome 10 deletions, frequent *EGFR* amplifications, deletion of *CDKN2A*, and loss of *PTEN* [30, 31]. The mesenchymal subtype is enriched in mesenchymal markers such as *YKL40* and *MET* and associated with loss of *NF1* and frequent inactivation of *PTEN* [30, 31]. Lastly, the proneural subtype is related to *PDGFRA* amplifications and aberrations in the p53 signaling pathway [30, 31]. The previously described neural subtype was identified as contamination with the non-tumoral cells [31].

The development of more advanced sequencing techniques allowed insight into the transcriptional profile at single cell resolution (reviewed in [32]). These studies captured the intra-tumoral heterogeneity and showed that glioblastoma does not consist of only one subtype but is rather composed of a mixed cell population of multiple TCGA subtypes [33–35]. It was also shown that malignant cells were differentially enriched for genes related to the cell cycle, hypoxia, the complement/immune response, and oligodendrocyte function [33]. Single cell RNA sequencing also revealed that specific transcriptomic subtypes are preferentially enriched in tumor cells that exhibit distinct recurrent expression states (Figure 3). These expression states were lineage specific and either resembled neural progenitor cells (NPCs), oligodendrocyte precursor cells (OPCs), astrocytes (AC) or mesenchymal (MES) cells [35]. The abundance of cellular states within one tumor is shaped by somatic mutations and microenvironmental cues. For example, *EGFR* aberrations drive the prevalence for AC-like cells, whereas amplifications of *CDK4* and *PDGFR* are associated with NPC-like and OPC-like states. *NF1* alterations and the abundance of microglia/macrophages affect the frequency of MES-like states [35]. Recent

studies also point out the spatial adaptability and plastic state of neoplastic glioblastoma cells. First indication for these dynamics is the switch between different transcriptional subtypes that can be frequently observed upon tumor recurrence [36]. Adding a further layer of complexity, individual glioma cells were observed to resemble transcriptomic subtypes that dramatically change between different locations in the same tumor [34, 37]. This dynamic and spatial plasticity appears to be at least partly controlled by transcriptional programming via the tumor microenvironment [34, 35, 37, 38].

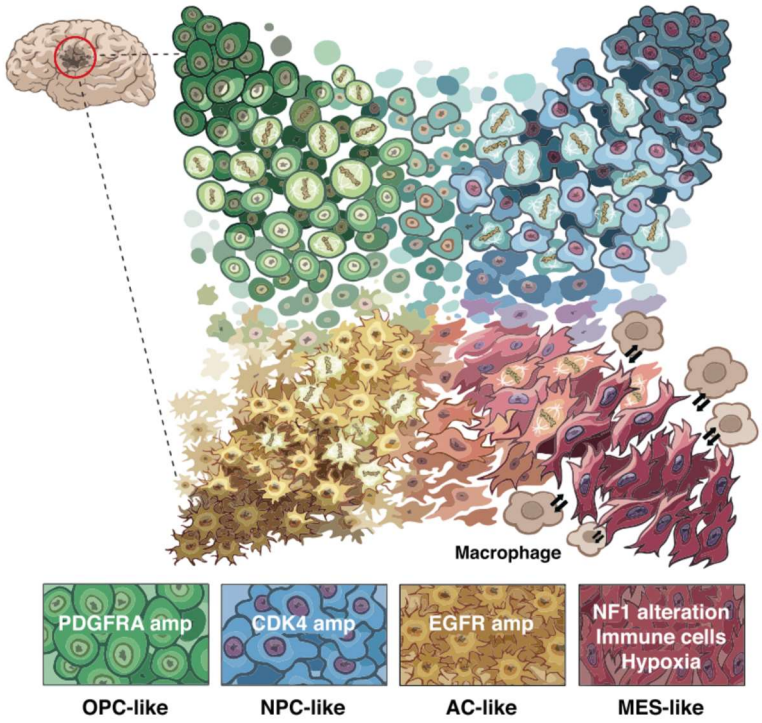

Figure 3. The intra-tumoral heterogeneity of glioblastoma converges into four different cellular states. Each tumor can be composed of four cellular states with OPC-like, NPC-like, AC-like and MES-like features. Cells of each state can proliferate and transition into other states. The prevalence of each state is determined by genetic and micro-environmental drivers. In this model, cycling cells are indicated by a mitotic spindle. Colors code for the different cellular states; the darker the color, the stronger is the cellular program. Transitions and intermediate states are shown at the passage between states. Image was adapted from [35].

The intra-tumoral heterogeneity is one of the key factors of intrinsic therapy resistance and its characterization largely contributes to the understanding of the tumor. From a translation and clinical point of view, the plasticity and diversity of molecular changes within one tumor points to the weaknesses of broadly applicable therapies, yet the clinical relevance of these subtypes is not fully understood.

1.1.2.3 Other subtypes of glioblastoma

Therefore, latest approaches attempt to classify glioblastoma into subtypes with higher predictive value to treatment response by considering core biological traits as well as the tumor microenvironment.

For example, using an unbiased computational approach combining single cell sequencing data, four new glioblastoma subtypes were found based on metabolic and developmental pathway activities [39]. These include two metabolic subtypes that are differentiated as mitochondrial and glycolytic subtype and two developmental subtypes, namely the neuronal subtype and the proliferative/progenitor subtype. The mitochondrial subtype is highly dependent on oxidative phosphorylation (OXPHOS), shows the most favorable outcome and is predictive for the sensitivity to OXPHOS inhibitors [39].

Tumors are not exclusively composed of diverse malignant cells but also of non-malignant cells in the tumor microenvironment (TME). Studies have shown that interactions between malignant cells and cells of the TME are tightly associated with clinical outcome and treatment response, particularly to immunotherapy [40–42]. As the composition of the TME is also heterogeneous and consists of various types of non-immune and immune cells with different phenotypes [43–45], a recent study investigated the composition of the TME to identify patients that would benefit from immunotherapy [46]. Using a computational approach to establish a TME-based classification system, they identified three novel TME-associated subtypes with unique composition of the TME, functional orientation markers and immune checkpoint proteins. These subtypes revealed specific TME-associated vulnerabilities and thus could help to guide the stratification of patients for improved precision immunotherapy [46].

However, these innovative classification approaches have to be yet incorporated and validated into prospective translation research and new clinical trials. It remains to be seen to what extent these novel subtypes become useful for clinical decision making.

1.2 Immunosuppressive landscape of glioblastoma

Glioblastomas are characterized by a highly immunosuppressive microenvironment. Reasons for that are tumor-intrinsic factors and the various types of immune cells at different phenotypic states that create an additional layer of heterogeneity. The communication of tumor cells with immune cells creates a pro-tumorigenic, anti-inflammatory environment that adds to the aggressive nature of glioblastoma and promotes tumor proliferation, invasion, and resistance to current therapies (reviewed in [47]). Therefore, understanding the immune landscape of glioblastoma is important for developing new therapies and especially critical for advances in immunotherapy.

1.2.1 Tumor-intrinsic factors

Several tumor-intrinsic factors lead to immune evasion in glioblastoma. These include the frequent upregulation of immune checkpoint molecules such as programmed death ligand 1 (PDL-1) [48] which binds to the co-inhibitory receptor PD-1 on cytotoxic T cells and induces T cell exhaustion and apoptosis [49, 50]. Furthermore, cytotoxic T cells depend on tumor antigen presentation by the human leukocyte antigen (HLA) class I peptide complex to become activated. However, tumor cells often have defects in antigen presentation and loss of heterozygosity in HLA class I is a frequent event in glioblastoma [51]. Another mechanism driving immune evasion is the upregulation of immune-suppressive signaling pathways such as signal transducer and activator of transcription 3 (STAT-3) (reviewed in [52]) and indoleamine 2,3-dioxygenase (IDO) [53, 54]. Finally, the release of immune-suppressive factors by tumor cells such as transforming growth factor beta (TGF-β) (reviewed in [55]), Interleukin-10 (IL-10), IL-1β, IL-6, and IL-8 [56] provide an environment for optimal immune evasion and tumor growth.

1.2.2 Tumor-extrinsic factors

In addition to tumor-intrinsic factors, the tumor immune landscape plays a pivotal role in glioblastoma immune evasion (Figure 4). It is characterized by lymphocyte depletion combined with high infiltration of myeloid cells [45, 57].

Moreover, the myeloid compartment comprises up to 30 % of all cells in the TME and is a major contributor of immune-suppression [45, 58, 59]. It consists of tumor-associated macrophages and microglia (TAMs), and myeloid-derived suppressor cells (MDSCs). The TAMs exist in a range of phenotypes that can be differentiated based on the expression of phenotypic markers and the most basic distinction is made between the pro-inflammatory M1 state and the anti-inflammatory, pro-tumorigenic M2 phenotype. Within the TAM population, especially the M2-polarized macrophages establish a pro-tumorigenic TME: they express cell surface markers and release growth factors and immune-suppressive cytokines, which inhibit the anti-tumor immune response and promote tumor proliferation and invasion [60–64]. Latest studies have also shown that glioblastoma induces a shift in the polarization from M1 to the M2 phenotype by secreting interleukins, cytokines and metabolites [62, 65]. Additionally, a recent study revealed a complex and unique relationship between the bone marrow niche of the skull and brain inflammation in several neurodegenerative diseases [66] and it will be fascinating to explore to which extent the microenvironment of glioblastoma is shaped by the skulls unique immune cell niche.

The heterogenous MDSC populations are powerful inhibitors of anti-tumor immune responses in glioblastoma [67]. They contribute to the immunosuppressive microenvironment by depleting amino acids essential for T cell function via expression of Arginase and inducible nitric oxide

(iNO) synthase, and increased production of reactive oxygen species (ROS), and IL-10 [68–70].

Within the tumor-infiltrating lymphocytes, regulatory T cells (Tregs) are the most abundant population [71]. They contribute to the local immune suppression by secreting immune-suppressive cytokines and downmodulating co-stimulatory molecules on antigen-presenting cells in order to hamper anti-tumor immune responses (reviewed in [72]).

Further tumor-infiltrating lymphocytes include $CD8^+$ and $CD4^+$ T cells, which play an important role in eliminating cancer cells and in enhancing the anti-tumor capabilities of other immune cells. However, their potent cytotoxic potential is often hindered by limited tumor infiltration or by acquiring a nonfunctional, exhausted state within the TME. This exhaustion state is characterized by the upregulation of inhibitory receptors such as PD-1, altered cytokine secretion profiles, as well as metabolic and epigenetic changes [73–75]. Persistent antigen exposure and chronic T cell activation, as well as the high levels of immune-suppressive cytokines such as IL-10, TGF-β within the TME are among the factors that contribute to T cell exhaustion in glioblastoma [70, 75].

Natural killer (NK) cells are part of the innate immune system and powerful eliminators of aberrant cells by secreting death ligands such as TRAIL and FasL and perforin/granzyme B. However, in the TME of glioblastoma, NK cells play a minor role and are often non-functional due to the negative regulation by TAMs, MDSCs and Tregs [22], the upregulation of the inhibitory ligand HLA-G [76, 77], and the secretion of TGF-β by tumor cells (reviewed in [55]).

Together, these mechanisms induce an immunosuppressive environment leading to dysfunctional and exhausted cytotoxic T cells unable to launch an effective immune response [70, 73]. In a clinical setting, counteracting the dysfunctionality to restore T cell anti-tumor activity by targeting immune checkpoints led to substantial progress in the treatment of other difficult-to-treat cancers [78]. Importantly, the use of similar immune checkpoint inhibitors is currently under clinical investigation in glioblastoma, however, yet published clinical trials are disappointing an did not lead to approval of the investigated drugs [16, 79, 80].

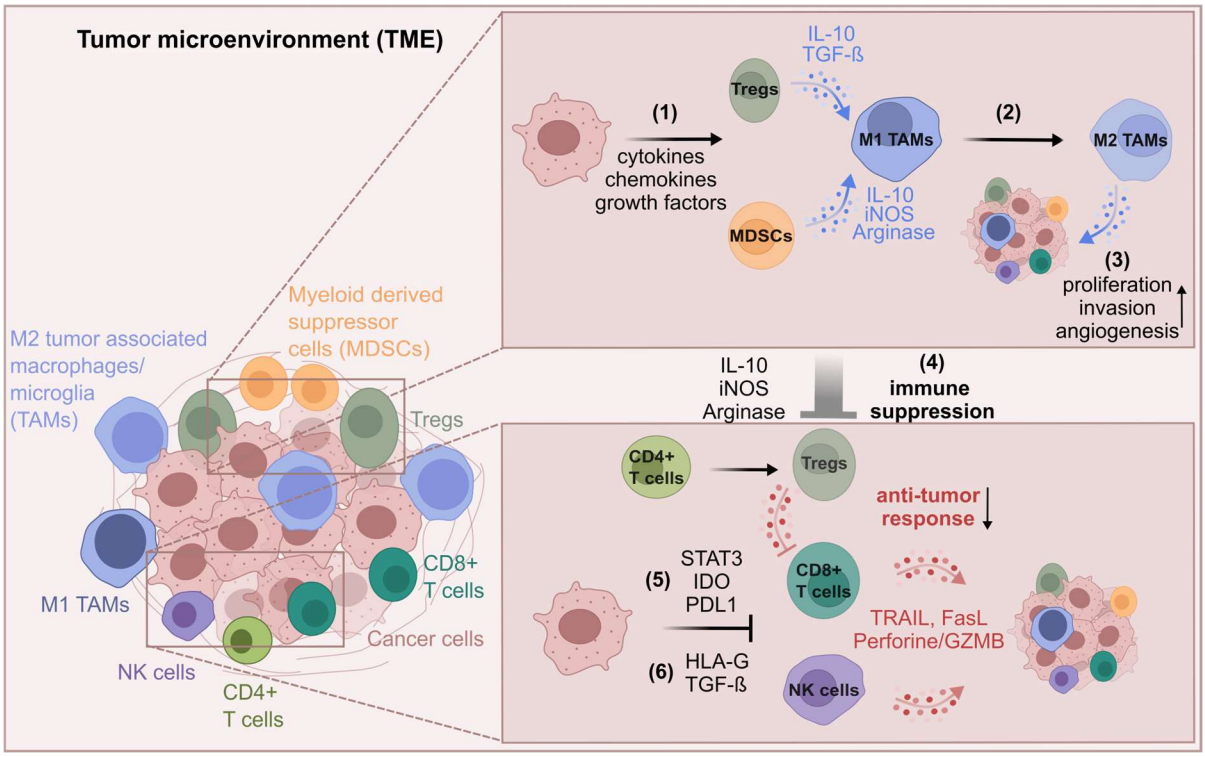

Figure 4. Simplified overview of the immune landscape of glioblastoma. (**1**) Cytokines, chemokines, and growth factors secreted by the tumor cells recruit MDSCs, TAMs and Tregs into the TME. (**2**) The anti-inflammatory TME polarizes pro-inflammatory M1 TAMs into pro-tumorigenic M2 TAMs, which support tumor growth, invasion and angiogenesis (**3**). The high levels of IL-10, Arginase and iNO secreted by Tregs, M2 TAMs and MDSCs suppress anti-tumor immune responses by T cells and NK cells (**4**). Upregulation of immune-suppressive pathways, such as STAT3 and IDO, and secretion of immune-suppressive cytokines by tumor cells further impedes an effective anti-tumor immune response (**5**). Surface expression of inhibitory ligands by tumor cells, such as HLA-G and PDL-1, contribute to impaired NK- and T cells, respectively (**6**). MDSC, myeloid-derived suppressor cells; TAM, tumor-associated macrophages/microglia; Tregs, regulatory T cells; IL-10, interleukin-10; iNO, inducible nitric oxide synthase; NK, natural killer; HLA-G, human leukocyte antigen-G; PDL-1, programmed death-ligand-1; GZMB, Granzyme B; STAT3, signal inducer and activator of transcription 3; IDO, indoleamine 2,3-dioxygenase; TGF-β, transforming growth factor beta.

1.3 Apoptosis

Apoptosis is a complex and highly regulated form of programmed cell death (PCD) that allows a cell to die without initiating a strong immune response. It is highly conserved in multi-cellular organisms and required for a multitude of physiological processes such as embryogenesis and maintaining cellular homeostasis. There are many alternative routes of programmed and non-programmed cell death that are activated by their specific triggers (reviewed in [81]), but apoptosis is the most studied one. However, apoptosis is not an isolated process but there is extensive crosstalk with other forms of PCD, which can reciprocally support or inhibit each other (reviewed in [81–83]).

Apoptosis requires the activation of cysteine-aspartic proteases (caspases) and occurs via two different pathways (reviewed in [84]) (Figure 5). These include the extrinsic pathway, which is activated by the binding of death ligands to their corresponding receptors on the cell surface or within the cytosol, and the intrinsic pathway, which is mediated by the mitochondria. These two pathways can act independently, but they also work synergistically to efficiently remove aberrant cells.

Dysregulated apoptosis is associated with many pathologies and already in 2000, Hanahan and Weinberg described the resistance to apoptotic cues as a hallmark of cancer, leading to uncontrolled growth of transformed cells [85]. Understanding how tumor cells evade apoptosis and identifying mechanisms that promote tumor cell death is an important goal for the development of more effective treatments for glioblastoma.

1.3.1 Extrinsic pathway of apoptosis

The immune system plays a major role in cancer immune surveillance. The main effector cells are NK cells and cytotoxic T cells, which release death ligands and cytolytic granules to stimulate tumor cell apoptosis [86, 87].

The extrinsic apoptotic pathway is triggered by the oligomerization of death receptors (DR) with their respective death ligands. These include the Tumor necrosis factor receptor 1 (TNFR1) and its ligand TNFα [88], TNF-related apoptosis inducing ligand (TRAIL) receptors DR4 and DR5, which bind TRAIL [89], and the Fas receptor and its ligand FasL [90].

Ligand-receptor interaction enables the formation of the death inducing signaling complex (DISC) [91]. The DISC consists of adaptor proteins, such as Fas-associated death domain protein (FADD) or TNFR1-associated death domain (TRADD), which recruit the initiator caspases procaspase-8 or procaspase-10 [92, 93]. Binding of the procaspases induces homodimerization and auto-catalytic cleavage into active caspase-8 or -10 [94]. Active caspase-8 or -10 are released into the cytosol and initiate apoptosis by cleaving and activating the executioner

caspases-3 or -7. DISC activation can be inhibited by cellular FLICE-like inhibitory protein (cFLIP), which is structurally similar to caspase-8 but lacks catalytic activity and thus competes for FADD binding [95].

1.3.2 Intrinsic pathway of apoptosis

In addition to the extrinsic pathway, there is an intrinsic apoptosis pathway that is dependent on mitochondria and is induced by e.g., nutrient deprivation, DNA damage, and UV radiation. It is strictly regulated by a fine balance between pro-apoptotic (BID, Bak, Bax etc.) and anti-apoptotic (Bcl-2, Mcl-1, Bcl-xL) B-cell lymphoma 2 (Bcl-2) family of proteins (reviewed in [96]). This family can be further divided into activator (BID, BIM, PUMA) and sensitizer proteins (BAD, Noxa, Bik) [96]. Upon activation of the intrinsic apoptotic pathway, activator proteins stimulate the oligomerization of the proteins BAX and BAK which start to form pores in the mitochondrial membrane [97, 98]. Sensitizer proteins contribute to apoptosis induction by binding and inhibiting anti-apoptotic Bcl-2 family proteins [96, 99]. The pores in the mitochondrial membrane result in loss of membrane potential, release of cytochrome c, and apoptosome formation. The apoptosome complex consists of cytochrome c, deoxyadenosine triphosphate (dATP), apoptotic protease activating factor-1 (Apaf-1) and procaspase-9 and induces the autocatalytic activation of caspase-9 and subsequent activation of the executioner caspase-3 or -7 [100].

Both, the extrinsic and the intrinsic pathway, can act independently, but they are also connected. For example, in many tumor cells, activation of the extrinsic pathway is insufficient to trigger apoptosis and simultaneous activation of the intrinsic pathway is required. This is accomplished by caspase-8, which can directly cleave BID, leading to the activation of the intrinsic pathway and amplification of the extrinsic signal [101].

Finally, the active executioner caspases cleave DNA repair enzymes and cytoskeleton proteins causing mitochondrial dysfunction, chromatin condensation, membrane blebbing and cell fragmentation (reviewed in [102, 103]). The cell is then packaged into apoptotic bodies and removed by phagocytic cells.

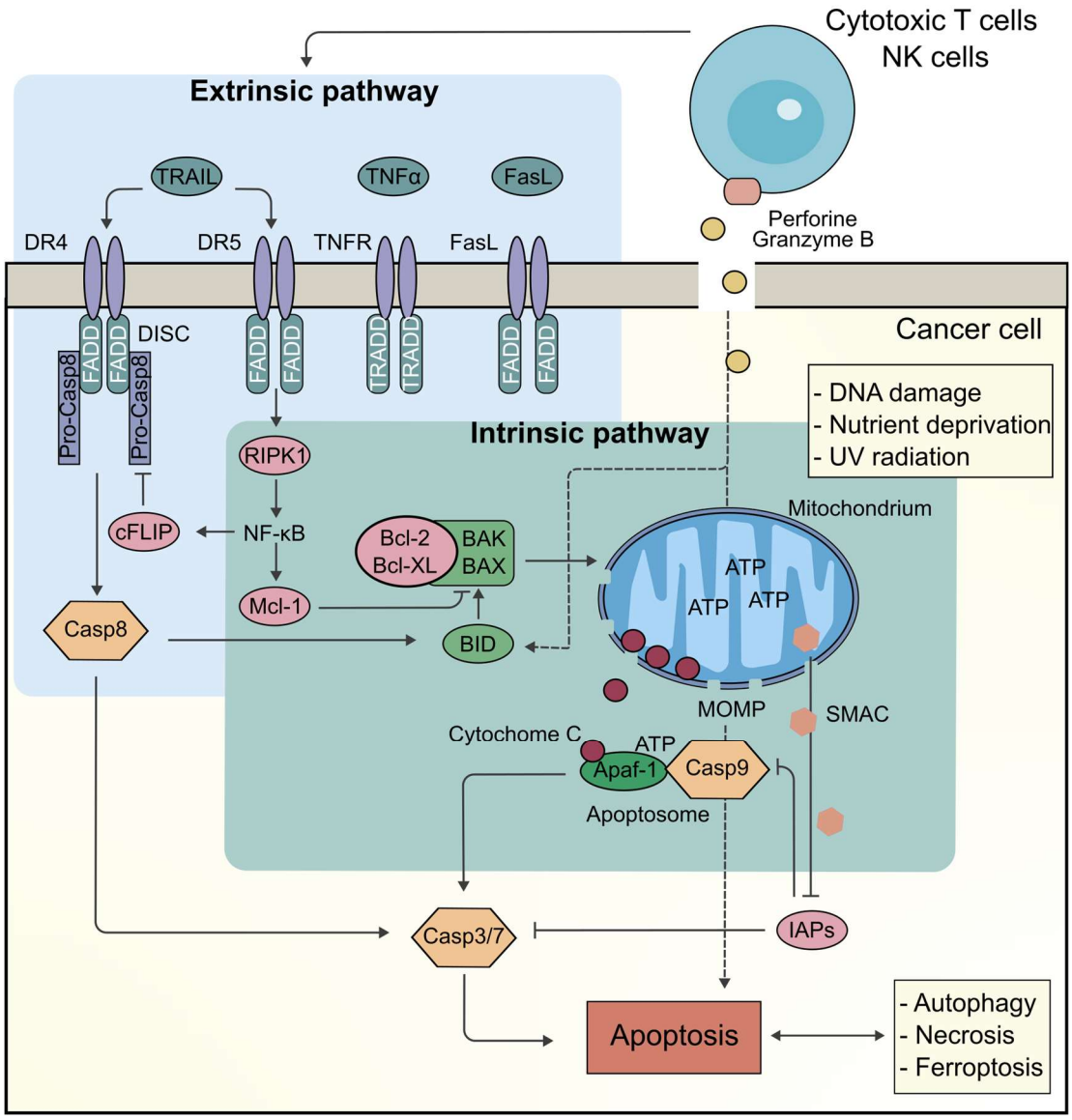

Figure 5. Overview of the extrinsic and intrinsic pathways of apoptosis. Cytotoxic T cells or natural killer (NK) cells produce death ligands or cytotoxic granules to induce apoptosis. Death ligands bind to their death receptors to initiate the extrinsic apoptotic cascade by activating caspase-8. TRAIL receptors can also induce NFκB to trigger pro-survival signaling. To amplify the apoptosis signal, caspase-8 activates the intrinsic pathway by cleaving BID. The intrinsic pathway is also induced by intrinsic factors such as DNA damage, nutrient deprivation or UV radiation and is regulated by anti- and pro-apoptotic proteins of the Bcl-2 family. Anti-apoptotic Bcl-2 proteins inhibit pro-apoptotic Bcl-2 proteins. Pro-apoptotic Bcl-2 proteins induce mitochondrial outer membrane permeabilization (MOMP), which leads to the mitochondrial release of pro-apoptotic factors such as cytochrome c and second mitochondria-derived activator of caspases (SMAC). SMAC inactivates inhibitor of apoptosis (IAP) proteins that negatively regulate caspase activation. Cytochrome c, together with ATP, Apaf-1 and caspase-9 (Casp9) form the apoptosome which activates caspase-3/-7. There are negative and positive interactions between apoptosis and other forms of cell death such as autophagy, necrosis, and ferroptosis. Anti-apoptotic regulators are shown in light red, pro-apoptotic regulators are shown in green. Own illustration based on [84].

1.3.3 TRAIL

The death receptor ligand TRAIL has received more attention than any other death ligand in cancer research. This is due to TRAIL´s ability to induce apoptosis in a broad range of tumor cells, while leaving untransformed cells unharmed [104, 105].

TRAIL is a type II transmembrane protein with a receptor binding domain on its extracellular carboxyl terminus [104]. Transmembrane TRAIL can be cleaved by metalloproteases to release a soluble form that remains biologically active [106]. Human TRAIL can bind two death receptors (DRs), DR4 and DR5, which include full-length death domains (DD), are ubiquitously expressed, and conduct apoptosis signaling via the caspase cascade (Figure 6) (reviewed in [107]). DR4 is activated by both soluble and membrane-bound TRAIL, whereas DR5 is only activated by membrane-bound TRAIL [108]. There are three alternative receptors, which include the two decoy receptors, DCR1 and DCR2, and osteoprotegerin (OPG). All of those either completely lack the intracellular DD domains or carry only a truncated domain, and thereby favor pro-survival signaling (Figure 6) (reviewed in [107]).

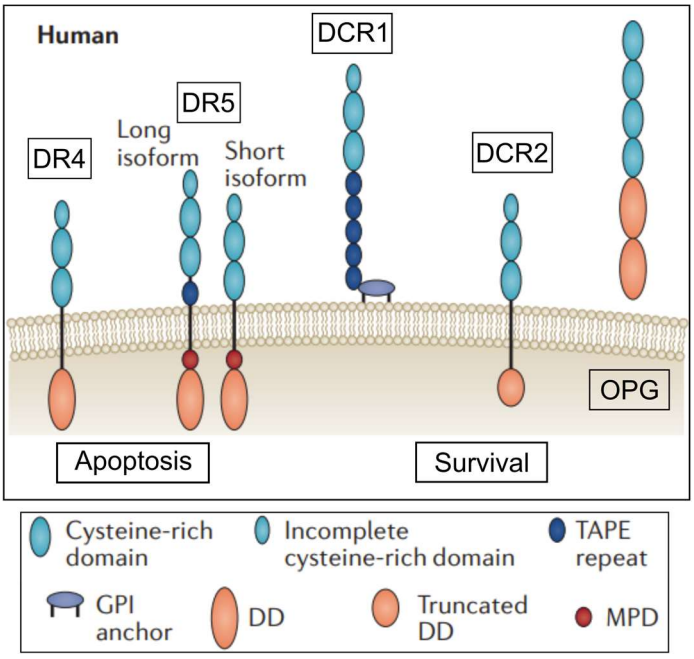

Figure 6. Human TRAIL can bind to five receptors. TRAIL receptor 1 (DR4) and TRAIL receptor 2 (DR5) contain intracellular death domains (DD) to conduct apoptosis signaling. There are two splice variants of DR5 which differ in the presence of the TAPE (threonine, alanine, proline, glutamine) domain. The TRAIL-R3 (DCR1) contains a glycosylphosphatidylinositol (GPI) anchor and misses an intracellular DD. TRAIL-R4 (DCR2) has a truncated DD that can induce pro-survival signaling but not apoptosis. Osteoprotegerin (OPG) is a soluble TRAIL receptor that binds TRAIL with low affinity (adapted and modified from [107]). MPD, membrane proximal domain.

TRAIL sensitivity can be regulated at multiple levels, and like many cancers, glioblastoma has developed various strategies to evade TRAIL-induced apoptosis. These include altered expression patterns or structural alterations of TRAIL death and decoy receptors, resulting in reduced sensitivity to TRAIL-induced apoptosis and a preference for pro-survival signaling [109, 110]. For example, studies have shown that TRAIL receptor binding can activate the nuclear factor (NF)-κB to induce transcription of anti-apoptotic, pro-survival and pro-inflammatory genes [111, 112]. The mitogen-activated protein (MAP) kinases, in particular the extracellular signal-regulated kinase (ERK), are also involved in TRAIL-induced non-apoptotic effects. TRAIL induces phosphorylation of ERK1/2, which leads to the transcription of pro-survival and pro-proliferative genes [113–115].

Furthermore, the TRAIL initiator caspase caspase-8 is heterogeneously expressed, with some tumors exhibiting low or even absent caspase-8 expression [116–118], and others often retaining variable levels of caspase-8 activity [119, 120]. These studies describe an alternative tumor-supporting role of active caspase-8 in glioblastoma, promoting tumor growth and malignancy rather than inducing apoptosis [119–121].

Finally, anti-apoptotic proteins like cFLIP, Bcl-2, Bcl-xL and Mcl-1 are associated with TRAIL-resistance and are frequently overexpressed in glioblastoma [122–125].

1.4 Metabolism

Metabolism is another feature that thoroughly interacts with glioblastoma-shaping events in the TME. Most importantly, to efficiently meet the increased energy demand of rapid proliferation, tumor cells have to adapt their metabolism accordingly.

Depending on their genetic background and the nutrient availability in the TME, tumor cells can modify the flow through metabolic pathways such as anaerobic and aerobic glycolysis, oxidative phosphorylation, pentose phosphate pathways, fatty acid oxidation and, amino acid- and nucleotide metabolism [126, 127]. Metabolic reprogramming can be attributed to alterations in signaling pathways such as PI3K-AKT-mTORC1, cMyc and p53 (reviewed in [128–130]). Alterations in these pathways can for example increase the metabolic flux via transcriptional upregulation and phosphorylation of metabolic transporters and metabolic enzymes (reviewed in [128–130]).

Glioblastoma cells are highly dependent on glucose as energy source. Glucose can either undergo glycolysis coupled to lactate fermentation or is processed and transported as pyruvate into the mitochondria, where oxidative phosphorylation takes place [131] (Figure 7). Inside the mitochondrial matrix, pyruvate is further metabolized in the tricarboxylic acid (TCA) cycle, which generates free electrons that are transferred to NAD and FAD. Through these electrons

carriers, electrons are channeled into the electron transport chain (ETC). The ETC consists of four multiprotein complexes and the stepwise movement of the electrons through these complexes is used to create a proton gradient across the inner mitochondrial membrane (IMM). The final electron acceptor is O_2, which is reduced to water. The generated proton gradient is then used to fuel the F_OF_1-ATPase (complex V) to produce large amounts of ATP (30-36 ATP) in a process called oxidative phosphorylation (OXPHOS). Although OXPHOS is more efficient in providing energy, some tumor cells use glycolysis and lactate fermentation to generate ATP with a much lower yield of 2 ATP even in the presence of oxygen (Warburg effect, i.e. aerobic glycolysis) [132]. The intermediates produced by aerobic glycolysis can be used for the synthesis of nucleotides, lipids and amino acids to support proliferation [133]. At the same time, increased lactate levels cause acidification of the TME, which contributes to the immunosuppressive environment [134–136].

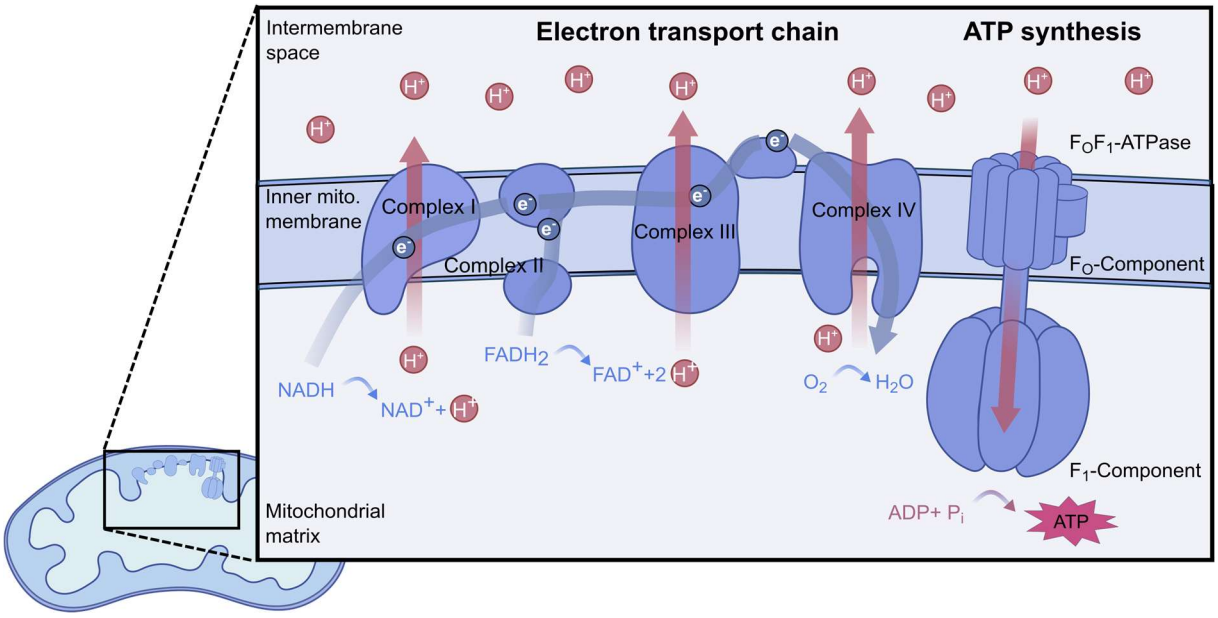

Figure 7. Overview of the electron transport chain and ATP synthesis in mitochondria. The electrons of the electron carriers NADH and $FADH_2$ enter the electron transport chain of the inner mitochondrial membrane. There, they pass through four large protein complexes (complex I-IV) until they are transferred to oxygen, which is reduced to H_2O. The energy released in this process is used to transfer protons from the mitochondrial matrix to the intermembrane space. Since the inner mitochondrial membrane is impermeable to protons, this generates a proton gradient. Protons then flow back into the mitochondrial matrix along the concentration gradient through the F_oF_1 ATPase. This proton motive force is used to generate ATP. Own illustration based on [131].

However, the majority of tumor cells are capable to switch between non-oxidative and oxidative pathways to produce both, macromolecular precursors and energy [137–139]. Additionally, a byproduct of high metabolic activity is the increased production of reactive oxygen species (ROS), which may promote tumor malignancy directly and indirectly (reviewed in [140]). More

specifically, glioblastoma cells are highly plastic and can switch between different carbon sources to overcome nutrient shortages [138, 141, 142].

Alterations and adaptations of the cellular metabolism is a major contributor to the malignancy and treatment resistance of glioblastoma. Therefore, the identification of new metabolic vulnerabilities is indispensable for novel treatment strategies.

1.5 TSPO

In 1977, an alternative receptor for benzodiazepines was discovered and named peripheral benzodiazepine receptor (PBR) [143]. Soon however, PBR was increasingly recognized for its affinity to cholesterol and its role in cholesterol transport across the mitochondrial membrane. Accordingly, its name was changed to translocator protein TSPO [144]. Due to its high conservation across the three phylogenetic kingdoms [145] and the reported embryonic lethality of TSPO knockout mice [146, 147], it has been considered a critical protein for steroidogenesis and has attracted considerable research interest. Studies mainly employed synthetic TSPO ligands and *in vitro* models and soon TSPO was described to be associated with a multitude of cellular functions. These include cholesterol transport and steroidogenesis [148, 149], but also cell proliferation [150], apoptosis [151], and mitochondrial functions [152, 153].

However, emerging discrepancies between recent *in vivo* genetic models and pharmacological studies of TSPO indicated that distinct molecular functions of TSPO are still enigmatic [154–157]. This highlights the demand for further experiments to determine the biological function of TSPO under physiological and pathological conditions.

1.5.1 TSPO expression

Studies in adult rats revealed that TSPO is expressed in many peripheral tissues and the highest concentrations are found in steroid-synthesizing tissues such as adrenal glands [158]. In the central nervous system (CNS) however, TSPO levels are generally low and mostly restricted to ependymal and glial cells [159]. Increased expression of TSPO has been observed in activated microglia during brain inflammation, in neurodegenerative disorders, and in brain tumors [159–161]. This led to the development of specific radiolabeled TSPO positron-emission tomography (PET) tracers to image the increased TSPO expression in areas of neuroinflammation and brain tumors *in vivo* [162, 163].

On a transcriptional basis, TSPO expression is regulated at multiple levels. The functional characterization of the *TSPO* promotor revealed a GC-rich promotor with several binding sites for transcription factors including Pu.1, Activator protein 1 (Ap1), STAT3, Specificity protein 1 (Sp1), Sp3, and Sp4 [164, 165]. There is evidence that TSPO expression is dependent on the

PKCε/ERK1/2-AP1-STAT3 signaling pathway, suggesting that increased TSPO levels in cancer may be attributed to abnormal signaling through this pathway [166]. Furthermore, aberrant promotor methylation patterns might contribute to an upregulation of TSPO expression, but the exact relationship remains to be elucidated [164, 167].

1.5.2 Protein structure and subcellular localization of TSPO

TSPO is an 18 kilodalton (kDa) transmembrane protein, located in the outer mitochondrial membrane (OMM). The current understanding of the TSPO structure at molecular level is based on a nuclear magnetic resonance (NMR) study of mouse TSPO in complex with the ligand PK11195 (ProteinDataBank ID: 2MGY, [168]. It shows that TSPO consists of 169 amino acids that span the OMM via five α-helical transmembrane domains [168]. The highly positive charged C-terminus protrudes into the cytoplasm and the N-terminal end is exposed into the intermembrane space [168]. TSPO encodes a cholesterol-recognition amino acid consensus (CRAC) motif close to the C-terminal end that allows binding of cholesterol at nanomolar affinity [168, 169].

The TSPO protein is encoded by chromosomal DNA and its mitochondrial targeting and import depends on its C-terminus and Schellman motif [170]. Once integrated into the OMM, TSPO can polymerize [171, 172] and form complexes with other mitochondrial proteins such as voltage-dependent anion channel 1 (VDAC1), adenine nucleotide translocase (ANT), steroidogenic acute regulatory protein (StAR), and others [173–175]. It is hypothesized that TSPO mediates a multitude of proposed cellular functions as part of these multi-protein complexes.

1.5.3 Endogenous and synthetic TSPO ligands

Endogenously, TSPO can bind to porphyrins [176], cholesterol [169], and the acyl-CoA-binding protein (ACBP), previously known as diazepam binding inhibitor (DBI) [177].

The majority of synthetic TSPO ligands were primarily developed as neuroimaging agents (reviewed in [178]). They include first generation TSPO ligands such as PK11195 and Ro5-486, but also pharmacokinetically improved ones such as GE-180 and ER176 (reviewed in [179]). Additionally, synthetic TSPO ligands were used to functionally characterize TSPO in a multitude of studies [148, 153, 180]. However, the mode of action is often not well defined and the specificity of TSPO ligands is debated. Several studies report off-target sites and effects independent of TSPO [156, 181, 182].

TSPO ligands were also shown to have therapeutic potential (reviewed in [178]). However, etifoxine (Stresam®) is the only ligand that is clinically approved for the treatment of anxiety-related disorders in France. It exerts its anxiolytic effects by targeting both, TSPO and $GABA_A$ receptors [183].

Still, the development of novel, more specific ligands with improved pharmacokinetic properties continues to progress, offering the opportunity to therapeutically target TSPO in patients.

1.5.4 TSPO in immunomodulation

TSPO is one of the most widely studied biomarkers for neuro-inflammation. During inflammatory processes, TSPO levels increase in specific cell types, but the precise function of this upregulation is far from being understood (reviewed in [184]).

Microglia/macrophages and astrocytes are major sources of TSPO in neuro-inflammation. Studies using *in vitro* and *in vivo* mouse models showed that TSPO is selectively upregulated in pro-inflammatory-polarized microglia/macrophages and astrocytes after treatment with pro-inflammatory stimuli [160, 185]. In line with these findings, TSPO was most prominently upregulated after treatment with pro-inflammatory IL-1β and IFNγ in a recent study using human C20 microglia [186]. The study also showed that treatment with TSPO ligands increased the secretion of anti-inflammatory cytokines, whereas the downregulation of TSPO resulted in an elevated secretion of pro-inflammatory cytokines [186].

However, also conflicting results have been reported. For instance, IFNγ and lipopolysaccharide (LPS) stimulation induced TSPO expression in rodent-derived macrophages and microglia, whereas TSPO expression did not change in human primary microglia and was even downregulated in human monocyte-derived macrophages [187].

In glioblastoma, TSPO is not exclusively expressed in tumor-infiltrating glial cells, but also at high levels in tumor cells [161]. There is evidence that pro-inflammatory stimuli also increase TSPO expression/levels in cancer cells. For example, TNFα was shown to upregulate TSPO via the induction of IL-8 in HT-29 human colon carcinoma cells [171]. This was coupled to increased ROS production and the induction of cell death, which could be prevented by the TSPO ligand PK11195 [171].

At this point, it is not known if high concentrations of TSPO in the tumor indirectly or directly affect immunosuppression of glioblastoma. For example, a link between TSPO activation and the impact on cytotoxic effector T cells has not been established so far. Recent studies suggest that TSPO is involved in ROS production [171, 188, 189]. ROS are known to stimulate the expression/release of immunomodulatory cytokines [190, 191] or to directly impact surrounding immune cell populations including effector T cells [192–194], possibly indicating a connection between TSPO expression and immunomodulation.

1.5.5 TSPO in apoptosis

As described before, mitochondria play a key role in regulating cell death through a variety of mechanisms. The localization of TSPO in the OMM designates it a reasonable candidate for

the modulation of apoptosis, however, data collected over the years are controversial (reviewed in [184]).

Intuitively, a high expression of TSPO in glioblastoma cells as well as the TME could suggest tumor-protective effects. However, TSPO knockdown in C6 rat glioma or human U118MG glioblastoma cells revealed a pro-apoptotic effect of TSPO, as TSPO-deficient cells were resistant to apoptosis-induction in both models [151, 195]. In addition, the exposure of several cancer cell lines, including glioblastoma, to various TSPO ligands resulted in the collapse of the mitochondrial membrane potential, activation of the caspase cascade and subsequent apoptosis [196–198]. In contrast to that, TSPO ligands were also described to reduce apoptosis in different glioma cells lines [151, 180, 199].

Furthermore, the mechanism how TSPO modulates apoptosis is also not clear yet. It has been suggested that TSPO, in cooperation with VDAC1 and ANT, controls mitochondrial membrane permeability by regulating the conductance of the mitochondrial permeability transition pore (mPTP) [200]. This assumption was supported by experimental evidence that shows that TSPO ligands modulate the activity of the mPTP [152, 201, 202]. Lately however, the role of TSPO on mPTP function has been challenged. A study in liver-specific TSPO $^{-/-}$ KO mice revealed that the TSPO protein is not a member of the mPTP complex and that the control of mPTP activity occurs through a mechanism independent of TSPO [156]. In addition, the effect of TSPO ligands on mPTP activity was mediated by interactions with different, yet unknown targets [156]. Nevertheless, there are recent studies in other model systems showing that knockout of TSPO significantly reduced the mitochondrial membrane potential [203–205].

In conclusion, the role of TSPO in apoptosis and mPTP function remains unclear, and controversies indicate that the impact of TSPO depends on species and cell type. Further studies are required to characterize TSPO as an apoptosis modulator in glioblastoma.

1.5.6 TSPO in mitochondrial respiration

Mitochondria not only play an important role in apoptosis, but they are also the central source of energy by producing large amounts of ATP for cell survival und functioning. In this context, there is increasing evidence that TSPO is linked to the cellular energy balance (reviewed in [184]).

For instance, microglia isolated from TSPO knockout mice showed an altered oxygen consumption and lower ATP levels compared to wildtype counterparts [206]. The stable overexpression of TSPO in Jurkat cells with low endogenous TSPO resulted in the upregulation of electron transport chain (ETC)-related genes, elevated mitochondrial ATP production, and, consequently, increased cell proliferation and motility [207]. Consistent with these findings,

loss of TSPO in C20 microglia decreased the mitochondrial membrane potential and cytosolic Ca^{2+} levels, which was accompanied by a reduction in mitochondrial respiration [205].

A study using a glioma animal model and patient-derived glioblastoma cells revealed that TSPO plays a key role in glioma malignancy by controlling the metabolic balance between OXPHOS and glycolysis [208]. The authors could show that TSPO knockout in these models resulted in increased mitochondrial fragmentation, reduced ATP production, and decreased mitochondrial oxidative phosphorylation. Moreover, TSPO-deficiency caused a metabolic shift towards glycolysis, evidenced by increased glucose uptake and lactic acid conversion [208].

However, a contradictory study has been published as well. In this study, the comparison of oxygen consumption rates of mitochondria from liver-specific TSPO knockout mice and wildtype counterparts showed no difference in basal, ATP-linked and -independent respiration [156].

Mechanistically, TSPO has been associated with the F_OF_1 ATPase, which is responsible for ATP production during OXPHOS, although the exact mode of action is not known yet [182, 209]. Liu and colleagues proposed that TSPO might modulate the F_OF_1 ATPase via a direct interaction with the ATP “synthasome” complex (composed of ATPase, phosphate carrier, and ANT) and the PBR complex composed of TSPO, VDAC1 and ANT [207] .

Taken together, the majority of these studies support the role of TSPO in mitochondrial energy metabolism. The conflicting results point out the idea that the response to loss of TSPO may be variable and dependent on cell type, tumor developmental state and microenvironmental dependencies. Further studies will be required to evaluate TSPO as a target for altered bioenergetics in glioblastoma.

1.5.7 TSPO in glioblastoma

Early on, it was recognized that TSPO expression was increased in glioblastoma compared to the non-neoplastic brain [210]. The level of TSPO expression correlates with the grade of malignancies among glioma cell proliferation, apoptotic indices and poor clinical outcome of patients [161, 180, 211]. Various studies also indicate an involvement of TSPO in several malignant hallmarks of glioblastoma (reviewed in [184, 212]) (Figure 8). However, the functional relevance of high TSPO levels in glioblastoma remains unresolved and warrants further investigations on TSPO's role in immune modulation, apoptosis, and metabolism, the deregulation of which contribute significantly to the malignancy of glioblastoma.

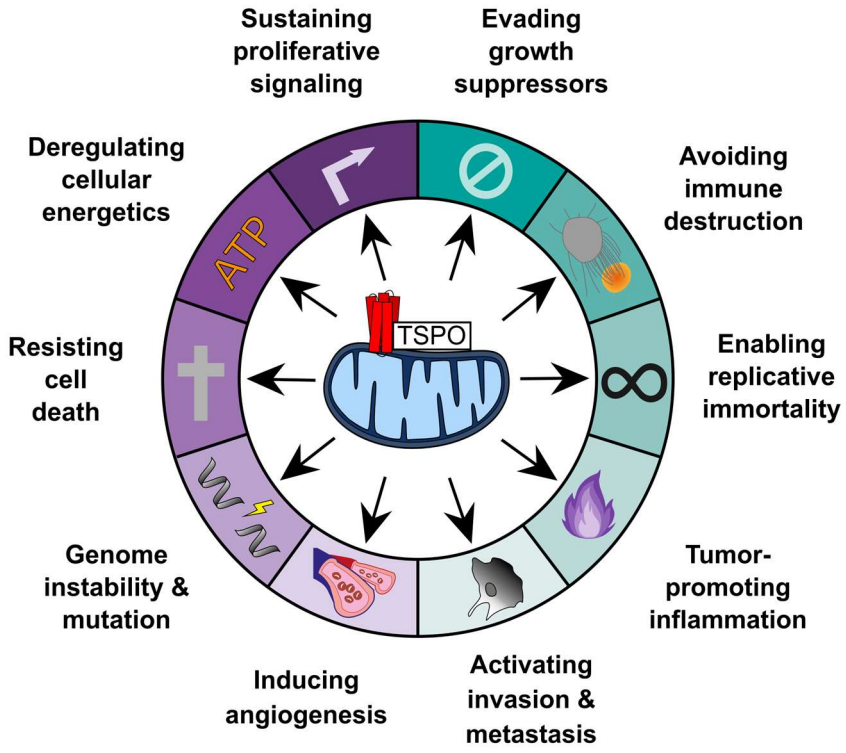

Figure 8. The role of TSPO in the hallmarks of glioblastoma. TSPO has been discussed to play a role in several hallmarks of cancer that were first described by Hanahan and Weinberg in 2000. However, the majority of studies focus on the role of TSPO in resisting cell death and deregulated cellular energetics. The image is based on the work of [212] and is adapted from [184].

2 Aims of the thesis

The ability of glioblastoma to evade T cell immune control adds largely to the devastating nature of this brain tumor. In this context, resistance to extrinsic and intrinsic apoptosis pathways and metabolic imbalances are key hallmarks of glioblastoma that further contribute to immune evasion, malignancy, and tumor progression. Despite intensive research, current therapy options are limited, and new therapeutic targets are desperately needed.

Based on evidence in the literature, TSPO, a protein significantly upregulated in glioblastoma, may be involved in these malignant features of glioblastoma.

Here, I hypothesize that TSPO might protect glioblastoma tumor cells against cytotoxic T cell attacks and that modulation of TSPO activity could represent a promising intervention in terms of glioblastoma immunotherapy. Therefore, my goal was to gain a functional understanding of TSPO in glioblastoma progenitor cells in response to T cell immune control. In particular, the work is focused on the role of TSPO in the regulation of and resistance to apoptosis and its impact on mitochondrial respiration.

Based on this background, the specific aims of this thesis are to,

- Characterize the relevance of TSPO in glioblastoma hallmark features such as cell viability, migration, and proliferation.
- Study the involvement of TSPO in mechanisms that follow T cell attack such as apoptotic cell death and the release of immune-modulatory cytokines triggered by cytotoxic effector molecules.
- Study the role of TSPO in basic mitochondrial functions such as mitochondrial respiration and ROS production.

3 Materials and Methods

3.1 Materials

3.1.1 Laboratory equipment

Table 1. Laboratory equipment used in this thesis including the company in alphabetical order.

Instrument	Company
-80 °C Freezer Forma 900	Thermo Scientific, USA
AF6000LX fluorescence microscope	Leica, Germany
Agarose gel chambers PeferctBlue Gelsystem Mini S and L	Peqlab, Germany
Agarose gel documentation/ Transilluminator	Peqlab, Germany
centrifuge 5430R, refrigerated	Eppendorf, Germany
FACS Canto™ II Flow Cytometer	BD Biosciences, USA
Fluorescence microscope Axio Observer Z1	Zeiss, Germany
Gilson™ PIPETMAN Classic 0.2-2 µl	Gilson, USA
Gilson™ PIPETMAN Classic 1-10 µl	Gilson, USA
Gilson™ PIPETMAN Classic 200-1000 µl	Gilson, USA
Gilson™ PIPETMAN Classic 20-100 µl	Gilson, USA
Gilson™ PIPETMAN Classic 20-200 µl	Gilson, USA
Gilson™ PIPETMAN Classic 2-20 µl	Gilson, USA
Heating Block Thermomixer 5436	Eppendorf, Germany
HeraCell incubator	Thermo Scientific, USA
Heraeus Biofuge Pico centrifuge	Hanau, Germany
Heraeus Multifuge 3 S-R	Thermo Scientific, USA
HeraSafe laminar flow	Thermo Scientific, USA
Image Quant LAS 4000	GE Healthcare, USA
Light microscope Fluovert Type 090-123.012	Leitz, Germany
Mastercycler ep gradient S	Eppendorf, Germany
Mehrfachdispenser-Pipette Multipette® M4	Eppendorf, Germany
Mini Trans-Blot® Cell	Bio-Rad, USA
NanoPhotometer P300	Implen, Germany
Neubauer hemacytometer (Depth 0.1 mm; 0.0025 mm^2	Assistent, Germany
Orbital Shaker DOS-10L	NeoLabLine, Germany
pH-meter CG842	Schott, Germany
Power Supply PowerPac™ Basic	Bio-Rad, USA

Powersupply EC4000P Series 90	EC Apparatus Corporation, USA
qTR-PCR Cycler Mx3005 P	Agilent Stratagene, USA
SDS Page PeferctBlue Dual Gel Twin S	Peqlab, Germany
Seahorse XFp Extracellular Flux Analyzer	Agilent Technologies, USA
Tilt/roller mixer RS-TR 05	Phoenix instrument, Germany
VarioSkan Flash Multimode Reader	Thermo Scientific, USA
Vortex Genie 2	Scientific industries, USA
Water bath 1083	GFL, Germany

3.1.2 Chemicals and reagents

Table 2. Chemicals and reagents used in this thesis including the company in alphabetical order.

Article	Order number	Company
2-Methylbutane	M32631	Sigma-Aldrich, Germany
30 % Acrylamide/Bis Solution	3029.1	Bio-Rad, Germany
Accutase	A6964	Sigma-Aldrich, Germany
AEBSF	A8456	Sigma- Aldrich, Germany
Ammoniumpersulfat (APS)	A9164	Sigma-Aldrich, Germany
Ampicillin	A9518-5G	Sigma-Aldrich, Germany
Bovine serum albumin (BSA)	821006	Sigma-Aldrich, Germany
Citronensäure Monohydrat	3958.1	Roth, Germany
Diemethylsufloxid (DMSO)	A994.2	Roth, Germany
Dithiothreitol (DTT)	D0632	Sigma-Aldrich, Germany
Donkey serum	S30-M	Merck, Germany
D-Sucrose	9097.1	Roth, Germany
Ethanol (> 99.8 %)	9065.4	Merck, Germany
Ethidium bromide	E1510	Sigma-Aldrich, Germany
Glucose (D+) Monohydrate	108342	Serva, Germany
Glycerol (99%)	G2025	Sigma-Aldrich, Germany
Glycin	0079.4	Roth, Germany
H_2DCFDA	D6883	Sigma, Germany
H_2O (RNase free, DNase free)	T143	Roth, Germany
HALT Protease inhibitor Cocktail, 100X	78441	Life Technologies, USA

Hydrochloric acid fuming (HCl) 37%	100317	Merck, Germany
Isopropanol	33539	Merck, Germany
Laminin	354232	Corning
LE Agarose	840004	Biozym, Germany
L-Glutamine	G7513	Sigma-Aldrich, Germany
Methanol	106007	Merck, Germany
Milk Powder Blotting grade	T 145.1	Roth, Germany
PageRuler Plus Prestained Protein Ladder	26619	Thermo Fisher Scientific, USA
Paraformaldehyd (PFA)	441244	Sigma-Aldrich, Germany
Phenylmethylsulfonyl fluoride (PMSF)	P7626-5G	Sigma-Aldrich, Germany
Ponceau S	P3504	Sigma-Aldrich, Germany
ProLong Gold Anti Fade Reagent	P36930	Thermo Fisher Scientific, USA
Resazurin	AR002	R&D Systems, USA
Sodium chloride	P029.3	Roth, Germany
Sodium deoxycholate	D6750	Sigma-Aldrich, Germany
Sodium dodecyl sulfate (SDS)	0183.3	Sigma-Aldrich, Germany
Sodium fluoride (NaF)	A0547 0500	AppliChem, Germany
Sodium hydroxide (NaOH)	109137	Merck, Germany
Sodium Orthovanadate (Na_3OV_4)	S6508	Sigma-Aldrich, Germany
Sodium pyruvate solution	S8636	Sigma-Aldrich, Germany
Sodiumcitrate-dihydrate	1.06448.1000	Merck, Germany
ß-Mercaptoethanol	M7154	Sigma-Aldrich, Germany
Tetramethylethylenediamine (TEMED)	T 9281	Sigma-Aldrich, Germany
Tris (Trizma Base)	T 1503	Sigma-Aldrich, Germany
Triton X-100	T8787	Sigma-Aldrich, Germany
Trypan Blue	T8154	Sigma-Aldrich, Germany
Trypsin	T3924	Sigma-Aldrich, Germany
Tryptone	8952.3	Roth, Germany
Tween 20	9127.1	Roth, Germany
Western HRP Substrate	WBLUFO100	Merck, Germany
XF Base Medium minimal DMEM	102353-100	Agilent Technologies, USA
XF Calibrant solution pH 7.4	103059-000, 100840-000	Agilent Technologies, USA
Yeast Extract	92144-500-G-F	Sigma-Aldrich, Germany

3.1.3 Cell culture media and supplements

Table 3. Cell culture media and supplements used in this thesis including the company in alphabetical order.

Media & Supplements	Order number	Company
CloneR™, 10 x	05888	STEMCELL technologies, Canada
DMEM Dulbecco´s Modified Eagle Medium	41965-039	Gibco™, Thermo Fisher Scientific, USA
Dulbecco´s Phosphate Buffered Saline (1x PBS)	14040133	Gibco™, Thermo Fisher Scientific, USA
Epidermal Growth Factor (EGF)	130-097-751	Miltenyi-Biotec, Germany
Fibroblast Growth Factor (FGF)	130-093-842	Miltenyi-Biotec, Germany
Penicillin-Streptomycin (P/S)	P4333	Sigma-Aldrich, Germany
RHB-A	Y40001	Takara, Japan
RPMI 1640	11875093	Gibco™, Thermo Fisher Scientific, USA

3.1.4 Recombinant proteins and functional antibodies

Table 4. Recombinant proteins and functional antibodies used in this thesis including the company in alphabetical order.

Recombinant protein	Order number	Concentration	Company
Anti-DR4 Clone HS101	GTX33944	1 mg/ml	GeneTex, USA
Anti-DR5 Clone HS201	GTX33945	1 mg/ml	GeneTex, USA
Recombinant human FasL	310-03H	100 µg/ml	PeproTech, Germany
Recombinant human IFNγ	300-02	100 µg/ml	PeproTech, Germany
Recombinant human TNFα	300-01A	100 µg/ml	PeproTech, Germany
Recombinant human TRAIL	310-04	100 µg/ml	PeproTech, Germany

3.1.5 Antibodies for Western blot

Table 5. Western blot antibodies used in this thesis including the company in alphabetical order.

Antigen	Species	Dilution	Order number	Company
Alpha Tubulin	Mouse	1:500	A11126	Invitrogen, USA
BAX	Rabbit	1:1000	2772	Cell Signaling, USA
Bcl-2	Rabbit	1:1000	4223	Cell Signaling, USA
Bcl-xL	Rabbit	1:1000	2764	Cell Signaling, USA
BID	Rabbit	1:1000	2022	Cell Signaling, USA

Caspase-3	Rabbit	1:1000	14220	Cell Signaling, USA
Caspase-9	Rabbit	1:1000	9502	Cell Signaling, USA
cFLIP	Mouse	1:500		Santa Cruz, USA
Cleaved Caspase-3	Rabbit	1:1000	9664	Cell Signaling, USA
Cytochrome C	Rabbit	1:5000	Ab1333504	Abcam, United Kingdom
ERK 1/2	Rabbit	1:1000	3192	Cell Signaling, USA
GAPDH	Mouse	1:2500	47724	Santa Cruz, USA
Mcl-1	Rabbit	1:1000	5453	Cell Signaling, USA
NFκB	Rabbit	1:1000	8242	Cell Signaling, USA
PARP1	Rabbit	1:1000	9532	Cell Signaling, USA
pERK1/2	Rabbit	1:1000	9101	Cell Signaling, USA
pNFκB	Rabbit	1:1000	3033	Cell Signaling, USA
pSTAT3	Rabbit	1:1000	9145	Cell Signaling, USA
STAT3	Rabbit	1:1000	4904	Cell Signaling, USA
TSPO	Rabbit	1:5000		Kind gift from Dr. V. Milencovic
VDAC1	Mouse	1:2500	Ab15895	Abcam, United Kingdom
β-Actin	Mouse	1:2500	A5316	Sigma Aldrich, Germany

3.1.6 Antibodies for immunocytochemistry

Table 6. Immunocytochemistry antibodies used in this thesis including the company in alphabetical order.

Antigen	**Species**	**Dilution**	**Order number**	**Company**
ATPB	Mouse	1:1000	Ab14730	Abcam, United Kingdom
DAPI		1 µg/ml	D9542	Sigma
PBR	Rabbit	1:500	Ab109497	Abcam, United Kingdom
α-mouse Alexa Fluor 565	Donkey	1:500	A-10042	Life Technologies, USA
α-rabbit Alexa Fluor 488	Donkey	1:1000	A-21206	Life Technologies, USA

3.1.7 Antibodies for flow cytometry

Table 7. Flow cytometry antibodies used in this thesis including the company in alphabetical order.

Antigen	Dilution	Order number	Company
APC anti-CD119 (IFN-RI)	1:10	130-128-197	Miltenyi Biotec, Germany
APC anti-CD120a (TNF-R1)	1:10	130-121-991	Miltenyi Biotec, Germany
APC anti-CD261 (DR4)	1:20	307406	BioLegend, USA
PE anit-CD120b-(TNF-R2)	1:50	130-119-777	Miltenyi Biotec, Germany
PE anti-CD262 (DR4)	1:20	307208	BioLegend, USA
PE anti-CD95 (Fas)	1:50	130-128-407	Miltenyi Biotec, Germany

REA control antibodies (Milentyi) with corresponding fluorescent labels were used in a dilution 1: 50 according to manufacturer's instruction.

3.1.8 Oligonucleotides

Table 8. Oligonucleotides used in this thesis including the company in alphabetical order.

Primer	Sequence	Company
Interleukin 6	Fw: 5´- CTCAGCCCTGAGAAAGGAGA -3´ Rev: 5´- AGGTTGTTTTCTGCCAGTGC -3´	Eurofins Scientific, Luxembourg
Interleukin 8	Fw: 5´- TGCGCCAACACAGAAATTAT -3´ Rev: 5´- TGAATTCTCAGCCCTCTTCAA -3´	Eurofins Scientific, Luxembourg
mutant_TSPO	Fw: 5´- GGCTGGCCTTCGCGAC-CACCCTTAATTATTGCGTATGGCGG -3´ Rev: 5´- CCGCCATACGCAA-TAATTAAGGGTGGTCGCGAAGGCCAGCC -3´	Sigma/Merck-Millipore, Germany
RPL13-A	Fw: 5´- CATAGGAAGCTGGGAGCAAG-3´ Rev: 5´- GCCCTCCAATCAGTCTTCTG-3´	Eurofins Scientific, Luxembourg
TSPO	Fw: 5´- TCTTTGGTGCCCGACAAA -3´ Rev: 5´-GGTACCAGGCCACGGTAG T -3´	Eurofins Scientific, Luxembourg
TSPO_exon2	Fw: 5´- CTGGAAATGCGTTCACTCAG -3´ Rev: 5´- GCCTGGAGAAGACCCTCTGT -3´	Eurofins Scientific, Luxembourg

3.1.9 shRNA and gRNAs

Table 9. shRNA and gRNAs used in this thesis in alphabetical order including the company.

Name	Target gene ID:	Sequence	Company
Guide T116	706	5´- CACCGTCCCGCTTTGTCCACGGCGA -3´	Kind gift from Stefanie Bader
Guide T126	706	5´- CACCGTCCACGGCGAGGGTCTCCGC -3´	Kind gift from Stefanie Bader
shRNA TSPO	706	Fw: 5'- CCGGCCACACTCAACTACTGCG-TATCTCGA GATACGCAGTAGTTGAG-TGTGGTTTTTG -3' Rev: 5´- AATTCAAAAACCACACTCAACTAC TGCGTATCTCGAGATACGCAGTAGTTGAG-TGTG G -3'	Eurofins Scientific, Luxembourg

3.1.10 Plasmids

Table 10. Plasmids used in this thesis including the company in alphabetical order.

Plasmid	Reference	Company
pCMV-VSG-G	Addgene plasmid #8454	Addgene, USA, kind gift from Bob Weinberg [213]
pGEM-T	A3600	Promega
pLJM1-EGFP	Addgene plasmid #19319	Addgene, USA, kind gift from David Sabatini [214]
pLKO.1 puro	Addgene plasmid #8453	Addgene, USA, kind gift from Bob Weinberg [213]
psPAX2	Addgene plasmid #12260	Addgene, USA, kind gift from Didier Trono
PX458	Addgene plasmid #48138	Addgene, USA, kind Kind gift from Feng Zhang [215]
T116 PX458		Kind gift from Stefanie Bader
T126 PX458		Kind gift from Stefanie Bader

3.1.11 Enzymes

Table 11. Restriction enzymes used in this thesis including the company in alphabetical order.

Restriction enzyme	Order number	Company
AgeI	R0552L	New England Biolabs, United Kingdom
BamHI-HF	R3136L	New England Biolabs, United Kingdom
EcoRI-HF	R3101L	New England Biolabs, United Kingdom
HindIII-HF	R3104L	New England Biolabs, United Kingdom
KpnI	R3142L	New England Biolabs, United Kingdom

Table 12. Polymerases used in this thesis including the company in alphabetical order.

Polymerase	Order number	Company
Herculase II Fusion DNA polymerase	600675	Agilent Technologies, USA
PfuUltra II Fusion HS DNA polymerase	600670	Agilent Technologies, USA

Table 13. Enzymes used in this thesis including the company in alphabetical order.

Enzymes	Order number	Company
Calf Intestinal Alkaline Phosphatase (CIP)	M0525S	New England Biolabs, United Kingdom
Proteinase K	740396	Macherey-Nagel, Germany
RNase A	740397	Macherey-Nagel, Germany
T4 DNA Ligase	M0202S	New England Biolabs, United Kingdom

3.1.12 Consumables

Table 14. Consumables used in this thesis including the company in alphabetical order.

Article	Order number	Company
Conical centrifuge tubes (15 and 50 ml)	62554502; 62547254	Sarstedt, Germany
Cover slips, 24 x 60 mm	H878.2	Roth, Germany
CryoPure Tubes, 2 ml, QuickSeal	72380007	Sarstedt, Germany
Disposable syringe (1 ml)	9161708V	Braun, Germany

Eppendorf Combitips advanced (0.2; 1; 2.5; 5 ml)	0030089774; 0030089430; 0030089650; 0030089456	Eppendorf, Germany
FACS Tubes Round Bottom (5 ml)	352052	Corning, USA
Nunc™ Lab-Tek™ II Chamber Slide™ 8 Well	16260661	Fisher Scientific, Germany
Pasteur Pipettes	4522.1	Roth, Germany
PCR strip of 8 (200 µl), flat cap	72.991.002	Sarstedt, Germany
Petrischale, (94 x 16 mm)	633180	Greiner, Germany
Pipette filter tips (10-1000 µl)	066025300; 076028300; 076228300; 07076938300	Nerbe plus, Germany
Pipette tips (10-1000 µl)	70.3010.;70.3030.20;70.3050.020	Sarstedt, Germany
Plate 96 wells black opaque	330042	Kisker, Germany
Plate 96 wells white opaque	6005680	Perkin Elmer, USA
PVDF blotting membrane (0.2 µm)	10600021	Amersham, United Kingdom
Safe-lock tubes (0.5, 1.5, 2 ml)	72.704; 72.706.400; 72.695.500	Sarstedt, Germany
Serological Pipettes (5, 10, 50 ml)	606180; 607180; 768180	Greiner, Germany
Sterican® disposable needle 26G	4665457	Braun, Germany
Tissue culture dish (96 x 21 mm)	93100	TPP, Switzerland
Tissue culture flask (25, 75 cm²)	90026 ;90076	TPP, Switzerland
Tissue Culture Test Plates F-base (6, 12, 24, 96 well)	92006: 92012; 92024; 92096	TPP, Switzerland
Twin.tec® PCR Plate 96	0030128583	Eppendorf, Germany
Whatman paper (0.34 mm)	588 31 92	VWR, Germany

3.1.13 Kits

Table 15. Kits used in this thesis including the company in alphabetical order.

Article	Order number	Company
BCA- Assay Solution A, Solution B	UPTIUP95424 A; UPTIUP95425 A	ThermoFisher Scientific, USA
Brilliant III Sybr Green Mix	600 883	Agilent, USA
Caspase-Glo® 8 Assay	G8200	Promega, USA
CyQUANT® Direct Cell proliferation Assay	C35012	ThermoFisher Scientific, USA
ECL Western Blot Bright	WBLUFO100	Merck-Millipore, Germany
FITC Annexin V Apoptosis Detection Kit wih 7-AAD	640922	BioLegend, USA
GoScript™ Reverse Transcriptase	A5001	Promega, USA
Halt Inhibitor Cocktail	1861281	ThermoFisher Scientific, USA
Human Interleukin 6 ELISA	31670069	ImmunoTools, Germany
Human Interleukin 8 ELISA	31670089	ImmunoTools, Germany
Incucyte® Caspase-3/7 Green Dye	4440	Satorious, Germany
JetOPTIMUS® DNA Transfection Reagent	101000051	Polyplus, France
Nucleo Spin DNARapid-Lyse	740100.50	Macherey-Nagel, Germany
Nucleo Spin Gel/ PCR Clean up	740609.250	Macherey-Nagel, Germany
Quiagen Plasmid Kit (Mini, Maxi)	127106; 2 162	Quiagen; Netherlands
RNA Plus Isolation Kit	74184.250	Macherey-Nagel, Germany
Seahorse XFe96 FluxPak	102601-100	Agilent, USA
Metafectene®	T020-1.0	Biontex Laboratories, Germany
Seahorse XFp FluxPak	103022-100	Agilent, USA

3.1.14 Solutions and buffers

Table 16. Solutions and buffers used in this thesis in alphabetical order.

Solution & Buffers	Composition	Utilization
Ammonium persulfate, 10 %	1 g APS 10 ml ddH_2O	SDS PAGE
Ammonium persulfate, 10 %	1 g APS 10 ml ddH_2O	SDS PAGE
Antibody buffer	1 % Triton X100 2 % donkey serum 1X PBS pH 7.4	Immunocytochemistry
Assay medium	12.125 ml XF Base medium minimal DMEM 125 µl (1mM) Sodium pyruvate solution (stock 100 mM) 125 µl (2 mM) L-Glutamine (stock 200 mM) 250 µl (20mM) α-D-Glucose (stock 1 M) Adjust pH to 7.4 with 0.1 N NaOH	Seahorse assay
Blocking buffer	0.5 % Triton X100 10 % donkey serum 1 X PBS pH 7.4	Immunocytochemistry
Blocking Solution 2.5 %	2.5 g non-fat dry milk powder 100 ml TBS-T	
Blocking Solution 5 %	5 g non-fat dry milk powder 100 ml TBS-T	Western blot
Citrate buffer	0,1 M Citric acid monohydrate 0,1 M Sodium citrate Adjust pH to 6,0 with 0,1M NaOH	Immunocytochemistry
EGTA/Tris, 0.1 M	3.81 g EGTA in 50 ml ddH_2O Adjust pH to 7.4 with Tris powder Adjust volume to 100 ml with ddH_2O	Mitochondrial isolation
MIBC buffer	5 ml Tris/MOPS	Mitochondrial isolation

	500 µl EGTA/Tris 10 ml sucrose Adjust volume to 50 ml with ddH_2O Add freshly 1 mM AEBSF 1 X Halt (10x) 1 mM DTT	
Paraformaldehyde, 4 %	4 % PFA 2.5 µM NaOH 0.4 µM $CaCl_2$ 50 µM Sucrose 0.2 M $NaPO_4$ (pH 7)	Cell fixation
Ponceau S	1 g Ponceau S (0.1 %) 50 ml acetic acid (5 %) Adjust volume to 1 l with ddH_2O	Western blot
RIPA	50 mM Tris-HCL (pH 8,0) 150 mM NaCl 0.5 % Trition X-100 0.5 % Sodium deoxycholate 1 mM DTT 1 mM AEBSF 1 x Halt Cocktail (Stock 100x)	Protein lysation for Western blot
SDS loading buffer (Laemmli)	12 % SDS 60 % Glycerol 600 mM DTT 60 mM Tris (pH 6.8) 0.06 % Bromphenolblue	SDS PAGE
SDS Running Buffer, 1 X	100 ml 10 X SDS Running Buffer 900 ml ddH_2O	SDS PAGE
SDS Running Buffer, 10 X	10 g SDS 30.3 g Tris base 144.1 g Glycin	SDS PAGE

	Adjust volume to 1 l with dd H_2O	
Sucrose, 1 M	34.23 g sucrose 100 ml ddH_2O	Mitochondrial isolation
TBE buffer, 10 X	0.89 M Tris- base 0.89 M Boric Acid 0.02 M Na_2EDTA (0.5 M) Adjust pH to 8.8	Agarose electrophoresis
TBS, 10 X	60.5 g/l Tris base 87.6 g/l NaCl Adjust pH to 7.5 with HCL Adjust volume to 1 l with ddH_2O	Western blot
TBST-T, 1 X	100 ml 10 X TBS buffer 900 ml ddH_2O 1 ml Tween20	Western blot, washing buffer
Transfer Buffer, 1 X	100 ml 10 X Transfer buffer 700 ml ddH_2O 200 ml Methanol	Western blot
Transfer Buffer, 10 X	30.3 g Tris base 144.1 g Glycin Adjust volume to 1 l with ddH_2O	Western Blot
Tris/MOPS 0.1 M	1,21 g Tris in 50 ml ddH_2O Adjust pH to 7.4 with MOPS powder Adjust volume to 100 ml with ddH_2O	Mitochondrial isolation

3.1.15 Software

Table 17. Software used in this thesis including the company in alphabetical order.

Software	Company or developer
Citavi, version 6.10	Swiss Academic Software GmbH, Swiss
FlowJo version,version 10.9	Tree star, Becton Dickison, USA
GraphPad Prism, version 8.0.2	GraphPad Software, USA
ImageJ, version 1.53	Wayane Rasband, NIH, USA
Inkscape, version 1.2.2	Inkscape Community
LasX, version 3.7.6.25997	Leica microsystems
Microsoft Office 2017	Microsoft, USA
MxPro QPCR Software	Agilent Technologies, USA
Seahorse Wave Desktop Software, version 2.6.1.53	Agilent Technologies, USA

3.2 Methods

3.2.1 Cell culture methods

3.2.1.1 Tumor cell lines and cultivation

The primary glioblastoma cell line BTIC13 was maintained in serum-free RHB-A medium supplemented with 1 % Penicillin/Streptomycin (P/S) and 20 ng/ml each of human epidermal growth factor (EGF) and human fibroblast growth factor (FGF) (RHB-A complete). Cells were cultured at 37 °C with 5 % CO_2 and 95 % humidity. For passaging, cells were detached with a 1:1 mixture of Accutase® and PBS when they reached 80 % of confluence. They were centrifuged for 4 min, 1,200 rpm at room temperature (RT), the supernatant was removed, and the pellet re-suspended in fresh medium. Following, cells were seeded at splitting ratio of 1:5 up to 1:10 in T75 flasks in 10 ml RHB-A complete.

3.2.1.2 Cryopreservation and thawing of cells

For preservation of the cell culture, cryostocks of the cell lines were generated. Therefore, cells were harvested as described in section 3.2.1.1 and cell pellets were re-suspended in RHB-A containing 10 % DMSO. 1 ml of the cell suspension was transferred into cryovials, placed in a freezing container and stored at -80 °C.

A frozen cryostock was thawed rapidly in a 37 °C water bath and transferred in a 15 ml falcon containing 5 ml of fresh culture medium. Cells were pelleted for 5 min, 800 rpm at RT, the supernatant was discarded, the pellet re-suspended in 1 ml of RHB-A complete and transferred into a culture flask.

3.2.1.3 Cell number quantification

To obtain a viable cell count, 10 µl of Trypan Blue were added to 40 µl of cell suspension. Then, the mixture was loaded on a hemocytometer and living cells were counted in a meandering fashion. The cell number per ml was calculated as follows:

$$\frac{amount\ of\ counted\ cells}{amount\ of\ counted\ squares} \times 1.25 \times 10{,}000 = \text{cells/ml}$$

3.2.1.4 Generation of stable TSPO knockdown BTIC13 lines

TSPO-specific shRNA as well as a non-targeting control shRNA were cloned into the lentiviral pLKO.1 puro plasmid using AgeI/EcoRI restriction enzymes. Following, the 10 µg shRNA plasmid together with 5 µg pCMV-VSV-G and 5 µg psPAX2 were co-transfected into human embryonic kidney (HEK) 293T cells to generate lentiviral particles. Metafectene (Biontex Laboratories) was used as transfection medium according to the manufacture´s protocol. After 24 hours, the supernatant containing the lentiviral particles was removed, filtrated, and used for the transduction of BTIC13 by spinoculation for 1 hour, 900 rpm at RT. The transduction procedure was performed by Dr. A. Vollmann-Zwerenz according to the S2 safety regulations

(GenTSV). Transduced cells were selected with RHB-A supplemented with 3 µg/ml puromycin 24 hours later. Surviving cells were pooled and cultured for further analysis.

3.2.1.5 Generation of monoclonal TSPO knockdown BTIC13 lines

Clonal cell lines of stably transduced BTIC13 TSPO knockdown and control cells were obtained by single cell dilution. Therefore, cells were harvested with a 1:1 mix of Accutase® : PBS and centrifuged for 4 min, 1,200 rpm at RT. The cell pellet was thoroughly re-suspended by passing the cells several times through a serological pipet in order to singularize the cells. After quantification of the cell concentration, several 1:5 dilution steps were performed to achieve a final concentration of 10 cells / ml. Then, 100 µl of the 10 cells / ml solution were transferred into each well of a 96-well plate. The following day, plates were observed via microscopy and wells containing a single colony were marked and expanded into larger culture dishes until they could be used for experiments.

3.2.1.6 TSPO re-expression in monoclonal TSPO knockdown BTIC13 lines

To ensure the on-target effect of the TSPO downregulation, TSPO was re-expressed in the clonal TSPO knockdown cell line KD1. Details of designing and cloning of the mutant (mt)TSPO re-expression vector are described in section 3.2.3.1. Therefore, 10 µg of pLJM1-mtTSPO vector, the 10µg pLJM1-empty control plasmid together with 5 µg pCMV-VSV-G and 5 µg psPAX2 were co-transfected into HEK 293T cells and transduction procedure was performed as described before in section 3.2.1.4.

3.2.1.7 Generation of TSPO knockout BTIC13 lines

For the generation of TSPO knockout BTIC13 cells, 24 hours prior transfection, 3 x 10^6 cells were seeded into T75 flasks in 10 ml RHB-A complete. On the following day, the cells were transfected with 10 µg of PX458 plasmid encoding for the Cas9- GFP fusion protein and either the gRNA T116 or gRNA T126 using the JetOPTIMUS® transfection kit (Polyplus). Briefly,10 µg of plasmid were diluted in 1 ml of JetOPTIMUS® Buffer and shortly vortexed. Afterwards, 10 µl of JetOPTIMUS® reagent were added, shortly vortexed, spun down and incubated for 10 min at RT. In the meantime, cells were changed to P/S-free RHB-A medium. After the incubation period, 1 ml of the transfection mixture was added dropwise to the cells. Four hours later the medium was changed to RHB-A complete. Cells were sorted for GFP expression by flow cytometry (FACSAria™, BD) in the central FACS facility of the Leibniz-Institute for Immunotherapy, 48 hours after the transfection. Following, single cells were seeded into 96-well plates per limiting dilution to obtain clonal population as described above. To increase single cell survival, cells were fed with serum-free 1X CloneR™ (STEMCELL™ technologies) at day 2 and day 4 after plating. After monoclonal lines have been sufficiently

expanded, they were screened for potential knockouts via Western blot and sequencing of genomic DNA.

3.2.1.8 Verification of CRISPR clones

3.2.1.8.1 Genomic DNA extraction

Genomic DNA was extracted from potential knockouts using the NucleoSpin® DNA Rapid Lyse kit (Macherey-Nagel™). Therefore, cells were harvested, washed with PBS and transferred into 2 ml tubes. Cells were lysed by adding 150 µl of RLY Buffer together with 10 µl Proteinase K and incubated for 30 min at 56°C. Samples were vortexed every 10 min to assure complete lysis. Following, samples were mixed with 440 µl RLB Buffer and loaded onto NucleoSpin® DNA RapidLyse Columns. Samples were centrifuged for 1 min at 11,000 x g at RT and flow through was discarded. After two washing steps with 500 µl RLW Buffer, silica membranes were dried by centrifugation (1 min, 11,000 x g) and DNA was eluted into a new tube with 50 µl of RLE Buffer. Concentration and purity of genomic DNA was quantified using a spectrophotometer. The genomic DNA was stored at -20 °C.

3.2.1.8.2 Exon 2 amplification

The gRNAs were designed to target exon 2 of TSPO. Therefore, to characterize and verify the CRISPR/Cas9-mediated edit, exon 2 was amplified from genomic DNA using the Herculase II Fusion DNA Polymerase (Agilent). The final volume of each sample reaction was 50 µl and was set up as described in table 18.

Table 18. Components of the PCR reaction for the amplification of genomic DNA.

Component	Amount per reaction
5X Herculase II Reaction Buffer	10 µl
dNTP mix (25 mM each dNTP)	1.25 µl
Genomic DNA	300 ng
Forward primer (10 µM)	1.25 µl
Reverse primer (10 µM)	1.25 µl
Herculase II Fusion DNA Pol	0.5 µl
Nuclease free dH_2O	To 50 µl

The PCR program was set as following: initial denaturation (95 °C for 2 min), 30 cycles of denaturation (95 °C, 20 sec), annealing (55 °C, 20 sec) and extension (72 °C, 30 sec), followed by the final extension (72 °C, 3 min). PCR products were stored at –20 °C or directly loaded on 1.5 % agarose gels stained with ethidium bromide.

3.2.1.8.3 Purification of PCR products from agarose gels

To analyze and purify successfully amplified PCR products, 1.5 % agarose gels with 0.5 x TBE buffer were casted and stained with ethidium bromide. PCR samples were mixed with 6X TriTrack DNA loading dye (Thermo Scientific™), loaded on the gel and separated at 120 Volts for 30 min in 0.5 x TBE buffer. The GeneRuler 50 bp DNA ladder (Thermo Scientific™) served as size standard. DNA bands were documented with an UV gel imager, desired DNA bands were cut out and transferred into 2 ml tubes.

3.2.1.8.4 Agarose gel clean-up

PCR amplicons and DNA were purified using the Nucleospin® Gel and PCR Clean up Kit (Machery-Nagel™) according to the manufactures protocol. Briefly, after adding 500 µl of NTI buffer, the cut-out agarose pieces were melted at 50 °C. Then, the molten product was loaded on a column and washed multiple times with NT3 buffer. In a final step, the DNA was eluted in 30 µl elution buffer (5 mM Tris-Hcl, pH 8.5).

3.2.1.8.5 Sequencing

To validate successful gene targeting, PCR amplicons were directly sent for sanger sequencing. Therefore, 10 ng/ml of the purified PCR product together with the sequencing primers TSPO_Exon2 were sent to LGC Genomics, Germany. To identify CRISPR-induced indels and de-convoluted overlapping spectra from different alleles in the obtained sequencing trace files, the web-based application CRISP-ID [216] was used. The resulting sequence was again verified for hetero- or homozygous edits by DNA nucleotide sequence alignment (Nucleotide BLAST; NCBI) in comparison to the human TSPO sequence. To account for frameshifts, the reading frame was examined using the Serial cloner software (SerialBasics, Franck Perez). Finally, the obtained amino acid sequence was compared to human TSPO protein sequence using the ClustalW2 website (https://www.ebi.ac.uk/Tools/msa/clustalw2/).

3.2.2 Functional assays

3.2.2.1 Proliferation assay

The resazurin reduction assay (R&D System) was used to assess the basal proliferation potential of cell lines, to determine EC_{50} values of cytokines and death ligands, and to examine their effects on cell viability. The resazurin assay is a $NADH/H^+$- dependent, fluorometric, metabolic assay. Resazurin is enzymatically reduced to resorufin, and the amount of resorufin produced is proportional to the number of viable cells. To determine the basal proliferation potential, proliferation was measured at five different points in time (0 hours, 24 hours, 48 hours, 72 hours, and 96 hours). For each time point, 5×10^3 cells per well were seeded in 100 µl RHB-A in black 96-well, flat-bottomed plates. After each growth period, 10 % of resazurin was directly added to the wells and after 4 hours of incubation at 37 °C, the fluorescence

was measured at 560 nm excitation / 590 nm emission with the Varioskan™ Flash Multimode Reader (Thermo Scientific™). For the determination of the EC_{50} values of cytokines TNFα, IFNγ, and death ligands FasL and TRAIL, 5×10^3 cells were plated in black 96-well, flat bottom plates in 50 µl RHB-A. The next day, cells were treated with a rising concentration of cytokines (0, 0.1,1,10, 25, 50, 100, 250, 500, 1,000 ng/ml per cytokine or death ligand) in 50 µl of RHB-A, resulting in a final volume of 100 µl per well. Five replicates were performed for each treatment. After 48 hours, resazurin was added and measured as described above.

The CyQUANT® Direct cell Proliferation Assay (Invitrogen™) is a metabolism-independent, direct proliferation assay and was used to detect impact of respiration inhibitor metformin on cell proliferation. 5×10^3 cells were seeded in 100 µl RHB-A in transparent flat-bottomed 96 well plates and incubated for 24 hours at 37 °C. Following, cells were exposed to 0 mM, 1 mM and 10 mM metformin and incubated for 48 hours. After that the CyQuant assay was performed according to the manufacturer protocol and the fluorescence was measured at 508 nm excitation / 527 emission with the Varioskan™ Flash Multimode Reader (Thermo Scientific™).

3.2.2.2 Spheroid assay

To evaluate basal migratory capacity of cells, a spheroid assay was performed. 96-well flat-bottomed plates were coated with 100 µl of 1 % agarose in PBS. Cells were seeded at a density of 5×10^3 cells/well in 200 µl of RHB-A medium and incubated at 37 °C. After 48 hours, spheroids were picked in a volume of 100 µl and transferred into 96-well U-bottomed plates, containing already 100 µl of medium. Images of spheroids were taken after 0 hours, 16 hours, 24 hours, and 40 hours at 2.4 x magnification with the ProgRes C3B camera and the ProgRes Capture Pro 2.6 software in a resolution of 2080 × 1542 pixels. Size of the spheroids was analyzed using the free drawing tool of ImageJ and the scale was set to 460 pixel/1000 µm. All values were normalized to the initial spheroid size (0 hours).

3.2.2.3 Real-time live-cell imaging for activated caspase-3/7

To monitor the activation of caspase 3/7 during co-culture of BTIC13 with cytotoxic Influenza-antigen-specific cytotoxic $CD8^+$ T cells (FluT) cells in real time the Incucyte® Live Cell analysis system (Essen Bioscience) was used in cooperation with Dr. A. Menevse. BTIC13 cells were plated on transparent flat-bottomed 96-well plates at a density of 5×10^3 cells per well. After 24 hours, cells were pulsed with 0.001 µg/ml Flu- peptide. After 1 hour of incubation, the pulsing medium was removed and 2×10^4 FluTCs or plain CM (complete lymphocyte medium containing 10 % AB serum, 1 % P/S, 1 % Hepes, and 0.01 % beta mercaptoethanol) were added in 100 µl to the wells. For the blockade of the TRAIL receptors DR4 and DR5, the α-DR4 and α-DR5 antibodies were added in 2X concentration (final concentration: 5 µg/ml) in 50 µl, 30 min before adding 50 µl of FluT cells or plain CM. Then, the Incucyte® Caspase-3/7 Green

Dye (Sartorius) was added to the cells. Cells were imaged every hour for 26 hours at a 10 x magnification. Tumor cell apoptosis was quantified with the Incucyte®2020B software.

3.2.2.4 Caspase-8 Glo assay

The Caspase-Glo® 8 Assay (Promega) was used to measure caspase-8 activity after TRAIL treatment. 1×10^4 cells were seeded in white opaque, flat-bottomed 96-well plates in 50 µl RHB-A and incubated for 48 h at 37 °C. A blank reaction containing medium without cells was also included to measure background luminescence. Then, cells were treated with 50 ng/ml TRAIL for 1 hours and 3 hours. Before adding the Caspase-Glo® 8 reagent, the reagent and the culture plate were equilibrated to RT. Following, 50 µl of Caspase-Glo® 8 reagent were added to each well and gently mixed. Luminescence was measured after 2 hours of incubation at RT with the Varioskan™ Flash Multimode Reader (Thermo Scientific™).

3.2.2.5 TRAIL receptor blocking assay

BTICs (3×10^3 cells / well) were plated in black 96-well, flat-bottomed plates in 50 µl RHB-A and incubated for 48 hours at 37 °C. Subsequently, α-DR4 and α-DR5 blocking antibodies were added together with 50 µl of RHB-A at a final concentration of 5 µg/ml. After 1 hour of incubation at 37 °C, cells were treated with 50 ng/ml TRAIL and 48 hours later, cell viability was measured using the resazurin assay as described in in section 3.2.2.1.

3.2.2.6 Mitochondrial stress test

To measure changes in the mitochondrial respiration, glycolysis and ATP production rate, the Seahorse XFe96 Cell Mito stress test (Agilent) was performed. 48 hours prior to the assay, cells were plated in a laminin-coated (10 µg/ml in PBS) Seahorse XF96 cell culture microplate at a density of 2×10^4 cells per well in 100 µl of RHB-A. Each cell line was seeded in replicates of four, the wells A1, A12, H1, and H12 remained empty as a blank control. To attach the cells evenly to the bottom of the wells, the plate was centrifuged at 300 x g for 2 min before being placed in the incubator at 37 °C. 24 hours prior to the assay, the sensor cartridge was hydrated by adding 200 µl of Seahorse XF Calibrant to each well of the utility plate and then placing it into a non-CO_2 37 °C incubator overnight. At the day of the assay, the assay medium was prepared by supplementing Seahorse XF DMEM with 1 mM Sodium pyruvate, 2 mM L-Glutamine and 20 mM α-D-Glucose and the pH value was adjusted to 7.4. Cells were washed with 200 µl of assay medium once. Subsequently, 180 µl of assay medium were added to each well and the plate was placed into a non-CO_2 37 °C incubator for 30 min up to one hour for degassing. In the meantime, the stress test modulators Oligomycin (10 mM), FCCP (20 mM) and Rotenone/Antimycin A (5 mM) were prepared by diluting the stock 1:1,000 in 5 ml of assay medium. The sensor cartridge was loaded with 20 µl of Oligomycin into injection port A (final concentration 1 µM), 22 µl of FCCP into injection port B (final concentration 2 µM) and 25 µl of

Rotenone/Antimycin A into injection port C (final concentration 0.5 µM). Then, the loaded sensor cartridge was placed into the XFe96 Flux instrument tray and calibrated for 15 to 30 min. After complete calibration, the utility plate of the sensor cartridge was replaced with the cell culture microplate and the measurement was started. The XF Cell Mito Stress Test begins with four baseline measurements to quantify the basal respiration, followed by the sequential injection of the modulators to measure parameters such as ATP-linked respiration, maximal respiration, and spare respiratory capacity. This provides information about the mean oxygen consumption rate (OCR) and extracellular acidification rate (ECAR) in order to assess mitochondrial function and cellular metabolism. At the end of the assay, the assay medium was removed and samples were normalized to the total protein amount to account for cell number variations. Therefore, cells were lysed with ice-cold RIPA buffer (60 µl /well) for 30 min on ice. Afterwards, the plate was centrifuged for 3 min at 300 x g and the samples were transferred into a standard 96-well plate by dividing the content of one well into 25 µl duplicates. The BCA assay was performed as described in section 3.2.5.1.1. The resulting protein amounts were used for normalizing the raw OCR measurements for each well to the total protein (µg) using the Wave software.

3.2.3 DNA-based methods

3.2.3.1 Site-directed mutagenesis

To rescue the TSPO expression in the TSPO knockdown clone KD1, site-directed mutagenesis was used to introduce silent point mutations in the shRNA-target region of TSPO. Forward and reverse HPLC-purified primers were designed to include 11-12 base pairs of complementary sequence on either side of four mismatched bases. Since smaller plasmids are more efficiently amplified, site-directed mutagenesis was performed with an intermediate pGEM-T vector (3015 bp) before cloning the mutant (mt)TSPO insert into the target plasmid pLJM.1-EGFP (8083 bp). Table 19 shows the mutagenesis PCR parameters.

Table 19. Components of the PCR reaction for the site-directed mutagenesis.

Component	Amount per reaction
10X PfuUltra II reaction buffer	5.0 µl
dNTP mix (25 mM each dNTP)	0.5 µl
DNA template	100 ng
Forward primer (10 µM)	1.0 µl
Reverse primer (10 µM)	1.0 µl
PfuUltra II fusion HS DNA pol	1.0 µl
DMSO (optional)	5-10 %
Nuclease free dH_2O	To 50 µl

The PCR program was set as the following: initial denaturation (95 °C for 2 min), 30 cycles of denaturation (95 °C, 30 sec), annealing (60 °C, 30 sec) and extension (72 °C, 3.5 min), followed by final extension (72 °C, 10 min). 5 µl of the PCR products were loaded on an analytical 0.8 % agarose gel stained with ethidium bromide to analyze for size and mass of the PCR products.

To eliminate the parent plasmid from the PCR products, 2 µl of *Dpn*I endonuclease were added to the 45 µl of remaining PCR product together with 10 µl of 10X CutSmart buffer. The reaction mix was filled up with nuclease-free water to 100 µl and incubated for 1 hour at 37 °C. Subsequently, 100 µl of the *Dpn*I digest were transformed into 100 µl of chemically competent *E.coli* bacteria as described in section 3.2.3.3. Prior to cloning the mtTSPO insert into the target plasmid, purification of the intermediate plasmid and validation of the desired construct by analytical gel electrophoresis and sequencing were performed as described in detail in the sections 3.2.1.8.3, 3.2.1.8.4, and 3.2.1.8.5, respectively.

3.2.3.2 Restriction digest and ligation

To prepare the ligation, the plasmid and the DNA insert had to be cut with the according restriction enzymes. 2 µg of plasmid and 7 µl of insert were digested with 1 µl of each restriction enzyme (see Table 11). After adding 10X CutSmart buffer, the digestion mix was filled up with ddH_2O to a total volume of 50 µl and incubated for 2 hours at 37 °C. To prevent re-circularization of the vector, 1 µl of CIP (Calf Intestinal Alkaline Phosphatase; NEB) was added to the digestion mix at 60 min and 90 min of incubation. In a following step, digested vector and insert were separated by agarose gel electrophoresis and purified using the NucleoSpin® Gel and PCR Clean up kit (Macherey-Nagel™) as described in section 3.2.1.8. Ligation was performed using a 1 to 3 ratio of digested, purified plasmid to insert, 10X T4 Ligase Buffer, and 1 µl of T4 DNA Ligase. The reaction mix was filled up to 20 µl with ddH_2O and incubated overnight at 16 °C in a Thermocycler and then immediately stored at 4 °C.

3.2.3.3 Transformation of bacteria

To amplify the ligated plasmids, they were transformed into chemically competent *E. coli* bacteria. Therefore, a frozen stock of NEB10 bacteria was thawed on ice. Accordingly, 20 µl of the ligation mixture were added to 100 µl of bacteria, gently mixed, and incubated for on ice for 60 min. Next, cells were heat shocked for 55 sec at 42 °C in a water bath and then immediately returned on ice for 2 min to induce plasmid uptake. After adding 900 µl of pre-warmed LB medium without antibiotics, the cell suspension was transferred into a 13 ml tube with assembled ventilation push cap and incubated for 1 hour at 37 °C shaking at 150 rpm. Afterwards, the cells were centrifuged for 5 min at 4,000 rpm, the supernatant was discarded by pouring and the pellet re-suspended in the remaining supernatant. The bacteria were then plated on LB agar plates with appropriate antibiotics for selection and incubated overnight at 37 °C.

3.2.3.4 Plasmid isolation from bacteria

Plasmids were isolated from bacteria in the mini- or maxi-scale as required. Single bacterial colonies were picked from selective agarose plates to directly inoculate 5 ml of overnight LB-mini-culture or a starter culture of 5 ml LB medium for the maxi-scale. Both cultures contained the appropriate selection antibiotic and were either incubated at 37 °C at 150 rpm overnight or in case of the starter culture for 6 hours. 500 µl of the starter culture were then used to inoculate 500 ml of the maxi culture followed by overnight incubation at 37°C and 150 rpm. After harvesting the bacterial cells by centrifugation (4,700 rpm for 30 min at 4 °C), plasmids were isolated according to the manufacturer´s protocol of the QIAprep Spin Miniprep Kit (Qiagen) or the QIAGEN Plasmid Maxi Kit (Qiagen). The concentration of the purified plasmids was quantified spectrophotometrically and the plasmid DNA was stored at -20 °C.

3.2.3.5 Control digest and DNA sequencing of plasmid

For analytical digest of plasmids, 20 µl of DNA were digested with 0.5 µl of each restriction enzyme in 3 µl of 10X CutSmart buffer filled up to a total volume of 30 µl with nuclease-free H_2O. The reaction mix was incubated for 1.5 hours at 37 °C before DNA fragments were analyzed for size and mass via agarose gel electrophoresis. As a second validation step, the correct DNA sequence was confirmed by DNA sequencing. Therefore, 100 ng/µl of plasmid DNA were diluted in 40 µl nuclease-free water and sent together with 10 µM of the according sequencing primer to LGC Genomics (LGC Genomics, Germany).

3.2.4 RNA-based methods

3.2.4.1 RNA isolation from mammalian cells

Cell pellets were harvested at 1,500 rpm, washed once with 1 ml PBS and shock frozen in 2-methylbutane at – 80 °C. Total RNA was isolated from cell pellets using the NucleoSpin® RNA plus Kit (Macherey-Nagel™) according to manufacturer´s guidelines. Here, samples were lysed with 350 µl LBP Lysis buffer. Genomic DNA was removed using the NucleoSpin® gDNA removal column and binding conditions of RNA to NucleoSpin® RNA Plus Column were adjusted by adding 100 µl of binding solution BS. The columns were washed once with wash buffer WB1 and two times with wash buffer WB2 to remove buffer residue and salts. Then, RNA was eluted in a volume of 30 µl with RNase-free H_2O and the RNA concentration measured using the NanoPhotometer® P300.

3.2.4.2 Reverse transcription

The GoScript™ Reverse Transcription System (Promega) was used to synthesize RNA into cDNA for qRT-PCR. For the reverse transcription of poly(A)+ mRNA, 500-1,000 ng of RNA template were diluted in 8 µl of RNase-free water in 0.2 ml thin-walled PCR tubes. Then, the template was thermally denatured at 70 °C for 10 min and chilled on ice. In the meantime, the

reverse transcription reaction mix was assembled on ice containing the following components (Table 20):

Table 20. Components of the reverse transcription to synthesize cDNA.

Component	Amount per reaction
GoScript™ 5X Reaction buffer	4.0 µl
$MgCl_2$	5 µl
PCR Nucleotide mix	1 µl
Oligo$(dT)_{15}$ Primer	0.5 µl
Random Primer	0.5 µl
Recombinant RNasin® Ribonuclease inhibitor	0.5 µl
GoScript™ Reverse Transcriptase	0.5 µl
Final volume	12 µl

Finally, 12 µl of the reaction mix were added to the template and the samples were quickly mixed and spun down. Following an initial annealing at 25 °C for 4 min, the reaction was incubated at 42 °C for 1 hour before heat inactivation of the reverse transcriptase at 75 °C for 10 min. The final cDNA was diluted 1:5 with nuclease-free water and stored at -20 °C.

3.2.4.3 Quantitative real time polymerase chain reaction (qRT-PCR)

The amount of target mRNA was determined by quantitative real-time polymerase chain reaction (qRT-PCR). For the comparative Ct method, 50-100 ng of template cDNA, 10 µl of 2X SYBR Green QPCR master mix (Agilent) and 250 nM forward and reverse primer were used per 20 µl reaction. Each sample was prepared in duplicates for the 96-well format. The specific amplification efficiency (90-110 %) of all primers used was verified by generating a standard curve. For this, cDNA was diluted in steps of 5 to final concentrations of 1:1, 1:5, 1:25 and 1:125. A no-template control (NTC) was included in each run to rule out contamination or non-specific amplification. *RPL13-A* mRNA expression was used as housekeeping expression control. For the list of target specific primers see table 8. The qRT-PCR performed at the Mx3005P cycler (Agilent) using the following program:

Table 21. qRT-PCR program and thermal profile.

Step	Temperature	Time	Cycle
Initial denaturation	95 °C	3:00 min	1X
Denaturation	95 °C	0:15 min	40X
Annealing/Extension	60 °C	0:25 min	
Melting Curve analysis	68 °C	0:30 min	1X
	95 °C	0:30 min	

3.2.5 Protein-based methods

3.2.5.1 Protein extraction from mammalian cells

3.2.5.1.1 Preparation of total protein lysates

Cell pellets were harvested at 1,500 rpm with a 1:1 Accutase®:PBS mixture, washed once with 1 ml PBS and immediately frozen in 2-methylbutane at – 80 °C. All steps of the protein isolation were performed on ice. Pellets were re-suspended in 50-150 µl ice-cold RIPA buffer supplemented with 1X Halt™ Protease-Inhibitor-Cocktail (100X, ThermoFisher Scientific), 1 mM AEBSF and 1 mM DTT. After 10 min of incubation on ice, the lysates were centrifuged at 14,000 rpm, for 10 min at 4 °C. Subsequently, the clear supernatant containing the protein was transferred into a new tube. To determine the protein concentration, 6 µl of the samples were diluted 1:10 in PBS for the bicinchoninic acid (BCA) assay (ThermoFisher Scientific). 25 µl of the BCA standard and 25 µl of the diluted samples were pipetted in duplicates on a transparent flat-bottomed 96-well plate. The BCA solution A and B were mixed (1:50) and 200 µl of the mixture were added to each well. After 30 min of incubation at 37 °C, the absorbance was measured at 562 nm with the Varioskan™ Flash Multimode Reader (Thermo Scientific). The protein concentration was interpolated from the standard curve. The lysates were stored at – 80°C.

3.2.5.1.2 Preparation of subcellular-fractionated protein lysates

At least two 10 ml dishes containing 1.5×10^6 cells/dish were seeded and harvested at 85 % confluence to avoid activation of intrinsic apoptosis by overgrowth. After exposure to 50 ng/ml TRAIL for 3 hours, cell pellets were harvested at 1,500 rpm with a 1:1 Accutase®:PBS mixture, washed once with 1 ml PBS and immediately placed on ice. The following steps of subcellular fractionation were carried out on ice as quickly as possible. All pellets were re-suspended in 200-400 µl of ice-cold MIBC buffer supplemented with 1X Halt™ Protease-Inhibitor-Cocktail (100X, ThermoFisher Scientific), 1 mM AEBSF and 1 mM DTT and incubated for 20 min on ice. After that, cells were gently lysed by passing the cell suspension 30 times through a 26-gauge needle tip using a 1 ml syringe. Subsequently, the samples were centrifuged at 700 x g

for 10 min at 4 °C. Without touching the cell pellet containing debris and the nuclei, the supernatant with the cytoplasm, membrane and mitochondria was transferred into a new tube. To increase the purity of this fraction the samples were centrifuged again for 5 min (700 x g, 4 °C). The supernatant was then transferred into a new tube. To avoid contamination of the mitochondrial fraction with lysosomes and peroxisomes, the centrifuge was set to “soft ramp” before centrifuging at 3,000 x g, for 15 min at 4 °C. The supernatant containing the cytoplasmic fraction was carefully transferred into a fresh tube without touching the mitochondrial pellet. The mitochondrial pellet was washed with 200 µl of MIBC buffer and centrifuged at 3,000 x g, 15 min at 4°C. The supernatant was then carefully removed and the pellet re-suspended in 40-60 µl of MIBC buffer depending on the size. The quantification of the protein concentration with the BCA Assay was carried out as described in section 3.2.5.1.1. Therefore, the cytosolic fraction was diluted 1:10 and the mitochondrial fraction 1:5 in PBS. The lysates were stored at – 80 °C and boiled with 5X Laemmli for 10 min at 95 °C before loading onto a SDS gel.

3.2.5.2 SDS polyacrylamide gel electrophoresis

Sodium dodecyl sulfate polyacrylamide gel electrophoresis (SDS PAGE) was used to separate and compare proteins based on their size. 12 % SDS gels were prepared according to table 22 and wrapped in wet paper towels for overnight storage at 4 °C.

Table 22. Recipe for 12 % SDS gels.

Component (in ml)	Separation gel (12 %)	Stacking gel (5 %)
H_2O	1.6	0.68
30 % Acrylamide	2.0	0,17
1.5 M Tris (pH. 8.8)	1.3	/
1.5 M Tris (pH 6.8)	/	0.13
10 % SDS	0.05	0.01
10 % APS	0.05	0.01
TEMED	0.002	0.001

Samples were diluted to 20-50 µg of protein with PBS, mixed with 5X Laemmli buffer and boiled for 10 min at 75 °C. The SDS gels were fixed in the PerfectBlue™ Double gel system (Peqlab) and buffer chambers were filled with 1X SDS running buffer. After a short spin, boiled samples and the PageRuler Prestained Protein ladder (Thermo Fisher) were loaded into each lane and gels run for 30 min at 80 Volts and ~1.5 hours at 120 Volts.

3.2.5.3 Western transfer and immunodetection of proteins

Following SDS Page, proteins were transferred onto PDVF membranes via wet electroblotting. Before assembling the blotting sandwich, foam pads, filter paper and SDS gels were equilibrated in 1X transfer buffer. The PDVF membranes were first activated with 100 % methanol for 1 min, before they were also incubated in 1X transfer buffer. After equilibration, the blotting sandwich was assembled starting with a foam pad on the negative electrode site (black frame) of the transfer cassette. This was followed by three filter papers, the SDS gel, the activated PDVF membrane and again three filter papers and the foam pad for the positive electrode site (red frame). After each assembling step, air bubbles were removed. Then the transfer cassette was closed and placed into the Mini Trans-Blot cell (BioRad) filled with 1X transfer buffer. Transfer took place at 150 mA for 2.5 hours at 4 °C. Afterwards, the membranes were stained with Ponceau S solution to verify protein transfer. Then, membranes were quickly de-stained with ddH_2O and incubated with 5 % blocking solution for 1 hour at RT while shaking. To detect phosphorylated proteins, the 5 % and 2.5 % blocking solution were supplemented with 1 mM NaF and 1 mM Na_3VO_4. Membranes were incubated with the appropriate primary antibody diluted in 2.5 % blocking solution overnight rotating at 4 °C. The next day, membranes were washed three times with TBS-T (0.1 % Tween-20 in TBS) for 10 min before incubating them with the appropriate secondary, horseradish peroxidase (HRP)-coupled antibody in 2.5 % blocking solution. All primary and secondary antibodies and the dilutions used are listed in table 5, section 3.1.5. Finally, blots were washed again three times with TBS-T and developed using the ECL Western Blot Bright chemiluminescence HRP solution (Merck-Millipore) and the Image Quant LAS 4000 (GE Healthcare).

3.2.5.4 ELISA

An enzyme-linked immunosorbent assay (ELISA) was used to quantify interleukin-6 (IL-6) and interleukin-8 (IL-8) protein secretion of BTICs. Therefore, 1.5×10^5 cells on 6-well were seeded and incubated for 48 hours at 37 °C before treatment. Supernatants from BTIC cell culture were collected after stimulation of cells with 50 ng/ml TNFα and IFNγ for 24 hours and 48 hours. To later normalize the protein concentration to the cell count, the cell number per well was also determined. Supernatants were stored at -80 °C and brought to RT before use. The experiments were performed according to the manufacturer´s instruction of the Human IL-6 ELISA (ImmunoTools) and Human IL-8 ELISA (ImmunoTools). The standard curve was generated from 200 pg/ml to 1.56 pg/ml for IL-6 and from 250 pg/ml to 2.015 pg/ml for IL-8 via serial dilution. The dilution of the samples had to be determined experimentally and adjusted for each run to be within the range of the standard curve. After several incubations and washing steps, the enzymatic conversion of the TMB substrate was stopped after 15 min of incubation

with 0.2 N H_2SO_4. After that, the absorbance was measured at 540 nm and 570 nm as reference wavelength using the Varioskan™ Flash Multimode Reader (Thermo Scientific) and the concentration of the samples was interpolated from the standard curve.

3.2.5.5 Flow cytometry

3.2.5.5.1 Surface receptor staining

For direct surface staining of unfixed cells by flow cytometry, cells were harvested as described in section 3.2.1.1, washed once with PBS, centrifuged (1,200 rpm, 4 min) and resuspended in PBS + 0.2 % BSA. Cell suspensions were then evenly distributed in FACS tubes, spun down and resuspended in 50 µl of PBS + 1 % BSA. After addition of antibodies (section 3.1.7, table 7), cells were briefly vortexed and incubated 1 hour on ice in the dark. Following incubation, cells were washed again by adding 500 µl of PBS + 0.2 % BSA per tube, spun down and resuspended in 250 – 500 µl PBS + 0.2 % BSA. Cells were kept on ice in the dark until analysis on a BD FACS Canto II (BD Biosciences).

3.2.5.5.2 Total ROS

To detect cellular ROS cells by flow cytometry, cells were harvested and counted as described in sections 3.2.1.1 and 3.2.1.3. Subsequently, cells were washed once with 2 ml of PBS (1,200 rpm, 4 min), and 2.5 to 5×10^5 cells were transferred into FACS tubes. Following, cells were washed with 1 ml FACS wash buffer (PBS + 2 % FCS) and again centrifuged (1,200 rpm, 4 min). In the meantime, the 2',7'-Dichlorodihydrofluorescein diacetate (H_2DCFDA) solution was prepared by diluting the stock concentration (20 mM) to 1:50 ration with PBS to obtain a concentration of 400 µM in 200 µl PBS.

After centrifugation, the supernatant was discarded, and the cells were resuspended in 500 µl FACS wash buffer. Then, 12.5 µl of H_2DCFDA dilution were added to each tubes to obtain a final concentration 10 µM. Additionally, an unstained control was prepared. The FACS tubes were covered with a lid to prevent oxidation of the H_2DCFDA and incubated for 20 min at 37 °C. After that, cells were washed with 3 ml cold PBS and directly analyzed on a BD FACS Canto II (BD Biosciences) in the FITC channel. Debris and cell doublets were excluded based on forward/sideward scatter parameters. The acquired data were further processed using FlowJo software.

3.2.5.5.3 Annexin V/ 7-AAD

To analyze the proportion of living in dead cells the FITC Annexin V Apoptosis Detection Kit (BioLegend) with 7-AAD was used. Therefore, cells were initially plated in 6-well plates and treated the following day with 50 ng/ml TRAIL for 1 hour, 3 hours, or 6 hours. After the treatment, cells were harvest as described before (section 3.2.1.1). The detached cells were collected in flow cytometry tubes and then centrifuged for 4 min at 1,400 rpm at RT. Subsequently,

the cell pellets were washed with 500 µl of ice-cold flow cytometry buffer (centrifugation: 4 min, 1,600 rpm, RT) and then resuspended in 50 µl of Annexin binding buffer. To each sample, 2.5 µl of Annexin solution was added, followed by vortexing. Next, 2.5 µl of 7-AAD solution was added and the samples were vortexed again. The cells were incubated for 15 min in the dark at RT. Subsequently, cell analysis was performed using a BD FACS Canto II flow cytometer, which measured the proportions of viable cells (double negative), early apoptotic cells (Annexin V positive), necrotic cells (7-AAD positive) and dead cells (7-AAD and Annexin V positive). Debris and cell doublets were excluded based on forward/sideward scatter parameters. The acquired data was further processed using FlowJo software.

3.2.5.6 Immunocytochemistry

To investigate structural integrity of mitochondria of TSPO KO cells and validate loss of TSPO, immunocytochemistry was performed. Therefore, 8-well Lab-Tek™ chamber slides (Thermo Scientific) or glass coverslips in 12 well plates were coated with laminin solution (10 µg/ml in PBS). 2.5×10^4 cells per well were plated in 200 µl of RHB-A and incubated for 48 hours at 37 °C. Cells were fixed with 4 % PFA for 10 min followed by three washing steps with PBS for 5 min. For the TSPO staining, an antigen retrieval step with 0.1 M sodium citrate buffer (pH 6) was performed to de-mask antigen sites. Therefore, a vegetable steamer was filled with ddH_2O and preheated to boiling temperature together with a flask of the retrieval buffer. Subsequently, 300 µl of hot retrieval buffer were added to the wells of the fixed cells, and the mixture was placed into the steamer. Both the lid of the plate as well as the lid of the steamer were closed to prevent the slides from drying out. After 15 min of steaming, slides were allowed to cool down and the standard protocol was continued. Important to mention, the antigen retrieval method is an optimized protocol for immunohistochemistry with a rack of glass slides. Neither the Lab-Teks™ nor the 12-well plates are particularly heat resistant, so further optimization steps will be necessary to better adapt to the immunocytochemistry protocol. After fixation and the optional antigen retrieval step, cells were blocked and permeabilized with 10 % donkey serum and 0.5 % TritonX100 in PBS (Blocking buffer) for 30 min at RT. Incubation with the primary antibodies rabbit-anti-PBR (1:500) and mouse-anti-ATPB (1:1,000) was performed overnight at 4 °C in 100 µl of antibody buffer containing 2 % donkey serum and 0.1 % TritionX100 in PBS. The next day, slides were washed three times with PBS for 10 min. Then, cells were incubated with Alexa Fluor™ 568-conjugated goat anti-mouse and Alexa Fluor™ 488-conjugated goat anti-rabbit secondary antibodies and Dapi (1 ng/ml) in antibody buffer for 1 hour at RT in the dark. After a quick wash with PBS, slides were mounted with Prolong Gold Anti Fade medium (ThermoFisher Scientific), dried for 24 hours at RT and stored light protected at 4 °C.

3.2.5.7 Microscopy

The cells were imaged with the Leica AF60000LX fluorescence microscope using the objective Leica HCX PL APO 63X/1.3 GLYC. Images were taken by the Leica DFC7000GT digital camera with the Leica LASX software. 3D stacks were recorded and processed with the Leica deconvolution software module.

3.2.6 Statistics

Statistical analysis was performed on datasets with three or more biological replicates. Statistical differences were analyzed using the GraphPad Prism 8 software. To determine statistical differences among the means of three or more independent groups, one-way analysis of variance (ANOVA) was applied, followed by Dunnett's *post hoc* test. To identify differences between treatment response of TSPO-deficient groups versus control groups, two-way ANOVA was used, followed by Dunnett´s *post hoc* test or another appropriate *post hoc* test. In all cases, *p* values ≤ 0.05 were defined as statistically significant and denoted as follows: * = $p \leq 0.05$; ** = $p \leq 0.01$, and *** = $p \leq 0.001$.

4 Results

4.1 TSPO expression in glioblastoma

TSPO levels are highly elevated in glioblastoma compared to the healthy brain [161]. To investigate the impact of increased TSPO expression in glioblastoma, primary, patient-derived brain tumor initiating cells (BTICs) were chosen as a model cell culture system. BTICs exhibit stem-like properties and are capable to initiate tumor growth upon xenotransplantation. They phenocopy the molecular characteristics and therapeutic resistance of the original tumor [217–219], which makes them a suitable model to study the aggressive and heterogenetic nature of glioblastoma.

First, the basal TSPO expression in various BTIC lines of different subtypes was determined. Western blot analysis revealed that TSPO protein expression was detected in all the 23 BTIC lines tested (Figure 9). As expected in this heterogenous tumor, the expression of TSPO was also heterogenous between BTIC lines. BTIC lines with high and comparatively low levels of TSPO were detected in both, proneural and mesenchymal subtypes. For further analyses, the well-characterized BTIC13 line [217, 220–222] was selected, since it exhibits stable proliferation and migration patterns in cell culture, grows adherently, and can be easily transfected. In addition, BTIC13 is human leukocyte antigen (HLA)-A2-positive which was required for subsequent T cell co-culture experiments.

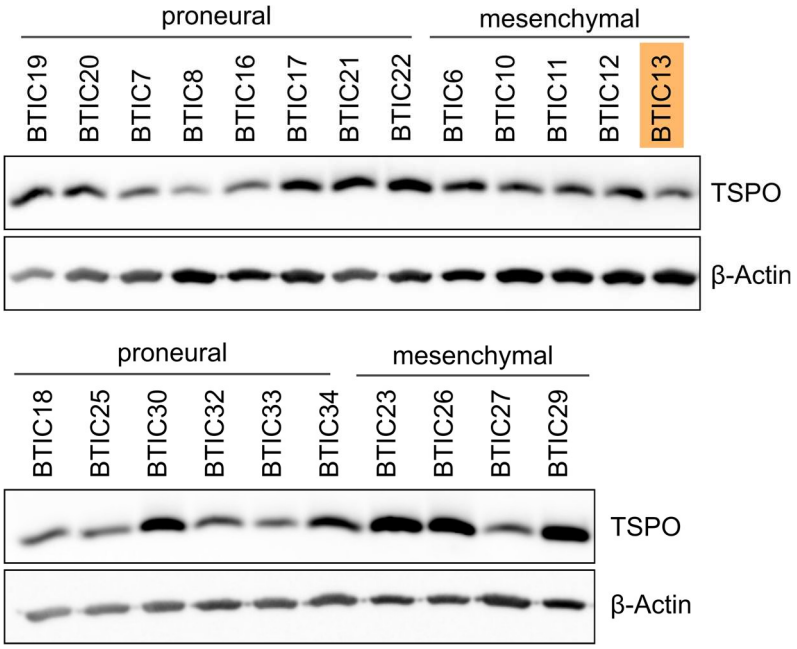

Figure 9. TSPO is heterogeneously expressed in patient-derived brain tumor initiating cells (BTICs). Western blot analysis of TSPO protein expression in various proneural and mesenchymal BTIC lines. Protein loading was confirmed by β-Actin staining. The well-characterized mesenchymal BTIC13 line (highlighted in orange) was selected for further analyses and showed intermediate TSPO expression levels compared to the other BTICs.

4.2 T cells and T cell-derived soluble factors induce TSPO expression in BTIC13

The precise causes driving the increased TSPO expression in glioblastoma remain elusive. However, elevated TSPO levels are not only observed within tumor tissue but also under inflammatory conditions within the brain. Moreover, there is evidence that pro-inflammatory stimuli increase TSPO expression in malignant cells [171]. Furthermore, TSPO expression positively correlates with the degree of T cell infiltration in a correlation analysis conducted in the TCGA glioblastoma dataset [222]. This led to the hypothesis that either T cell-derived soluble factors or direct contact between T cells and tumor cells could contribute to the elevated levels of TSPO in glioblastoma. The samples for the Western blot analysis were kindly provided by Dr. A. Menevse who generated the human leukocyte antigen (HLA)-A2-positive Influenza (Flu)-antigen specific $CD8^+$ T cells and the polyclonally activated T cell supernatant and conducted the T cell-tumor cell co-culturing experiment at the Leibniz Institute for Immunotherapy (LIT) in Regensburg.

Briefly, the HLA-A2-positive BTIC13 [222] was pulsed with an HLA-A2-specific Influenza peptide (FluP) at concentrations of 1, 0.1, and 0.01 ng/ml. Subsequently, the peptide-loaded BTIC13 was co-cultured with Flu-antigen-specific, cytotoxic $CD8^+$ T cells (FluT) at an effector to target ratio of 1:1. Additionally, BTIC13 cells were exposed to cell culture supernatant of activated FluT cells (FluT sup). After 20 hours of co-culture or FluT sup stimulation, TSPO expression levels of BTIC13 were determined by Western blot.

Results indicate that both FluT sup and co-culturing strongly increased the TSPO expression in BTIC13 (Figure 10). The most potent effect was observed in cells loaded with the highest Flu-peptide concentration (1 ng/ml) which resulted in a roughly threefold upregulation of TSPO compared to the control medium (Figure 10A). Cells pulsed with lower peptide concentrations (0.1 and 0.01 ng/ml) still exhibited higher TSPO levels than the FluT sup-treated samples, though there was no appreciable difference in TSPO expression between the two lower concentrations (Figure 10). Considering the almost twofold increase of TSPO expression in FluT sup-treated samples compared to the control medium, soluble factors in the supernatant of cytotoxic T cells already contribute to the increased TSPO levels. However, direct cell interactions and sufficient recognition of the Flu-antigen is required to maximize this effect.

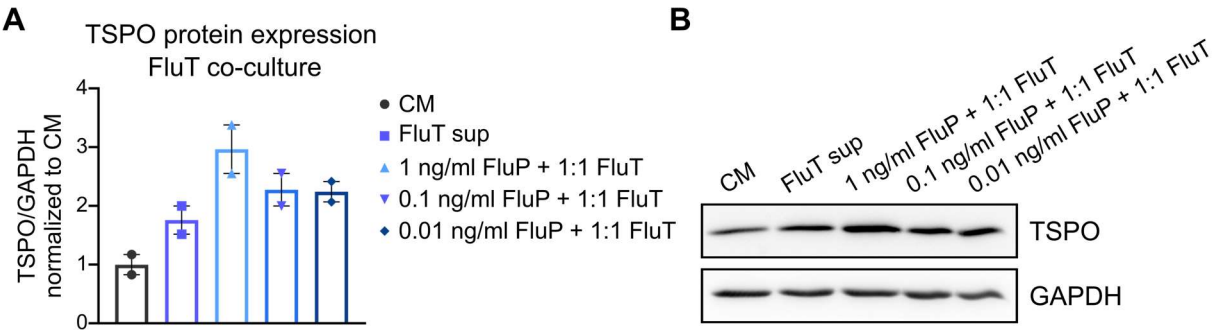

Figure 10. Induction of TSPO expression in the presence of T cells and T cell supernatant. Western blot analysis of TSPO protein expression in BTIC13. TSPO protein induction was evaluated after 20 hours of stimulation with supernatant of polyclonally activated FluT cells (FluT sup) or co-culture with FluT cells in a 1:1 ratio. To perform the co-culture, BTIC13 was pulsed with decreasing concentrations of flu-peptide (FluP). (**A**) The graph shows the relative protein quantification of two independent experiments. Data are normalized to GAPDH expression and presented as fold change compared to the control medium (CM). Data are shown as mean ± SD. (**B**) Representative Western blot of TSPO protein induction by FluT sup and FluT cell co-culture. Equal loading was confirmed by GAPDH staining. Samples were kindly provided by Dr. A. Menevse, LIT, Regensburg.

Recent research has revealed a positive link between *TSPO* expression and the genes encoding for the Interferon gamma (IFNγ) receptors (*IFNGR1, IFNGR2*) and Tumor necrosis factor alpha (TNFα) receptors (*TNFRSF1A, TNFRSF1B*) in glioblastoma [222]. IFNγ and TNFα are pro-inflammatory effector molecules secreted by cytotoxic T cells which can induce a plethora of functions upon neighboring immune and malignant cells [223, 224]. This led to the hypothesis that T cell-derived IFNγ and/or TNFα activate an IFNR- and/or TNFR-dependent signaling cascade that contributes to the upregulation of TSPO in glioblastoma.

To investigate this, BTIC13 was stimulated with 50 ng/ml of recombinant human IFNγ and TNFα for 24 and 48 hours. Then, TSPO mRNA and protein level were evaluated via quantitative real-time PCR (qPCR) and Western blot analysis.

IFNγ significantly increased TSPO mRNA expression at both 24 and 48 hours compared to the untreated control (Figure 11A). Similarly, TSPO protein levels were elevated at 24 hours and were significantly increased at 48 hours (Figure 11B, C). In comparison, treatment with TNFα resulted only in a modest increase in TSPO mRNA levels and had no effect on TSPO protein levels (Figure 11).

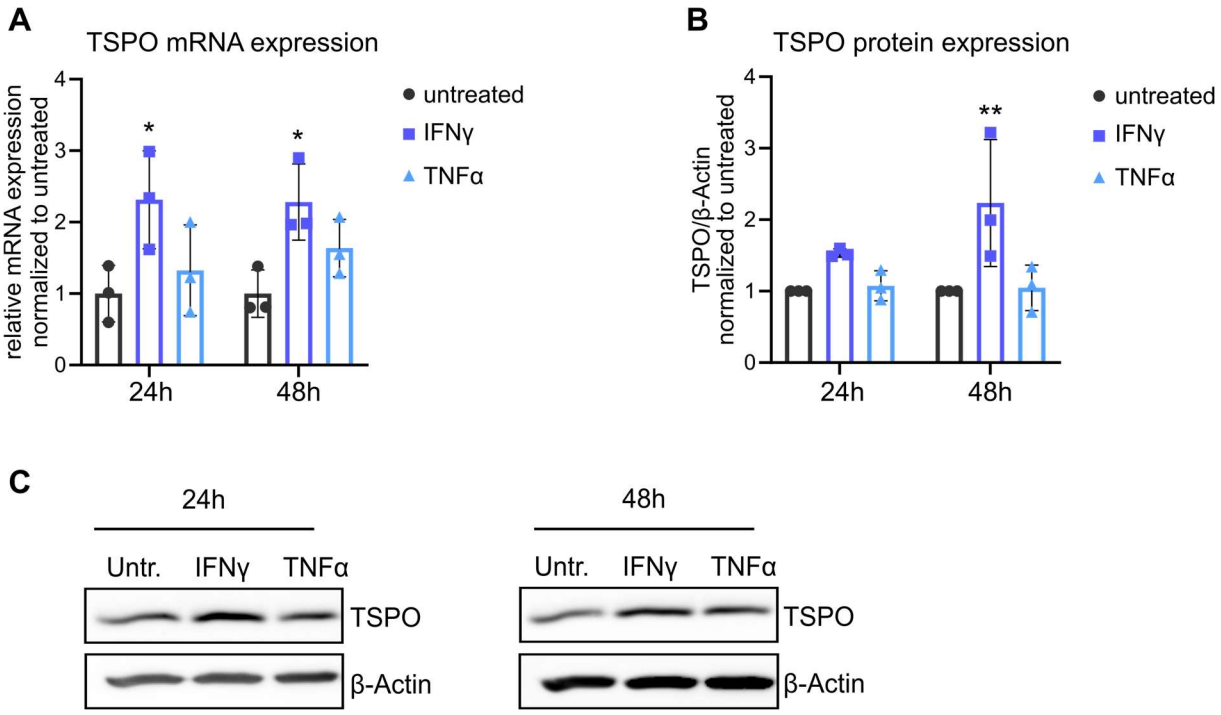

Figure 11. IFNγ induces TSPO expression in BTIC13. qPCR (**A**) and Western blot analysis (**B, C**) of TSPO expression in BTIC13. Cells were stimulated with recombinant human IFNγ and TNFα for 24- and 48 hours. (**A**) TSPO mRNA levels are shown relative to RPL13A expression and presented as fold change compared to the untreated control. Cumulative data of three independent experiments are represented as mean ± SD. (**B**) Quantified TSPO protein levels are shown relative to β-Actin expression and presented as fold change compared to the untreated control. Cumulative data of three independent experiments are represented as mean ± SD. (**C**) Representative Western blots for TSPO expression. Equal loading was confirmed by β-Actin staining. Asterisks indicate significant differences between treatment and control conditions. P-values for (**A**) and (**B**) were calculated using two-way ANOVA followed by Dunnett´s *post hoc* test (*P ≤ 0.05; **P ≤ 0.01).

To confirm these observations, the IFN receptor and TNF receptors of BTIC13 were blocked with neutralizing antibodies raised against IFN-R1, TNF-R1, and TNF-R2, 30 minutes prior to the treatment (samples were kindly provided by Dr. A. Menevse, LIT, Regensburg). After stimulating the cells with FluT sup for 24 hours, the impact on TSPO expression was evaluated via Western blot.

Each of the TNF-R1, TNF-R2, and IFN-R1 blockade alone proved insufficient to prevent FluT-sup-mediated TSPO induction compared to the control condition (CM) (Figure 12). However, concurrent blockade of all three receptors attenuated the TSPO induction upon FluT sup treatment (Figure 12).

Collectively, these findings suggest that both direct T cell-tumor cell contact and T cell-derived pro-inflammatory soluble factors, particularly IFNγ, contribute to the increased TSPO expression in BTIC13.

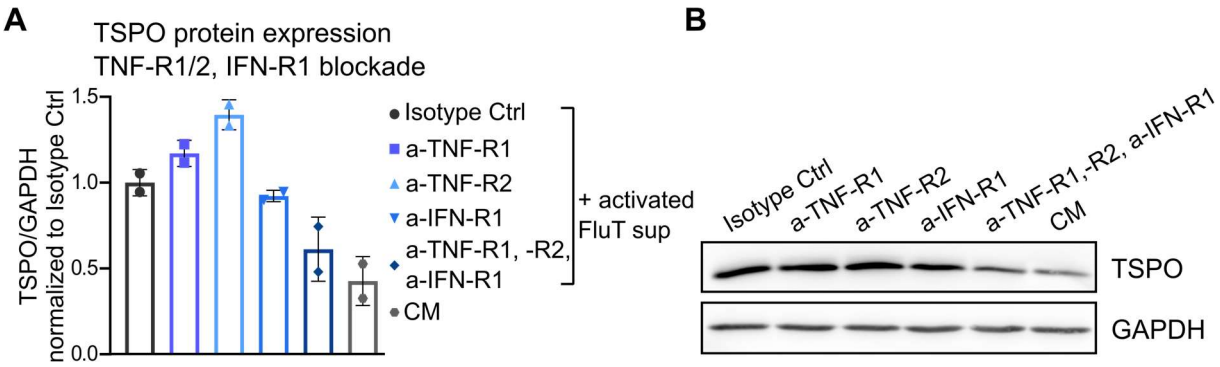

Figure 12. Simultaneous blockade of TNF- and IFN-receptors attenuates TSPO induction by T cell supernatant. Western blot analysis of TSPO expression in BTIC13. BTIC13 was pre-incubated for 30 min with either Isotype Control (Ctrl), anti-TNF-R1, anti-TNF-R2, anti-IFN-R1, or all three blocking antibodies combined. TSPO protein expression was evaluated after 24 hours of stimulation with supernatant of polyclonally activated FluT cells. Basal TSPO expression is shown in the control medium (CM). (**A**) Graph shows the relative protein quantification of two independent experiments. Data are normalized to GAPDH expression and presented as fold change compared to the isotype control. Data are shown as mean ± SD. (**B**) Representative Western blot of TSPO protein expression after TNF- and IFN- receptor blockade and FluT sup stimulation. Equal loading was confirmed by GAPDH staining. Samples were kindly provided by Dr. A. Menevse, LIT, Regensburg.

4.3 Generation of TSPO-deficient BTICs

To gain insight into the function of TSPO and its physiological significance in BTIC13, two distinct loss-of-function approaches were carried out. First, TSPO-deficient BTICs were generated using a lentiviral knockdown system via short hairpin RNAs (shRNAs). The lentiviral transduction of the pLKO.1 plasmid (kind gift from Bob Weinberg Addgene ID #8453 http://n2t.net/addgene:8453; RRID:Addgene_8453) containing the shRNAs and the puromycin antibiotic selection were performed by Dr. A. Vollmann-Zwerenz under S2 laboratory safety standards.

BTIC13 was transduced with two TSPO-specific shRNAs to generate the stable polyclonal TSPO-knockdown cell lines shTSPO_1 Bulk and shTSPO_2 Bulk. A non-targeting control shRNA was used to establish the control cell line Scr Bulk. Both, the shTSPO_1 Bulk and shTSPO_2 Bulk were effective in downregulating TSPO expression (Figure 13A). Compared to the Scr Bulk, they reduced the protein levels of TSPO by 76 % and 72 %, respectively. To obtain a deeper understanding of the intrinsic heterogeneity of BTIC13, single cell-derived monoclonal cell lines were generated in addition. Therefore, bulk parental cell lines were seeded as single cells by limiting dilution and transferred stepwise into larger culture vessels until they could be used for experiments. The clonal knockdown cell lines KD1 and KD2 originated from shTSPO_1 Bulk, and the KD3 clone was obtained from shTSPO_2 Bulk. The control clone Scr C1 was derived from the Scr Bulk control cell line. TSPO protein levels were

significantly reduced in all three knockdown clones (Figure 13B). Compared to the control clone Scr C1, TSPO expression was decreased by 91 %, 96 %, and 83 % in KD1, KD2, and KD3, respectively.

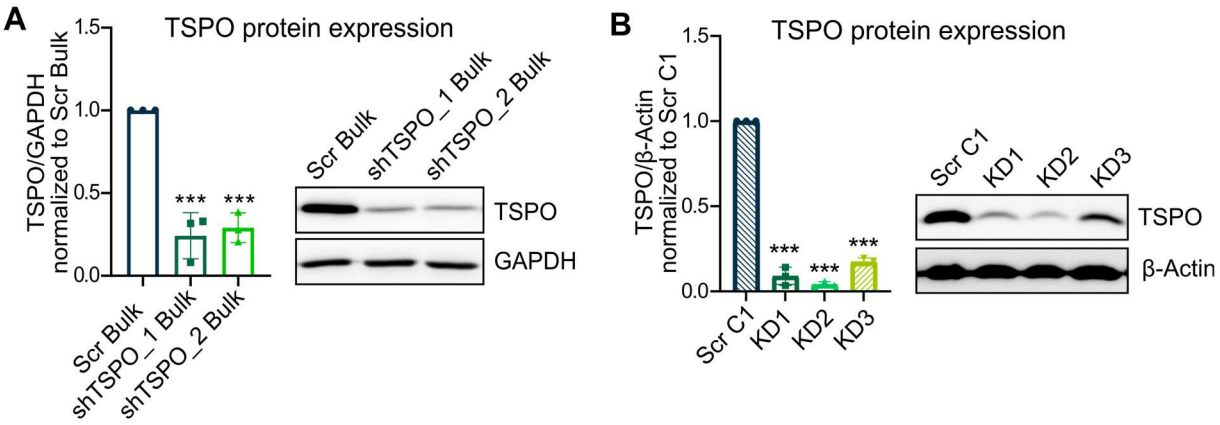

Figure 13. Stable TSPO knockdown in BTIC13 cells. Western blot analysis of TSPO expression in shRNA-transduced BTIC13. (**A**) Heterogenous TSPO-deficient "bulk" cell lines were obtained by lentiviral transduction of BTIC13 TSPO-specific shRNA (shTSPO_1 Bulk, shTSPO_2 Bulk). Non-targeting control shRNA was used to generate a control cell line (Scr Bulk) (**B**) Monoclonal cell populations were derived from bulk parental cell lines by single cell dilution (Scr C1, KD1, KD2, KD3). (**A, B**) Graphs show the relative protein quantification of three independent experiments. Data are normalized to GAPDH or β-Actin expression and presented as fold change compared to the Scr control. Representative Western blots of TSPO protein levels in (**A**) TSPO-deficient bulk and (**B**) single cell-derived clonal populations. Equal loading was confirmed either by GAPDH or β-Actin staining. Lentiviral transduction was performed by Dr. A. Vollmann-Zwerenz, UKR, Regensburg. P-values were calculated using one-way ANOVA followed by Dunnett´s *post hoc* test (***$P \leq 0.001$).

As a second, complementary loss-of-function approach, stable TSPO knockout (KO) BTIC13 cell lines were generated using the CRISPR/Cas9 system. S. Bader kindly provided the Cas9-GFP fusion plasmid (pSPCas9 (BB)-1A-GFP (PX458) (gift from Feng Zhang, Addgene plasmid # 48138; http://n2t.net/addgene:48138; RRID: Addgene_48138), containing either the single guide RNA (sgRNA) T116 or T126. Both guide RNAs are designed to specifically target exon 2 of the *TSPO* gene (Figure 14A).

To achieve a high transfection efficiency of the Cas9/GFP_T116 and Cas9/GFP_T126 encoding plasmid in BTIC13, the JetOptimus® transfection system (Polyplus) was used, which is specifically designed for difficult-to-transfect cells. 48 hours after the transfection, cells were sorted for GFP expression in the central fluorescence activated cell sorting (FACS) facility of the LIT, Regensburg. After sorting, TSPO protein levels were determined to ascertain the efficiency of the Cas9_T116 and Cas9_T126 system. Both guide RNAs resulted in an almost complete reduction of TSPO expression compared to BTIC13 wildtype (Figure 14B).

Next, single cell-derived clonal populations were generated using a limiting dilution series to obtain monoclonal cell lines with a complete and stable knockout of TSPO. After clonal expansion, cells were screened by Western blot for loss of TSPO expression (Figure 14C). Clones that still expressed TSPO were chosen as control cells. Following that, CRISPR/Cas9-induced genome editing events of potential KO and control clones were analyzed. Therefore, exon 2 nucleotide sequence of the *TSPO* gene was amplified from genomic DNA by PCR and sequenced by Sanger sequencing. The obtained chromatograms were compared to the TSPO wildtype genomic sequence and screened for insertion/deletion (INDEL) events at the target site of the guide RNAs. Based on this analysis, the clones highlighted in orange (Figure 14C) were selected for all further experiments and their names were changed to control C_Ctrl (T126 BI G2), KO1 (T116 A1 F11), KO2 (T116 III E5), and KO3 (T126 AII C9) for better readability.

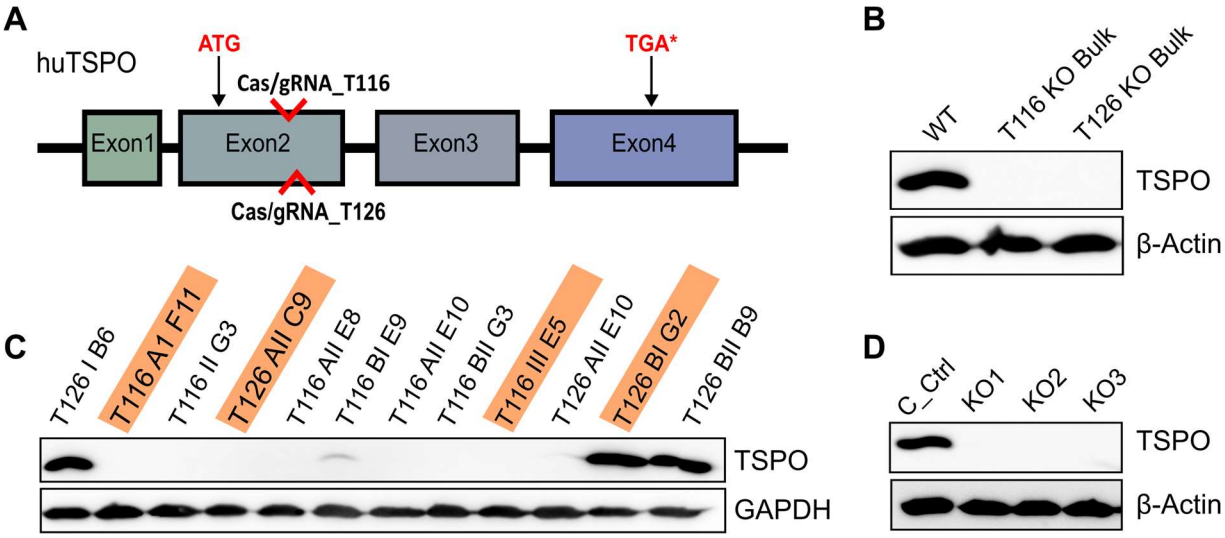

Figure 14. Generation of CRISPR/Cas9-mediated TSPO knockout in BTIC13. BTIC13 was transfected with a Cas9-GFP/gRNA_T116- or Cas9-GFP/gRNA_T126-encoding plasmid. 48 hours after the transfection, cells were FACS-sorted for GFP expression. (**A**) Schematic illustration of the exon/intron structure of the human (hu) *TSPO* gene and the sites targeted by guide RNAs T116 and T126. The transcription start site (ATG) and stop site (TGA) are indicated. (**B**) Western blot showing TSPO levels of T116- and T126-transfected BTIC13 Bulk lines obtained after sorting for GFP expression. (**C**) Screening for homozygous TSPO KO clones by Western blot analysis. Monoclonal populations were derived from bulk parental cell lines by single cell dilution. Clones that were chosen for further analysis are highlighted in orange. (**D**) Representative Western blot confirms loss of TSPO in clones T116 A1 F11 (KO1), T126 AII C9 (KO2), and T116 II E5 (KO3) compared to control clone T126 BI G2 (C_Ctrl). (**B-D**) Equal loading was confirmed by β-Actin or GAPDH staining.

Figure 15A shows the chromatogram alignment of the selected control clone and the knockout clones. The target sites of the guides T116 and T126 are highlighted in grey and blue, respectively, and the site of the INDEL event is marked in yellow. In KO1, a homozygous deletion of five base pairs (Figure 15A) resulted in a shift in the translational reading frame of the TSPO protein (Figure 15B). Similarly, in KO2 a homozygous deletion of two base pairs, and in KO3 a homozygous deletion of one base pair altered the reading frame and thus the amino acid sequence (Figure 15A, B). As the extensive missense in the amino acid sequence occurs early at position E29Sfs for KO1, E29Gfs for KO2, and R32Afs for KO3 with a protein length of 169 amino acids, a disrupted structure and functionality of the TSPO protein can be assumed (Figure 15B).

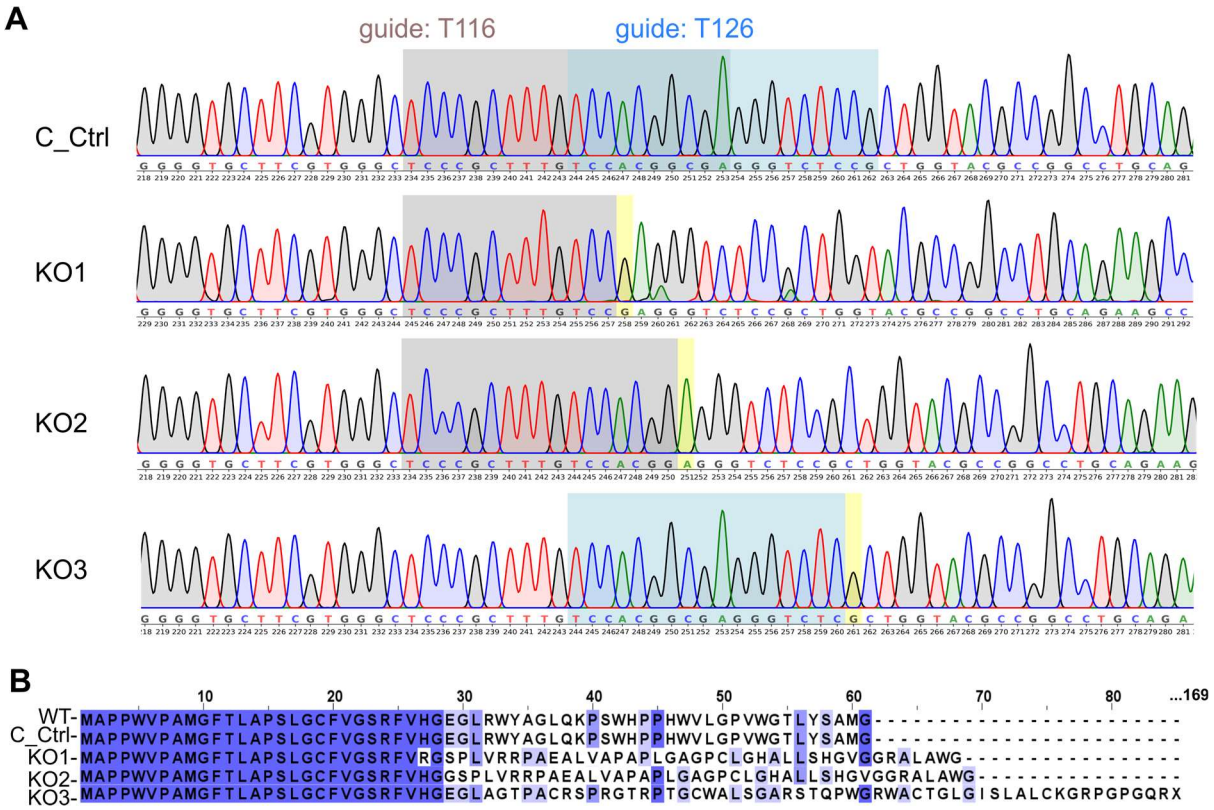

Figure 15. Validation of CRISPR/Cas9-mediated TSPO knockout in BTIC13. (**A**) Representative chromatograms of C_Ctrl and TSPO KO clones obtained after Sanger sequencing. Target sequences of guide RNAs T116 and T126 are highlighted in gray and blue, respectively. Yellow region indicates a single nucleotide polymorphism (SNP) or insertion/deletion (INDEL) events. Sequence alignment and image was generated using python code from Chang Y, cfutils, (version 0.0.0.dev54, 2022) GitHub repository, https://github.com/y9c/cfutils.git. (**B**) Multiple protein sequence alignment of the first ~60 amino acids of BTIC13 wildtype (WT), C_Ctrl, and TSPO KO clones shows an altered protein sequence for KO1 and KO2 starting at position E29 (E29Sfs; E29Gfs), and for KO3 at R32 (R32Afs). Color code indicates sequence similarity ranging from dark blue (identical) to light blue. Numbering indicates amino acid residues.

Next to genomic sequence analysis and Western blot detection, the TSPO knockout was validated by immunofluorescence. Therefore, an immunocytochemistry staining with antibodies raised against TSPO and the mitochondrial marker ATP synthase subunit beta (ATPB) was performed in the control and all three KO clones. TSPO staining was only detectable in the control clone C_Ctrl and co-localized with the mitochondrial marker ATPB (Figure 16). The KO clones exhibited ATPB fluorescence signals similar to the C_Ctrl, however, the TSPO signal was completely absent, confirming the loss of TSPO (Figure 16).

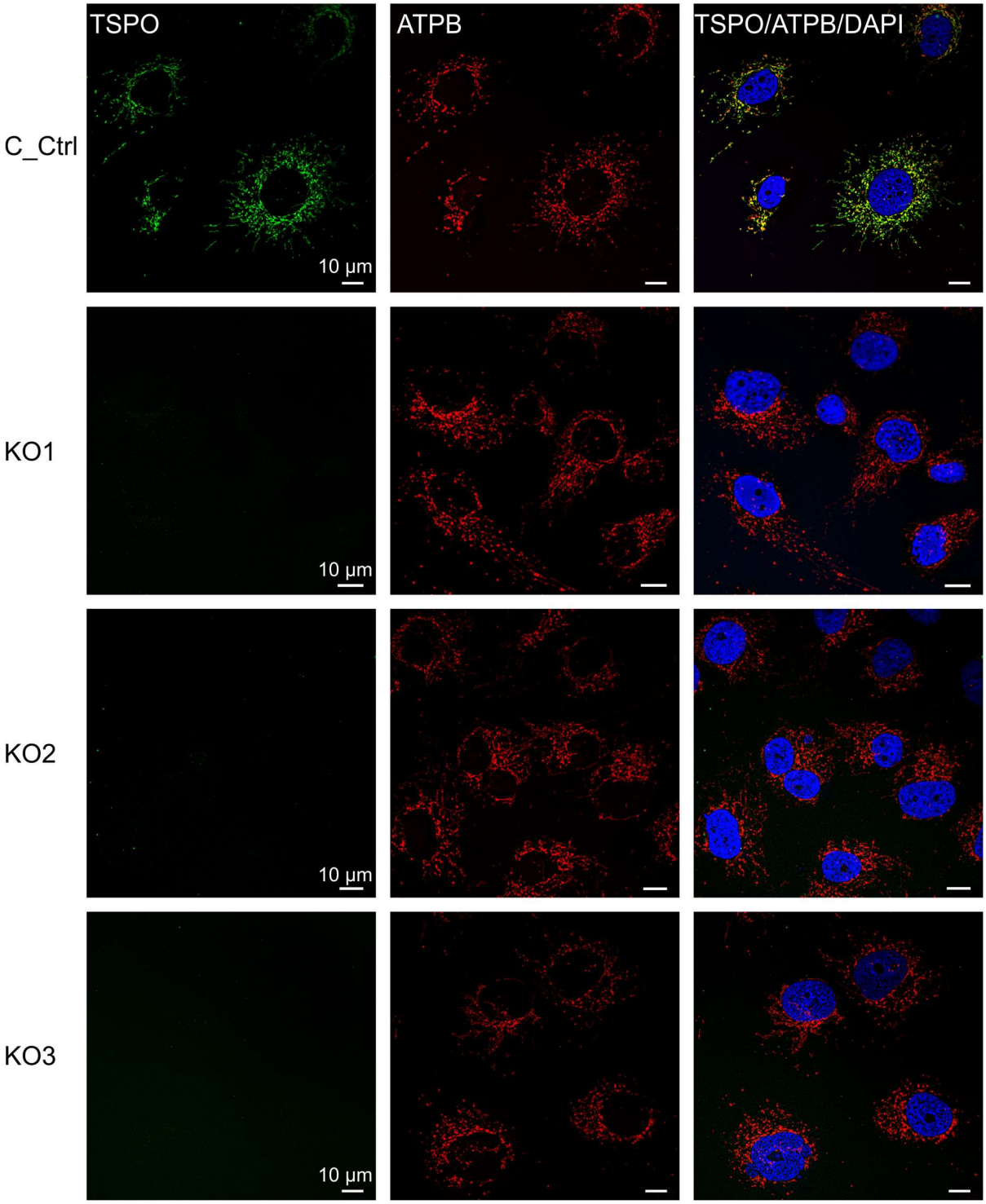

Figure 16. Immunocytochemistry analysis to validate the loss of TSPO. Representative images show fixed cells after heat-mediated antigen retrieval, stained with antibodies against TSPO (green) and the mitochondrial marker ATPB (red). Images were analyzed by fluorescence microscopy and 3D-deconvolution. DAPI was used for nuclear staining. Merged images on the right reveal overlapping signals for TSPO and ATPB only in control cells and not in the KO clones. Scale bars: 10 µm.

Sufficient TSPO staining requires an antigen retrieval step, which, however, interferes with the quality of the ATPB staining. To investigate whether the loss of TSPO altered the overall mitochondrial morphology in BTIC13, cells were single-stained for ATPB and subjected to fluorescence microscopy. An altered mitochondrial morphology is displayed by atypically elongated or fragmented mitochondria besides others, which may be a sign of mitochondrial dysfunction. In BTIC13, however, there was no obvious overall difference in basic mitochondrial morphology of KO clones KO1, KO2, and KO3, compared to the control clone C_Ctrl (Figure 17).

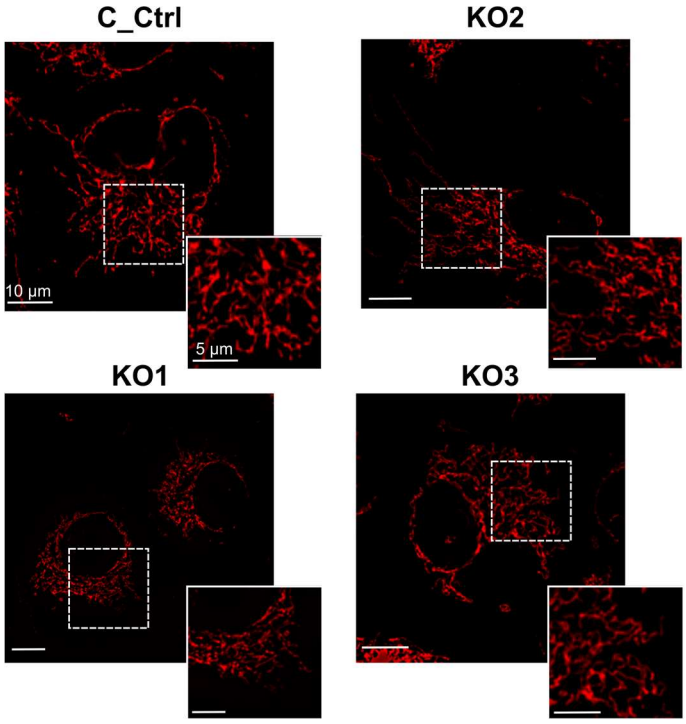

Figure 17. TSPO deficiency does not alter basic mitochondrial morphology. ATPB antibody-stained mitochondria of BTIC13 CRISPR Ctrl (C_Ctrl) and TSPO KOs (KO1, KO2, KO3) were analyzed by fluorescence microscopy and 3D-deconvolution. Representative image of two independent experiments with comparable results are shown. Scale bars: 10 µm (overview), 5 µm (insets).

4.4 Characterization of TSPO-deficient BTICs

Rapid proliferation and high migratory rates are fundamental features of aggressive cancer cells, and there is evidence that TSPO plays a role in both malignant traits. Therefore, the following experiments characterize how the loss of TSPO affects the basic proliferation and migratory capacity of BTIC13. In addition, the expression levels of receptors corresponding to important T cell effector molecules were evaluated and the effect of these molecules on cell viability was investigated. This helped to identify which effector molecules would be best to use in subsequent experiments.

4.4.1 Impact of TSPO deficiency on cell proliferation

First, the basic proliferation rates of TSPO-deficient BTICs compared to control BTICs were determined. Therefore, TSPO-deficient and control bulk and clonal cells were seeded at defined cell numbers, and proliferation was measured at 0, 24, 48, 72, and 96 hours using the Resazurin® reduction assay (R&D Systems).

All three model systems (knockdown bulk, knockdown clones and knockout clones) showed robust proliferation rates characterized by exponential growth rates. Notably, the bulk cell lines exhibited the highest proliferation rates compared to the clonal cell lines. Within 48 hours, the number of cells more than tripled compared to the initial (0 hour) measurement and reached a nine-fold increase after 96 hours (Figure 18A). Both clonal models were less proliferatively active compared to the bulk cell lines. After 48 hours, the cell numbers doubled and they reached a relative maximum of three to four-fold after 96 hours (Figure 18B, C). Noteworthy, each cell line showed a unique proliferative capability independent of TSPO status.

However, after normalizing to the 0-hour baseline, no significant differences were found between the TSPO-deficient and control cell lines for each cell line model (Figure 18). KO1 is the only exception, with a considerable higher growth rate that became significant at 48 hours when compared to C_Ctrl (Figure 18C). In summary, however, these results suggest that TSPO-deficiency does not impact the basic proliferation rates of BTIC13.

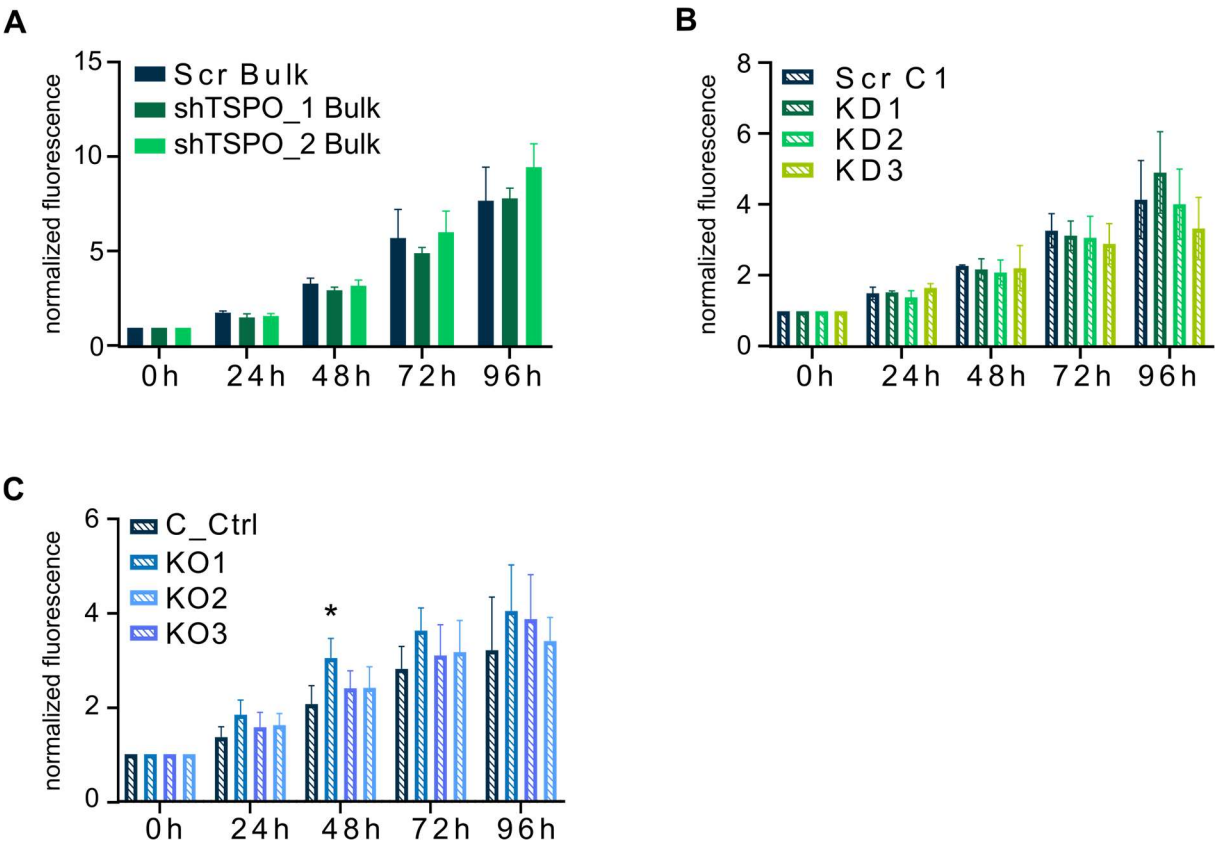

Figure 18. TSPO deficiency does not impact basal proliferation rates of BTIC13. The Resazurin assay was performed to analyze the basal proliferation rates of TSPO-deficient bulk (**A**), TSPO KD clones (**B**), and TSPO KO clones (**C**) compared to their respective controls. Fluorescence emission was measured at the specified time points and normalized to 0 hour values. Asterisk indicates significant differences between KO1 cell line and control C_Ctrl. Cumulative data of three independent experiments are shown as mean ± SD. P-values were calculated using two-way ANOVA followed by Dunnett´s *post hoc* test (*$P \leq 0.05$).

4.4.2 Impact of TSPO deficiency on cell migration

To identify whether TSPO impacts the basal migratory capacity of BTIC13, a two-dimensional spheroid migration assay was performed. Therefore, TSPO-deficient and control bulk and clonal cells were seeded in agarose-coated plates to initiate spheroid formation. After spheroid initiation, single spheroids were transferred into laminin-coated U-bottom plates and spheroid outgrowth was monitored at 0, 16, 24, and 40 hours. The relative migration rate was determined by measuring the area covered by the cells at each time point and subsequent normalization to the initial spheroid size (0 hours).

TSPO knockdown in the BTIC13 bulk cell lines had varying effects on the migration rates. The shTSPO_1 Bulk exhibited a high migratory capacity similar to that of the control Scr Bulk (Figure 19A). In contrast, the migratory capacity of shTSPO_2 Bulk was significantly impaired, showing a substantial reduction in the migration rate already at 16 hours (Figure 19A).

The migratory rate of all three TSPO knockdown clones was significantly reduced in comparison to the control clone, and approximately only one quarter of the area was covered after 40 hours (Figure 19B).

Overall, the migratory capacity of the TSPO KO clones was lower than that of the KD cell lines. Whereas the Scr Bulk and Scr C1 showed migration rates within the same range, the migratory capacity of the knockout control C_Ctrl was reduced by one third (Figure 19). Nevertheless, the TSPO KO clones showed a significantly decreased migration at 40 hours compared to C_Ctrl. Noteworthy, KO3 exhibited no migratory activity at all (Figure 19C). In conclusion, these findings imply that TSPO deficiency exerts a suppressive effect on the basic migratory rate of BTIC13.

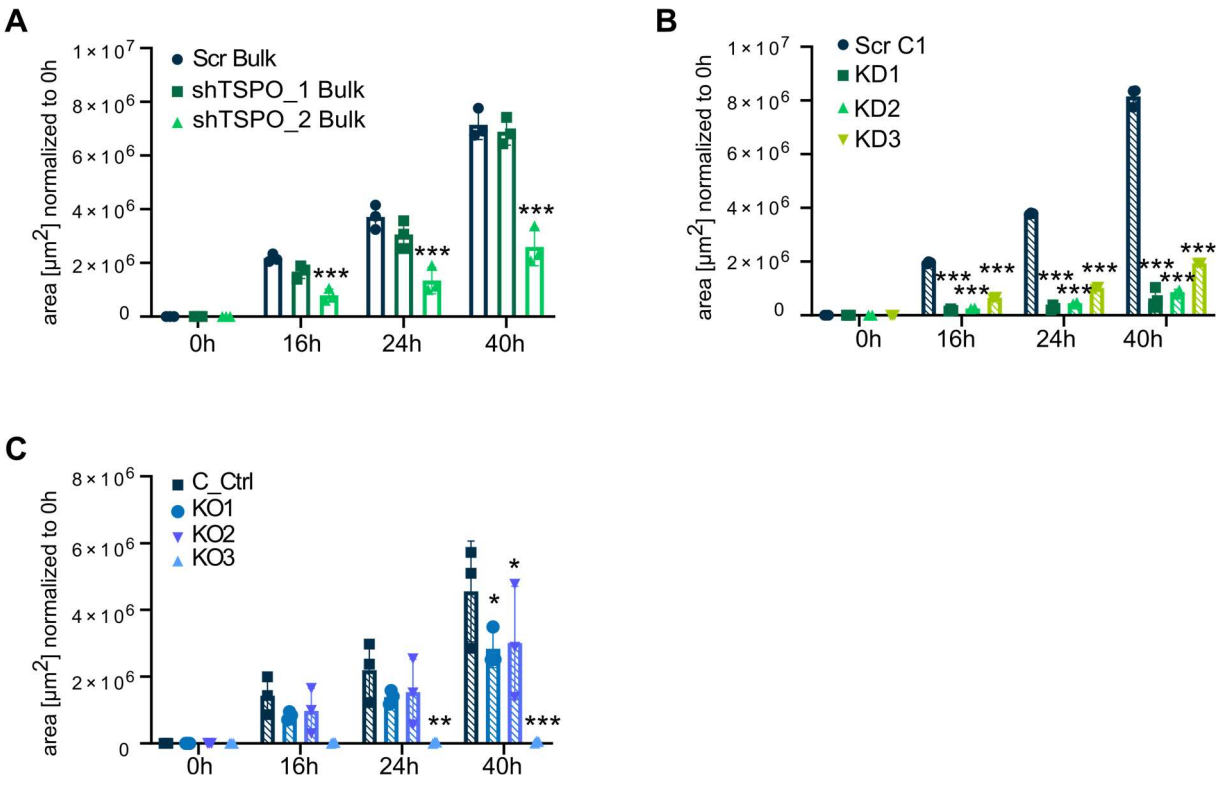

Figure 19. TSPO deficiency impairs basal migration rates of BTIC13. Spheroid migration assay was performed to analyze the basic migratory capacity of TSPO-deficient bulk (**A**), TSPO KD clones (**B**), and TSPO KO clones (**C**) compared to their respective controls. Migration was measured at indicated time points and is presented as the relative area expansion normalized to the initial spheroid size at 0 hours. Cumulative data of three independent experiments are shown as ± SD. Asterisks indicate significant differences between TSPO-deficient cell line and control. P-values were calculated using two-way ANOVA followed by Dunnett´s *post hoc* test (*P ≤ 0.05; **P ≤ 0.01; ***P ≤ 0.001).

4.4.3 Characterization of the relevant T cell effector molecules of BTIC13

To enable the activity of T cell effector molecules on tumor cells, it is necessary that tumor cells express the corresponding receptors. Consequently, a primary goal was to obtain an overview of effector molecules that could be used for subsequent experiments. Therefore, the surface expression of relevant receptors for effector molecules in BTIC13 was characterized by flow cytometry.

First, receptors of the pro-inflammatory cytokines TNFα and IFNγ including TNF-R1, TNF-R1 and IFN- R1 were evaluated (Figure 20, upper panel). Within BTIC13, 78.4 % of the cells express TNF-R1. In contrast, only a minority fraction of BTIC13 (27.8 %) showed a positive TNF-R2 surface expression. IFN-R1 was expressed by the majority of BTIC13 cells (97.1 %).

Furthermore, the expression levels of receptors mediating the extrinsic apoptosis response were evaluated (Figure 20, lower panel). Those include the Fas receptor which interacts with the death ligand FasL that was found to be expressed in 100 % of the BTIC13 population. In addition, the receptors of the death ligand TRAIL, namely death receptors (DR)-4 and -5, were expressed by 69 % and 98 % of the cells, respectively.

In summary, BTIC13 showed a generally high surface expression of relevant cytokine- and death receptors.

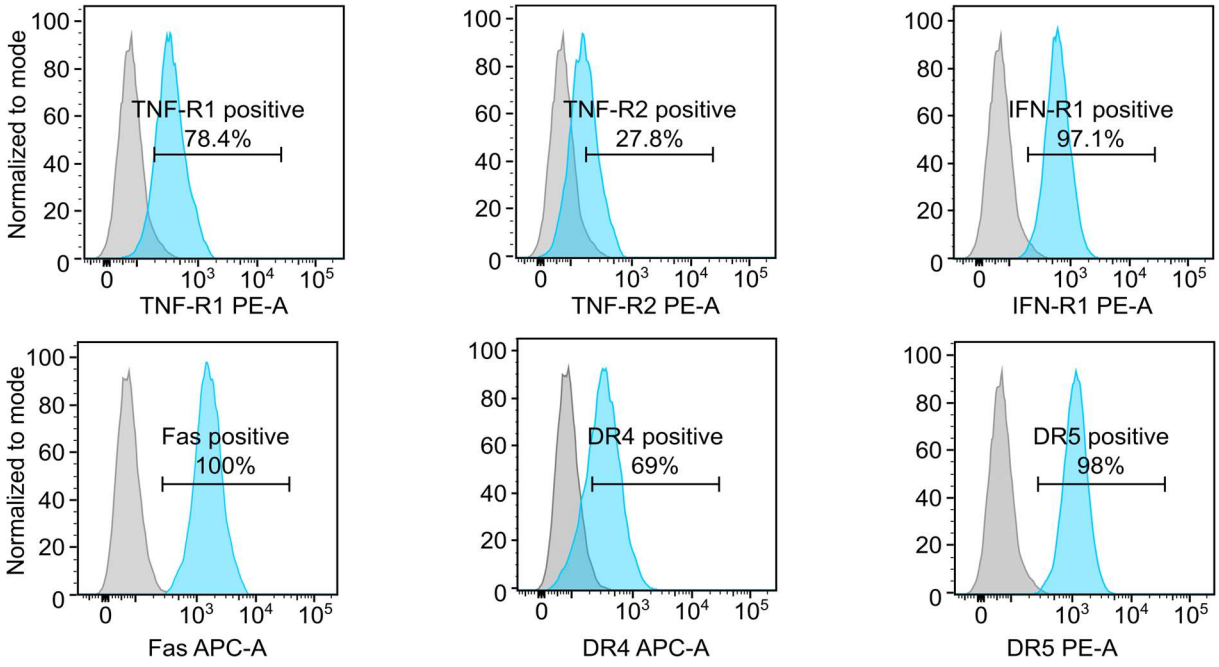

Figure 20. Cell surface expression of receptors of key T cell effector molecules in BTIC13. Flow cytometry analysis of TNFα (TNF-R1, TNF-R1) and IFNγ (IFN-R1) cytokine receptors as well as the death ligand receptors, Fas, DR4, and DR5. Representative histogram plots show the antibody-stained samples (blue) against the isotype control (grey).

The preceding experiments confirmed that BTIC13 expresses surface receptors of relevant cytokines and death ligands. However, there are also intrinsic mechanisms that determine sensitivity to these factors and may shape TSPO-induced apoptotic events. As this thesis is dedicated to the role of TSPO in apoptosis, the next step was to evaluate the impact of intrinsic mechanisms on cell viability and to establish a working concentration of these factors for further experiments.

For this experiment, TSPO-deficient and -control BTICs were exposed to increasing concentrations of recombinant human TNFα, IFNγ, FasL, and TRAIL. The concentrations ranged from 0 ng/ml up to 1,000 ng/ml, and the relative proportion of viable cells was measured after 48 h with the Resazurin® reduction assay.

Figure 21 displays the impact of TNFα, IFNγ, FasL and TRAIL on the cell viability of the TSPO-KD bulk cells. A 25 % reduction in cell viability at the highest concentration was defined as cutoff for considerable effects on cell viability. As evident from figure 21A and figure 21B, TNFα and FasL had only minimal effects on cell viability even at high concentrations and did not reach the 25 % cut-off mark. IFNγ evoked a modest but dose-dependent reduction of cell viability (Figure 21C). At a concentration of 1,000 ng/ml, the relative proportions of viable cells of shTSPO_1 Bulk, shTSPO_2 Bulk and Scr Bulk were 78 %, 85 %, and 71 %, respectively. The strongest effect on cell viability was observed with TRAIL (Figure 21D). In all three cell lines, TRAIL reduced the cell viability starting at concentration of 1 ng/ml until reaching a plateau phase at 250 ng/ml. At this plateau phase, the proportion of viable cells was reduced by approximately 50 %. This indicates that about one half of the population in BTIC13 is responsive to TRAIL, while the other half is resistant due to yet unknown reasons. Notably, there were no significant differences between the two TSPO- deficient cell lines (shTSPO_1 Bulk, shTSPO_2 Bulk) and the control Scr Bulk.

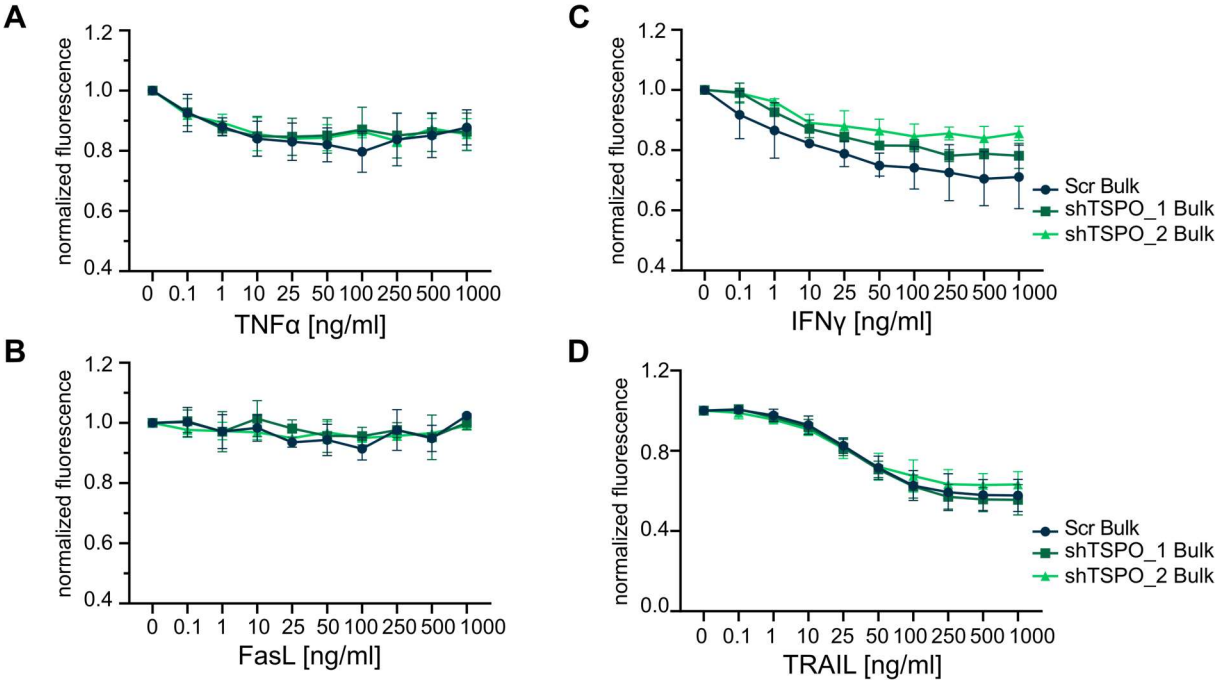

Figure 21. Effect of TNFα, IFNγ, FasL, and TRAIL on cell viability of BTIC13 KD bulk cells. Cells were treated with increasing concentrations of TNFα, IFNγ, FasL, and TRAIL as indicated. After 48 hours, cell viability was measured with the Resazurin reduction assay. Data are presented as relative fluorescence normalized to 0 ng/ml treatment. Cumulative data of three independent experiments are shown as mean ± SD.

Comparable to the results of the KD bulk cells (Figure 21), TNFα, FasL, and IFNγ had no substantial effect on cell viability in the TSPO KD clones (Figure 22A, B, C). Exposure to TRAIL, on the other hand, resulted in a dose-dependent reduction of cell viability. This effect was particularly pronounced in KD1 and KD2. After passing the threshold dose of 1 ng/ml, increasing concentrations of TRAIL resulted in a steep decline of viable cells until reaching a plateau phase at 250 ng/ml with around 30 % of viable cells remaining (Figure 22D). In contrast, KD3 showed a similar TRAIL response compared to the control Scr C1. Here, increasing exposure to TRAIL resulted in a moderate but dose-dependent reduction of viability that plateaued at a concentration of 250 ng/ml with approximately 60 % of the cells still viable. Given the differential responses of the KD clones, these findings support the assumption that subpopulations of the BTIC13 bulk cells are intrinsically TRAIL-responsive or -resistant.

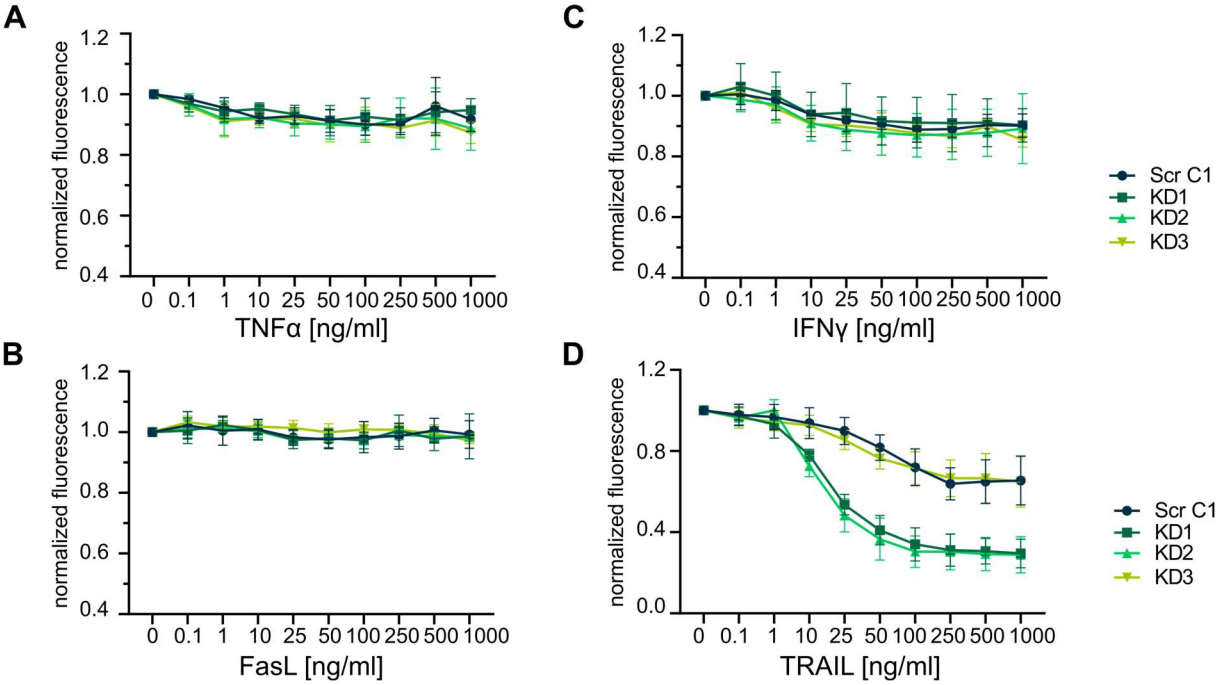

Figure 22. Effect of TNFα, IFNγ, FasL, and TRAIL on cell viability of BTIC13 KD clones. Cells were treated with increasing concentrations of TNFα, IFNγ, FasL, and TRAIL as indicated. After 48 hours, cell viability was measured with the Resazurin reduction assay. Data are presented as relative fluorescence normalized to 0 ng/ml treatment. Cumulative data of three independent experiments are shown as mean ± SD.

Consistent with the results for the TSPO KD Bulk and clonal cell lines, TNFα, IFNγ and FasL did not significantly reduce the cell viability of the TSPO KO clones as the cut-off threshold of 25 % was not reached (Figure 23A, B, C). However, contrasting the previous findings, TRAIL did not have a strong impact on cell viability in the TSPO KO clones (Figure 23D). While KO1 and KO2 showed an almost negligible response (84 % and 72 % survival rates at the plateau phase starting at 250 ng/ml), KO3 and the control C_Ctrl were almost completely resistant to TRAIL treatment (Figure 23D).

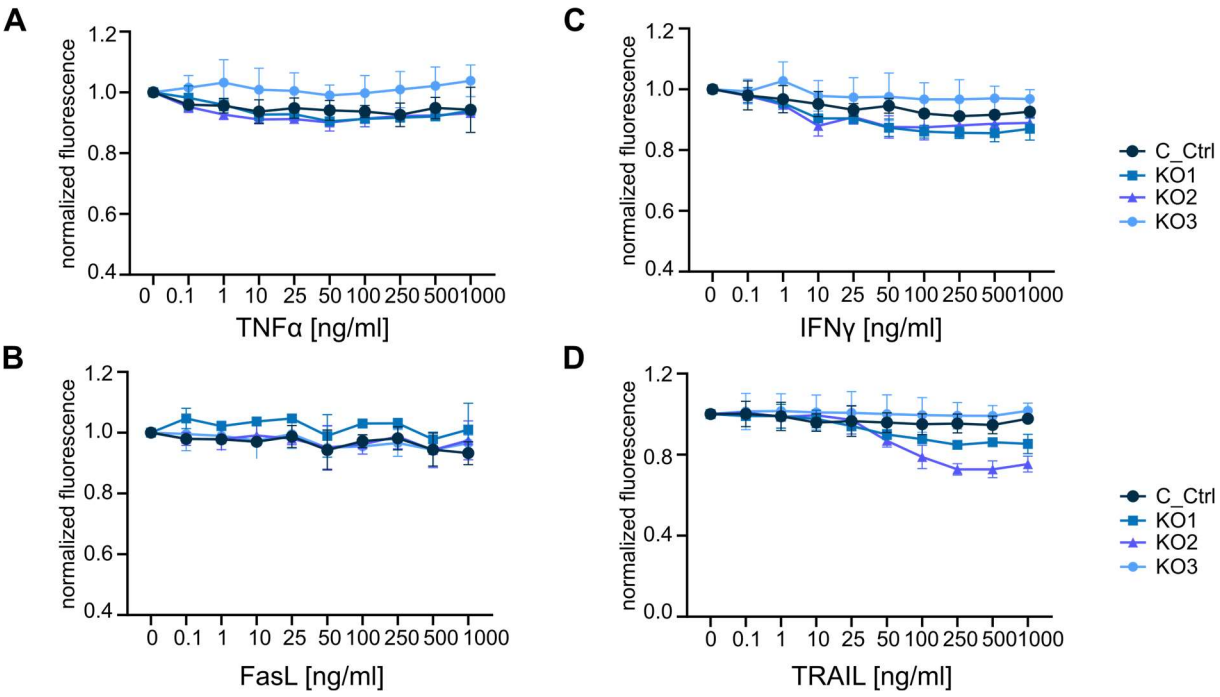

Figure 23. Effect of TNFα, IFNγ, FasL, and TRAIL on cell viability of BTIC13 KO clones. Cells were treated with increasing concentrations of TNFα, IFNγ, FasL, and TRAIL as indicated. After 48 hours, cell viability was measured with the Resazurin reduction assay. Data are presented as relative fluorescence normalized to 0 ng/ml treatment. Cumulative data of three independent experiments are shown as mean ± SD.

Based on these experiments, a working concentration of 50 ng/ml of TRAIL was selected for the in-depth apoptosis analysis. This concentration is approximately within the median of the dose-response range of TRAIL-sensitive BTIC13 cells. The percentage of viable cells at 50 ng/ml for each cell line is summarized in table 23.

Table 23. Percentage of viable cells at 50 ng/ml TRAIL.
The relative number of viable cells was determined using the Resazurin reduction assay and normalized to the 0 ng/ml treatment.

TSPO Knockdown cell line	% cell viability at [50 ng/ml TRAIL]	TSPO Knockout cell line	% cell viability at [50 ng/ml TRAIL]
Scr Bulk	62 %	C_Ctrl	96 %
shTSPO_1 Bulk	62 %	KO1	89 %
shTSPO_2 Bulk	72 %	KO2	75 %
Scr_C1	82 %	KO3	100 %
KD1	41 %		
KD2	37 %		
KD3	76 %		

In summary, despite expressing the corresponding receptors on the cell surface, the impact of TNFα, IFNγ, and FasL on cell viability was found to be negligible in both, TSPO-deficient and -control BTIC13, which excludes them for an in-depth apoptosis analysis. In contrast, TRAIL exhibited a dose-dependent reduction of cell viability in TSPO KD bulk and clones, albeit to a different extent. Furthermore, TSPO KO clones were not sensitive to TRAIL. These observations warranted further investigations on the impact of TSPO function on the response to TRAIL in the different cell populations.

4.5 Impact of TSPO deficiency on apoptosis

Cellular resistance to apoptosis is an important mechanism by which glioblastoma evades the immune system. Recent findings revealed that stable downregulation of TSPO augments T cell-mediated killing of human glioblastoma cell lines and BTICs [222]. This notion is reinforced by multiple studies that suggest a role of TSPO in apoptosis [151, 195, 199].

These observations gave rise to the following hypothesis: elevated levels of TSPO in glioblastoma contribute to the resistance against the anti-tumor effects of cytotoxic T cells by modulating the apoptotic response. In this context, the impact of TSPO in apoptosis was investigated in BTIC13 in more detail.

4.5.1 TRAIL-induced apoptosis response of TSPO-KD bulk BTIC13

The previous experiments showed that the death ligand TRAIL affects cell viability of BTIC13. Accordingly, a cytotoxic T cell attack in a cell culture setting using TRAIL was simulated to explore the apoptosis signaling of TSPO-deficient and control BTICs.

In a first experiment, shTSPO_1 Bulk and Scr Bulk cells were treated with 50 ng/ml TRAIL for 6 hours. To differentiate between early and late apoptotic cells as well as necrotic cells, cells were stained with Annexin V (AnxV) and 7-amino-actinomycin D (7-AAD). Early apoptotic cells express phosphatidylserines on the outer leaflet of the plasma membrane, which can be labeled with AnxV. Late apoptotic cells and necrotic cells lose their cell membrane integrity and become permeable to 7-AAD. By this method, the percentage of dead cells (early, late apoptotic, and necrotic cells) was analyzed by flow cytometry.

TRAIL strongly increased the percentage of dead cells in shTSPO_1 Bulk compared to the untreated control (Figure 24A). Exposure to TRAIL also resulted in a significantly higher percentage of dead cells in shTSPO_1 Bulk compared to the control Scr Bulk. Notably, the percentage of dead cells in Scr Bulk was already higher in the untreated samples (~20 % vs. ~10 % in shTSPO_1 Bulk) and TRAIL did not profoundly elevate this number (Figure 24A). Exposure to TRAIL resulted in a significantly higher percentage of dead cell in shTSPO_1 Bulk compared to the control Scr Bulk (Figure 24A).

As a next step, the activation of the caspase cascade was investigated to gain a deeper understanding of the underlying apoptosis pathways. First, the optimal timing for TRAIL treatment was determined. Therefore, BTIC13 cells were stimulated with 50 ng/ml of TRAIL at five different time points (0.5, 1, 3, 6, and 16 hours) and the processing of key components of the caspase cascade was investigated via Western blot. These included caspase-9 (Casp9), which is the initiator caspase of the mitochondrial-mediated apoptosis pathway. Once mitochondrial apoptosis is activated, caspase-9 is processed to its active form, which becomes apparent in the Western blot by detecting the cleaved (cl) Casp9 fragments. Activation of the effector caspase-3 (Casp3) is evidenced by the detection of clCasp3 fragments (fragments at 20 kDa, 17 kDa and 12 kDa). Finally, the processing of the DNA repair enzyme PARP1 was examined, as its degradation to clPARP1 by active caspases is considered as hallmark event of apoptosis.

Exposure to TRAIL resulted in a fast activation of Casp3. As early as 30 min post-exposure, clCasp3 fragments were present in the Western blot (Figure 24B). The activation of Casp9 appeared slightly later at 3 hours of treatment (Figure 24B). This suggests that the initial response to TRAIL occurred directly via the extrinsic apoptosis pathway (Casp3 activation) followed by a subsequent shift towards the mitochondrial pathway (Casp9 activation). The fragmentation of PARP1, an event downstream of caspase-activation, also became evident after 3 hours. At the 6-hour mark, apoptosis activation was at its strongest, as the strongest cleavage bands were detected in the Western blot. By 16 hours, PARP1 was fully degraded which implies that the apoptotic cascade was maximally activated and had reached its final state (Figure 24B).

This experiment revealed that first distinct patterns of apoptosis induction occur as early as 1 hour of TRAIL treatment. Based on these findings, 1 and 3 hours were selected as exposure times for the apoptosis experiments.

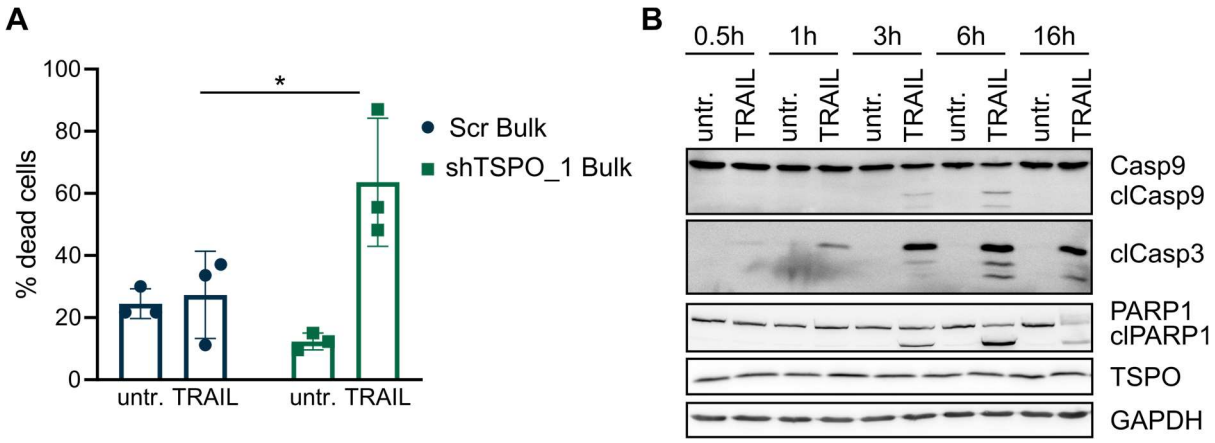

Figure 24. TRAIL induces apoptosis in the BTIC13 bulk cell line. (**A**) Flow cytometry analysis of shTSPO_1 Bulk and Scr Bulk. Cells were treated with 50 ng/ml of TRAIL for 6 hours and stained with Annexin V (AnxV)-FITC-A and 7-amino-actinomycin D (7-AAD)-APC-A. Percentage of dead cells was calculated as 100 %–%AnxV$^-$ 7-AAD$^-$. Cumulative data of three independent experiments are shown as mean ± SD. (**B**) Representative Western blots for caspase-9 (Casp9), caspase-3 (Casp3) and PARP1 processing into cleaved (cl)Casp9, clCasp3, and clPARP1. BTIC13 was treated with TRAIL (50 ng/ml) for 0.5, 1, 3, 6, and 16 hours. Equal loading was confirmed by GAPDH staining. P-values were calculated using two-way ANOVA followed by Sidak´s *post hoc* test (*$P \leq 0.05$).

Following that, it was investigated whether there are temporal differences in the caspase cascade activation of TSPO-deficient compared to TSPO-proficient bulk cells. Accordingly, TSPO-KD and control bulk cells were stimulated with 50 ng/ml TRAIL for 1 or 3 hours, and the processing of the caspase cascade was investigated via Western blot.

Exposure to TRAIL for 1 hour triggered a rapid activation of Casp3, whereas processing of Casp9 and PARP1 was not detectable (Figure 25; Supplementary figure 1). However, 3 hours of TRAIL exposure induced cleavage of Casp3, Casp9, and PARP1 (Figure 25; Supplementary figure 1).

As evident from the representative Western blot, bands for cleavage products of Casp3, Casp9 and PARP1 were more intense in the TSPO-deficient bulk cells compared to the Scr Bulk control (Figure 25A, Supplementary figure 1A). Yet, relative protein quantification including four independent experiments demonstrated variable results for both, shTSPO_1 Bulk and shTSPO_2 Bulk (Figure 25B, C, D, Supplementary figure 1B, C, D). Notably, although PARP1 fragmentation was significantly higher in TSPO-deficient bulk cells compared to the control, caspase activation was inconclusive (Figure 25D, Supplementary figure 1D). For instance, shTSPO_1 Bulk showed increased activation of Casp9 but no difference in activation of Casp3 when compared to Scr Bulk (Figure 25). In contrast, shTSPO_2 Bulk showed lower levels of Casp9 activation, but no difference in Casp3 compared to Scr Bulk as well (Supplementary figure 1).

Taken together, these events collectively indicate that TRAIL induces cell death via the caspase cascade. However, it remains unclear whether TSPO deficiency sensitizes BTIC13 towards TRAIL-induced apoptosis. To determine whether the observed variances in apoptosis response were caused by TRAIL-resistant subpopulations within the BTIC13 bulk, apoptosis in TSPO-deficient clonal cell lines was investigated next.

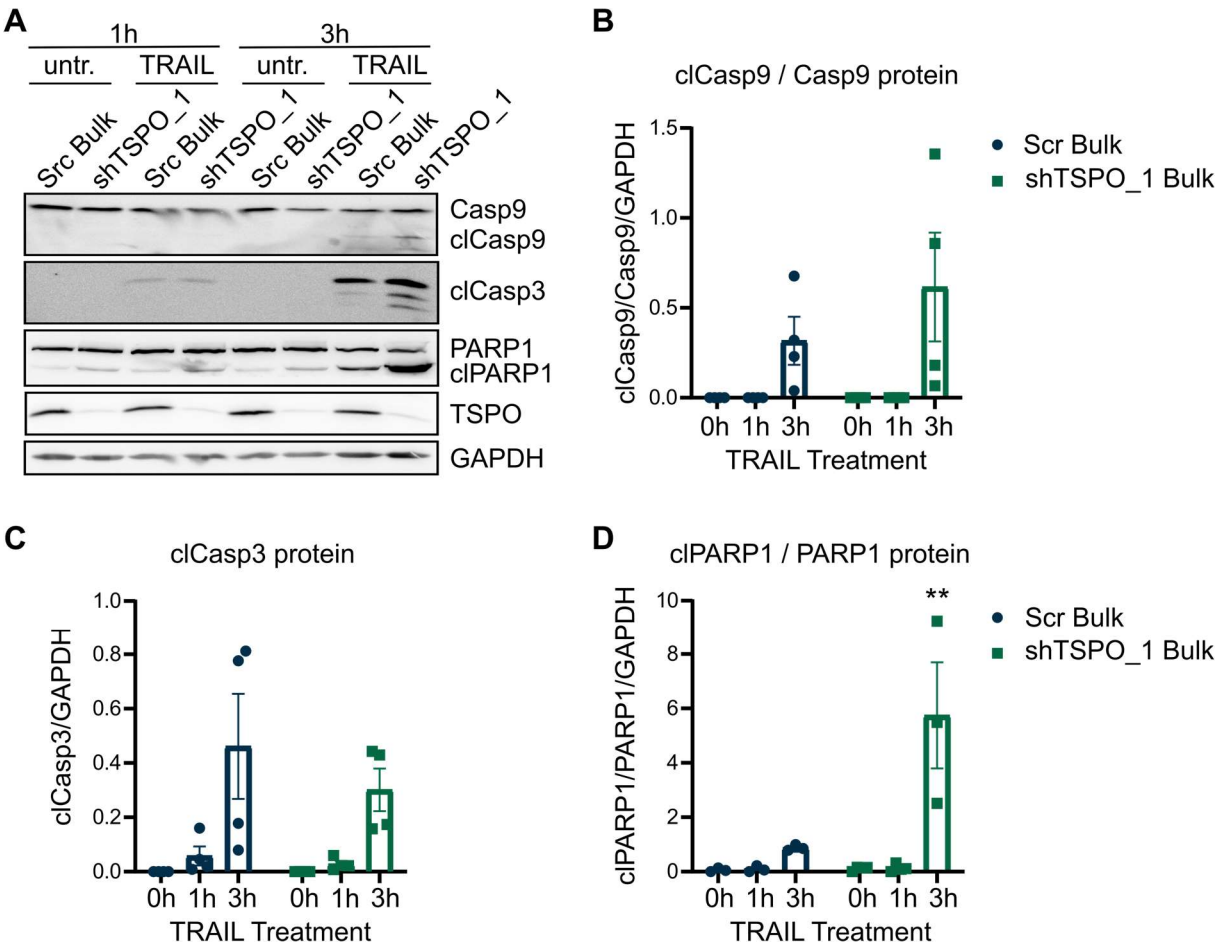

Figure 25. Impact of TRAIL on caspase activation in TSPO-deficient bulk cells. Western blot analysis of caspase-9 (Casp9), caspase-3 (Casp3) and PARP1 processing in shTSPO_1 Bulk compared to the control Scr Bulk. Cells were treated with TRAIL (50 ng/ml) for 0, 1, and 3 hours. (**A**) Representative Western blot of cleaved and full-length forms of Casp9, Casp3, and PARP1. Equal loading was confirmed by GAPDH staining. (**B-D**) Graphs show the relative protein quantification of three independent experiments. Data are presented as the ratio of cleaved to full-length protein of Casp9 (**B**), Casp3 (**C**) and PARP1 (**D**). Data are normalized to GAPDH expression shown as mean ± SD. P-values were calculated using two-way ANOVA followed by Sidak´s *post hoc* test (**$P \leq 0.01$).

4.5.2 TRAIL-induced apoptosis response of TSPO-KD clones

The next goal was to elucidate whether the cellular response to TRAIL depends on TSPO expression or on intrinsic heterogeneity of BTIC13. Therefore, the TRAIL-induced apoptotic response of TSPO-KD and control clones was more deeply investigated.

Using the established experimental setup, TSPO-KD clones (KD1, KD2, KD3) and the control clone Scr C1 were treated with 50 ng/ml TRAIL for 1 and 3 hours, and the activation of the extrinsic and intrinsic apoptotic cascade was systematically analyzed. First, the impact of TRAIL on cell death was assessed by AnxV and 7-AAD staining of TSPO KD clones and control clones followed by flow cytometry.

Representative histograms depict a time-dependent increase of TRAIL-induced cell death in KD1 and KD2 which was substantiated by an increase in AnxV-positive cells after 3 hours of treatment (Figure 26A). Notably, the exposure to TRAIL did not elevate the number of AnxV-positive cells in KD3 and Scr C1 (Figure 26). In more detail, in KD1 and KD2, TRAIL increased the percentage of cells in early apoptosis stages in comparison to KD3 and Scr C1. (Figure 26, Supplementary figure 2). As expected, short-term exposure of TRAIL had no impact on late stages of apoptosis (Figure 26B, Supplementary figure 2). In addition, no significant differences were observed in necrosis between KD clones and control clone (Figure 26B, Supplementary figure 2).

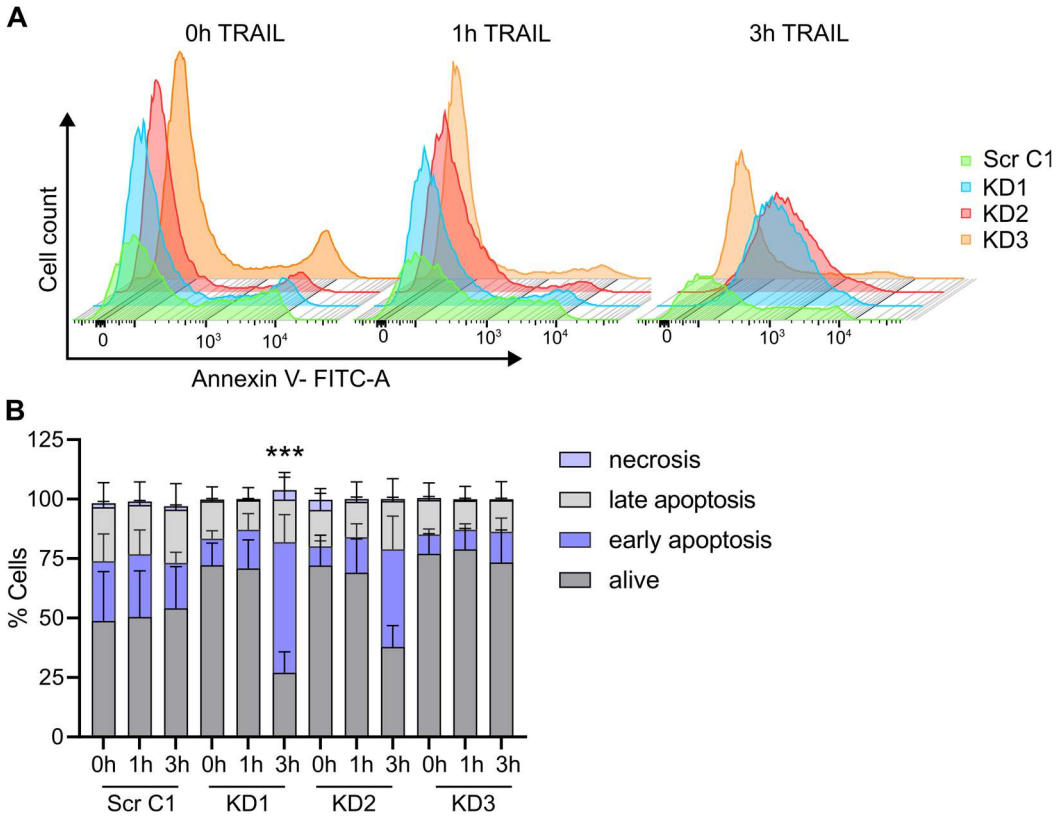

Figure 26. TRAIL induces cell death in KD1 and KD2. Flow cytometry analysis of TSPO KD clones (KD1, KD2, KD3) and the control clone Scr C1. Cells were treated with 50 ng/ml of TRAIL for 1 and 3 hours and stained with AnxV-FITC-A and 7-AAD-APC-A. (**A**) Representative histograms showing the number of AnxV positive cells. (**B**) Percentage of cells in living (% AnxV$^-$ / 7-AAD$^-$), early apoptotic (% AnxV$^+$ / 7-AAD$^-$), late apoptotic (% AnxV$^+$ / 7-AAD$^+$) and necrotic (% AnxV$^-$ / 7-AAD$^+$) condition. Cumulative data of three independent experiments are shown as mean ± SD. Asterisks indicate significant differences of KD clones compared to Scr C1. P-values were calculated using two-way ANOVA followed by Tukey´s *post hoc* test (***$P \leq 0.001$).

As second a step, the activity of the initiator caspase (caspase-8) of the extrinsic apoptosis pathway was evaluated. Since it was not possible to detect caspase-8 by Western blot, a luciferase-based assay was used to measure caspase-8 activity. As shown in figure 27, 1 hour and 3 hours of TRAIL treatment resulted in a significantly higher activation of caspase-8 in KD1 and KD2 compared to the control Scr C1. In contrast, KD3 displayed limited levels of caspase-8 activity after TRAIL exposure, comparable to that of Scr C1 (Figure 27).

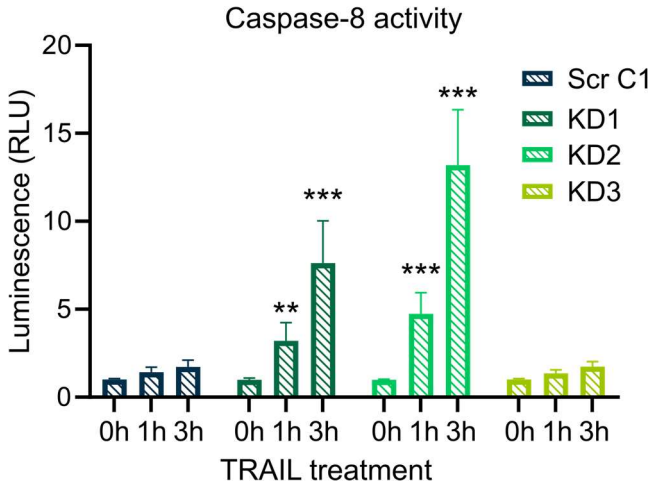

Figure 27. TRAIL induces stronger caspase-8 activity in KD1 and KD2. A luciferase-based caspase-8 Glo assay was used to measure the activity of caspase-8 in BTIC13 KD clones. Data are presented as fold change relative to 0 hours of treatment. Cumulative data of three independent experiments are shown as mean ± SD. Asterisks indicate significant differences of KD clones compared to the Scr C1. P-values were calculated using two-way ANOVA followed by Dunnett´s *post hoc* test (***P* ≤ 0.01; ****P* ≤ 0.001).

The Western blot analysis of processing of Casp9, Casp3 and PARP1 revealed a more prominent activation of the apoptotic cascade in KD1 and KD2 compared to the control clone Scr C1 (Figure 28A). The elevated apoptotic activity of KD1 and KD2 was consistent across biological replicates and highly significant when compared to the Scr C1 (Figure 28). In line with previous experiments, KD3 showed a similar apoptosis response as Scr C1, and only a slight activation of Casp9 and Casp3 along with weak PARP1 fragmentation was detected (Figure 28).

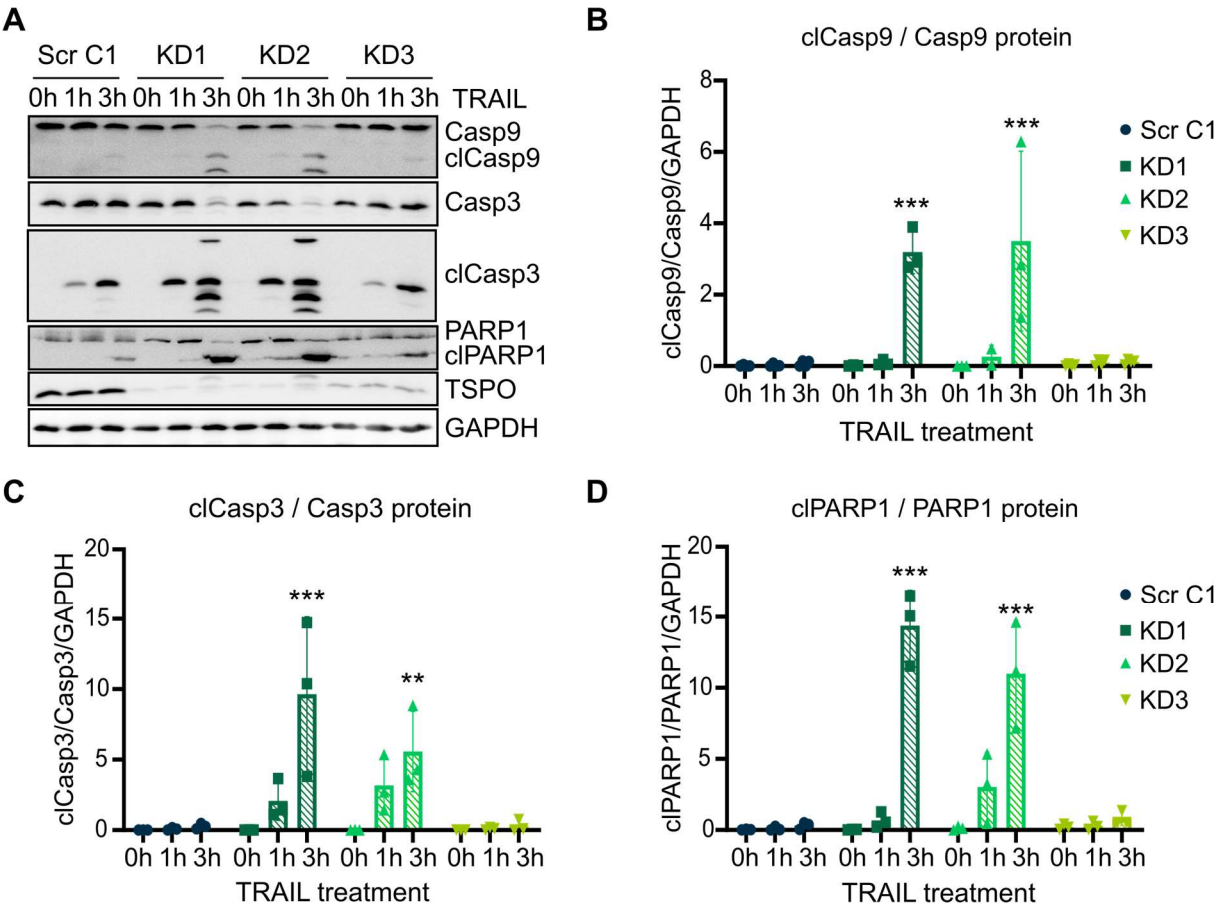

Figure 28. Impact of TRAIL on caspase cascade activation in TSPO KD clones. Western blot analysis of caspase-9 (Casp9), caspase-3 (Casp3) and PARP1 processing in TSPO KD clones (KD1, KD2, KD3) compared to the control clone (Scr C1). Cells were treated with 50 ng/ml TRAIL for 0, 1, and 3 hours. (**A**) Representative Western blot for cleaved and full-length forms of Casp9, Casp3, and PARP1. Equal loading was confirmed by GAPDH staining. (**B-D**) Graphs show the relative protein quantification of three independent experiments. Data are presented as the ratio of cleaved to full-length protein of Casp9 (**B**), Casp3 (**C**) and PARP1 (**D**). Data are normalized to GAPDH expression shown as mean ± SD. Asterisks indicate significant differences between KD clones and control clone Scr C1. P-values were calculated using two-way ANOVA followed by Dunnett´s *post hoc* test (***P* ≤ 0.01; ****P* ≤ 0.001).

Activation of Casp9 indicates that the mitochondrial apoptosis pathway is involved in TRAIL-induced apoptosis of BTIC13. Mitochondrial apoptosis is highly regulated by members of the Bcl-2 protein family. For example, BID plays a critical role in activating the intrinsic apoptosis pathway by linking it to the extrinsic pathway. BID is activated by caspase-8, which cleaves it into its truncated form. In turn, truncated BID activates pore-forming proteins like BAX, leading to the permeabilization of the outer mitochondrial membrane. Consequently, pro-apoptotic factors such as cytochrome c are released into the cytosol, ultimately resulting in the activation of Casp9. Key anti-apoptotic regulators of the Bcl-2 family include Bcl-2, Mcl-1, and Bcl-xL. Simplified, they prevent apoptosis initiation by binding and inhibiting BH-3 activator proteins such

as BID as well as pore-forming proteins. As said, differences in expression ratios of pro- and anti-apoptotic Bcl-2 family members may profoundly regulate the cell sensitivity to TRAIL. Therefore, the expression of key Bcl-2 family proteins was investigated via Western blot analysis.

TRAIL treatment reduced the levels of full-length BID protein levels which indicates that BID is cleaved to its truncated form to initiate intrinsic apoptosis (Figure 29A, B). This decrease in BID was significant in KD1 and KD2 compared to Scr C1 (Figure 29B). Degradation of BID was not as apparent in KD3 and Scr C1 after TRAIL treatment (Figure 29B). All three knockdown clones exhibited significantly lower levels of Bcl-2 compared to the control Scr C1 (Figure 29C). Notably, despite low Bcl-2 protein expression, the TRAIL-insensitivity of KD3 suggests the involvement of other underlying mechanisms that determine the observed apoptosis response. In addition, TRAIL treatment facilitated the degradation of the anti-apoptotic Mcl-1 protein, specifically in KD1 and KD2, but not in KD3 and Scr C1 (Figure 29A, D). In contrast, the expression of Bcl-xL and BAX, did not reveal conclusive differences between KD clones and control (Figure 29A, E, F).

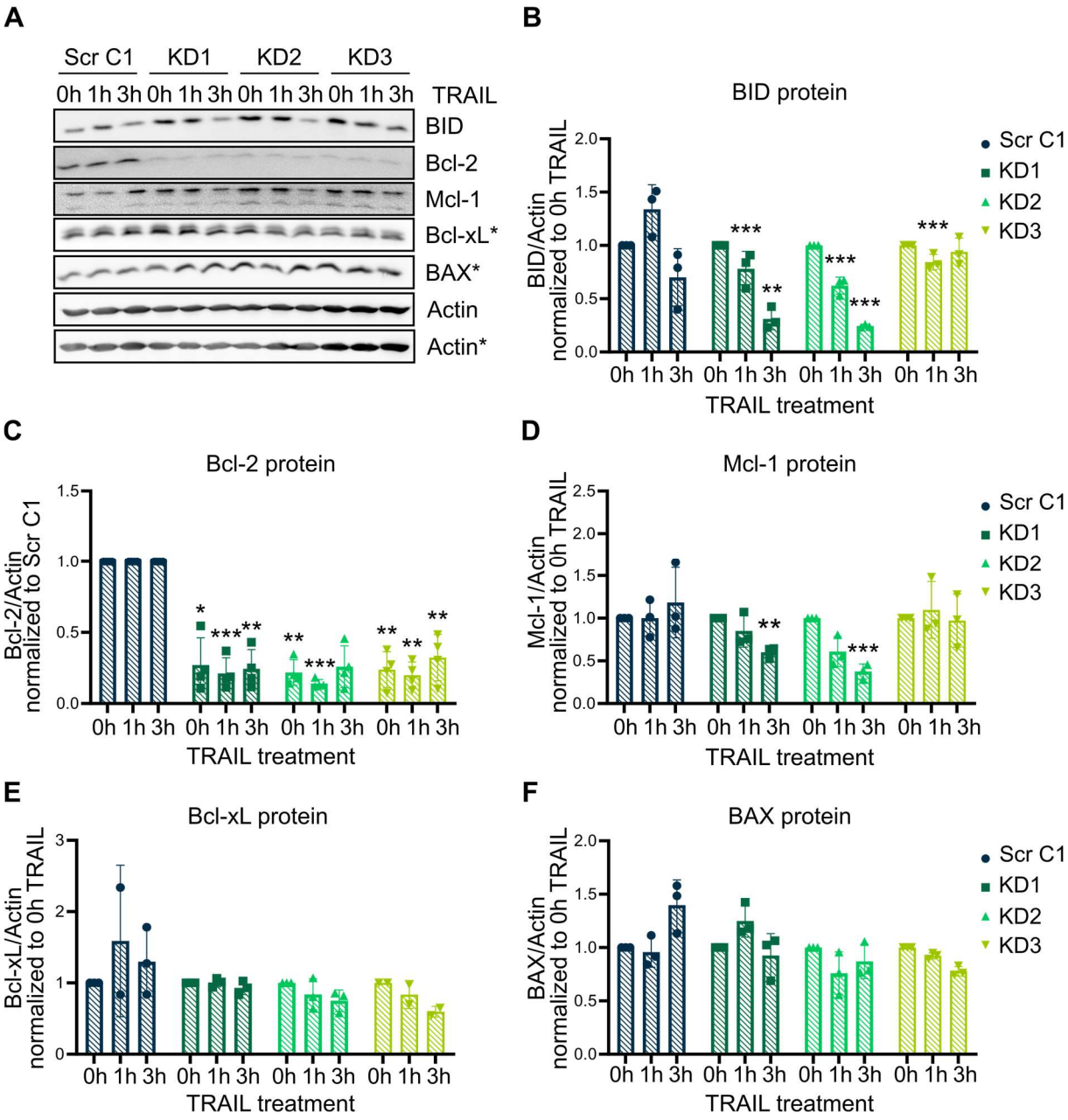

Figure 29. Impact of TRAIL on the expression of Bcl-2 protein family members in TSPO KD clones. Western blot analysis of the apoptosis initiator BID, anti-apoptotic proteins Bcl-2, Mcl-1, Bcl-xL, and pro-apoptotic pore forming protein BAX in TSPO KD clones (KD1, KD2, KD3) compared to the control clone (Scr C1). Cells were treated with 50 ng/ml TRAIL for 0, 1, and 3 hours. (**A**) Representative Western blot of the levels of BID, Bcl-2, Mcl-1, Bcl-xL and BAX. Equal loading was confirmed by β-Actin staining. (**B-F**) Graphs show the relative protein quantification of three independent experiments. BID (**B**), Mcl-1 (**D**), Bcl-xL (**E**) and BAX (**F**) are presented as fold change relative to 0 hours of TRAIL. Bcl-2 level are shown as fold change relative to Scr C1 (**C**). Data are normalized to β-Actin expression shown as mean ± SD. Asterisks indicate significant differences between KD clones and control clone Scr C1. P-values were calculated using two-way ANOVA followed by Dunnett´s *post hoc* test (*P ≤ 0.05; **P ≤ 0.01; ***P ≤ 0.001).

Following mitochondrial membrane permeabilization, cytochrome c is released from mitochondria into the cytosol. To obtain insight into these dynamics, whole cell lysates of the TSPO-deficient KD1 and control Scr C1 clonal cells were prepared and separated into cytosolic and mitochondrial fractions. This allowed the assessment of BAX protein translocation from the cytosol into the mitochondria and the subsequent accumulation of cytochrome c into the cytosolic compartment in response to TRAIL exposure.

As shown by a representative Western blot, subcellular fractionation resulted into pure mitochondrial and cytosolic fractions (Figure 30A), confirmed by the absence of cytosolic tubulin within the mitochondrial fraction and the lack of contamination of mitochondrial VDAC within the cytosolic fraction. Exposure to TRAIL facilitated the accumulation of the pore-forming protein BAX into the mitochondria (Figure 30). Concomitant with that, increased levels of cytochrome c were detected in the cytosolic fractions after TRAIL treatment (Figure 30). As expected, this effect was stronger in the TRAIL-sensitive clone KD1 compared to the control Scr C1.

Taken together, these experiments demonstrated that both, the extrinsic and intrinsic apoptotic cascades are involved in the TRAIL response of the TSPO KD clones. TRAIL sensitivity of TSPO-deficient KD1 and KD2 was notably heightened compared to the TSPO-proficient control. However, despite low TSPO expression, KD3 shows a similar response to TRAIL as the control.

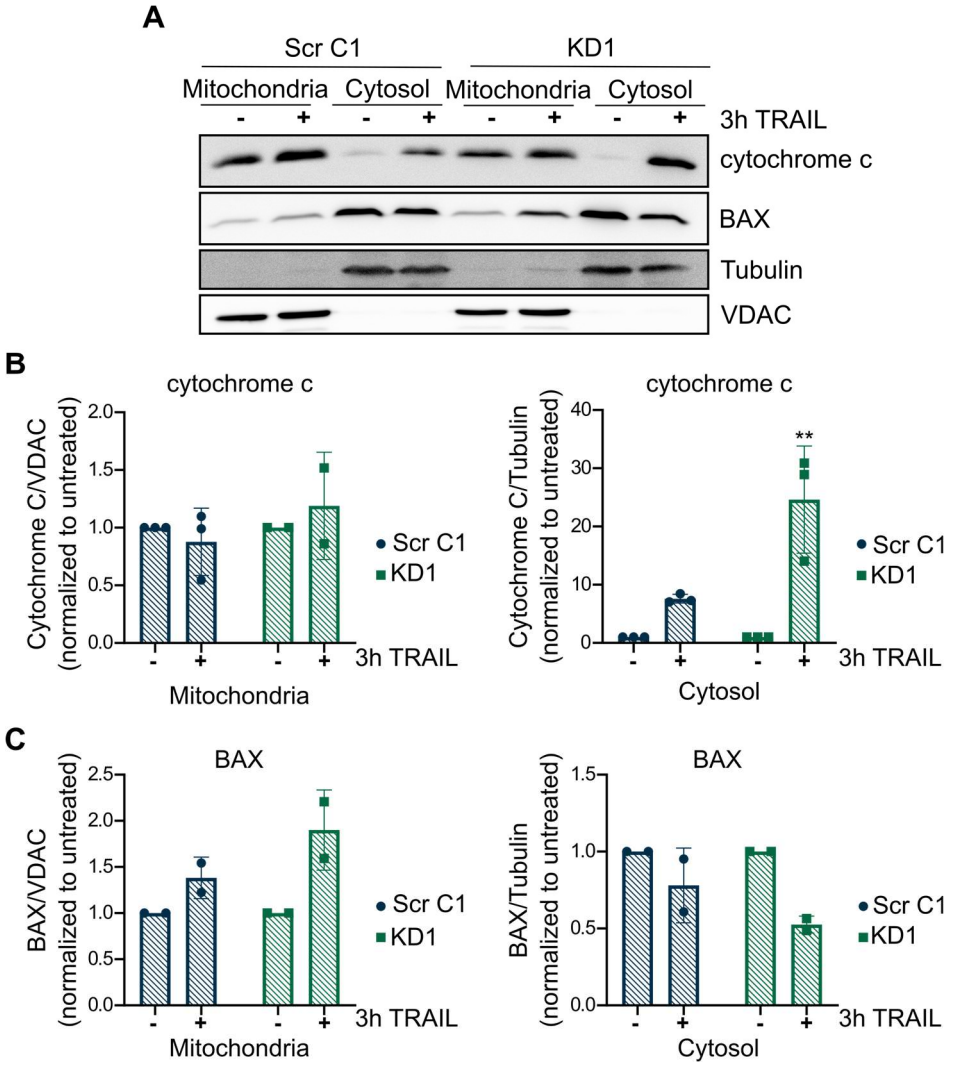

Figure 30. Increased cytochrome c release in KD1 compared to control cells after TRAIL treatment. Western blot analysis of cytochrome c release in TSPO-deficient KD1 and control Scr C1. Cells were treated with 50 ng/ml TRAIL for 3 hours. (**A**) Representative Western blot of cytochrome c and BAX in mitochondrial and cytosolic cell fractions. Purity of the mitochondrial fractions was confirmed by VDAC staining, purity of the cytosolic fraction was confirmed by tubulin staining. (**B,C**) Graphs show the relative protein quantification of at least two independent experiments. Data are normalized to 0 hours of TRAIL and presented relative to VDAC for the mitochondrial fraction and relative to tubulin for the cytosolic fractions. Asterisks indicate significant differences between KD1 and control Scr C1. P-values were calculated using two-way ANOVA followed by Sidak´s *post hoc* test (**$P \leq 0.01$).

4.5.3 TRAIL-induced apoptosis response of TSPO-re-expressing clones

To answer the question, if the differential apoptotic sensitivity outlined above is a TSPO-dependent effect or rather dependent on the genetic background of individual cells within the original culture, a TSPO re-expressing plasmid (pLJM1-EGFP, gift from David Sabatini (Addgene ID #19319, http://n2t.net/addgene:19319; RRID:Addgene_19319) was designed which encodes a mutated human TSPO cDNA sequence. The integration of four base pair substitutions resulted into silent mutations within the shRNA binding region to prevent efficient

shRNA-induced mRNA degradation (Figure 31A). The TSPO-deficient KD1 clone was lentivirally transduced with either the control plasmid pLJM1 or with the pLJM_mutant (mt) TSPO plasmid. Since the TSPO-re-expression effect was small in bulk cells, single cell clones were generated, and those showing the highest TSPO-re-expression were selected for further experiments along with an empty vector control (highlighted in orange). For better readability, names were changed to rescue control R_C1 (KD1_pLJM C5), KD1_R1 (KD1 mtTSPO C8), and KD1_R2 (KD1 mtTSPO E11) (Figure 31B).

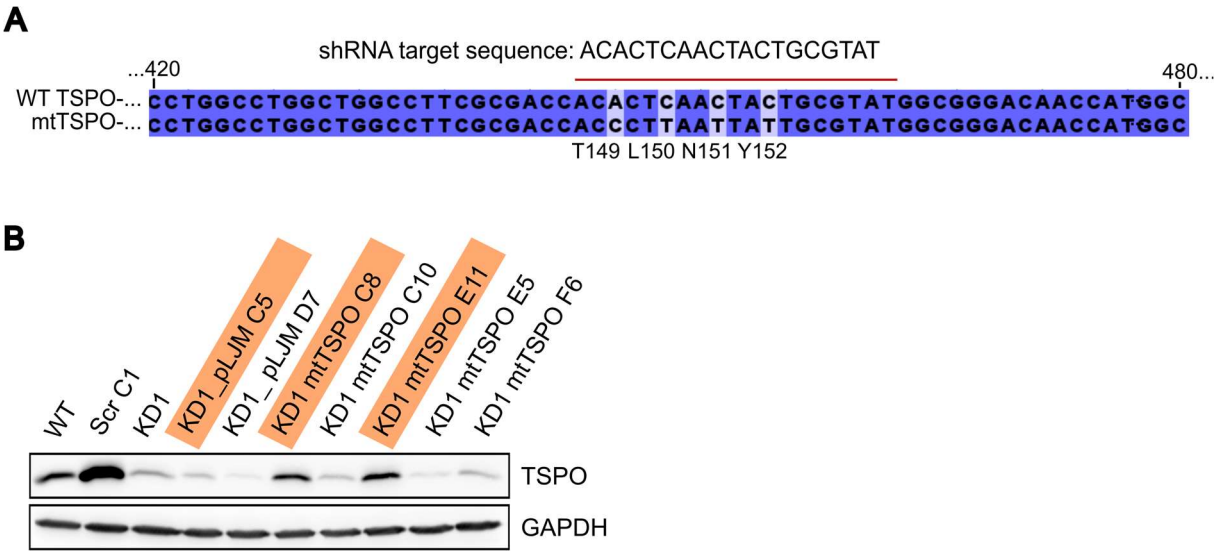

Figure 31. TSPO re-expression in the BTIC13 knockdown clone KD1. (**A**) Nucleotide sequence alignment of wildtype (WT) and shRNA-resistant mutant TSPO cDNA is shown. Color code represents sequence similarity from dark blue (identical) to light blue. The four base pair exchanges leading to the silent mutations are indicated. (**B**) Western blot shows screening for successful TSPO re-expression after viral transduction in comparison to WT, Scr C1, and KD1 cells. The clones chosen for further experiments are highlighted orange. Equal loading was confirmed by GAPDH staining.

To test the hypothesis that TSPO re-expressing clones would reacquire resistance to TRAIL, the induction of apoptosis was compared between BTIC13 wildtype (WT), Scr C1, KD1, R_C1, KD1_R1, and KD1_R2. Therefore, cells were exposed to TRAIL for 3 hours and Casp9, Casp3, and PARP1 processing was examined via Westen blot. Additionally, the expression of the anti-apoptotic regulator Bcl-2 and the phosphorylation status of the pro-survival transcription factor NFκB p65 as alternative resistance mechanism was investigated.

Consistent with earlier findings, KD1 demonstrated a more pronounced induction of apoptosis compared to BTIC13 WT and Scr C1 (Figure 32A-D). Similarly, the rescue control clone R_C1, exhibited comparable levels of apoptosis akin to those of the KD1 clone (Figure 32A-D). However, both TSPO re-expressing clones, KD1_R1 and KD1_R2, differed in their sensitivity to

TRAIL as indicated by diverging levels of Casp9, Casp3 and PARP1 processing. Moreover, the clone KD1_R2, showing higher TSPO-re-expressing levels, displayed a comparably higher activation of apoptosis in contrast to the clone KD1_R1 with lower levels of TSPO re-expression for which a lower extent of Casp9, Casp3 and PARP1 processing was observed (Figure 32A-D).

Regarding Bcl-2 expression, Scr C1 exhibited increased Bcl-2 levels relative to all other clones as well as BTIC13 WT cells (Figure 32F). The decreased TRAIL sensitivity of KD1_R1, as described before, did not correlate with levels of Bcl-2 expression, which were found to be within the same range as for KD1, R_C1 and KD_R2, suggesting other resistance mechanisms. Notably, the cell lines less responsive to TRAIL (BTIC13 WT, Scr C1 and KD1_R1) showed higher levels of NFκB p65 phosphorylation (Figure 32E). This suggests that stimulation with TRAIL favors pro-survival signaling instead of apoptosis induction in these less responsive cell lines.

Collectively, these results imply that the response to TRAIL does not solely rely on TSPO expression and is rather influenced by a multitude of intrinsic resistance mechanisms. These include a high expression of anti-apoptotic Bcl-2 protein and the activation of pro-survival signaling such as the NFκB pathway. However, it remains uncertain whether TSPO deficiency sensitizes a subpopulation of BTIC13 to TRAIL. In addition, the experiments performed did not show consistent markers that clearly predict the response to TRAIL.

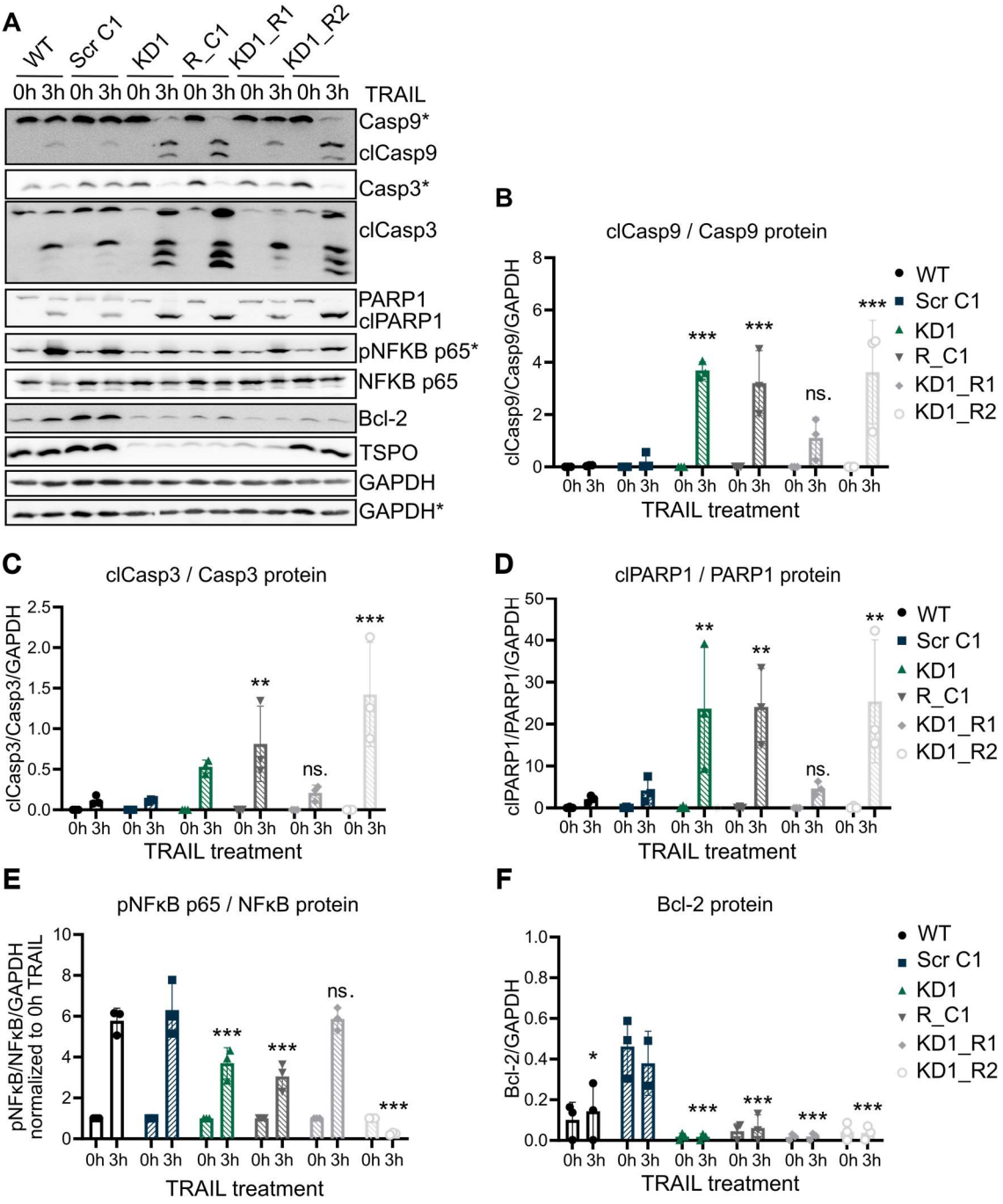

Figure 32. Impact of TRAIL on caspase activation in TSPO-re-expressing clones. Western blot analysis of caspase-9 (Casp9), caspase-3 (Casp3) and PARP1 processing, NFκB p65 phosphorylation and Bcl-2 expression in TSPO re-expressing clones (KD1_R1, KD1_R2) compared to the rescue control clone (R_C1), KD1, Scr C1, and BTIC13 wildtype (WT). Cells were treated with 50 ng/ml TRAIL for 0 and 3 hours. (**A**) Representative Western blot for cleaved and full-length forms of Casp9, Casp3, and PARP1, phosphorylated (p) NFκB p65, total NFκB p65 and Bcl-2. Equal loading was confirmed by GAPDH staining. (**B-F**) Graphs show the relative protein quantification of three independent experiments. Data are presented as the ratio of cleaved to full-length protein of Casp9 (**B**), Casp3 (**C**) and PARP1 (**D**), and ratio of phosphorylated to total of NFκB p65 (**E**). (**E**) pNFκB/NFκB level are shown relative to the 0 hour treatment. Data are normalized to GAPDH expression shown as mean ± SD. Asterisks indicate significant differences of rescue and KD clones compared to control clone Scr C1. P-values were calculated using two-way ANOVA followed by Dunnett´s *post hoc* test (*$P \leq 0.05$; **$P \leq 0.01$; ***$P \leq 0.001$; ns, non-significant).

4.5.4 TRAIL-induced apoptosis response of TSPO KO clones

One of the primary motivations for generating TSPO KO clones, was to substantiate the observations made for TSPO KD clones. However, previous results already pointed to the diminished susceptibility of TSPO KO clones towards TRAIL-induced apoptosis. Given that the TRAIL response is presumably highly dependent on a variety of resistance mechanisms within BTIC13, the following experiments were aimed to elucidate the underlying factors behind the acquired TRAIL resistance in the TSPO KO clones.

First, TSPO KO clones were exposed to TRAIL for 6 hours and their respective responses were screened in the established Western blot setting that includes investigation of processing of Casp9, Casp3, and PARP1 as well as levels of the Bcl-2 protein.

Compared to the TSPO KD clones, the apoptosis induction in the TSPO KO clones was low even after 6 hours of TRAIL exposure (Figure 33). As evident by the exemplary Western blot, exposure to TRAIL resulted in minimal Casp9 activation in KO1 and KO3 that was even too low for protein quantification (Figure 33A). Correspondingly, the levels of Casp3 activation and PARP1 processing remained notably subdued and were in no comparison to the induction observed in the TSPO KD clones (Figure 28). Despite individual differences of the KO clones in apoptosis response, no conclusive correlations with TSPO expression were possible (Figure 33A, B). Notably, KO2 showed the highest Bcl-2 expression and the lowest sensitivity to TRAIL (Figure 33). This points to Bcl-2 as a potential resistance mechanism specific to this clone that is independent of TSPO expression.

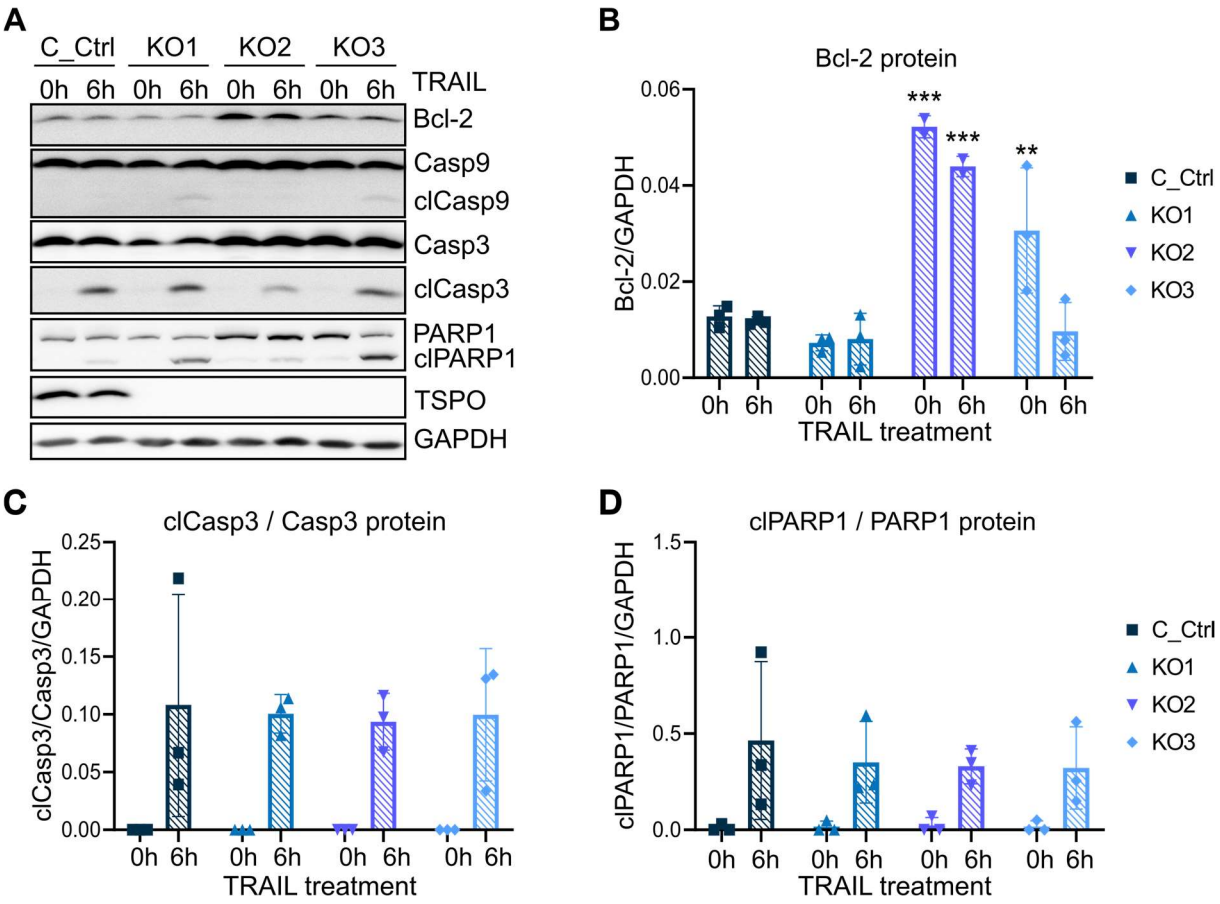

Figure 33. Impact of TRAIL on caspase activation in TSPO KO clones. Western blot analysis of caspase-9 (Casp9), caspase-3 (Casp3) and PARP1 processing, and Bcl-2 expression in TSPO KO clones (KO1, KO2, KO3) compared to the control clone (C_Ctrl). Cells were treated with 50 ng/ml TRAIL for 0 and 6 hours. (**A**) Representative Western blot for cleaved and full-length forms of Casp9, Casp3, PARP1, and Bcl-2. Equal loading was confirmed by GAPDH staining. (**B-D**) Graphs show the relative protein quantification of three independent experiments. Data are presented as the ratio of cleaved to full-length protein for Casp3 (**C**) and PARP1 (**D**). Data are normalized to GAPDH expression shown as mean ± SD. Asterisks indicate significant differences between KO clones and control clone C_Ctrl. P-values were calculated using two-way ANOVA followed by Dunnett´s *post hoc* test (**$P \leq 0.01$; ***$P \leq 0.001$).

4.5.5 Pro-survival signaling as a potential TRAIL resistance mechanism

It has been shown that non-canonical TRAIL signaling includes pathways that activate the transcription of anti-apoptotic and pro-survival genes to evade apoptosis [107]. Therefore, the activation of respective pro-survival signaling pathways such as of NFκB, STAT3, and ERK1/2 was investigated next as a potential resistance mechanism to TRAIL.

TSPO KO clones (KO1, KO2, KO3) and the control clone C_Ctrl were exposed to 50 ng/ml TRAIL for 3 hours and pathway activation by phosphorylation of NFκB p65, STAT3 and ERK1/2 was analyzed by Western blotting.

As apparent from the Western blot, 3 hours of TRAIL exposure increased the levels of phosphorylated NFκB, and STAT3 (pNFκB and pSTAT3) (Figure 34A). Notably, this effect was particularly pronounced in the KO clones KO1 and KO2 (Figure 34A). However, no differences in ERK1/2 phosphorylation were detected after TRAIL treatment (Figure 34A).

Important to mention, the detection and quantification of the phosphorylated proteins posed challenges, resulting in variations between replicates. Nevertheless, cumulation of three biological replicates revealed a noteworthy trend: exposure to TRAIL resulted in increased levels of pNFκB in KO1 and KO2, reaching significance for KO1 (Figure 34B). Additionally, pSTAT3 levels were increased upon TRAIL treatment, with the most prominent effect in KO2 and C_Ctrl (Figure 34C). Finally, a subtle reduction in levels of pERK1/2 was observed following TRAIL treatment (Figure 34D).

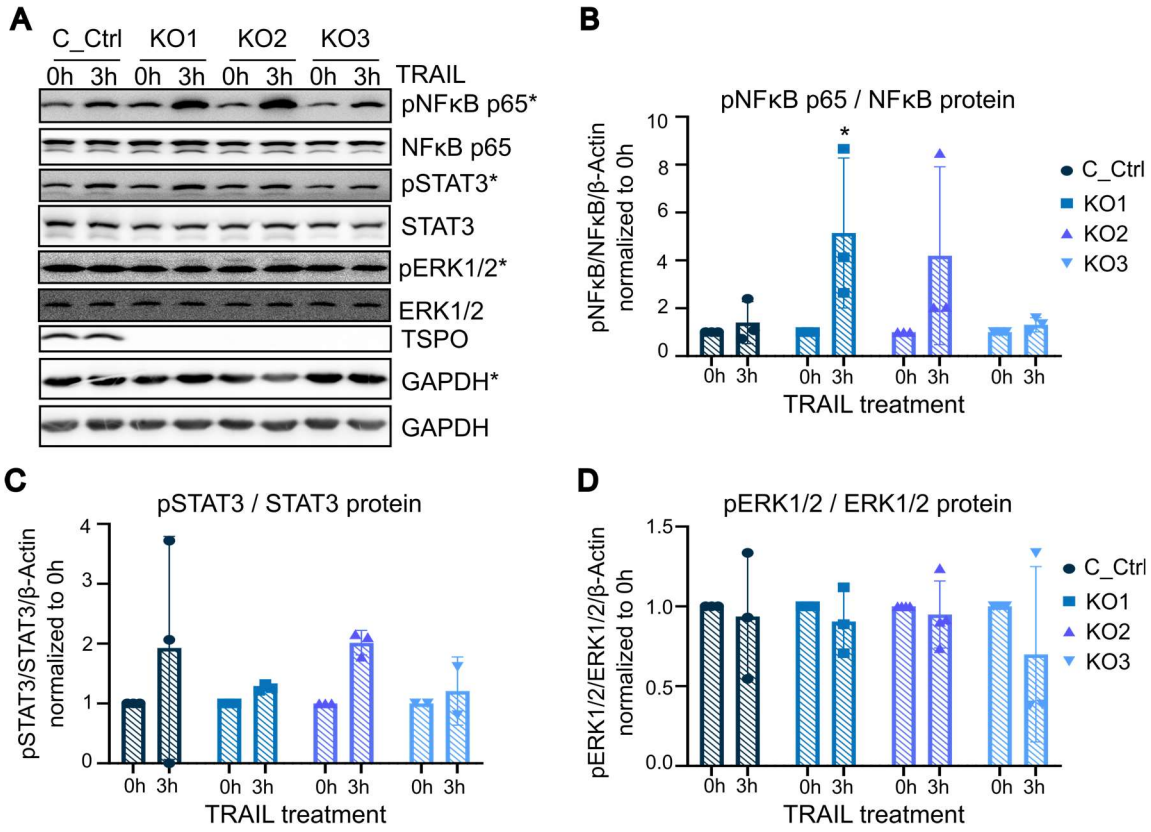

Figure 34. Impact of TSPO deficiency on TRAIL-induced NFκB, STAT3 and ERK1/2 activation. Western blot analysis of NFκB p65, STAT3, and ERK1/2 activation in BTIC13 control clone (C_Ctrl) and TSPO KO clones (KO1, KO2, KO3). Cells were stimulated with 50 ng/ml of TRAIL for 3 hours. (**A**) Representative Western blot for phosphorylated (p)NFκB p65 (S536), pSTAT3 (Y705), and pERK1/2 (T202/Y204) compared to the levels of total NFκB, STAT3, and ERK1/2. TSPO staining validates TSPO deficiency in KO clones. Equal loading was confirmed by β-Actin staining. (**B-D**) Graphs show the relative protein quantification of three independent experiments. Data are presented as the ratio of phosphorylated to total protein of NFκB (**B**), STAT3 (**C**), and ERK1/2 (**D**). Data are normalized to β-Actin expression and expressed as fold change relative to the 0 hours of treatment. Data are shown as mean ± SD. P-values were calculated using two-way ANOVA followed by Dunnett´s *post hoc* test (*$P \leq 0.05$).

Definitive conclusions whether the activation of a specific pro-survival signaling pathway changes the sensitivity towards TRAIL cannot be drawn at this point. However, collectively these findings substantiate that a multitude of factors determine the cell susceptibility towards TRAIL-induced apoptosis.

4.5.6 DR4 TRAIL receptor expression is essential for TRAIL-induced apoptosis

TRAIL mediates its apoptosis-inducing effects by binding the two death receptors DR4 and DR5. As shown in section 4.4.3, BTIC13 exhibits high expression of DR4 (64 % of total cells) and DR5 (98 %) (Figure 20). To rule out the possibility that TSPO KO clones and the control clone do not express the TRAIL receptors anymore, and are therefore resistant to TRAIL, the surface expression of DR4 and DR5 was evaluated by flow cytometry.

As shown in figure 35, DR5 was highly expressed on the surface of all KO clones (KO1, KO2, KO3) and of the control clone C_Ctrl (Figure 35, lower panel). In contrast, only a very small subset of cells, ranging from a minimum of 1.69 % in KO3 to a maximum of 5.45 % in KO2, were found to be positive for DR4 surface expression (Figure 35, upper panel).

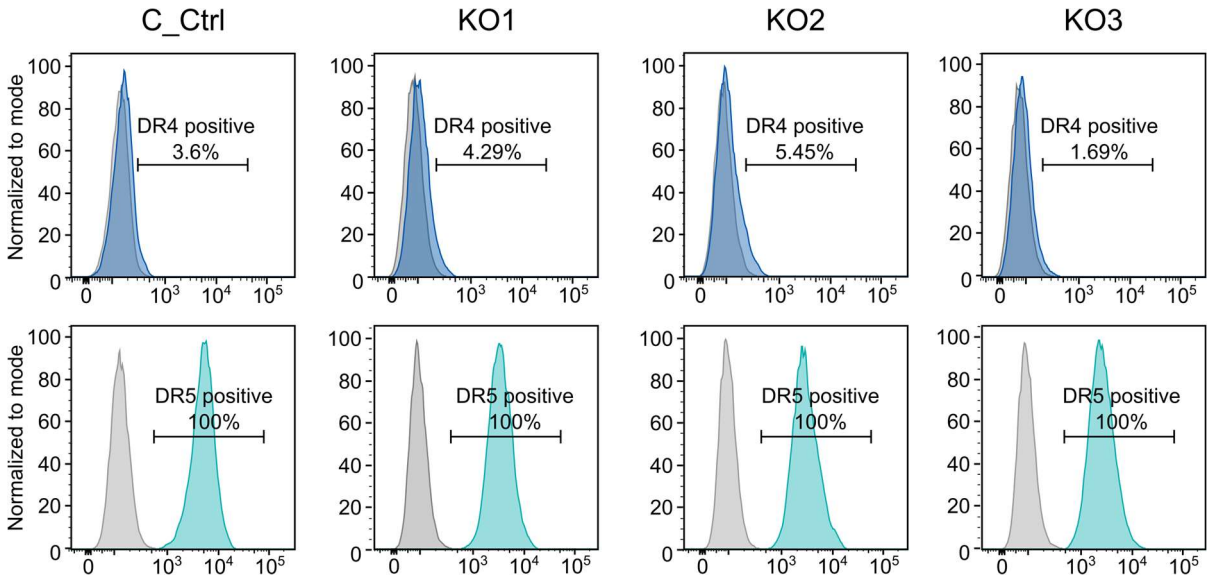

Figure 35. Cell surface expression of TRAIL receptors DR4 and DR5 in TSPO KO clones. Flow cytometry analysis of DR4-PE-A, and DR5-APC-A. Histogram plots show the antibody-stained samples (DR4 in blue, DR5, in green) and the isotype control (grey). Representative data for two independent experiments with comparable results are shown.

Accordingly, the next goal was to explore whether DR4 receptor signaling is pivotal for the TRAIL-induced apoptosis response in BTIC13. Therefore, TRAIL receptor expression of the TRAIL-responsive KD clones was evaluated first.

Again, 100 % of the cells analyzed were positive for DR5 expression (Figure 36, lower panel). The majority of TSPO KD clones were also positive for DR4 expression (Figure 36, upper panel). For instance, in the Scr_C1 control, 87.2 % of the cells exhibited DR4 expression. For the KD clones, 77.4 %, 63 % and 75 % of KD1, KD2, and KD3 cells, respectively, expressed the DR4 receptor.

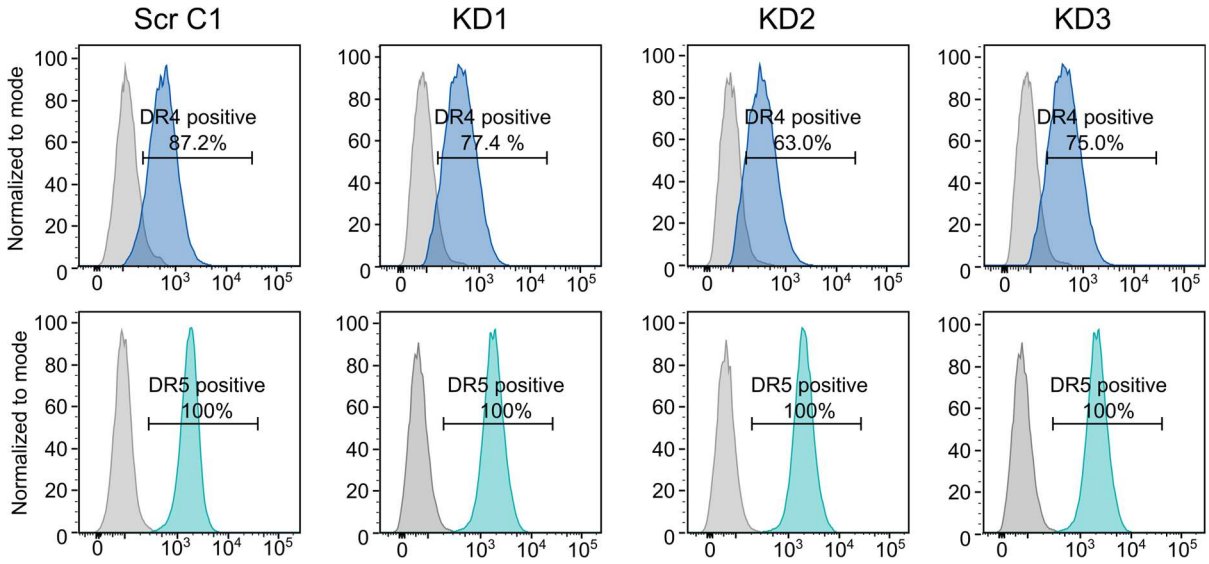

Figure 36. Cell surface expression of TRAIL receptors DR4 and DR5 in TSPO KD clones. Flow cytometry analysis of DR4-PE-A, and DR5-APC-A. Histogram plots show the antibody-stained samples (DR4 in blue, DR5 in green) and the isotype control (grey). Representative data for two independent experiments with comparable results are shown.

To understand which of the two TRAIL receptors DR4 and DR5 is responsible for TRAIL-induced apoptosis in the TSPO KD clones, TRAIL receptor signaling was inhibited by using DR4 and DR5 blocking antibodies. TSPO KD clones along with the control clone Scr C1 were pre-incubated with anti-DR4, anti-DR5, or both blocking antibodies for 30 min. Subsequently, cells were exposed to 50 ng/ml TRAIL and the impact on cell viability was assessed 48 hours later using the Resazurin® reduction assay. As shown in figure 37, TRAIL significantly reduced the cell viability in KD1 and KD2, but not in KD3 compared to the control clone Scr C1. This effect was strongly abolished when cells were pre-incubated with the DR4-blocking antibody (Figure 37). Conversely, DR5 blocking was not effective in neutralizing the TRAIL apoptosis response of KD1 and KD2 (Figure 37). Simultaneous blockade of both DR4 and DR5 receptors completely abrogated the TRAIL effect on cell viability in KD1 and KD2 (Figure 37).

Together, these findings strongly suggest that cell surface DR4 receptor expression is critical for the TRAIL-induced apoptosis in BTIC13. This indicates that the acquired TRAIL resistance in TSPO KO clones can be at least partly attributed to the loss of DR4 expression.

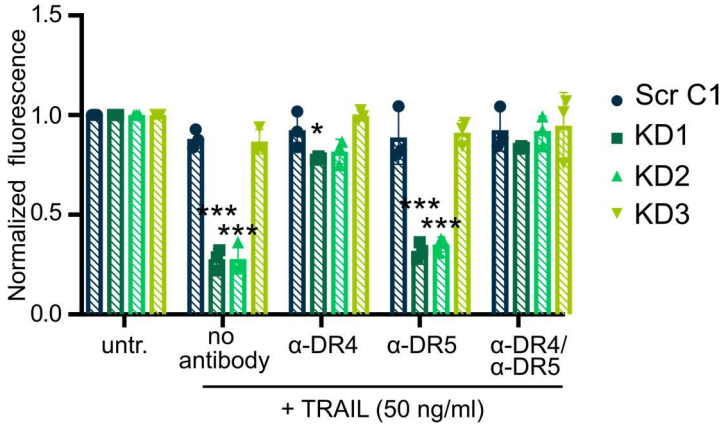

Figure 37. TRAIL-induced apoptosis in BTIC13 KD clones depends on DR4 receptor function. The Resazurin assay was performed to analyze the impact of TRAIL on cell viability in the presence and absence of DR4 and DR5 blocking antibodies in TSPO-deficient clone KD1 and the control Scr C1. Fluorescence emission was measured after 48 hours TRAIL exposure and normalized to untreated control. Asterisks indicates significant differences between KDs and control Scr C1. Cumulative data of three independent experiments are shown as mean ± SD. P-values were calculated using two-way ANOVA followed by Dunnett´s *post hoc* test (*$P \leq 0.05$; ***$P \leq 0.001$).

4.5.7 T cell-mediated cytotoxicity acts via the DR5 receptor

In the experiments described above, it was shown that cell surface DR4 receptor expression is essential for TRAIL-induced apoptosis in TSPO-deficient BTIC13 KD clones using the soluble, recombinant form of TRAIL. Although TRAIL can also be secreted as a soluble protein, its primary physiological mode of action occurs as membrane-bound protein on the surface of activated effector T cells (reviewed in [225]). It was shown before that DR4 is activated by both soluble and membrane-bound TRAIL, whereas DR5 exclusively responds to membrane-bound TRAIL [108].

As already published, TSPO deficiency enhanced T cell-mediated killing of BTIC13 cells in a tumor cell-T cell co-culture setting [222]. Therefore, it was investigated if DR4, DR5 or both receptors are required for T-cell mediated cytotoxicity.

To this end, KD1 and Scr C1 were pulsed with 0.01 µg/ml Flu peptide, followed by a 30 min pre-incubation step with blocking antibodies targeting DR4 and DR5. Subsequently, KD1 and Scr C1 were co-cultured with Flu-antigen-specific cytotoxic T cells at an effector-to-target ratio of 1:1. Cells were subjected to real-time cell microscopy using the IncuCyte® Zoom system in cooperation with Dr. A. Menevse, LIT, Regensburg. This system, in combination with IncuCyte® Caspase-3/7 Green dye, allowed to monitor activation of caspase-3/7 activation as an indication of apoptosis over a time course of 26 hours.

Co-culture of BTICs with FluT cells resulted in a rapid, time-dependent increase of caspase-3/7 activation in BTICs which reached a plateau phase at around 14 hours of incubation (Figure

38). Apoptosis induction remained minimal in tumor cells that were not exposed to FluT (Figure 38). Caspase-3/7 activation was more pronounced in the TSPO-deficient KD1 compared to the control Scr C1 (Figure 38).

While blockade of the DR4 receptor had only a modest effect on T cell-mediated caspase-3/7 activation (Figure 38A), DR5 blockade had a marked effect on T cell-mediated killing in both KD1 and Scr C1. For instance, when comparing caspase-3/7 activation at 12 hours of co-culture, DR5 blockade in KD1 facilitated a reduction of T cell-mediated cytotoxicity by 40 % (Figure 38B). Similarly, blocking DR5 in Scr C1 cells reduced caspase-3/7 activation by approximately 50 % (Figure 38B).

The strongest effect was observed when both the DR4 and DR5 receptors were blocked simultaneously. At 12 hours of co-culture, DR4/DR5 blockade caused a reduction of T cell killing in KD1 and Scr C1, by 50 % and 60 %, respectively (Figure 38C).

Together, these findings indicate that in the described co-culture setting, T cell-mediated cytotoxicity primarily involves the action of the DR5 receptor and only secondarily the action of the DR4 receptor.

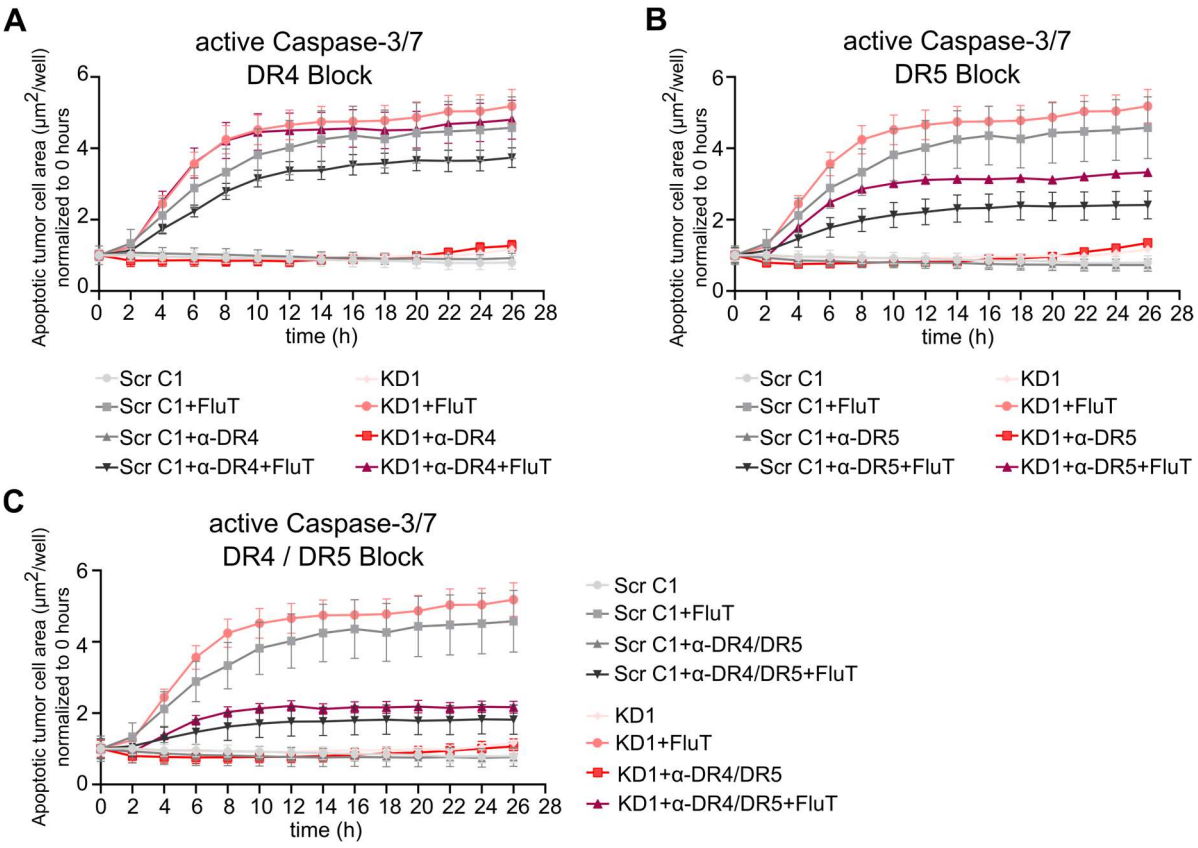

Figure 38. T cell-mediated cytotoxicity in BTIC13 KD clones depends on DR5 receptor function. Real time cell microcopy (IncuCyte® ZOOM system) to analyze the activation of caspase-3/7 as indication of apoptosis induction. TSPO-deficient KD1 and the control Scr C1 were loaded with 0.01 µg/ml Flu peptide and co-cultured with Flu-antigen-specific cytotoxic T cells (FluT) in the presence or absence of DR4 and DR5 blocking antibodies. Graphs shows the effect of DR4 blockade (**A**), the effect of DR5 blockade (**B**), and the effect of DR4 and DR5 blockade (**C**) on caspase-3/7 activation over a time course of 26 hours of co-culture. Data are presented as the total apoptotic tumor cell area (green object area) per well (µm² / well) and were normalized to 0 hours of co-culture. Each sample was prepared in triplicates; error bars indicate mean ± SD. Representative data of two independent experiments with comparable results are shown. Experiments were conducted in cooperation with Dr. A. Menevse, LIT, Regensburg.

By TSPO downregulation, BTIC13 became significantly more sensitive towards T-cell mediated killing [222]. As demonstrated by the previous assay, apoptosis induction by T cells is primarily mediated by the DR5 receptor. The loss of DR4 surface expression in TSPO KO and control clones rendered them unsuitable for apoptosis analysis using the soluble, recombinant form of TRAIL. However, TSPO KO and control clones retain a robust DR5 surface expression which provides an opportunity to explore their response to T cell-induced apoptosis.

To this end, Flu-pulsed TSPO KO clones and the control C_Ctrl were co-cultured with activated FluT cells in the presence of IncuCyte® Caspase-3/7 Green dye and apoptosis induction was monitored for 26 hours in the IncuCyte® Zoom system.

As depicted in figure 39, exposure to FluT cells resulted in a time-dependent increase in active caspase 3/7 in TSPO KO and control clones, and a maximum was reached at around 12 hours of co-culture. In line with published data for the TSPO KD BTIC13, the activation of caspase-3/7 was higher in KO1 and KO2 compared to the control C_Ctrl. Conversely, KO3 exhibited a similar response to T cells similar to that of the control C_Ctrl. This assay again substantiates the hypothesis that TSPO-deficiency does not exclusively sensitize BTICs towards T cell-induced apoptosis. Instead, other resistance mechanisms, such as increased Bcl-2 levels in case of KO2, may be superior in certain contexts and dictate the response to apoptosis.

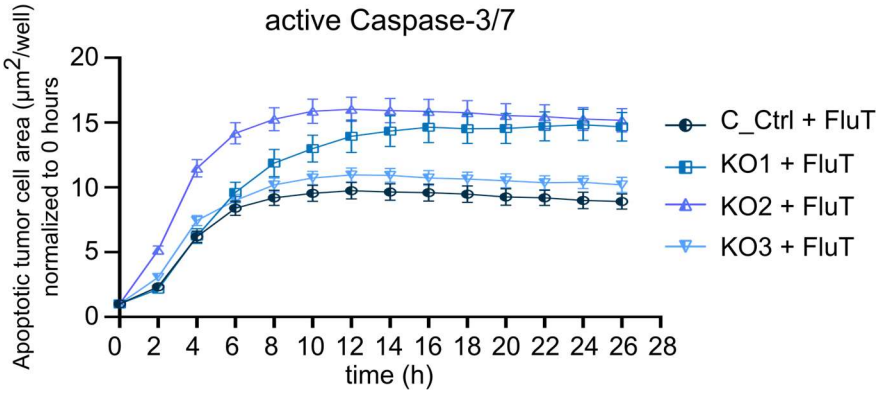

Figure 39. Caspase-3/7 activity in TSPO KO clones upon T cell confrontation. Real time cell microcopy (IncuCyte® ZOOM system) to analyze the activation of caspase-3/7 as indication of apoptosis induction in TSPO KO clones (KO1, KO2, KO3) and control clone C_Ctrl. BTICs were pulsed with 0.01 µg/ml Flu peptide and co-cultured with Flu-antigen-specific cytotoxic T cells (FluT) for 26 hours. Data are presented as the total apoptotic tumor cell area (green object area) per well (µm² / well) and were normalized to 0 hours of co-culture. Each sample was prepared in triplicates; error bars indicate mean ± SD. Representative data of two independent experiments with comparable results are shown. Experiment was conducted in cooperation with Dr. A. Menevse, LIT, Regensburg.

4.6 Impact of TSPO deficiency on secretion of immune-modulatory cytokines

Tumor cells are capable to release immune-suppressive factors to provide an optimal environment for their own tumor growth and immune evasion. As presented before, pro-inflammatory cytokines such as TNFα and IFNγ induce the expression of TSPO on mRNA and protein levels (Figure 11, Figure 12). These cytokines are also recognized for inducing the production of immune-modulating factors like interleukin-6 (IL-6) and interleukin-8 (IL-8) [226–228]. Accumulating evidence indicates that glioblastoma-derived IL-6 and IL-8 positively correlate with enhanced tumorigenicity and therapy resistance [229, 230]. Due to the influence of cytokines

on TSPO expression and the involvement of TSPO in a multitude of cellular processes related to mitochondrial function, inflammation, and steroidogenesis, TSPO might be part of a larger regulatory network that controls cytokine production and affects immune cell activation. This led to the hypothesis that TSPO, either directly or indirectly, influences the production and release of IL-6 and IL-8, thereby contributing to immune evasion of glioblastoma. Consequently, the impact of TSPO-deficiency on the expression and secretion of IL-6 and IL-8 was investigated in the established BTIC13 cell culture models.

Initially, the basal levels of IL-6 and IL-8 secretion in TSPO-deficient and control BTIC13 lines were characterized. Therefore, the protein concentration of IL-6 and IL-8 in cell culture supernatants of short-term cultured BTICs were assessed via enzyme-linked immunosorbent assay (ELISA).

Under baseline conditions, IL-6 and IL-8 protein levels varied in between, as well as within the different TSPO-deficient model systems (Figure 40). For both TSPO KD bulk cell lines (shTSPO_1 Bulk and shTSPO_2 Bulk), IL-6 secretion was elevated compared to the control bulk cell line Scr bulk (Figure 40A, upper panel). Notably, the basal concentration of IL-8 in the supernatant of the same cell lines was at least five times higher than that of IL-6 (for Scr Bulk: ~138 pg/ml IL-8 versus ~21 pg/ml IL-6). While the concentration of IL-8 in the supernatant of shTSPO_1 Bulk was only slightly elevated compared to the control, a strong increase in IL-8 levels were observed for shTSPO_2 Bulk (Figure 40B, upper panel).

The basal concentration of IL-6 for TSPO-KD (KD1 and KD3) and control (Scr C1) clonal cell lines were within the same range as observed for the bulk cells. However, KD1 displayed lower levels of IL-6 release compared to Scr C1, whereas KD3 exhibited significantly elevated levels of IL-6 secretion (Figure 40A, middle panel). Although for both, KD1 and KD3, higher levels of IL-8 release were observed compared to Scr C1, the overall supernatant concentration of IL-8 was low (from ~0.5 pg/ml for Scr C1 control up to ~1.8 pg/ml for KD3) (Figure 40B, middle panel). When compared to the bulk cell lines, the concentration of IL-8 in the supernatant of KD clones was nearly 200 times lower.

Lastly, the TSPO KO clones also displayed distinct secretion profiles. Whereas the IL-6 protein concentration for KO1 and KO2 resembled that of the control C_Ctrl, KO3 exhibited decreased levels of IL-6 secretion (Figure 40A, lower panel). The IL-6 concentration in the supernatant of the KO clones ranged between 4.3 pg/ml (KO3) and 13.2 pg/ml (KO2). Similarly, each KO clone showed a unique IL-8 secretion. In comparison to the control, KO1 and KO3 exhibited elevated levels of IL-8 release, whereas KO2 supernatant displayed a reduced concentration

(Figure 40B, lower panel). The concentrations of IL-8 in the supernatant of the KO clones ranged from 118 pg/ml (KO2) to 269 pg/ml (KO1).

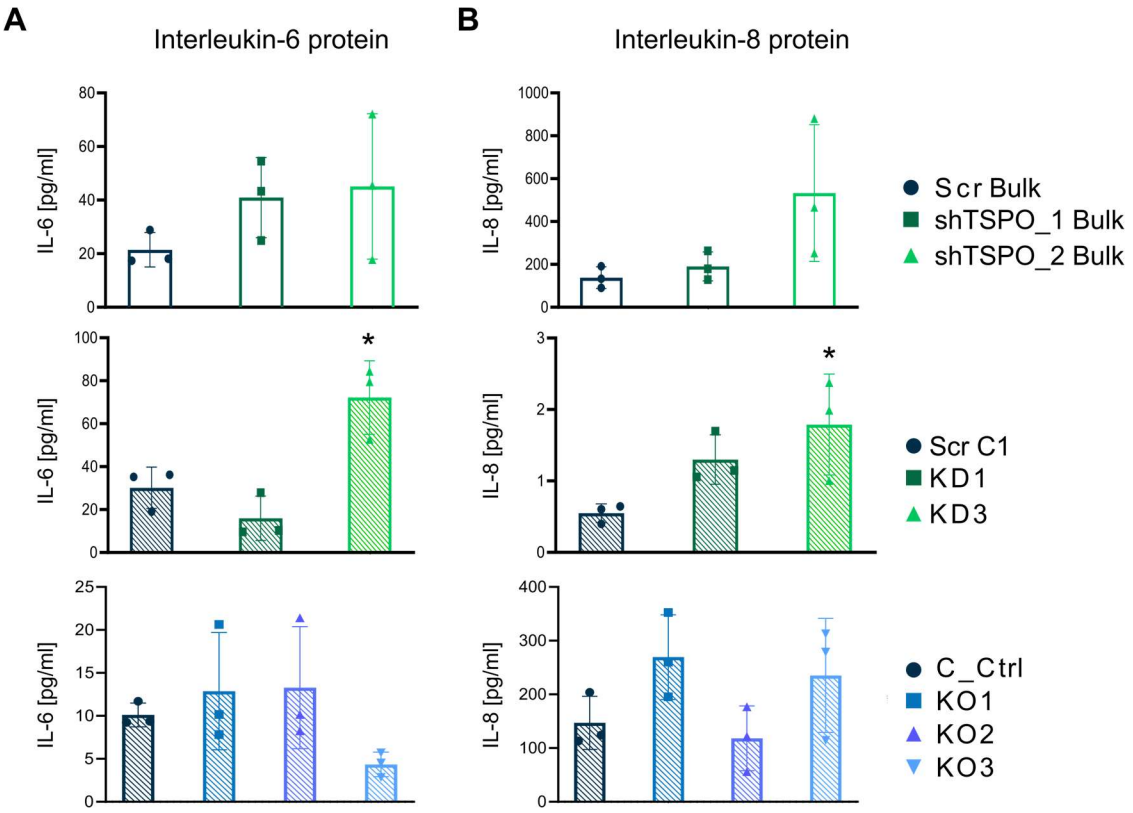

Figure 40. Basal levels of IL-6 and IL-8 in the supernatant of TSPO-deficient BTIC13. ELISA analysis of interleukin-6 (IL-6) (**A**) and interleukin-8 (IL8) (**B**) protein level in the cell culture supernatant of TSPO-deficient BTIC13. Shown are the protein level for TSPO KD bulk (shTSPO_1 Bulk, shTSPO_2 Bulk) compared to the control bulk (Scr Bulk) (upper panel), TSPO KD clones (KD1, KD3) compared to the control clone (Scr C1) (middle panel), and TSPO knockout clones (KO1, KO2, KO3) compared to the CRISPR control clone (C_Ctrl) (lower panel). Protein levels [pg/ml] were normalized to 10^5 cells. Asterisks indicate significant differences between KD3 clone and control clone Scr C1. Cumulative data of three independent experiments are shown as mean ± SD. P-values were calculated using one-way ANOVA followed by Dunnett´s *post hoc* test (*$P \leq 0.05$).

Next, the impact of TSPO-deficiency on TNFα- and IFNγ- induced IL-6 and IL-8 mRNA and protein levels was investigated. To achieve this, TSPO-deficient and control BTIC13 were treated with 50 ng/ml TNFα or IFNγ for 24 and 48 hours. Subsequently, IL-6 and IL-8 mRNA and protein level were quantified via qPCR and ELISA, respectively.

Figure 41 depicts the relative levels of TNFα- and IFNγ-induced IL-6 and IL-8 mRNA expression and protein release by the TSPO KD and control clones after normalization to the baseline condition.

TNFα stimulation resulted in a time-dependent augmentation in both, IL-6 mRNA levels and protein release, with highest levels reached at 48 hours of treatment (Figure 41A, B). In more detail, the control clone Scr C1 showed the highest expression of IL-6 mRNA (Figure 41A). At protein level, KD1 showed similar levels of IL-6 release compared to control Scr C1, whereas significantly diminished IL-6 protein secretion levels were observed for KD3 (Figure 41B).

Comparable to the TNFα treatment, the exposure of cells to IFNγ resulted in a time-dependent increase in IL-6 mRNA levels and protein release, with peak levels after 48 hours. Both KD clones showed lower IL-6 mRNA expression compared to the Scr C1 clone (Figure 41A). At protein level, KD3 exhibited similar levels of IL-6 release compared to the control (Figure 41B). Noteworthy, KD1 displayed a distinctive feature at 48 hours of IFNγ treatment. Despite low levels of IL-6 mRNA, IL-6 protein release levels were significantly increased compared to the control Scr C1 (Figure 41A, B).

IL-8 mRNA expression in response to TNFα or IFNγ treatment aligned well with levels of secreted protein. Both, IL-8 mRNA and protein levels, were increased in a time-dependent manner in the control clone Scr C1 and in KD3 after TNFα stimulation (Figure 41C, D). For KD1, already 24 hours of TNFα exposure resulted in high levels of IL-8 mRNA and protein release that remained constant until 48 hours (Figure 41C, D).

IFNγ treatment, in contrast, caused an overall reduction of IL-8 mRNA and protein levels. In both, Scr C1 and KD1, a reduction of mRNA and released protein levels of more than 50 % was observed after 24 hours of IFNγ stimulation, which progressed to almost 100 % reduction after 48 hours (Figure 41C, D). For KD3, IL-8 mRNA and released protein levels did not change after 24 hours of treatment but were also reduced by more than 50 % after 48 hours of IFNγ treatment (Figure 41C, D).

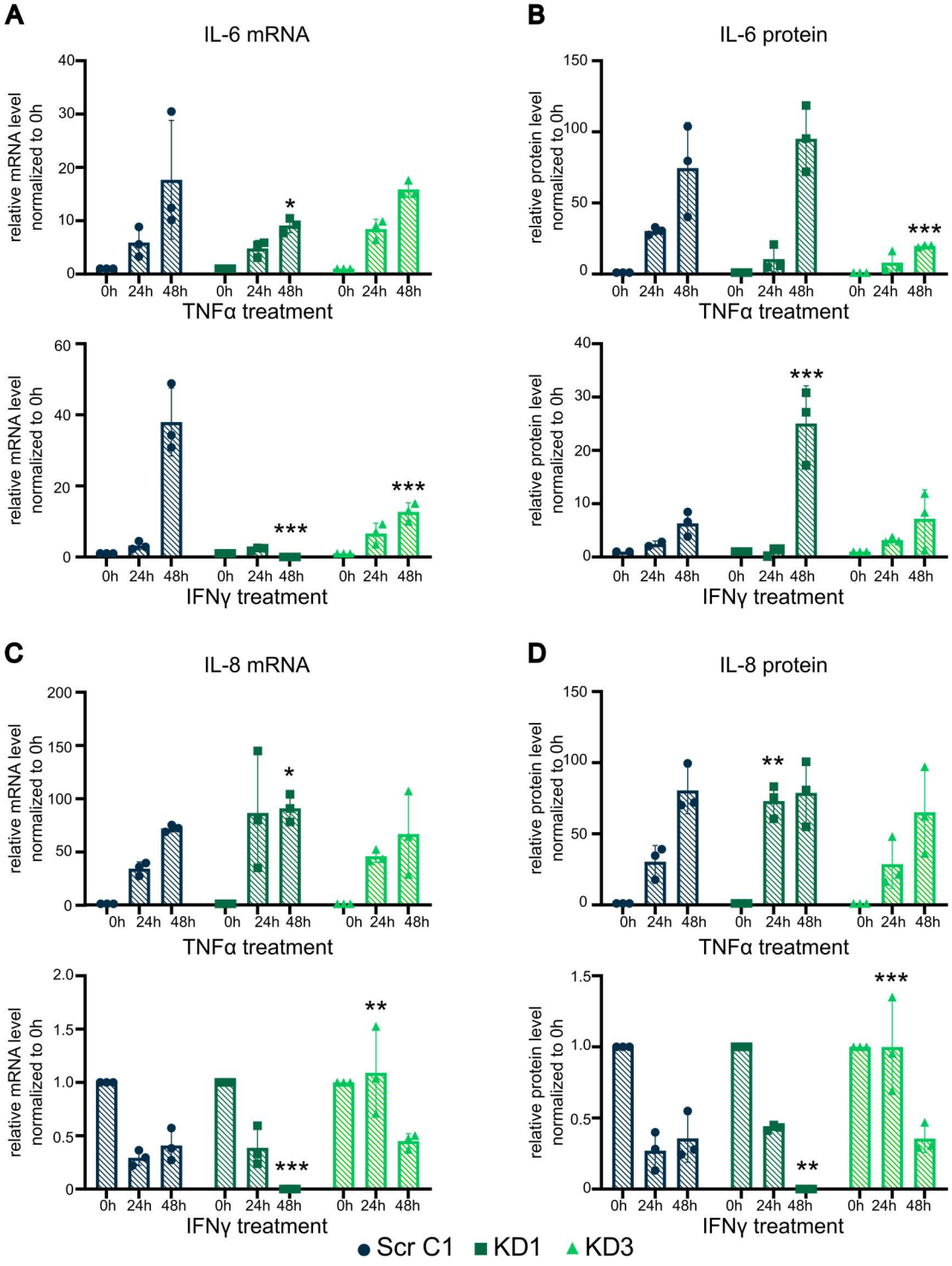

Figure 41. TNFα- and IFNγ-induced IL-6 and IL-8 mRNA expression and protein secretion in BTIC13 KD clones. (**A, C**) qPCR analysis of Interleukin-6 (IL-6) and Interleukin-8 (IL-8) mRNA levels in TSPO KD and control clones. (**B, D**) ELISA analysis of IL-6 and IL-8 protein levels in the supernatant of TSPO KD and control clones. Cells were stimulated for 24 hours or 48 hours with 50 ng/ml TNFα or IFNγ. Shown are the relative mRNA and protein levels of TSPO KD clones (KD1, KD3) compared to the control clone Scr Ctrl. Released IL-6 and IL-8 protein levels [pg/ml] were normalized to 10^5 cells and presented as fold change relative to 0 hours of treatment. Cumulative data of three independent experiments are shown as mean ± SD. Asterisks indicate significant differences between KD clones and the control clone Scr Ctrl. P-values were calculated using two-way ANOVA followed by Dunnett´s *post hoc* test (*$P \leq 0.05$; **$P \leq 0.01$; ***$P \leq 0.001$).

Identical experiments were repeated using the TSPO KO (KO1, KO2, KO3) and control (C_Ctrl) clones. In the case of the KO clones, 24 and 48 hours of TNFα treatment resulted in increased IL-6 mRNA and released protein levels. At mRNA level, all three KO clones exhibited lower IL-6 levels compared to the control C_Ctrl for both treatment times reaching significance at 24 hours for all clones (Figure 42A, B). While 24 hours of IFNγ stimulation did not have a strong impact on IL-6 mRNA and protein levels for all clones, 48 hours of treatment resulted in significantly higher IL-6 mRNA and released protein levels in all KO clones compared to the control C_Ctrl (Figure 42A, B).

Similar to the findings for KD clones, treatment of KO clones with TNFα resulted in a time-dependent induction of IL-8 mRNA expression. While the level of induction was comparable between KO1, KO3, and the control C_Ctrl within a smaller range, the KO2 clone exhibited significantly increased IL-8 mRNA levels (Figure 42C, D). However, this effect was not consistently confirmed for the levels of secreted protein. Whereas the IL-8 protein levels for KO1 resembled the corresponding mRNA levels, KO2 and KO3 demonstrated significantly lower levels of IL-8 secretion compared to the control C_Ctrl after 48 hours of TNFα exposure (Figure 42C, D).

Lastly, the analysis of the IFNγ-induced IL-8 expression and secretion in TSPO KO clones did not reveal any significant TSPO-dependent effect. It is worth noting that treatment with IFNγ for 24 hours tended to decrease IL-8 mRNA expression in KO1 and KO3 clones and the control clone (Figure 42C, D). At the protein level, IFNγ exposure caused a time-dependent decrease in IL-8 release for C_Ctrl, while the IL-8 secretion levels for the KO clones remained nearly consistent (Figure 42C, D).

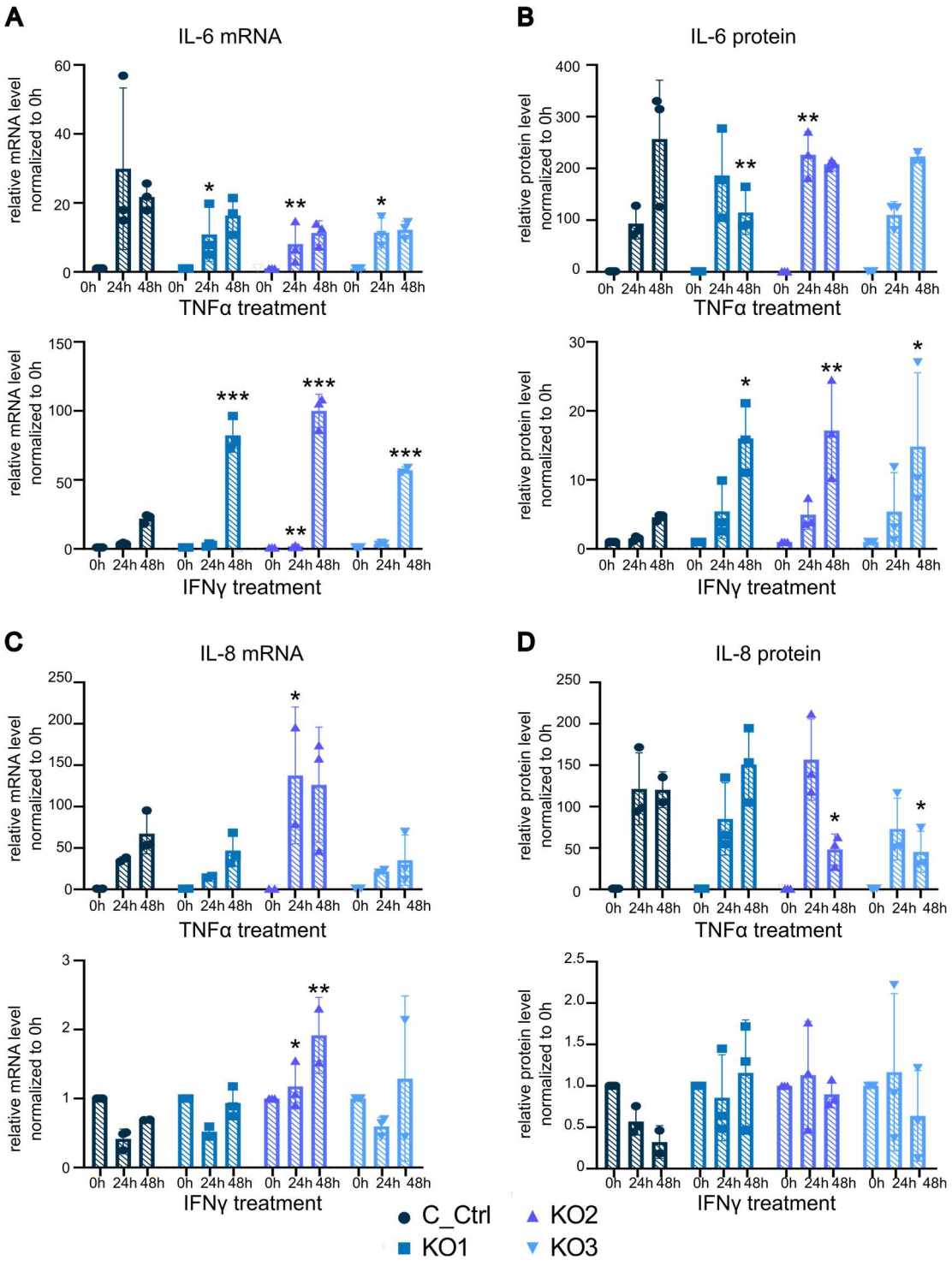

Figure 42. TNFα- and IFNγ-induced IL-6 and IL-8 mRNA expression and protein secretion in TSPO KO clones. (**A, C**) qPCR analysis of Interleukin-6 (IL-6) and Interleukin-8 (IL-8) mRNA levels in TSPO KO and control clones. (**B, D**) ELISA analysis of IL-6 and IL-8 protein levels in the supernatant of TSPO KO and control clones. Cells were stimulated for 24 hours or 48 hours with 50 ng/ml TNFα or IFNγ. Shown are the relative mRNA and protein levels of TSPO KO clones (KO1, KO2, KO3) compared to the control clone C_Ctrl. Released IL-6 and IL-8 protein levels [pg/ml] were normalized to 10^5 cells and presented as fold change relative to 0 hours of treatment. Cumulative data of three independent experiments are shown as mean ± SD. Asterisks indicate significant differences between KO clones and control clone C_Ctrl. P-values were calculated using two-way ANOVA followed by Dunnett´s *post hoc* test (*$P \leq 0.05$; **$P \leq 0.01$; ***$P \leq 0.001$).

Supplementary figure 3 depicts the relative protein levels for TNFα- and IFNγ-induced IL-6 and IL-8 protein secretion within the TSPO KD bulk cell lines. Here, TNFα stimulation resulted in a time-dependent increase of IL-6 levels in the cell culture supernatants of TSPO-deficient and control bulk cell lines (Supplementary figure 3A). However, there were no significant differences in TNFα-induced IL-6 levels between KD bulk and control bulk cell lines. IFNγ treatment increased IL-6 levels for Scr Bulk in a time-dependent manner (Supplementary figure 3B). In contrast, TSPO KD bulk cells showed a distinct pattern. IFNγ stimulation for 24 hours increased secreted IL-6 protein levels, whereas 48 hours of stimulation resulted in a significant reduction of released IL-6 levels compared to the control Scr Bulk (Supplementary figure 3B).

Exposure to TNFα strongly elevated IL-8 protein levels released from TSPO KD bulk and control bulk cells after both, 24 and 48 hours. In more detail, in Scr Bulk the level of IL-8 secretion increased with treatment time (Supplementary figure 3C). However, in both TSPO-deficient bulk cell lines, longer treatment periods did not substantially increase IL-8 release (Supplementary figure 3C). Noteworthy, IFNγ treatment had no distinctive impact on IL-8 protein levels released from the BTIC13 bulk cell lines (Supplementary figure 3D).

Summarizing these findings, it was robustly demonstrated that TNFα, and to a lesser extent IFNγ, induced IL-6 expression and release in BTIC13. Additionally, TNFα predominantly induced IL-8 expression and secretion, in contrast to IFNγ. However, based on these experiments, TSPO has no clear impact on IL-6 and IL-8 secretion as no distinct pattern was observed comparing TSPO-deficient and control BTICs. Furthermore, the baseline concentrations of IL-6 and IL-8 exhibited substantial variations across different TSPO-deficient cell culture systems. Collectively, this implies that within BTIC13, intrinsic factors beyond TSPO play a crucial role in shaping the cytokine milieu.

4.7 Impact of TSPO deficiency on mitochondrial respiration

Metabolic reprogramming, for example the switch to glycolysis in the presence of oxygen, to supply rapidly growing tumor cells with glycolytic intermediates, is a critical phenomenon in many cancers, including glioblastoma. Growing evidence also substantiates the involvement of TSPO in the mitochondrial energy metabolism [205, 207, 208].

Given this context, a complementary goal of this thesis was to investigate the role of TSPO in mitochondrial respiration and energy dynamics in the primary glioblastoma cell line BTIC13. To assess mitochondrial function in real-time in intact TSPO-deficient and -control cells, the Mitostress test was performed using the Seahorse XFe96 analyzer.

To gain insight into mitochondrial respiration and oxidative phosphorylation (OXPHOS), the oxygen consumption rate (OCR) was measured. In addition, to provide an overview of glycolytic activity, the extracellular acidification rate (ECAR) was evaluated. Moreover, by systematically inhibiting key components of the electron transport chain (ETC), various parameters linked to mitochondrial health and ETC function were measured. This provided insights into basal respiration, maximal respiration, and spare respiratory capacity. Furthermore, respiration coupled to ATP production, non-mitochondrial energy consumption and proton leak were also assessed.

Figure 43 shows the OCR and ECAR profiles, and mitochondrial parameters of TSPO-deficient and -control bulk cells. Measurement of the baseline oxygen consumption rate revealed a significantly increased basal respiration of shTSPO_2 Bulk compared to the Scr Bulk control that was not observed for shTSPO_1 Bulk (Figure 43A, C). The injection of the F_OF_1 ATPase inhibitor Oligomycin decreased the OCR and thereby displays the respiration coupled to ATP production. Notably, the ATP production was significantly elevated in shTSPO_2 Bulk compared to the control, although this effect was not observed in the shTSPO_1 Bulk cell line (Figure 43A, F). The remaining basal respiration, uncoupled from ATP production, provides insights in proton leakage across the inner mitochondrial membrane. Although this parameter was elevated in shTSPO_2 Bulk, no significant differences were found compared to the control (Figure 43H).

Next, Carbonyl cyanide 4-(trifluoromethoxy)phenylhydrazone (FCCP)-induced maximal respiration was investigated. Maximal respiration was significantly enhanced in both TSPO KD bulk cell lines compared to the Scr Bulk (Figure 43A, D). However, no substantial differences were found in the spare respiratory capacity, an indicator of the cells adaptability to respond to energy stress (Figure 43E). In addition, the ETC complex I inhibitor Rotenone and complex III inhibitor Antimycin A were used to completely inhibit mitochondrial respiration, with the goal to observe the rate of non-mitochondrial oxygen consumption. Here, no significant differences

between TSPO-deficient bulk cells and the control cells in the mitochondria-independent OCR were observed (Figure 43G).

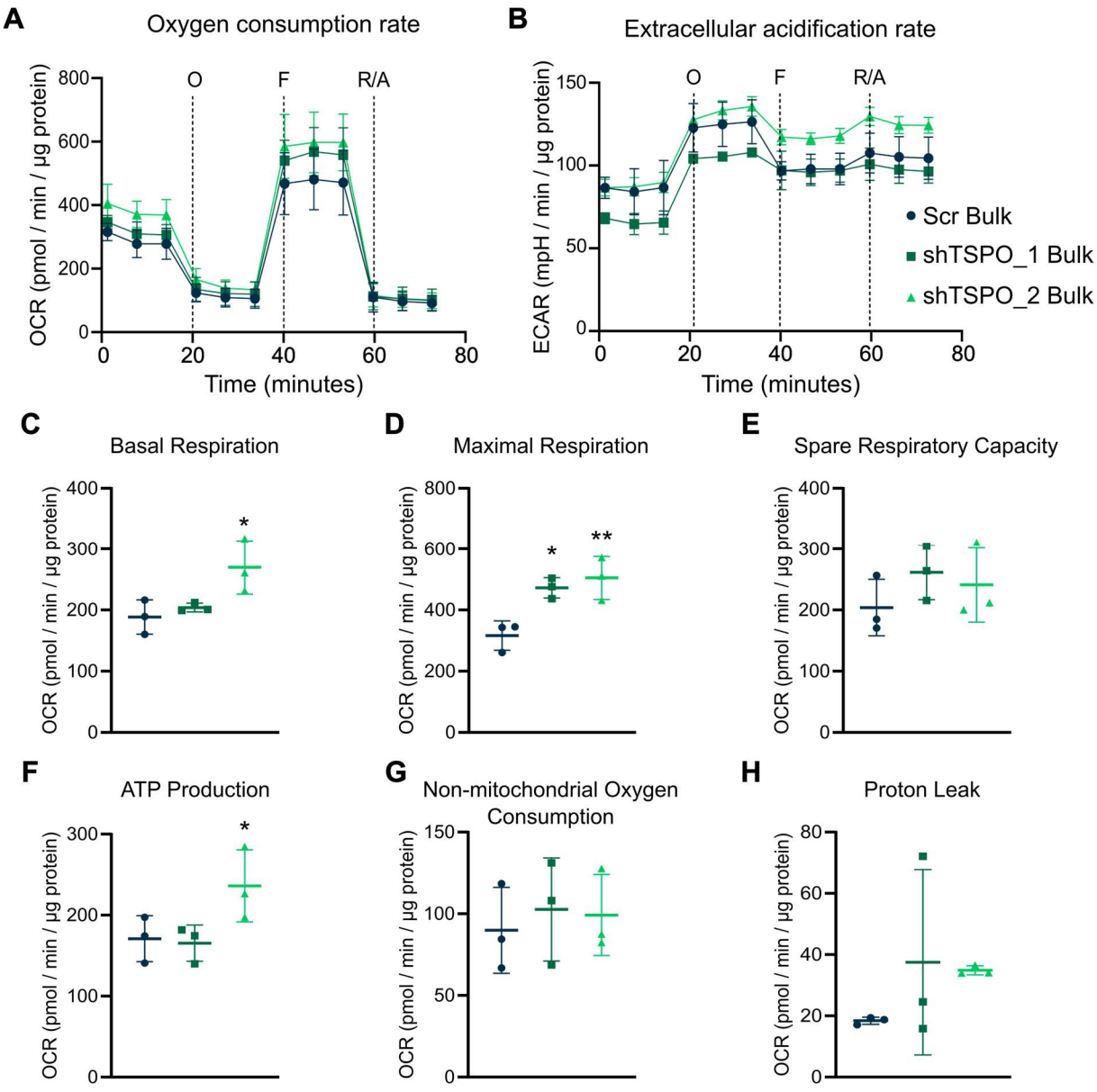

Figure 43. Impact of TSPO deficiency on mitochondrial respiration in BTIC13 KD bulk cells. Mitostress test of TSPO-deficient bulk cells (shTSPO_1 Bulk, shTSPO_2 Bulk) versus control bulk cell line Scr Bulk using the Seahorse XFe96 analyzer. Profiles of the (**A**) oxygen consumption rate (OCR) and (**B**) extracellular acidification rate (ECAR) in TSPO-deficient and -control bulk cells. The sequential injection of 1 µM Oligomycin (O), 2 µM FCCP (F), and 0.5 µM Rotenone/Antimycin A (R/A) is indicated. (**C-H**) The graphs display key respiratory parameters calculated from the OCR. (**A-H**) Seahorse raw data were normalized to total protein amount (µg) per well. Cumulative data of three independent experiments are shown as mean ± SD. Asterisks indicate significant differences between KD bulk and control cells. P-values were calculated using one-way ANOVA followed by Dunnett´s *post hoc* test (*$P \leq 0.05$; **$P \leq 0.01$).

The same analyses were performed using TSPO KD clones. Here, the Mitostress test revealed significant differences in several parameters of mitochondrial function in comparison to the control Scr C1 (Figure 44). While there were comparable rates of basal respiration and ATP-production in TSPO KD and control clones (Figure 44A, C, F), FCCP-induced maximal respiration was elevated in KD clones compared to the control Scr C1. This increase was significant for KD1 and KD3 (Figure 44D). Similarly, compared to the Scr C1 control, the spare respiratory capacity was significantly increased in KD1 and KD3 and tended towards significance ($p=0.072$) in KD2 (Figure 44E). Although not significant, non-mitochondrial oxygen consumption was elevated in all TSPO KD clones compared to the control Scr C1 (Figure 44G). Notably, the extent of proton leak showed variabilities between TSPO KD clones and the control, which was significantly reduced for KD2, slightly reduced for KD1, but, slightly elevated for KD3 compared to the control (Figure 44H).

Data in the TSPO KO clones were comparable to findings in the TSPO KD clones (Figure 45). In more detail, complete loss of TSPO resulted in a significantly increased maximal respiration and spare respiratory capacity in KO1 and KO3 and elevated levels in KO2 compared to the control C_Ctrl (Figure 45A, D, E). Additionally, although not significant, basal respiration, ATP production, and non-mitochondrial oxygen consumption were also increased in the TSPO KO clones compared to the control C_Ctrl (Figure 45C, F, G). No substantial differences were observed for proton leak between the TSPO KO and control clones (Figure 45H).

Glycolysis activity of the cells was simultaneously assessed by measuring the extracellular acidification rate (ECAR). In contrast to the OCR, the ECAR did not show conclusive differences between TSPO-deficient and control BTIC13 cells (Figure 43B, 44B; 45B).

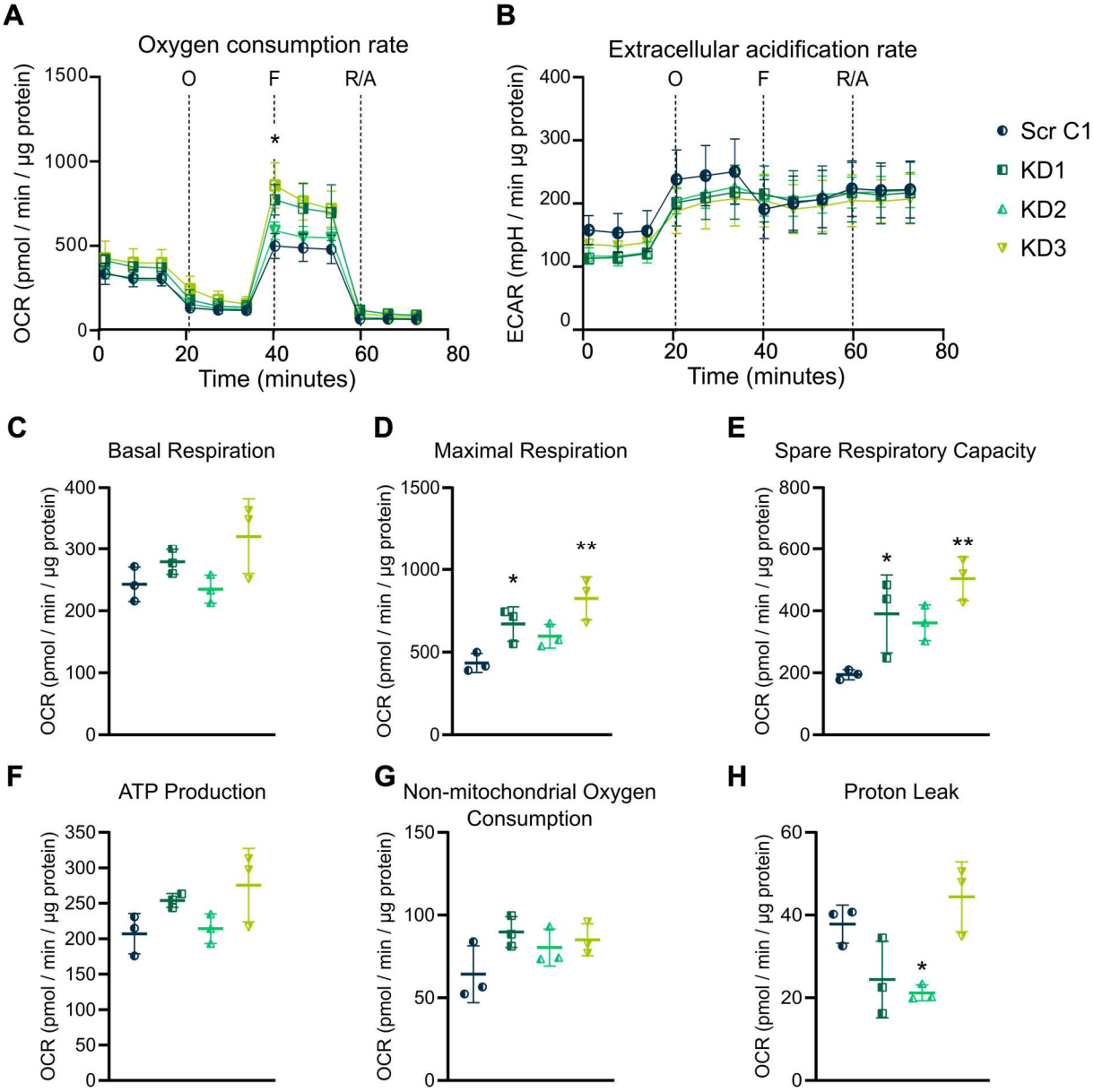

Figure 44. Impact of TSPO deficiency on mitochondrial respiration in BTIC13 KD clones. Mitostress test of TSPO-deficient KD clones (KD1, KD2, KD3) versus control clone Scr C1 using the Seahorse XFe96 analyzer. Profiles of the (**A**) oxygen consumption rate (OCR) and (**B**) extracellular acidification rate (ECAR) in TSPO-deficient and control clones. The sequential injection of 1 µM Oligomycin (O), 2 µM FCCP (F), and 0.5 µM Rotenone/Antimycin A (R/A) is indicated. (**C-H**) The graphs display key respiratory parameters calculated from the OCR. (**A-H**) Seahorse raw data were normalized to total protein amount (µg) per well. Cumulative data of three independent experiments are shown as mean ± SD. Asterisks indicate significant differences between KD clones and control clone. P-values were calculated using two-way (**A**) and one-way (**D, E, H**) ANOVA followed by Dunnett´s *post hoc* test (*$P \leq 0.05$; **$P \leq 0.01$).

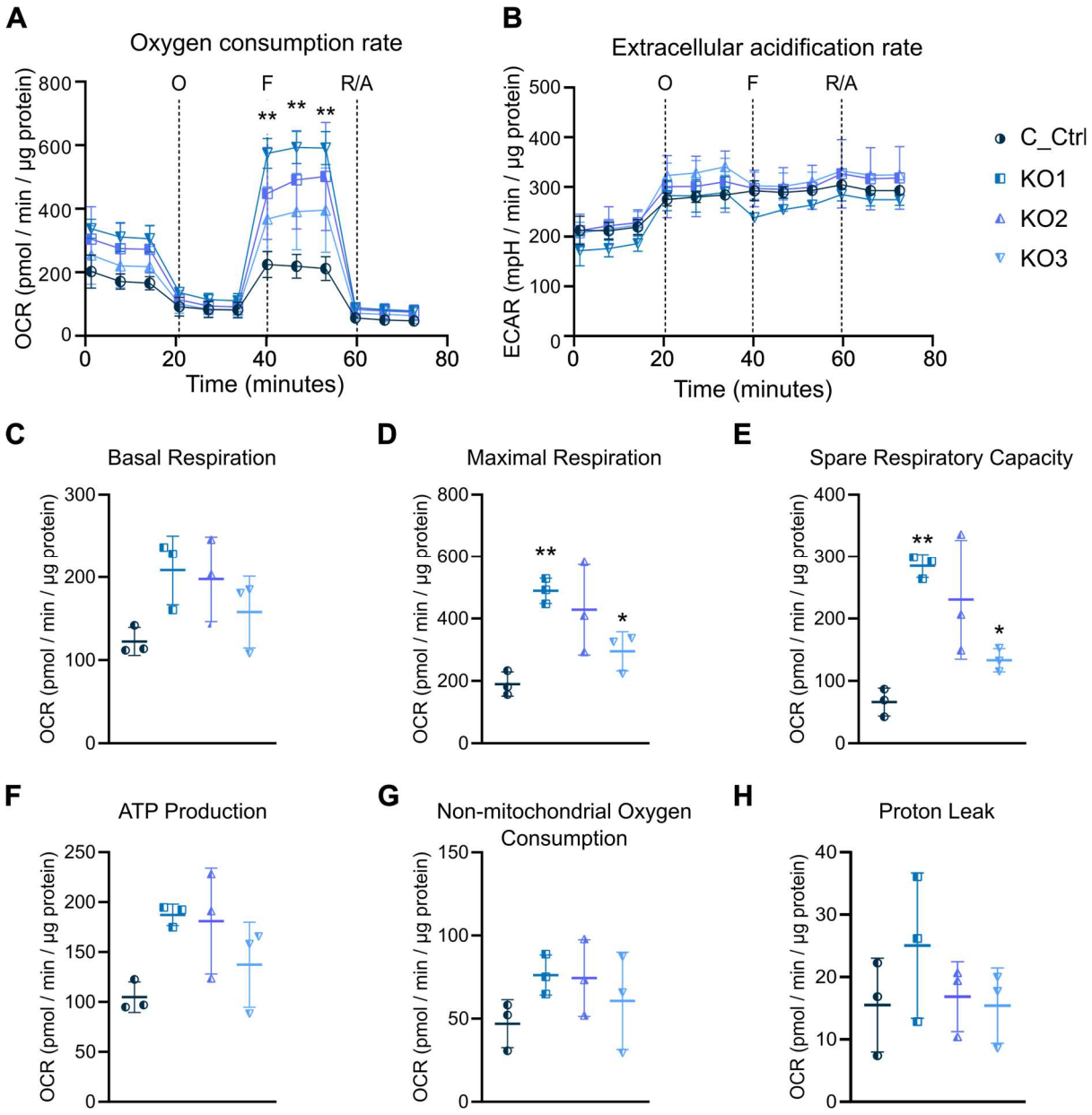

Figure 45. Impact of TSPO deficiency on mitochondrial respiration in BTIC13 KO clones. Mitostress test of TSPO-deficient KO clones (KO1, KO2, KO3) versus control clone C_Ctrl using the Seahorse XFe96 analyzer. Profiles of the (**A**) oxygen consumption rate (OCR) and (**B**) extracellular acidification rate (ECAR) in TSPO-deficient and control clones. The sequential injection of 1 µM Oligomycin (O), 2 µM FCCP (F), and 0.5 µM Rotenone/Antimycin A (R/A) is indicated. (**C-H**) The graphs display key respiratory parameters calculated from the OCR. (**A-H**) Seahorse raw data were normalized to total protein amount (µg) per well. Cumulative data of three independent experiments are shown as mean ± SD. Asterisks indicate significant differences between KO clones and control clone. P-values were calculated using two-way (**A**) and one-way (**D, E**) ANOVA followed by Dunnett´s *post hoc* test (*$P \leq 0.05$; **$P \leq 0.01$).

To validate the increased oxygen consumption rate (OCR) in TSPO-deficient clones, cells were treated with metformin. Metformin is known to impair OXPHOS by inhibiting complex I of the electron transport chain [220, 231]. The hypothesis tested in this assay was that cells with

higher OCR would be more dependent on OXPHOS and, therefore, more susceptible to OXPHOS inhibitors.

To investigate the proliferation of BTIC13 clones under OXPHOS inhibition, cells were treated with 1 mM or 10 mM metformin. These concentrations are commonly used for OXPHOS inhibition in *in vitro* studies but exceed the physiological range of metformin plasma concentrations in patients [232]. 48 hours post-exposure, proliferation was measured using a fluorescence-based CyQuant Cell Proliferation Assay (ThermoFisher), which allowed direct quantification of cell numbers without relying on the metabolic status of the cell.

There was no substantial difference in proliferation of TSPO KD clones (KD1, KD2, KD3) and control clone Scr C1 after exposure to 1 mM metformin (Figure 46A). However, the dose of 1 mM metformin significantly reduced the proliferation in the KO clones (KO1, KO2, KO3), while it had no effect in the control clone C_Ctrl (Figure 46B). 10 mM of metformin decreased proliferation in all clones. The effect was significantly stronger in the TSPO-deficient KD clones (KD1, KD2, KD3) and KO clones (KO1, KO2, KO3) compared to their respective control clones Scr C1 and C_Ctrl (Figure 46A, B). This suggests that the TSPO-deficient clones exhibited a higher sensitivity to OXPHOS inhibition, as proliferation was more affected by metformin in those cells.

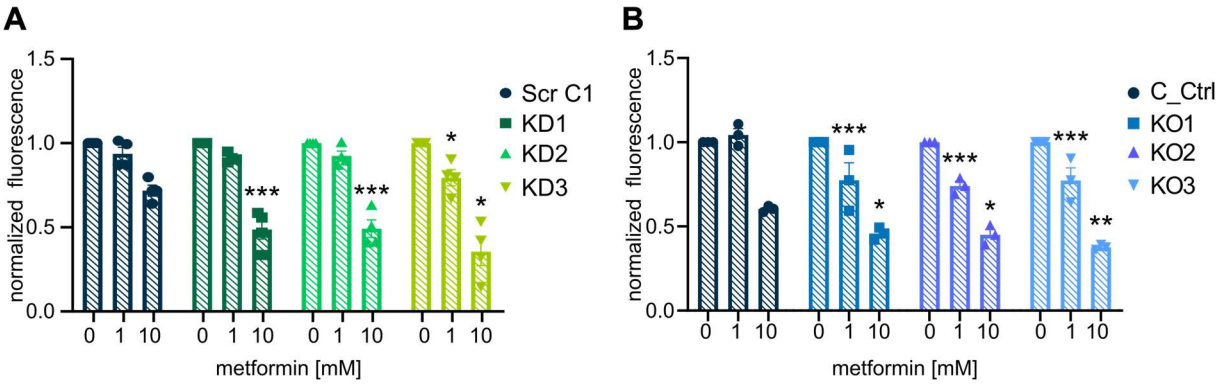

Figure 46. Impact of OXPHOS inhibitor metformin on cell viability of BTIC13 KD and KO clones. The CyQuant assay was performed to analyze the impact of metformin on cell viability in (**A**) TSPO-deficient KD clones and the control Scr_C1 and (**B**) TSPO-deficient KO clones and the control C_Ctrl. Fluorescence emission was measured after 48 hours exposure to 0-, 1- or 10 mM metformin and normalized to untreated control. Asterisks indicates significant differences between TSPO-deficient clones and control clones. Cumulative data of three independent experiments are shown as mean ± SD. P-values were calculated using two-way ANOVA followed by Dunnett´s *post hoc* test (*$P \leq 0.05$; **$P \leq 0.01$; ***$P \leq 0.001$).

Mitochondrial respiration is linked to the production of reactive oxygen species (ROS). In view of this connection, it was investigated whether the increased mitochondrial respiration of the TSPO-deficient clones impacts the intracellular levels of ROS. Therefore, TSPO-deficient KD

and KO and as well as control clones were stained with the ROS-sensitive fluorescent dye 2',7'-Dichlorodihydrofluorescein diacetate (H_2DCFDA) and subjected to flow cytometry.

Quantification of intracellular ROS levels revealed increased levels of ROS in the TSPO KD clones KD1, KD2 and KD3 compared to the Scr C1 control clone, which reached significance for KD1 and KD2 (Figure 47A). Notably, KD1 displayed a two-fold increase in ROS levels, which resembled the high OCR observed in the Mitostress test (Figure 47A). In contrast, KD3, which exhibited the highest respiratory activity, showed only a slight increase in intracellular ROS compared to Scr C1 (Figure 47A). Additionally, there was a small, yet significant, elevation in ROS levels in all TSPO KO clones compared to the C_Ctrl clone (Figure 47B). Nonetheless, this modest increase in ROS levels did not reflect the strong OCR increase in the TSPO KO clones.

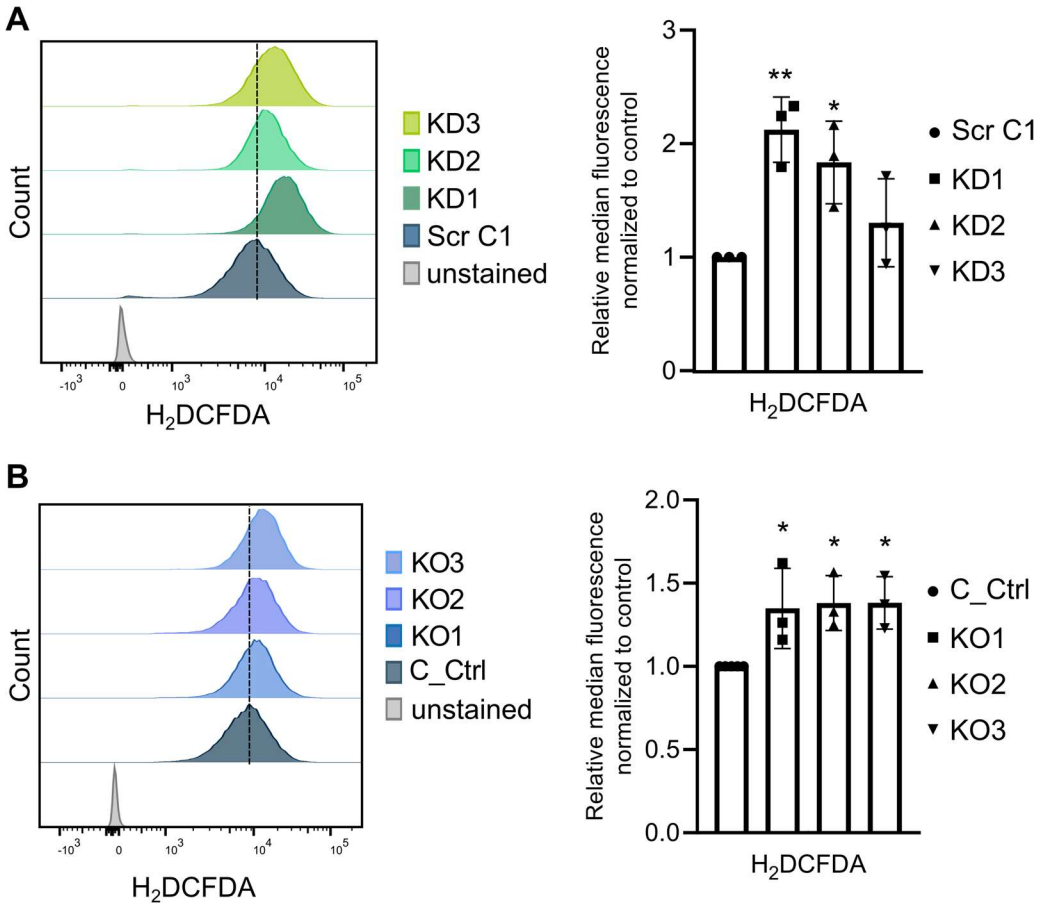

Figure 47. Impact of TSPO deficiency on intracellular ROS levels. Flow cytometry analysis in TSPO-deficient KD and KO clones stained with H_2DCFDA to measure the intracellular ROS levels. (**A, B**) Representative histogram plots of TSPO KD and KO clones and their respective controls clones. The grey histogram indicates the unstained control. The graphs display the relative median fluorescence of H_2DCFDA-positive cells of three independent experiments. Data are presented as fold change compared to the control and are shown as mean ± SD. Asterisks indicate significant differences between TSPO-deficient clones and control clones. P-values were calculated using one-way ANOVA followed by Dunnett´s *post hoc* test (*$P \leq 0.05$; **$P \leq 0.01$).

Collectively, these findings suggest that TSPO deficiency increases the oxygen consumption rate of BTIC13 without altering glycolytic activity. This increase in mitochondrial respiration coincides with a slight but significant increase in intracellular ROS levels. Still, differences within TSPO-deficient groups reflect the intrinsic heterogeneity of BTIC13.

5 Discussion

Given today´s clinical situation, the rationale for exploring innovative approaches and searching for new molecular targets for glioblastoma is clear. Despite comprehensive therapy consisting of surgery, chemo- and radiotherapy, patients diagnosed with glioblastoma have a particularly poor prognosis [1, 9]. To date, an effective treatment to significantly prolong the relapse-free period and to prevent tumor recurrence is still missing except in small molecularly defined subgroups, largely due to its inherent heterogeneity and immunosuppressive tumor microenvironment.

In an ongoing effort to address this challenge, the 18 kDa translocator protein TSPO has recently attracted considerable attention. TSPO is highly expressed in glioblastoma and during neuroinflammation in comparison to the healthy brain, making TSPO an attractive target for positron emission (PE) imaging of glioblastoma and the tumor microenvironment [233, 234]. Nevertheless, the specific functional implications of increased TSPO levels in the course of tumor malignancy are not yet known.

Over the years, TSPO has emerged as a multifaceted protein with implications in diverse cellular processes, including apoptosis [151, 199], mitochondrial metabolism [205, 208] and immunomodulation [160, 185]. Resistance to apoptosis and the secretion of immunosuppressive cytokines as response to cytotoxic T cells is a major mechanism how glioblastoma cells evade immune surveillance, thereby significantly contributing to the malignancy of glioblastoma.

Therefore, this work investigates the role of TSPO in tumor-intrinsic mechanisms that follow cytotoxic T cell attack. First, TSPO expression in tumor cells in response to cytotoxic T cells or pro-inflammatory cytotoxic effector molecules was examined. Second, the role of TSPO in death ligand-mediated apoptosis, as well as the production and release of immune-modulatory cytokines in response to pro-inflammatory cytokines has been explored. On a complementary trait, the adaptation of the cellular energy metabolism is crucial for glioblastoma to meet its increased energy demand for rapid tumor growth. Mitochondria play a vital role in cellular energy dynamics and TSPO has been considered as prime candidate for regulating metabolic balance in glioblastoma [208]. Therefore, the role of TSPO in mitochondrial respiration of glioblastoma cells was investigated.

To address these objectives, the patient-derived mesenchymal brain tumor initiating cell line BTIC13 was used as *in vitro* cell culture model for glioblastoma. BTICs effectively recapitulate the molecular traits and therapeutic resistance observed in the original tumor, which makes them a valuable model system for investigating the aggressive and heterogeneous nature of glioblastoma [217–219]. To obtain a functional understanding of TSPO in glioblastoma, TSPO

expression in BTIC13 was downregulated with two complementary loss of function approaches. First, a stable but partial downregulation of TSPO was achieved using a lentiviral shRNA-based method and second, a complete knockout of TSPO was attained using the CRISPR/Cas9 methodology.

A multitude of studies used synthetic TSPO ligands to functionally characterize TSPO [148, 153, 180]. Nevertheless, TSPO ligands were not used in this thesis and all functional assays were carried out with genetically modified cells only, as TSPO's biological role is already complex and it is challenging to decipher its precise function in specific contexts. TSPO ligands might add to the complexity as their specificity and mode of action are not well defined and their effect might vary on species and concentration used in the experiments [184]. However, the development of TSPO ligands is still an active area of research and as their clinical applications continue to evolve, they may play an increasingly important tool to therapeutically target TSPO.

5.1 Evaluation of TSPO-deficient BTIC13 cells to study the role of TSPO in glioblastoma

Patient-derived primary BTICs are a versatile and relevant cell culture model system to study cellular and molecular mechanism of glioblastoma. They recapitulate key aspects of glioblastoma tumor biology such as high heterogeneity, molecular characteristics, and resistance to therapy [218, 219]. Furthermore, they are characterized by stem-like properties such as high proliferative capacity, clonogenicity, and migratory behavior [235, 236].

To investigate the role of TSPO in malignant hallmarks of glioblastoma, the mesenchymal BTIC13 cells were used. This cell line has been comprehensively characterized in terms of its proliferative, migratory, and metabolic properties [217, 220]. Consistent with previous research, BTIC13 showed a high basic proliferative and migratory capacity in the *in vitro* cell culture setting. However, TSPO deficiency had no impact on basic proliferation rates within the different TSPO-deficient cell culture models. Interestingly, loss of TSPO significantly impaired the basal migratory capacity in the different TSPO-deficient BTIC13 model systems. These results contrast earlier studies showing that TSPO deficiency promotes proliferation and migration of glioblastoma U118 MG cells [237], and the proliferation of GL261 mouse glioma cells [208]. However, also alternative findings have been reported. For example, TSPO expression is positively correlated with proliferation and migration of C6 rat glioma cells [180, 238]. The underlying reasons for these discrepancies may include variations in species, cell types, experimental conditions, and methodological approaches. Additionally, the multifunctional nature of TSPO, impacting various cellular processes, could contribute to its diverse effects on glioblastoma cells in different contexts. Interestingly, the data also revealed that cell line intrinsic

variables may also determine the migratory capacity. Moreover, in shTSPO_1 Bulk cells other predominant, yet unknown mechanisms seem to overrule the inhibitory effect of the TSPO knockdown on cell migration.

To investigate the role of TSPO in BTIC13, TSPO expression was genetically silenced using two different loss of function approaches. For the shRNA-mediated TSPO knockdown two TSPO-specific shRNAs were used. Interestingly, shTSPO_1 and shTSPO_2 have the same target site on the TSPO mRNA and only differ in the adjacent flanking regions. Still, the two obtained cell lines, shTSPO_1 Bulk and shTSPO_2 Bulk often showed differential responses in experimental analysis despite having a comparable knockdown efficiency. Consequently, a CRISPR/Cas9-based complete TSPO knockout was performed to complement the shRNA-based knockdown experiments and allow for the exclusion of potential off target effects. The two different guide RNAs T116 and T126 both target sequences within exon 2 of the TSPO gene. Importantly, exon 2 is the first exon relevant for protein synthesis containing the translational start codon. Hence, both guide RNA-mediated CRISPR events resulted in frameshift mutations early in the translated gene region. These frameshift-induced protein sequences differ remarkably from the wildtype TSPO protein sequence already starting after ~ 30 amino acids. These impacts make a misfolded, degraded or overall non-functional protein highly likely. Additionally, it is worth noting that TSPO contains functional domains, such as the cholesterol recognition sequence situated near the carboxy terminus of TSPO (residues A147-S159) [168]. Consequently, early frameshift mutations are likely to disrupt cholesterol binding, potentially contributing to significant alterations in the functionality of TSPO. Lastly, the frameshift occurs within the second transmembrane regions of the TSPO protein and might therefore potentially prevent integration of TSPO in the outer mitochondrial membrane.

Notably, CRISPR events can lead to different types of edits within a mixed population of cells [239]. To ensure an understandable, stable and complete knockout of TSPO, single cell clonal populations were isolated. However, the single cell-derived clonal KO cell lines showed molecular and functional heterogeneity in different experiments. Similarly, also the KD clonal cell lines derived from the KD bulk cell lines showed variable responses in the different experiments. This heterogeneity could be reflective of the high intra-tumoral heterogeneity of the parental bulk cell line and is therefore highly relevant for glioblastoma. However, it is also plausible that single cell clonal culture itself could contribute to the heterogenous outcomes, since the challenge for a cell line to propagate from a single progenitor cell may also select for certain genetic alterations [239].

In summary, while highly relevant in glioblastoma, the observed heterogeneity makes it challenging to determine a biologically meaningful effect of the target gene. Future studies should

consider incorporating multiple TSPO control cell lines as well as TSPO re-expression within TSPO-deficient cell lines to validate observed experimental outcomes. The experiments of this study were all performed using cell lines derived from the parental BTIC13 line. However, the several model systems derived from BTIC13, such as TSPO-deficient bulk, TSPO KD clones and TSPO KO clones provided insight into molecular and biologically diverse cell lines and therefore were valuable in reflecting the highly heterogenous character of glioblastoma. Nevertheless, to further enhance the relevance for glioblastoma research, it is advisable to employ several BTIC lines representing different molecular subtypes of the disease. Finally, it is essential to acknowledge that the complete spectrum of intrinsic tumor heterogeneity and the complexities of tumor microenvironment are challenging to replicate within a BTIC system. Recent advancements in patient-specific glioblastoma models, such as the cerebral organoid glioma (GLICO) model, offer promising opportunities to investigate glioblastoma ex vivo, within a microenvironment closely resembling that of the human brain in its primitive state [240].

Nonetheless, the development of an efficient shRNA-based TSPO knockdown and CRISPR/Cas9-based TSPO knockout in BTIC13 served as the foundation for future studies aimed at elucidating the role of TSPO in glioblastoma.

5.2 TSPO expression in glioblastoma

The frequent overexpression of TSPO in glioblastoma [161] and within pro-inflammatory brain environments [241] suggests a potential link between TSPO expression and pro-inflammatory signaling. Furthermore, TSPO expression appears to be most pronounced in tumors characterized by high immune cell infiltration [161, 167, 242]. Therefore, the first objective addressed in this thesis was to investigate whether pro-inflammatory T cell-derived factors contribute to the TSPO overexpression in BTICs.

In this thesis, robust TSPO expression was observed in short-term cultured, patient-derived primary BTICs of mesenchymal and proneural origins. As evident from the results, both, direct contact of tumor cells and T cells, and T cell-derived soluble factors, increase TSPO expression in BTIC13. This observation aligns with an *in situ* correlation analysis, which revealed a positive association between TSPO expression and the expression of T cell marker genes [222].

Different BTIC lines exhibited varying levels of TSPO with TSPO-low and -high expressing BTICs in both subtypes. Interestingly, previously published data indicate that in the absence of immune cells, TSPO expression between mesenchymal and proneural BTICs was not significantly different [222]. However, other studies using glioblastoma tissue samples revealed that TSPO expression correlates with different molecular subgroups of glioblastoma and the

highest expression was detected in patients with the mesenchymal subtype [161, 167]. Furthermore, the mesenchymal subtype not only exhibits elevated TSPO levels, but also a significant enrichment of immune cells, including cytotoxic T cells [43, 242]. Given this context, it is possible that short-term monocultured BTICs exhibit individual levels of TSPO independent of the molecular subgroup. However, TSPO expression might be modulated by T cell-derived factors and thus, the elevated immune cell infiltration in mesenchymal glioblastoma may contribute to the higher TSPO levels in this subtype in the *in vivo* situation. Nevertheless, it is important to note that this analysis was conducted exclusively in one mesenchymal BTIC line. In addition, the influence of other immune cells as well as other cellular and non-cellular players in the tumor microenvironment (TME) on TSPO expression in tumor cells has not been investigated. Further research is required to clarify the relationship between glioblastoma subtype, tumor immune cell infiltration and TSPO expression in both *in vitro* and *in vivo* experiments.

In addition to tumor cells, also other immune cell populations such as tumor associated microglia and macrophages (TAMs) within the TME express TSPO. While this study has primarily focused on the impact of TSPO in tumor cells, the impact of T cell-derived pro-inflammatory cytokines such as IFNγ and TNFα on TAMs has not been addressed. However, studies in mice and human C20 microglia have shown that pro-inflammatory cytokines are able to upregulate TSPO expression and are specifically associated with the pro-inflammatory microglia phenotype [160, 185]. Conversely, another study showed that IFNγ did not change TSPO expression in a human primary microglia cell line [187]. With this in mind, future experiments should investigate the consequence of T cell-derived IFNγ and TNFα on TSPO expression in the TME and specifically in TAMs.

Alternatively, it has been suggested that the increased TSPO expression in glioblastoma is primarily attributed to TSPO expressing infiltrating myeloid derived suppressor cells (MDSCs) and TAMs [243]. However, in line with other studies [161, 167], this work showed that TSPO is indeed also highly expressed by tumor cells and that moreover, immune cell-derived factors further increase TSPO expression in BTICs.

The immune cell-derived factors that increase TSPO expression were identified based on respective exposure and receptor blocking experiments. These experiments revealed that mainly IFNγ and, to a lesser extent, TNFα are the key pro-inflammatory factors in the T cell supernatant responsible for inducing TSPO expression. This finding is supported by a correlation analysis conducted in a single cell RNA Seq data set, which revealed a correlation between TSPO and the expression of IFNγ- and TNFα-receptors, as well as of genes induced by IFNγ- and TNFα-signaling [222].

IFNγ and TNFα are pro-inflammatory cytokines that are critical for the innate and adaptive immune response and associated with diverse cellular functions (reviewed in [223, 224]). IFNγ mediates its various biological effects by multiple signaling pathways such as the canonical JAK-STAT1 signaling pathway [223], but also by PI3K/AKT [244], and MAPK signaling [245]. Pathways induced by TNFα include signaling for apoptosis induction, but also NFκB and MAPK pathways and others [224]. These pathways are known to activate transcription factors such as STAT1, STAT3 and c-Jun [246–248]. This is of interest, because TSPO gene expression seems to be driven by PKCε-dependent MAPK (Raf-1-MEK1/2-ERK1/2) signaling and its promotor contains bindings sites for transcription factors such as STAT3, c-Jun, ETS1/3, and Sp1/3 [164–166]. This provides a possible link between IFNγ/TNFα signaling and the transcriptional activation of TSPO. However, the molecular pathways engaged in TSPO induction have not been further addressed in this study and should be the focus of future research.

According to previous findings, TSPO expression can be induced by TNFα in human colon carcinoma cells [171]. In the present study however, exposure to TNFα or blocking of TNF-R1 and TNF-R2 alone did not affect TSPO expression. Interestingly, the simultaneous blockade of IFN-R1 and both TNFα receptors had the greatest impact on preventing the increase in TSPO expression by T cell supernatant. This suggests a potential synergy between TNFα and IFNγ signaling and is consistent with previous findings showing that TNFα enhances IFNγ signaling by upregulating the expression of IFNγ- receptors [249]. However, the combined effects of IFNγ and TNFα and their potential synergism on TSPO expression were not evaluated in this study and need to be addressed in future experiments.

While TSPO expression was strongly inhibited by concurrent TNF-R1/2 and IFN-R1 blockade, it is worth noting that complete inhibition of activated T cell supernatant-mediated upregulation of TSPO was not achieved. The analysis of cytokine secretion of Flu-peptide-activated T cells revealed high levels of IFNγ (~6500 pg/ml) and to a lower extent TNFα (~650 pg/ml) [222], making IFNγ and TNFα highly relevant for the T cell-mediated TSPO upregulation. However, it cannot be excluded that there are additional factors in the supernatant that were not analyzed but contribute to the increased TSPO expression. It is crucial to note that not only other factors next to IFNγ and TNFα, but also other immune cells next to cytotoxic T cells could additionally modulate TSPO expression especially in the highly complex *in vivo* setting. Therefore, it is probable that the linear relationship between TSPO expression in the tumor cells and T cell contact does not completely reflect the *in vivo* situation.

Besides induction by pro-inflammatory signaling, there are also alternative mechanisms that could contribute to increased TSPO expression in glioblastoma. These include TSPO gene amplifications [250] or epigenetic regulations such as aberrant promotor methylations [164,

167]. Furthermore, the PKCε/ERK1/2-AP1-STAT3 signaling pathway regulating TSPO expression on a transcriptional level, is often deregulated in glioblastoma (reviewed in [251]).

These findings conclusively demonstrate that TSPO is highly expressed by tumor cells and that contact with cytotoxic T cells further increases this expression.

Collectively, the results also support the hypothesis that pro-inflammatory T cells contribute to an elevated TSPO expression in glioblastoma. Future experiments should expand these findings into a larger cohort of mesenchymal and proneural BTICs. Furthermore, these observations need to be translated into the *in vivo* situation to take the complex interaction of the TME into account.

5.3 TSPO's role in TRAIL-induced apoptosis of glioblastoma

Resistance to apoptosis strongly contributes to immune evasion and therapy resistance of glioblastoma. Several studies have implicated TSPO in the regulation of apoptosis [151, 195, 199]. This has led to the hypothesis that elevated TSPO levels in glioblastoma may modulate the apoptosis response, thus contributing to the resistance against cytotoxic T cell control.

To address this question, the involvement of TSPO in the apoptosis response of tumor cells after T cell attack was investigated. Specifically, the impact of TSPO on TRAIL-induced apoptosis in BTIC13 was examined.

This study uncovered that despite expressing relevant cytokine and death receptors, only TRAIL exhibited a dose-dependent reduction of cell viability in BTIC13. Examination of the underlying apoptosis signaling pathways revealed that TRAIL-induced apoptosis via the extrinsic and intrinsic apoptotic caspase cascades. However, it became evident that the response to TRAIL did not solely rely on TSPO expression. Instead, multiple cell-intrinsic factors were observed that determined the susceptibility towards TRAIL-induced apoptosis.

Among the death ligands tested in the cell culture setting, TRAIL was the only ligand that reduced the cell viability of BTIC13. This observation is intriguing, particularly because the receptor of the death ligand FasL was highly expressed in BTIC13, and both the TRAIL and Fas pathways utilize a similar signal transduction machinery [252]. Various apoptosis resistance mechanisms, such as the downregulation of the adaptor protein FADD [253] and caspase-8 [254], or the increased expression of the caspase-8 structural homologue cFLIP [122], can affect both pathways. Notably, the data presented here demonstrate that apoptosis induction by TRAIL is possible, suggesting that the basic apoptotic signaling components are functional in both apoptosis pathways. However, there are also more selective resistance mechanisms that might specifically impact Fas, such as somatic mutations in the *Fas* gene [255] or the

overexpression of Fas-associated phosphatase-1 (FAP-1) [256, 257] which impair Fas-mediated apoptosis induction but have no impact on TRAIL signaling.

TRAIL-induced apoptosis was mediated by both the extrinsic and intrinsic apoptotic cascade in BTIC13. Sequentially, exposure to TRAIL resulted in a rapid activation of caspase-3 already within one hour of TRAIL treatment followed by a slightly delayed induction of caspase-9 after three hours of TRAIL exposure. Apoptosis induction in cells can be classified as a type I or type II reaction. In type I apoptosis, activation of the initiator caspase caspase-8 directly triggers the activation of effector caspases such as caspase-3 and caspase-7. In type II apoptosis, the pro-apoptotic signal must be amplified via the activation of the intrinsic mitochondrial pathway in addition to the extrinsic pathway to efficiently induce apoptosis, which includes activation of caspase-9 and cytochrome c release from the mitochondria. The crucial point at which extrinsic and intrinsic pathway converge is the BH-3 only protein BID. BID is cleaved by active caspase-8 to generate truncated BID, which subsequently activates intrinsic apoptosis [101].

The findings of this study suggest that apoptosis in BTIC13 can be classified as type II. Exposure to TRAIL resulted in the degradation of BID, cytochrome c release, and activation of caspase-9.

The physiological difference of type I or type II apoptosis is not fully understood. However, the levels of active caspase-8 can determine whether a cell reacts as type I or type II cell [258]. In BTIC13, caspase-8 was not detectable by Western blot analysis and caspase-8 activity could only be demonstrated using a luciferase-based glo assay. This implies that the caspase-8 activity might by insufficient to directly activate the effector caspases, and mitochondria are required to amplify the low caspase-8 activity. It is worth noting that other studies have also described an activation of mitochondrial apoptosis in type I cells [258], and there is evidence of a transitional state between type I and type II, in which the response depends on the dose or exposure time of TRAIL [259]. To further validate the classification of apoptosis as type II in BTIC13, future experiments could explore the impact of genetic overexpression of anti-apoptotic Bcl-2 proteins or downregulation of BID on mitochondrial apoptosis induction.

The study revealed that various TSPO-deficient cell lines derived from BTIC13 exhibited a differential response to TRAIL. This response did not solely rely on TSPO expression, as different TSPO KD clones displayed different sensitivities towards TRAIL-induced apoptosis, despite comparable low TSPO expression. This assumption was further supported by the finding that lentiviral-induced TSPO re-expression in the highly TRAIL-responsive KD1 clone cell line and subsequent clonal selection resulted in a TRAIL-sensitive (KD1_R2) and a less sensitive clone (KD1_R1). Notably, treatment with TRAIL reduced cell viability of the polyclonal BTIC13 bulk cell line only by approximately 50 %. This suggests the presence of TRAIL-responsive

and TRAIL-resistant subpopulations within BTIC13. These findings were corroborated by monoclonal cell lines obtained from the heterogenous bulk. While two BTIC13 knockdown clones (KD1 and KD2) showed an increased sensitivity towards TRAIL-induced apoptosis, the other two clones (KD3 and Scr C1) demonstrated a muted response. Moreover, the BTIC13-derived TSPO KO clones and control clones were almost completely resistant to TRAIL, and the loss of the TRAIL receptor DR4 expression was identified as potential resistance mechanism. Interestingly, the loss of TRAIL receptor surface expression is a frequently observed mechanism in acquired TRAIL resistance [260].

Intratumoral heterogeneity is a major contributor to therapy resistance and tumor recurrence. Several studies have shown that the majority of cancer cells are inherently resistant to TRAIL or acquire resistance to TRAIL during the course of therapy [261]. As a result, TRAIL resistance in BTIC13 might be a consequence of both clonal expansion of already existing resistant tumor cells within the heterogenous bulk or new acquisition of a resistant state.

To which extent genetically or epigenetically distinct subsets within BTIC13 contribute to TRAIL resistance remains to be determined. However, the BTIC13 clones provide insight into diverse resistance mechanisms that could potentially influence the TRAIL response. These mechanisms include elevated levels of anti-apoptotic Bcl-2 in Scr C1 and KO2, or a preference for the activation of NFκB pro-survival signaling upon TRAIL exposure in BTIC13 WT, Scr C1 and KD_R1. Additionally, the loss of DR4 surface expression in the TSPO KO clones adds another layer to these resistance mechanisms. Furthermore, other studies have also identified other resistance mechanisms that were not investigated in this study. These include the low expression of caspase-8 [254], overexpression of the apoptosis inhibitor cFLIP [122], as well as the surface expression of pro-survival TRAIL decoy receptors [262]. Given the multitude of different resistance mechanisms, a robust molecular marker that predicts TRAIL response in BTIC13 could not be identified. Moreover, these results underscore the complexity of TRAIL resistance and emphasize that targeting TSPO alone may not be sufficient to overcome it.

TRAIL can bind to two apoptosis-inducing receptors, DR4 and DR5 (reviewed [107]). As shown by DR4 and DR5 blocking experiments, the recombinant soluble form of TRAIL used in the cell culture experiments needs sufficient expression of the DR4 receptor to activate apoptosis in BTIC13. In contrast, T-cell mediated cytotoxicity primarily involved the action of the DR5 receptor and only secondarily the action of the DR4 receptor. This observation aligns with findings from other studies showing that DR4 is activated by both the soluble and the membrane-bound form, whereas DR5 typically requires the membrane-bound form or secondary cross-linked antibodies for activation [108, 263]. Alternatively, studies have also shown that DR5 can be activated via soluble TRAIL variants or antibodies without the need for secondary cross-

linking to induce apoptosis [264, 265]. Collectively, this suggests that depending on the context, DR4 and DR5 seem to have partly overlapping but also distinct functions. However, in BTIC13, DR4 expression is required for apoptosis induction by soluble TRAIL. Considering the observed disparities between monoculture and co-culture experiments, it becomes evident that translating findings from *in vitro* studies to the *in vivo* context may pose challenges. This is especially true when accounting for the intricate interactions among various cell populations within the TME. Future experiments should include the re-expression of DR4 in TSPO KO clones and the knockdown of DR4 in KD clones to further substantiate the significance of DR4 signaling in soluble TRAIL-induced apoptosis.

Similar to findings in this thesis, previous research on TSPO's role in apoptosis also revealed several inconsistencies. Depending on the cell line, TSPO-deficiency reduced or increased sensitivity towards apoptosis-inducing stimulants. For instance, while TSPO-deficiency increased the apoptotic rate of GL261 mouse glioma cells [208], TSPO-deficient C6 rat glioma cells or U118 MG glioblastoma cells were resistant to apoptosis [151, 195]. Furthermore, the mechanism by which TSPO modulates apoptosis is not fully understood yet and needs further investigations on a molecular and cellular scale. TSPO has been proposed to modulate the mitochondrial permeability transition pore (mPTP), which is a non-selective channel of the inner mitochondrial membrane hypothesized to play a role in mitochondrial apoptosis [266]. However, Šileikyté and colleagues recently challenged the role of TSPO as critical modulator of the mPTP as TSPO played neither a role in the regulation nor in the structure of the mPTP [156]. When summarizing these findings, the exact role of TSPO in apoptosis and mPTP function remains unclear.

It is important to note that in our recently published study, downregulation of TSPO was found to augment T cell-mediated killing of human glioblastoma cell lines and BTICs, including BTIC13 [222]. Furthermore, the study demonstrated that TSPO knockdown sensitizes BTICs specifically towards TRAIL-induced apoptosis by modulating the expression of apoptosis-related genes, potentially through retrograde mitochondria-to-nucleus signaling [222, 267, 268]. In line with this, two out of three TSPO KO clones also showed increased susceptibility towards T cell cytotoxicity when compared to the control cell lines. However, an extended in-depth analysis of TSPO's impact in TRAIL-induced apoptosis in the monoculture showed remarkable disparities in apoptosis response, depending on the cell culture system used (TSPO-regulated bulk vs. TSPO KD vs TSPO KO cells), again pointing into the direction of distinct tumor-cell and microenvironment-dependent context factors. It is crucial to acknowledge that in tumor-T cell co-cultures, additional mechanism next to TRAIL-apoptosis signaling may be involved in the TSPO-sensitizing effect, dependent of the mentioned context factors. These could include perforin/granzyme B signaling or other co-stimulatory mechanism that were not accounted for

in the BTIC13 monoculture. As already mentioned, differences between soluble TRAIL and membrane-bound TRAIL signaling became evident. Therefore, while it may not be the case that TSPO deficiency is the single factor to sensitize BTIC13 towards TRAIL, TSPO deficiency might have a sensitizing effect in the context of T cell-mediated cytotoxicity or cytotoxicity occurring in a more complex 3D-culture or *in vivo* model.

A limitation of the studies on TSPO's impact on apoptosis is, that only one BTIC line was used. Given the high intertumoral heterogeneity of glioblastoma, the findings of TSPO's role in apoptosis may not be universally applicable to other BTIC lines. However, the investigation of bulk, TSPO KD, TSPO KO and control sublines of BTIC13 unexpectedly provided a broad overview of distinct genotypes and phenotypes, that in part reflects intratumoral heterogeneity in glioblastoma. A potential source of bias is the fact that, while several knockdown and knockout clonal cell lines were generated, there was only one corresponding control clone for each TSPO deficiency model system. To detect if TRAIL responses truly depend on inherent heterogeneity, it would be beneficial to investigate whether there are differences in TRAIL response among a variety of control clones. Nevertheless, it is important to note that the susceptibility of the control clones to TRAIL is comparable to that of BTIC13 wildtype cells, suggesting that control clones are representative of BTIC13 wildtype cells in this respect. Additionally, it should be noted that the generation of single cell-derived clonal cell lines may artificially contribute to TRAIL resistance, as it cannot be ruled out that increased TRAIL resistance provides a survival advantage to the single cell-derived clones. Finally, it needs to be mentioned that the TSPO expression in the TSPO re-expressing clones was lower than in the BTIC13 wildtype and control clone. Interestingly, the clones that were less responsive to TRAIL showed lower TSPO re-expression levels as the highly TRAIL-sensitive clone. This finding further highlights the complexity of the TRAIL response, which depends on various mechanisms beyond TSPO expression.

This research underscores the remarkable heterogeneity observed in glioblastoma. Contrary to the initial hypothesis, TSPO deficiency alone did not sensitize BTIC13 towards TRAIL-induced apoptosis. Instead, the response to TRAIL was rather dependent on a diverse array of resistance mechanisms and could not be attributed to a specific expression pattern. Therefore, the identification of a predictive marker for the tumor cell TRAIL- or apoptosis-response in general will be crucial to guide a successful treatment strategy for glioblastoma. Based on that, a promising approach may involve the combination of TSPO modulation together with direct targeting of TRAIL-induced apoptosis and additional therapeutic agents that specifically target TRAIL-resistant subsets.

In addition, the observed differences in monoculture and co-culture experiments already implied that the TRAIL response may be context dependent, and thus a direct translation of findings into the patient may also be difficult. This modeling problem can be addressed, at least in part, in future research that includes, in the best case, syngeneic immunocompetent animal models. Nevertheless, this study emphasizes the need to predict and overcome potential and diverse resistance mechanism within subsets of tumor cells, which might represent an important step towards improved treatment for glioblastoma patients.

5.4 TSPO's role in the secretion of immunomodulatory cytokines

Tumor cells have the ability to actively shape the cytokine milieu within the tumor microenvironment (TME) to support their growth and evade the immune system [56]. In this study, IFNγ and TNFα were identified as inducers of TSPO expression in BTICs. Interestingly, these pro-inflammatory cytokines are also known to increase the production of immunomodulatory cytokines such as interleukin-6 (IL-6) [227] and interleukin-8 (IL-8) [269] in glioma cells. Given the potential involvement of TSPO in mitochondrial function, inflammation, and steroidogenesis, it was hypothesized that TSPO can modulate, either directly or indirectly, the production and release of IL-6 and IL-8, thereby contributing to immune evasion of glioblastoma.

To address this hypothesis, TNFα- and INFγ-induced IL-6 and IL-8 production and release in different TSPO-deficient BTIC13 cells was systematically characterized. The analysis revealed that baseline levels of IL-6 and IL-8 varied between and within TSPO-deficient model systems of BTIC13 (KD vs. KO). While TNFα and IFNγ stimulation both induced IL-6 mRNA expression and protein release in all cell lines analyzed, IL-8 was primarily upregulated by TNFα. However, there was no distinct TSPO-dependent pattern in IL-6 and IL-8 production and release under baseline conditions or after TNFα and IFNγ stimulation.

The results clearly indicated that exposure to TNFα and IFNγ increased IL-6 mRNA expression and protein secretion in BTIC13 in a time-dependent manner. This is in line with previous findings, showing that IL-6 is induced upon TNFα and IFNγ exposure in various human glioma cells [226, 227, 270]. In contrast to IL-6, IL-8 expression and secretion was specifically upregulated only by TNFα. Exposure to IFNγ had either no effect on IL-8 production (KD Bulk and KO clones) or even decreased the IL-8 concentration within the cell culture supernatant (KD clones). According to several publications, stimulation by TNFα leads to an elevated production of IL-8 in different types of cancer including glioblastoma [171, 228, 269].

IL-6 and IL-8 are proinflammatory cytokines with critical roles in the innate and adaptive immune system (reviewed in [271, 272]). Both cytokines have been implicated with various tumor-promoting intrinsic functions such as tumor cell survival, proliferation, and invasion [271,

272]. This suggests that the TNFα- and IFNγ-mediated upregulation of IL-6 and IL-8 within BTIC13 could enhance aggressive growth and migratory behavior of tumor cells. However, cell-intrinsic functions of IL-6 and IL-8 have not been addressed in this study. Furthermore, both cytokines have been described to exert diverse tumor-supporting functions within the TME. These include tumor angiogenesis, recruitment of immunosuppressive TAMs and MDSCs, as well as the inhibition of the anti-tumor immune response of cytotoxic effector cells [230, 273–276]. In this context, T cell-derived TNFα and IFNγ may trigger an adaptive resistance mechanism within BTICs by increasing the production and secretion of IL-6 and IL-8, which in turn, counteracts T cell-mediated cytotoxicity to escape immune control.

As shown in the experiments, downregulation of TSPO had no clear effect on IL-6 and IL-8 mRNA expression and protein secretion in BTIC13. Notably, the concentration of IL-6 and IL-8 protein in the cell culture supernatant of unstimulated BTIC13 cells already varied between and within the different TSPO-deficiency models. For instance, while IL-8 levels in the cell culture supernatant of BTIC13 KD bulk and KO cell lines were at a comparable range, the secreted IL-8 protein levels of the KD clones were considerably reduced. Furthermore, when looking at differences within one model system, for example within the KD clones, KD1 displayed slightly lower levels of IL-6 secretion whereas KD3 exhibited significantly higher levels of IL-6 compared to the control. To account for these differences at the baseline levels, TNFα- and IFNγ-induced IL-6 and IL-8 concentrations were normalized to the unstimulated condition. Nevertheless, it was still not possible to detect a TSPO-dependent pattern in TNFα- and IFNγ-stimulated IL-6 and IL-8 production and release in this experimental setting.

It should be emphasized that these experiments were exclusively performed using different clonal cell lines derived from the mesenchymal BTIC13. As previously discussed, the immune microenvironment can exhibit significant variations among different molecular subtypes of glioblastoma with highest immune cell infiltration in the mesenchymal subtype [43, 242]. Given that IL-6 and IL-8 are induced by pro-inflammatory cytokines, their secretion profile within glioblastoma might be strongly influenced by the infiltrating immune cells. Therefore, it is reasonable to assume that IL-6/IL-8 secretion of mesenchymal and pronounal BTICs may differ accordingly as immune cell infiltration is lower in the proneural subtype. In support of this, it has been shown that the mesenchymal subtype is associated with increased IL-8 levels compared to the proneural subtype [277, 278]. In addition, preliminary unpublished data from our laboratory also indicate that proneural BTICs have lower basal levels of IL-6 and IL-8 compared to the mesenchymal BTIC13. This intriguing observation warrants further investigation of possible disparities between basal, TNFα- and IFNγ-induced IL-6 and IL-8 expression and secretion and the potentially differential impact of TSPO in mesenchymal and proneural BTICs.

It is worth mentioning that, in most cases, the IL-6 and IL-8 mRNA levels corresponded to the concentration of the secreted proteins. However, in some cases the observed trend at mRNA level did not consistently translate to the secreted protein level. While there is no obvious explanation for this discrepancy, it is important to note that, when focusing on the matching mRNA expression and protein release data, the key findings of the study remain the same.

There is not a direct well-documented link between TSPO and IL-6 and IL-8 production in glioblastoma. However, in human colon carcinoma cells, it has been shown that TNFα-induced IL-8 expression which, as a consequence, resulted in an increase in reactive oxygen species (ROS) and subsequent TSPO overexpression [171]. However, in the current study, a direct relationship between TNFα-induced IL-8 expression and subsequent ROS and TSPO induction was not apparent. Admittedly, the impact of TNFα and IFNγ on ROS levels were not investigated here and thus should be a focus of future experiments. Further evidence for a connection between TSPO and IL-6 and IL-8 production was found in microglia. For example, stable downregulation of TSPO expression in pro-inflammatory polarized human C20 microglia decreased IL-8 levels [186]. In addition, knockout of TSPO in human C20 microglia significantly decreased basal IL-6 and IL-8 mRNA levels [279].

Dysregulated IL-6 and IL-8 expression and signaling is a common event in cancer and elevated levels of IL-6 and IL-8 have been linked to increased tumorigenicity in glioblastoma in *in vitro* studies [229, 230, 280, 281] and have been also associated with poor survival of glioblastoma patients [229, 282]. In this thesis, it has been shown that the pro-inflammatory cytokines TNFα and IFNγ contribute to the increased expression and cytokine secretion of IL-6 and IL-8 in the mesenchymal BTIC13 line. However, under the experimental conditions of this study, TSPO presence or absence had no impact on the IL-6 and IL-8 production in BTIC13.

Considering the observed differences in TRAIL-DR4 and -DR5 receptor signaling and apoptosis induction between the monoculture experiments using recombinant, soluble TRAIL and direct interactions of tumor cells and T cells in the co-culture setting, it would be interesting to investigate TSPO's impact on IL-6 and IL-8 production by BTIC13 after confrontation with cytotoxic T cells in contrast to cytokine cell stimulations. In addition, further research is needed to address the biological consequences of TNFα- and IFNγ-mediated upregulation of IL-6 and IL-8 within BTICs as well as on the surrounding TME. In this context, it would also be valuable to compare potential differences between proneural and mesenchymal BTICs. Finally, it is important to consider other crucial immunomodulatory cytokines, such as IL-10 and TGF-β, which play key roles in the immunosuppressive microenvironment of glioblastoma [55, 70]. Exploring the potential involvement of TSPO in regulating expression and secretion of these cytokines

warrants further investigation. In conclusion, within BTIC13, intrinsic factors beyond TSPO appear to play a role in TNFα- and IFNγ-induced IL-6 and IL-8 production.

5.5 TSPO's role in mitochondrial respiration

A major energy source in the brain is glucose and glioblastoma cells heavily rely on it [283]. Nevertheless, the ability to dynamically switch between different metabolic pathways, including glycolysis and mitochondrial respiration, is crucial for the tumor to adapt to nutrient shortages and meet the increased energy demand of uncontrolled cell division [141, 142]. Growing evidence supports a role of TSPO in the cellular energy metabolism [204, 205, 207] and TSPO has been proposed as an essential factor in mitochondrial metabolism by modulating the dynamic balance between oxidative phosphorylation and glycolysis in glioma [208]. The named dynamic adaption may also shape the response to apoptotic stimuli and local immunosuppression in the TME [135, 136, 284, 285]. Therefore, as a complementary objective of this thesis, the role of TSPO in the mitochondrial energy metabolism of BTIC13 was investigated.

As shown by the experiments, TSPO deficiency increased the maximal oxygen consumption rate without altering the glycolytic activity. This finding coincides with a slight but significant increase in levels of cellular reactive oxygen species (ROS) in TSPO-deficient clonal cell lines.

The loss of TSPO resulted in an increase in both, maximal respiration, and spare respiratory capacity in the different TSPO deficiency model systems of BTIC13. However, alterations in basal respiration were only observed in one TSPO KD bulk cell line (shTSPO_2 Bulk) and in the TSPO KO clones (KO1, KO2, and KO3), but not in shTSPO_1 Bulk and in the TSPO KD clones (KD1, KD2, and KD3). Consistently, basal respiration-coupled ATP production was only increased in shTSPO_2 Bulk and in the TSPO KO clones. These findings indicate that the loss of TSPO primarily enhances the adaptability of BTIC13 to specifically respond to high energy demands by having the ability to rapidly oxidize substrates. The data suggest that TSPO deficiency in BTIC13 is particularly relevant when the physiological system is pushed to its maximal capacity. While it is important to mention that in most cases maximal respiration does not represent a physiological state of cells [286], an increased maximal respiratory capacity could provide advantages for cancer cells during mechanisms such as uncontrolled cell division and rapid proliferation.

By measuring the extracellular acidification rate (ECAR), the effect of TSPO deficiency on glycolysis was additionally determined. Interestingly, there were no conclusive differences in ECAR of TSPO-deficient cells in comparison to control cells. However, the ECAR measured in the Mitostress test does not correspond to glycolysis alone and rather reflects the combined production of acids from both, glycolysis and the tricarboxylic acid (TCA) cycle. Nevertheless,

injecting modulators of the electron transport chain (ETC) can offer limited insights into the relative contributions of glycolysis and the TCA cycle to the ECAR [287]. For example, when mitochondrial respiration is inhibited by the injection of Oligomycin, it restricts both, the electron flow through the TCA cycle and mitochondrial respiration. Consequently, any increase in ECAR following Oligomycin corresponds to an increase in glycolysis, which compensates for the reduced mitochondrial respiration. Subsequent injection of FCCP enhances both, mitochondrial respiration, and TCA cycle electron flux. Importantly, if the ECAR remains constant after the injection of Rotenone and Antimycin A, which completely inhibit the ETC and consequently also the flux through the TCA cycle, this indicates that the ECAR measured here primarily results from glycolysis. Based on the ECAR profile of BTIC13, inhibition of mitochondrial respiration with Oligomycin increased compensatory glycolysis of TSPO-deficient and control BTIC13 equally. The ECAR remained at a high level after Rotenone and Antimycin A injection. This suggests that the respiratory CO_2 produced in the TCA cycle only marginally contributed to the ECAR of TSPO-deficient and control BTIC13 and, therefore, the ECAR profile predominantly reflects glycolysis.

In summary, the results indicate that in the control cell lines glycolysis is not increased as a compensatory mechanism to counteract lower oxygen consumption rates in comparison to the TSPO-deficient BTIC13 cells. However, for a direct measurement of basal glycolysis and overall glycolytic capacity, it would be beneficial to perform additional tests such as the glycolytic rate assay or the glycolysis stress kit. Worth noting, TSPO has also been described to play a role in fatty acid oxidation [288]. Considering the ability of glioblastoma cells to adapt and switch between different kinds of energy sources, it would be interesting to investigate the impact of TSPO on other potentially compensatory mechanisms.

Elevated proton leakage across the inner mitochondrial membrane can be a sign of mitochondrial damage or dysfunction. However, there was no significant difference in proton leak of TSPO-deficient and control cells. This is supported by the finding that the overall mitochondrial morphology remained intact in TSPO KO clones compared to the control clone. In line with this, other studies also showed that TSPO deficiency did not affect the overall mitochondrial morphology [189, 288, 289]. However, other authors reported that the loss of TSPO resulted in a greater number of fragmented mitochondria [208]. Changes in mitochondrial morphology were also observed in a TSPO-deficient human neuroblastoma cell line and in mouse embryonic fibroblast cells, in which, however, TSPO downregulation resulted in more elongated and branched mitochondria [290, 291]. Although in the present study, mitochondrial morphology was not readily affected by loss of TSPO, there is some hint in the literature that TSPO might play a role in morphology regulation. An in-depth analysis of mitochondrial morphology for

TSPO-KD/KO cells might be interesting for future studies employing more sophisticated 3D-fluorescence microscopy and image analysis tools.

Overall, cellular ROS levels were slightly increased in all TSPO-deficient clones compared to the corresponding control cell lines. This outcome aligns with previous expectations, as ROS are predominantly produced during oxidative phosphorylation (OXPHOS) [292], and the basal respiration was only modestly enhanced in TSPO-deficient clones. It is important to note, that this study did not assess ROS levels during maximal respiration. Interestingly, non-mitochondrial oxygen consumption was also slightly elevated in TSPO-deficient clones. This suggests the involvement of other oxygen-consuming processes outside of the mitochondria.

NADPH oxidase (NOX) complexes within the cell membrane are another essential source for endogenous ROS generation. ROS produced by NOX have been recently demonstrated to play a role in glioblastoma malignancy and treatment resistance [293–295]. Furthermore, TSPO has been linked to induce ROS production via NOX [188, 189, 291]. In these studies, TSPO has been shown to increase cytosolic Ca^{2+} levels which activates NOX via calcium-dependent signaling mechanism resulting in ROS production in mouse retinal resident microglia and mouse embryonic fibroblast cells [189, 291]. This mechanism seems counterintuitive, given that TSPO deficiency in BTIC13 appears to elevate ROS levels. However, in line with findings of this study, Fu and colleagues revealed that TSPO KO in GL261 mouse glioma cells also significantly increased ROS levels [208]. TSPO might thus function as part of an antioxidant response pathway, contributing to redox regulation to maintain cellular homeostasis in a context dependent manner [188]. Further experiments are needed to investigate the role of TSPO in redox regulation, for example during acute oxidative stress in TSPO-deficient versus control BTIC13 cells. Additionally, it is important to consider that TSPO regulates cellular ROS and mitochondrial ROS levels via separate mechanisms. Therefore, future experiments should investigate TSPO's role in total versus mitochondrial ROS production.

Interestingly, the OXPHOS inhibitor metformin had stronger effects on the proliferation of TSPO-deficient clones when compared to the respective control clones. This effect was especially apparent at the lower dosage of 1 mM metformin in the TSPO KO clones. This observation aligns with the finding that the TSPO KO clones show elevated levels of basal respiration and thus are potentially more dependent on OXPHOS. However, it is important to mention that metformin is not a selective inhibitor of OXPHOS and other targets such as AMP-activated protein kinases (AMPKs) and the mTOR pathway have been described to inhibit the proliferation of glioblastoma cells [296].

This study reports for the first time that TSPO deficiency increased mitochondrial respiration in primary patient-derived glioblastoma cells. Interestingly, these findings contradict previous

research conducted in other cell culture model systems. For example, in studies involving human and mouse microglia, TSPO deficiency resulted in decreased ATP production, as well as decreased basal and maximal respiration [204–206]. ATP production and mitochondrial respiration was also decreased in the TSPO-deficient mouse glioma GL261 and human GBM1B cells. Concomitant with that, TSPO expression in Jurkat cells with low endogenous TSPO levels increased ATP production and the expression of genes involved in mitochondrial respiration [207]. However, there are also alternative studies showing that TSPO deficiency had no impact on mitochondrial respiration [156, 189, 288, 289].

These differences further highlight the complexity of TSPO's role in mitochondrial function, which might be dependent on species, cell type, and experimental conditions. Furthermore, given the high heterogeneity of glioblastoma, TSPO's impact on respiration might also vary within different subtypes of glioblastoma. For example, it has been shown that BTICs from mesenchymal and proneural origin differ in metabolic phenotypes. While mesenchymal BTICs showed a preference for glycolysis and were less responsive to OXPHOS inhibition by metformin, proneural BTICs metabolized glucose preferentially via the pentose phosphate pathway and showed an elevated susceptibility towards OXPHOS inhibition [220]. Consequently, future research is needed to directly compare the effect of TSPO deficiency on mitochondrial respiration in mesenchymal versus proneural BTICs.

Overall, these findings show that TSPO plays a role in the mitochondrial respiration of BTIC13. However, it could not be validated here that TSPO is a critical regulator for the dynamic balance of OXPHOS and glycolysis as observed by Fu and colleagues [208]. Although the described findings do not allow to draw definitive conclusions about TSPO's potential as a target for altered mitochondrial energy metabolism in glioblastoma to date, the experimental results set a valuable starting point and pave the way for future experiments.

6 Conclusion and future perspectives

Glioblastoma represents the most common type of malignant brain tumors and in view of its highly aggressive and complex character, patients with glioblastoma face a particularly poor prognosis. Regarding this, the research for glioblastoma therapy is driven by the urgent need to advance treatment options to ultimately improve the patient's prognosis and quality of life.

In this pursuit, TSPO has recently emerged as a promising target candidate for potential glioblastoma therapy. The overexpression of TSPO in glioblastoma, in combination with its association with neuroinflammation, already positions it as a compelling non-invasive biomarker for the detection and monitoring of both, glioblastoma tumors and the complex immune microenvironment surrounding it. Besides that, the involvement of TSPO in a variety of cellular processes also implies a functional role of the protein in the malignant hallmarks of glioblastoma.

In consideration of those aspects, the primary objective of the present thesis was to reveal the putative functional relevance of TSPO in glioblastoma and thus to assess its potential as a novel target for glioblastoma therapy. To address this critical research question, a wide methodological array was employed including various molecular techniques as well as cell culture setups, all centered around the primary patient-derived mesenchymal tumor cell line, BTIC13. These methodologies encompassed state-of-the-art genetic loss of function approaches, comprehensive examination of mitochondria-dependent and -independent apoptosis pathways, multilayer examination of pro-inflammatory cytokine effects, and the analysis of mitochondrial respiration.

The intrinsic heterogeneity of glioblastoma is not solely a well-recognized challenge for patients facing therapy resistance and tumor recurrence, but also for experimental analyses as well. For this reason, it is worth noting that it significantly influenced the investigations conducted within this thesis, too. Apart from that, based on the findings presented in this thesis, TSPO has been at least partly identified to be a valuable candidate as a therapeutic target for glioblastoma treatment. Arguments in favor of this assumption include the selective upregulation of TSPO in tumor cells in response to direct contact to T cells, and following exposure to pro-inflammatory cytokines. Together, this positions TSPO as a potential marker for effector T cell activity in glioblastoma. Furthermore, TSPO deficiency significantly impaired cancer cell migration suggesting that further studies investigating the role of TSPO in tumor invasion might be of great importance. Finally, it turned out that TSPO deficiency results in elevated levels of maximal mitochondrial respiration in our model system.

However, it is crucial to acknowledge that other findings within this study rather suggest alternative perspectives. For instance, the TRAIL-induced apoptosis response of cultured cells did

not solely depend on TSPO expression but is rather influenced by a multitude of tumor cell intrinsic mechanisms in monoculture conditions. Nevertheless, when accounting for results of co-culture experiments, it is tempting to suggest that in a more complex setting, in which apoptosis responses rely more on the cumulative effects of apoptosis-inducing and -sensitizing factors, TSPO deficiency could indeed prime tumor cells for T cell-mediated cytotoxicity.

In light of the various facets explored in this study, concrete conclusions regarding TSPO's potential as a therapeutic target still remain elusive to this point. However, it is important to recognize that the results presented here set the groundwork for unravelling a putatively tightly regulated role of TSPO in glioblastoma and serve as a basis for future experiments. The methodology established and refined within this thesis will substantially help to undertake such approaches.

Several critical avenues for further research emerged already by the end of this study. First, it is highly important to expand the BTIC cohort in use including a variety of mesenchymal and proneural BTIC lines. This diversification will help to elucidate how TSPO may function differently across distinct glioblastoma subtypes. Furthermore, more extensive studies are required to comprehensively understand the impact of TSPO on mitochondrial respiration and other metabolic pathways within tumor cells. These insights can provide a deeper understanding of TSPO's role in glioblastoma metabolic biology. Finally, investigating the function of TSPO in a more complex environment, such as sophisticated *in vitro* glioblastoma models (e.g., GLICO), and certainly *in vivo* animal models of glioblastoma, will provide a more accurate representation of the dynamic interactions and mechanisms involved.

These advanced models and other research attempts might help to validate TSPO as a therapeutic target, and if so, it becomes feasible to consider pharmacological TSPO inhibition as part of a combinational immunotherapeutic strategy or metabolic therapy for glioblastoma treatment. A multitude of future efforts will be essential for the ongoing search of new treatments of glioblastoma to finally find successful therapy solutions offering hope to patients facing this challenging disease.

7 Supplementary figures

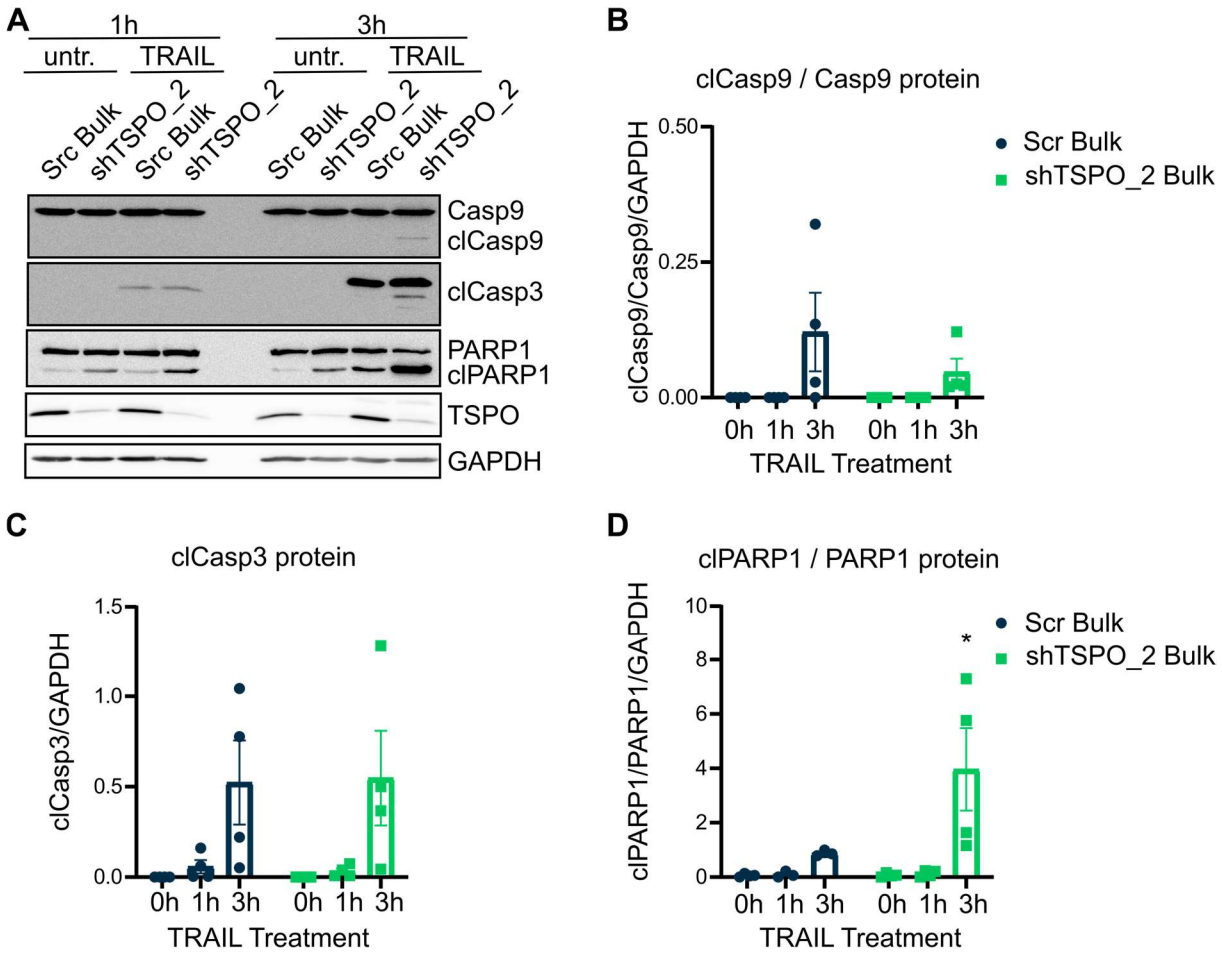

Supplementary figure 1. Impact of TRAIL on caspase activation in TSPO-deficient bulk cells. Western blot analysis of caspase-9 (Casp9), caspase-3 (Casp3) and PARP1 processing in shTSPO_2 Bulk compared to the control Scr Bulk. Cells were treated with TRAIL (50 ng/ml) for 0, 1, and 3 hours. (**A**) Representative Western blot of cleaved and full-length forms of Casp9, Casp3, and PARP1. Equal loading was confirmed by GAPDH expression. (**B-D**) Graphs show the relative protein quantification of three independent experiments. Data are presented as the ratio of cleaved to full-length protein of Casp9 (**B**), Casp3 (**C**) and PARP1 (**D**). Data are normalized to GAPDH expression shown as mean ± SD. P-values were calculated using two-way ANOVA followed by Sidak´s *post hoc* test (*$P \leq 0.05$).

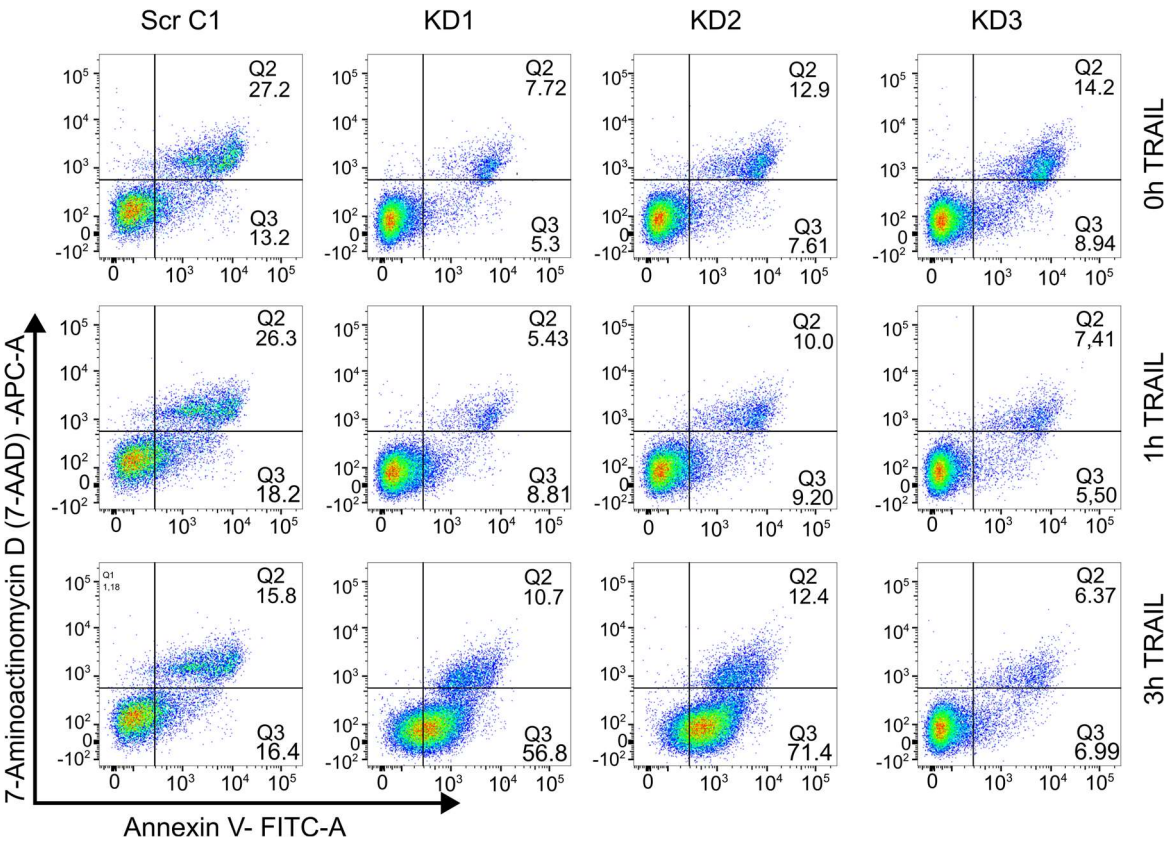

Supplementary figure 2. TRAIL induces cell death in KD1 and KD2. Flow cytometry analysis of TSPO KD clones (KD1, KD2, KD3) and the control clone Scr C1. Cells were treated with 50 ng/ml of TRAIL for 1 and 3 hours and stained with AnxV-FITC-A and 7-AAD-APC-A. Gating strategy to determine the percentage of cells in living (% $AnxV^-$ / $7\text{-}AAD^-$), early apoptotic (% $AnxV^+$ / $7\text{-}AAD^-$), late apoptotic (% $AnxV^+$ / $7\text{-}AAD^+$) and necrotic (% $AnxV^-$ / $7\text{-}AAD^+$) condition. Representative data of three independent experiments with comparable results are shown.

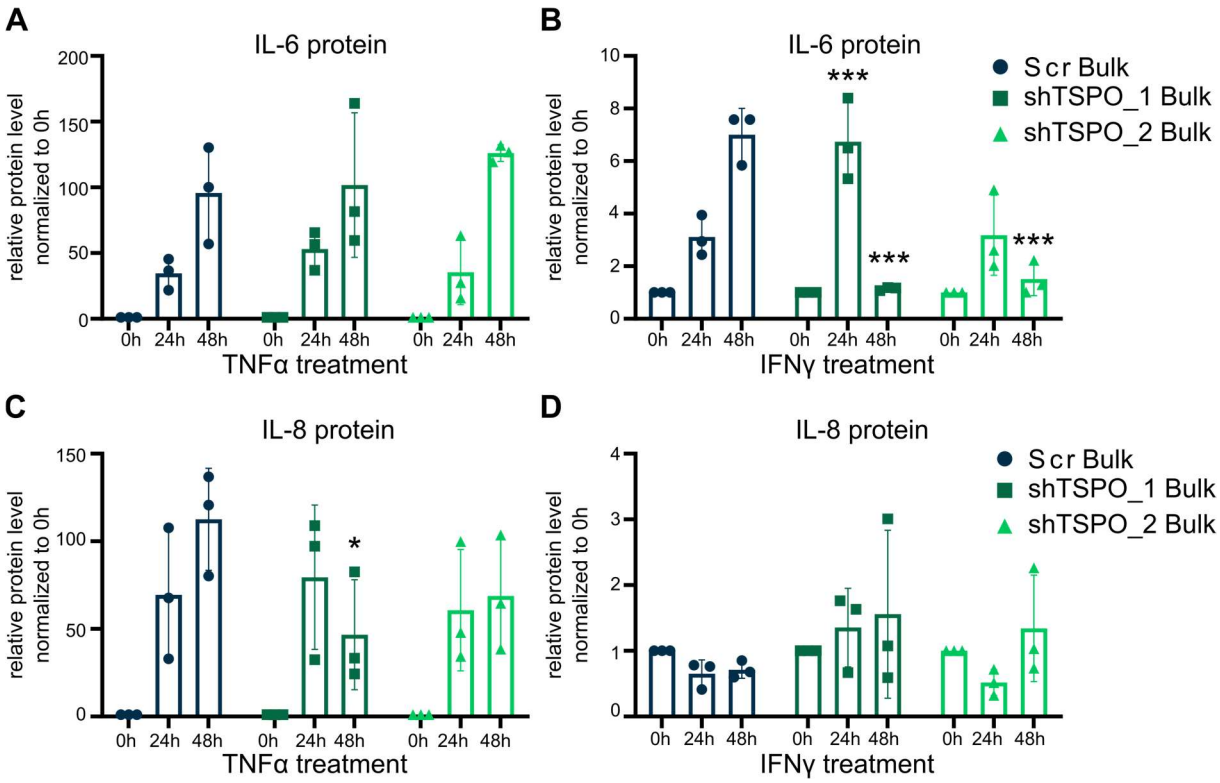

Supplementary figure 3. TNFα- and IFNγ-induced IL-6 and IL-8 protein secretion in BTIC13 KD bulk cells. ELISA analysis of IL-6 and IL-8 protein levels in the supernatant of TSPO KD bulk (shTSPO_1 Bulk and shTSPO_2 Bulk) and control cells Scr Bulk. Cells were stimulated for 24 hours or 48 hours with 50 ng/ml TNFα (**A, C**) or IFNγ (**B, D**). Released IL-6 (**A, B**) and IL-8 (**C, D**) protein levels [pg/ml] were normalized to 10^5 cells and presented as fold change relative to 0 hours of treatment. Cumulative data of three independent experiments are shown as mean ± SD. Asterisks indicate significant differences between KD bulk and the control Scr Bulk. P-values were calculated using two-way ANOVA followed by Dunnett´s *post hoc* test (*P ≤ 0.05; ***P ≤ 0.001).

References

1. Ostrom QT, Price M, Neff C et al. (2022) CBTRUS Statistical Report: Primary Brain and Other Central Nervous System Tumors Diagnosed in the United States in 2015-2019. Neuro Oncol 24:v1-v95. https://doi.org/10.1093/neuonc/noac202
2. Laug D, Glasgow SM, Deneen B (2018) A glial blueprint for gliomagenesis. Nat Rev Neurosci 19:393–403. https://doi.org/10.1038/s41583-018-0014-3
3. Louis DN, Perry A, Reifenberger G et al. (2016) The 2016 World Health Organization Classification of Tumors of the Central Nervous System: a summary. Acta Neuropathol 131:803–820. https://doi.org/10.1007/s00401-016-1545-1
4. Louis DN, Perry A, Wesseling P et al. (2021) The 2021 WHO Classification of Tumors of the Central Nervous System: a summary. Neuro Oncol 23:1231–1251. https://doi.org/10.1093/neuonc/noab106
5. Weller M, van den Bent M, Preusser M et al. (2021) EANO guidelines on the diagnosis and treatment of diffuse gliomas of adulthood. Nat Rev Clin Oncol 18:170–186. https://doi.org/10.1038/s41571-020-00447-z
6. Brat DJ, Aldape K, Colman H et al. (2020) cIMPACT-NOW update 5: recommended grading criteria and terminologies for IDH-mutant astrocytomas. Acta Neuropathol 139:603–608. https://doi.org/10.1007/s00401-020-02127-9
7. Shirahata M, Ono T, Stichel D et al. (2018) Novel, improved grading system(s) for IDH-mutant astrocytic gliomas. Acta Neuropathol 136:153–166. https://doi.org/10.1007/s00401-018-1849-4
8. Brat DJ, Aldape K, Colman H et al. (2018) cIMPACT-NOW update 3: recommended diagnostic criteria for "Diffuse astrocytic glioma, IDH-wildtype, with molecular features of glioblastoma, WHO grade IV". Acta Neuropathol 136:805–810. https://doi.org/10.1007/s00401-018-1913-0
9. Miller KD, Ostrom QT, Kruchko C et al. (2021) Brain and other central nervous system tumor statistics, 2021. CA Cancer J Clin 71:381–406. https://doi.org/10.3322/caac.21693
10. Stupp R, Mason WP, van den Bent MJ et al. (2005) Radiotherapy plus concomitant and adjuvant temozolomide for glioblastoma. N Engl J Med 352:987–996. https://doi.org/10.1056/NEJMoa043330
11. Giladi M, Schneiderman RS, Voloshin T et al. (2015) Mitotic Spindle Disruption by Alternating Electric Fields Leads to Improper Chromosome Segregation and Mitotic Catastrophe in Cancer Cells. Sci Rep 5:18046. https://doi.org/10.1038/srep18046
12. Stupp R, Taillibert S, Kanner A et al. (2017) Effect of Tumor-Treating Fields Plus Maintenance Temozolomide vs Maintenance Temozolomide Alone on Survival in Patients With Glioblastoma: A Randomized Clinical Trial. JAMA 318:2306–2316. https://doi.org/10.1001/jama.2017.18718
13. Herrlinger U, Tzaridis T, Mack F et al. (2019) Lomustine-temozolomide combination therapy versus standard temozolomide therapy in patients with newly diagnosed glioblastoma with methylated MGMT promoter (CeTeG/NOA-09): a randomised, open-label, phase 3 trial. Lancet 393:678–688. https://doi.org/10.1016/S0140-6736(18)31791-4
14. Lassman A, Pugh S, Wang T et al. (2019) ACTR-21. A RANDOMIZED, DOUBLE-BLIND, PLACEBO-CONTROLLED PHASE 3 TRIAL OF DEPATUXIZUMAB MAFODOTIN (ABT-414) IN EPIDERMAL GROWTH FACTOR RECEPTOR (EGFR) AMPLIFIED (AMP) NEWLY DIAGNOSED GLIOBLASTOMA (nGBM). Neuro Oncol 21:vi17-vi17. https://doi.org/10.1093/neuonc/noz175.064
15. Sharma M, Schilero C, Peereboom DM et al. (2019) Phase II study of Dovitinib in recurrent glioblastoma. J Neurooncol 144:359–368. https://doi.org/10.1007/s11060-019-03236-6
16. Reardon DA, Brandes AA, Omuro A et al. (2020) Effect of Nivolumab vs Bevacizumab in Patients With Recurrent Glioblastoma: The CheckMate 143 Phase 3 Randomized Clinical Trial. JAMA Oncol 6:1003–1010. https://doi.org/10.1001/jamaoncol.2020.1024

17. Weller M, Butowski N, Tran DD et al. (2017) Rindopepimut with temozolomide for patients with newly diagnosed, EGFRvIII-expressing glioblastoma (ACT IV): a randomised, double-blind, international phase 3 trial. Lancet Oncol 18:1373–1385. https://doi.org/10.1016/S1470-2045(17)30517-X
18. O'Rourke DM, Nasrallah MP, Desai A et al. (2017) A single dose of peripherally infused EGFRvIII-directed CAR T cells mediates antigen loss and induces adaptive resistance in patients with recurrent glioblastoma. Sci Transl Med 9. https://doi.org/10.1126/scitranslmed.aaa0984
19. Roth P, Mason WP, Richardson PG et al. (2020) Proteasome inhibition for the treatment of glioblastoma. Expert Opin Investig Drugs 29:1133–1141. https://doi.org/10.1080/13543784.2020.1803827
20. Wen PY, Touat M, Alexander BM et al. (2019) Buparlisib in Patients With Recurrent Glioblastoma Harboring Phosphatidylinositol 3-Kinase Pathway Activation: An Open-Label, Multicenter, Multi-Arm, Phase II Trial. J Clin Oncol 37:741–750. https://doi.org/10.1200/JCO.18.01207
21. Wick W, Gorlia T, Bady P et al. (2016) Phase II Study of Radiotherapy and Temsirolimus versus Radiochemotherapy with Temozolomide in Patients with Newly Diagnosed Glioblastoma without MGMT Promoter Hypermethylation (EORTC 26082). Clin Cancer Res 22:4797–4806. https://doi.org/10.1158/1078-0432.CCR-15-3153
22. Segura-Collar B, Hiller-Vallina S, Dios O de et al. (2023) Advanced immunotherapies for glioblastoma: tumor neoantigen vaccines in combination with immunomodulators. Acta Neuropathologica Communications 11:79. https://doi.org/10.1186/s40478-023-01569-y
23. Yang K, Wu Z, Zhang H et al. (2022) Glioma targeted therapy: insight into future of molecular approaches. Molecular Cancer 21:39. https://doi.org/10.1186/s12943-022-01513-z
24. Eisenbarth D, Wang YA (2023) Glioblastoma heterogeneity at single cell resolution. Oncogene:1–11. https://doi.org/10.1038/s41388-023-02738-y
25. Ohgaki H, Dessen P, Jourde B et al. (2004) Genetic pathways to glioblastoma: a population-based study. Cancer Res 64:6892–6899. https://doi.org/10.1158/0008-5472.CAN-04-1337
26. Nobusawa S, Watanabe T, Kleihues P et al. (2009) IDH1 mutations as molecular signature and predictive factor of secondary glioblastomas. Clin Cancer Res 15:6002–6007. https://doi.org/10.1158/1078-0432.CCR-09-0715
27. The Cancer Genome Atlas Research Network (2008) Comprehensive genomic characterization defines human glioblastoma genes and core pathways. Nature 455:1061–1068. https://doi.org/10.1038/nature07385
28. van Meir EG, Hadjipanayis CG, Norden AD et al. (2010) Exciting new advances in neuro-oncology: the avenue to a cure for malignant glioma. CA Cancer J Clin 60:166–193. https://doi.org/10.3322/caac.20069
29. Phillips HS, Kharbanda S, Chen R et al. (2006) Molecular subclasses of high-grade glioma predict prognosis, delineate a pattern of disease progression, and resemble stages in neurogenesis. Cancer Cell 9:157–173. https://doi.org/10.1016/j.ccr.2006.02.019
30. Verhaak RGW, Hoadley KA, Purdom E et al. (2010) Integrated genomic analysis identifies clinically relevant subtypes of glioblastoma characterized by abnormalities in PDGFRA, IDH1, EGFR, and NF1. Cancer Cell 17:98–110. https://doi.org/10.1016/j.ccr.2009.12.020
31. Wang Q, Hu B, Hu X et al. (2017) Tumor Evolution of Glioma-Intrinsic Gene Expression Subtypes Associates with Immunological Changes in the Microenvironment. Cancer Cell 32:42-56.e6. https://doi.org/10.1016/j.ccell.2017.06.003
32. Hernández Martínez A, Madurga R, García-Romero N et al. (2022) Unravelling glioblastoma heterogeneity by means of single-cell RNA sequencing. Cancer Letters 527:66–79. https://doi.org/10.1016/j.canlet.2021.12.008
33. Patel AP, Tirosh I, Trombetta JJ et al. (2014) Single-cell RNA-seq highlights intratumoral heterogeneity in primary glioblastoma. Science 344:1396–1401. https://doi.org/10.1126/science.1254257

34. Yu K, Hu Y, Wu F et al. (2020) Surveying brain tumor heterogeneity by single-cell RNA-sequencing of multi-sector biopsies. Natl Sci Rev 7:1306–1318. https://doi.org/10.1093/nsr/nwaa099
35. Neftel C, Laffy J, Filbin MG et al. (2019) An Integrative Model of Cellular States, Plasticity, and Genetics for Glioblastoma. Cell 178:835-849.e21. https://doi.org/10.1016/j.cell.2019.06.024
36. Wang J, Cazzato E, Ladewig E et al. (2016) Clonal evolution of glioblastoma under therapy. Nat Genet 48:768–776. https://doi.org/10.1038/ng.3590
37. Ravi VM, Will P, Kueckelhaus J et al. (2021) Spatiotemporal heterogeneity of glioblastoma is dictated by microenvironmental interference. https://doi.org/10.1101/2021.02.16.431475
38. Heiland DH, Gaebelein A, Börries M et al. (2018) Microenvironment-Derived Regulation of HIF Signaling Drives Transcriptional Heterogeneity in Glioblastoma Multiforme. Mol Cancer Res 16:655–668. https://doi.org/10.1158/1541-7786.MCR-17-0680
39. Garofano L, Migliozzi S, Oh YT et al. (2021) Pathway-based classification of glioblastoma uncovers a mitochondrial subtype with therapeutic vulnerabilities. Nat Cancer 2:141–156. https://doi.org/10.1038/s43018-020-00159-4
40. Chen AX, Gartrell RD, Zhao J et al. (2021) Single-cell characterization of macrophages in glioblastoma reveals MARCO as a mesenchymal pro-tumor marker. Genome Med 13:88. https://doi.org/10.1186/s13073-021-00906-x
41. Zhao J, Chen AX, Gartrell RD et al. (2019) Immune and genomic correlates of response to anti-PD-1 immunotherapy in glioblastoma. Nat Med 25:462–469. https://doi.org/10.1038/s41591-019-0349-y
42. Abdelfattah N, Kumar P, Wang C et al. (2022) Single-cell analysis of human glioma and immune cells identifies S100A4 as an immunotherapy target. Nat Commun 13:767. https://doi.org/10.1038/s41467-022-28372-y
43. Martinez-Lage M, Lynch TM, Bi Y et al. (2019) Immune landscapes associated with different glioblastoma molecular subtypes. Acta Neuropathologica Communications 7:203. https://doi.org/10.1186/s40478-019-0803-6
44. Doucette T, Rao G, Rao A et al. (2013) Immune heterogeneity of glioblastoma subtypes: extrapolation from the cancer genome atlas. Cancer Immunol Res 1:112–122. https://doi.org/10.1158/2326-6066.CIR-13-0028
45. Darmanis S, Sloan SA, Croote D et al. (2017) Single-Cell RNA-Seq Analysis of Infiltrating Neoplastic Cells at the Migrating Front of Human Glioblastoma. Cell Reports 21:1399–1410. https://doi.org/10.1016/j.celrep.2017.10.030
46. White K, Connor K, Meylan M et al. (2023) Identification, validation and biological characterisation of novel glioblastoma tumour microenvironment subtypes: implications for precision immunotherapy. Annals of Oncology 34:300–314. https://doi.org/10.1016/j.annonc.2022.11.008
47. Quail DF, Joyce JA (2017) The Microenvironmental Landscape of Brain Tumors. Cancer Cell 31:326–341. https://doi.org/10.1016/j.ccell.2017.02.009
48. Berghoff AS, Kiesel B, Widhalm G et al. (2015) Programmed death ligand 1 expression and tumor-infiltrating lymphocytes in glioblastoma. Neuro Oncol 17:1064–1075. https://doi.org/10.1093/neuonc/nou307
49. Ishida Y, Agata Y, Shibahara K et al. (1992) Induced expression of PD-1, a novel member of the immunoglobulin gene superfamily, upon programmed cell death. EMBO J 11:3887–3895. https://doi.org/10.1002/j.1460-2075.1992.tb05481.x
50. Sun C, Mezzadra R, Schumacher TN (2018) Regulation and Function of the PD-L1 Checkpoint. Immunity 48:434–452. https://doi.org/10.1016/j.immuni.2018.03.014
51. Yeung JT, Hamilton RL, Ohnishi K et al. (2013) LOH in the HLA class I region at 6p21 is associated with shorter survival in newly diagnosed adult glioblastoma. Clin Cancer Res 19:1816–1826. https://doi.org/10.1158/1078-0432.CCR-12-2861

52. Chang N, Ahn SH, Kong D-S et al. (2017) The role of STAT3 in glioblastoma progression through dual influences on tumor cells and the immune microenvironment. Mol Cell Endocrinol 451:53–65. https://doi.org/10.1016/j.mce.2017.01.004
53. Zhai L, Bell A, Ladomersky E et al. (2021) Tumor Cell IDO Enhances Immune Suppression and Decreases Survival Independent of Tryptophan Metabolism in Glioblastoma. Clin Cancer Res 27:6514–6528. https://doi.org/10.1158/1078-0432.CCR-21-1392
54. Wainwright DA, Balyasnikova IV, Chang AL et al. (2012) IDO expression in brain tumors increases the recruitment of regulatory T cells and negatively impacts survival. Clin Cancer Res 18:6110–6121. https://doi.org/10.1158/1078-0432.CCR-12-2130
55. Lazarova M, Steinle A (2019) Impairment of NKG2D-Mediated Tumor Immunity by TGF-β. Front Immunol 10:2689. https://doi.org/10.3389/fimmu.2019.02689
56. Albulescu R, Codrici E, Popescu ID et al. (2013) Cytokine patterns in brain tumour progression. Mediators Inflamm 2013:979748. https://doi.org/10.1155/2013/979748
57. Thorsson V, Gibbs DL, Brown SD et al. (2018) The Immune Landscape of Cancer. Immunity 48:812-830.e14. https://doi.org/10.1016/j.immuni.2018.03.023
58. Khan F, Pang L, Dunterman M et al. (2023) Macrophages and microglia in glioblastoma: heterogeneity, plasticity, and therapy. J Clin Invest 133. https://doi.org/10.1172/JCI163446
59. Charles NA, Holland EC, Gilbertson R et al. (2012) The brain tumor microenvironment. Glia 60:502–514. https://doi.org/10.1002/glia.21264
60. Coniglio SJ, Eugenin E, Dobrenis K et al. (2012) Microglial stimulation of glioblastoma invasion involves epidermal growth factor receptor (EGFR) and colony stimulating factor 1 receptor (CSF-1R) signaling. Mol Med 18:519–527. https://doi.org/10.2119/molmed.2011.00217
61. Komohara Y, Ohnishi K, Kuratsu J et al. (2008) Possible involvement of the M2 anti-inflammatory macrophage phenotype in growth of human gliomas. J Pathol 216:15–24. https://doi.org/10.1002/path.2370
62. Dumas AA, Pomella N, Rosser G et al. (2020) Microglia promote glioblastoma via mTOR-mediated immunosuppression of the tumour microenvironment. EMBO J 39:e103790. https://doi.org/10.15252/embj.2019103790
63. Peng P, Zhu H, Liu D et al. (2022) TGFBI secreted by tumor-associated macrophages promotes glioblastoma stem cell-driven tumor growth via integrin αvβ5-Src-Stat3 signaling. Theranostics 12:4221–4236. https://doi.org/10.7150/thno.69605
64. Shi Y, Ping Y-F, Zhou W et al. (2017) Tumour-associated macrophages secrete pleiotrophin to promote PTPRZ1 signalling in glioblastoma stem cells for tumour growth. Nat Commun 8:15080. https://doi.org/10.1038/ncomms15080
65. Takenaka MC, Gabriely G, Rothhammer V et al. (2019) Control of tumor-associated macrophages and T cells in glioblastoma via AHR and CD39. Nat Neurosci 22:729–740. https://doi.org/10.1038/s41593-019-0370-y
66. Kolabas ZI, Kuemmerle LB, Perneczky R et al. (2023) Distinct molecular profiles of skull bone marrow in health and neurological disorders. Cell 186:3706-3725.e29. https://doi.org/10.1016/j.cell.2023.07.009
67. Dubinski D, Wölfer J, Hasselblatt M et al. (2016) CD4+ T effector memory cell dysfunction is associated with the accumulation of granulocytic myeloid-derived suppressor cells in glioblastoma patients. Neuro Oncol 18:807–818. https://doi.org/10.1093/neuonc/nov280
68. Kamran N, Kadiyala P, Saxena M et al. (2017) Immunosuppressive Myeloid Cells' Blockade in the Glioma Microenvironment Enhances the Efficacy of Immune-Stimulatory Gene Therapy. Mol Ther 25:232–248. https://doi.org/10.1016/j.ymthe.2016.10.003

69. Jia W, Jackson-Cook C, Graf MR (2010) Tumor-infiltrating, myeloid-derived suppressor cells inhibit T cell activity by nitric oxide production in an intracranial rat glioma + vaccination model. J Neuroimmunol 223:20–30. https://doi.org/10.1016/j.jneuroim.2010.03.011
70. Ravi VM, Neidert N, Will P et al. (2022) T-cell dysfunction in the glioblastoma microenvironment is mediated by myeloid cells releasing interleukin-10. Nat Commun 13:925. https://doi.org/10.1038/s41467-022-28523-1
71. Jacobs JFM, Idema AJ, Bol KF et al. (2009) Regulatory T cells and the PD-L1/PD-1 pathway mediate immune suppression in malignant human brain tumors. Neuro Oncol 11:394–402. https://doi.org/10.1215/15228517-2008-104
72. See AP, Parker JJ, Waziri A (2015) The role of regulatory T cells and microglia in glioblastoma-associated immunosuppression. J Neurooncol 123:405–412. https://doi.org/10.1007/s11060-015-1849-3
73. Woroniecka K, Chongsathidkiet P, Rhodin K et al. (2018) T-Cell Exhaustion Signatures Vary with Tumor Type and Are Severe in Glioblastoma. Clin Cancer Res 24:4175–4186. https://doi.org/10.1158/1078-0432.CCR-17-1846
74. Miller BC, Sen DR, Al Abosy R et al. (2019) Subsets of exhausted CD8+ T cells differentially mediate tumor control and respond to checkpoint blockade. Nat Immunol 20:326–336. https://doi.org/10.1038/s41590-019-0312-6
75. Watowich MB, Gilbert MR, Larion M (2023) T cell exhaustion in malignant gliomas. Trends in Cancer 9:270–292. https://doi.org/10.1016/j.trecan.2022.12.008
76. Zheng G, Guo Z, Li W et al. (2021) Interaction between HLA-G and NK cell receptor KIR2DL4 orchestrates HER2-positive breast cancer resistance to trastuzumab. Signal Transduct Target Ther 6:236. https://doi.org/10.1038/s41392-021-00629-w
77. Wan R, Wang Z-W, Li H et al. (2017) Human Leukocyte Antigen-G Inhibits the Anti-Tumor Effect of Natural Killer Cells via Immunoglobulin-Like Transcript 2 in Gastric Cancer. Cell Physiol Biochem 44:1828–1841. https://doi.org/10.1159/000485819
78. Romani M, Pistillo MP, Carosio R et al. (2018) Immune Checkpoints and Innovative Therapies in Glioblastoma. Front Oncol 8:464. https://doi.org/10.3389/fonc.2018.00464
79. Omuro A, Brandes AA, Carpentier AF et al. (2023) Radiotherapy combined with nivolumab or temozolomide for newly diagnosed glioblastoma with unmethylated MGMT promoter: An international randomized phase III trial. Neuro Oncol 25:123–134. https://doi.org/10.1093/neuonc/noac099
80. Lim M, Weller M, Idbaih A et al. (2022) Phase III trial of chemoradiotherapy with temozolomide plus nivolumab or placebo for newly diagnosed glioblastoma with methylated MGMT promoter. Neuro Oncol 24:1935–1949. https://doi.org/10.1093/neuonc/noac116
81. Chen Q, Kang J, Fu C (2018) The independence of and associations among apoptosis, autophagy, and necrosis. Signal Transduct Target Ther 3:18. https://doi.org/10.1038/s41392-018-0018-5
82. Wan S, Zhang G, Liu R et al. (2023) Pyroptosis, ferroptosis, and autophagy cross-talk in glioblastoma opens up new avenues for glioblastoma treatment. Cell Commun Signal 21:115. https://doi.org/10.1186/s12964-023-01108-1
83. Zhang L, Wang H, Ding K et al. (2015) FTY720 induces autophagy-related apoptosis and necroptosis in human glioblastoma cells. Toxicol Lett 236:43–59. https://doi.org/10.1016/j.toxlet.2015.04.015
84. Carneiro BA, El-Deiry WS (2020) Targeting apoptosis in cancer therapy. Nat Rev Clin Oncol 17:395–417. https://doi.org/10.1038/s41571-020-0341-y
85. Hanahan D, Weinberg RA (2000) The hallmarks of cancer. Cell 100:57–70. https://doi.org/10.1016/s0092-8674(00)81683-9
86. Kägi D, Vignaux F, Ledermann B et al. (1994) Fas and perforin pathways as major mechanisms of T cell-mediated cytotoxicity. Science 265:528–530. https://doi.org/10.1126/science.7518614

87. Martínez-Lostao L, Anel A, Pardo J (2015) How Do Cytotoxic Lymphocytes Kill Cancer Cells? Clin Cancer Res 21:5047–5056. https://doi.org/10.1158/1078-0432.CCR-15-0685
88. Gon S, Gatanaga T, Sendo F (1996) Involvement of two types of TNF receptor in TNF-alpha induced neutrophil apoptosis. Microbiol Immunol 40:463–465. https://doi.org/10.1111/j.1348-0421.1996.tb01095.x
89. Pan G, O'Rourke K, Chinnaiyan AM et al. (1997) The receptor for the cytotoxic ligand TRAIL. Science 276:111–113. https://doi.org/10.1126/science.276.5309.111
90. Schneider P, Bodmer JL, Holler N et al. (1997) Characterization of Fas (Apo-1, CD95)-Fas ligand interaction. The Journal of Biological Chemistry 272:18827–18833. https://doi.org/10.1074/jbc.272.30.18827
91. Kischkel FC, Hellbardt S, Behrmann I et al. (1995) Cytotoxicity-dependent APO-1 (Fas/CD95)-associated proteins form a death-inducing signaling complex (DISC) with the receptor. EMBO J 14:5579–5588. https://doi.org/10.1002/j.1460-2075.1995.tb00245.x
92. Sprick MR, Weigand MA, Rieser E et al. (2000) FADD/MORT1 and caspase-8 are recruited to TRAIL receptors 1 and 2 and are essential for apoptosis mediated by TRAIL receptor 2. Immunity 12:599–609. https://doi.org/10.1016/s1074-7613(00)80211-3
93. Sprick MR, Rieser E, Stahl H et al. (2002) Caspase-10 is recruited to and activated at the native TRAIL and CD95 death-inducing signalling complexes in a FADD-dependent manner but can not functionally substitute caspase-8. EMBO J 21:4520–4530. https://doi.org/10.1093/emboj/cdf441
94. Oberst A, Pop C, Tremblay AG et al. (2010) Inducible dimerization and inducible cleavage reveal a requirement for both processes in caspase-8 activation. Journal of Biological Chemistry 285:16632–16642. https://doi.org/10.1074/jbc.M109.095083
95. Krueger A, Schmitz I, Baumann S et al. (2001) Cellular FLICE-inhibitory protein splice variants inhibit different steps of caspase-8 activation at the CD95 death-inducing signaling complex. The Journal of Biological Chemistry 276:20633–20640. https://doi.org/10.1074/jbc.M101780200
96. Kale J, Osterlund EJ, Andrews DW (2018) BCL-2 family proteins: changing partners in the dance towards death. Cell Death Differ 25:65–80. https://doi.org/10.1038/cdd.2017.186
97. Kim H, Tu H-C, Ren D et al. (2009) Stepwise activation of BAX and BAK by tBID, BIM, and PUMA initiates mitochondrial apoptosis. Mol Cell 36:487–499. https://doi.org/10.1016/j.molcel.2009.09.030
98. Kuwana T, Mackey MR, Perkins G et al. (2002) Bid, Bax, and lipids cooperate to form supramolecular openings in the outer mitochondrial membrane. Cell 111:331–342. https://doi.org/10.1016/s0092-8674(02)01036-x
99. Yang E, Zha J, Jockel J et al. (1995) Bad, a heterodimeric partner for Bcl-XL and Bcl-2, displaces Bax and promotes cell death. Cell 80:285–291. https://doi.org/10.1016/0092-8674(95)90411-5
100. Li P, Nijhawan D, Budihardjo I et al. (1997) Cytochrome c and dATP-dependent formation of Apaf-1/caspase-9 complex initiates an apoptotic protease cascade. Cell 91:479–489. https://doi.org/10.1016/s0092-8674(00)80434-1
101. Huang K, Zhang J, O'Neill KL et al. (2016) Cleavage by Caspase 8 and Mitochondrial Membrane Association Activate the BH3-only Protein Bid during TRAIL-induced Apoptosis. Journal of Biological Chemistry 291:11843–11851. https://doi.org/10.1074/jbc.M115.711051
102. Green DR (2022) Caspases and Their Substrates. Cold Spring Harb Perspect Biol 14. https://doi.org/10.1101/cshperspect.a041012
103. Ziegler U, Groscurth P (2004) Morphological features of cell death. News Physiol Sci 19:124–128. https://doi.org/10.1152/nips.01519.2004
104. Pitti RM, Marsters SA, Ruppert S et al. (1996) Induction of apoptosis by Apo-2 ligand, a new member of the tumor necrosis factor cytokine family. The Journal of Biological Chemistry 271:12687–12690. https://doi.org/10.1074/jbc.271.22.12687

105. Walczak H, Miller RE, Ariail K et al. (1999) Tumoricidal activity of tumor necrosis factor-related apoptosis-inducing ligand in vivo. Nat Med 5:157–163. https://doi.org/10.1038/5517
106. Mariani SM, Krammer PH (1998) Differential regulation of TRAIL and CD95 ligand in transformed cells of the T and B lymphocyte lineage. Eur J Immunol 28:973–982. https://doi.org/10.1002/(SICI)1521-4141(199803)28:03<973:AID-IMMU973>3.0.CO;2-T
107. Karstedt S von, Montinaro A, Walczak H (2017) Exploring the TRAILs less travelled: TRAIL in cancer biology and therapy. Nat Rev Cancer 17:352–366. https://doi.org/10.1038/nrc.2017.28
108. Wajant H, Moosmayer D, Wüest T et al. (2001) Differential activation of TRAIL-R1 and -2 by soluble and membrane TRAIL allows selective surface antigen-directed activation of TRAIL-R2 by a soluble TRAIL derivative. Oncogene 20:4101–4106. https://doi.org/10.1038/sj.onc.1204558
109. Kuijlen JMA, Mooij JJA, Platteel I et al. (2006) TRAIL-receptor expression is an independent prognostic factor for survival in patients with a primary glioblastoma multiforme. J Neurooncol 78:161–171. https://doi.org/10.1007/s11060-005-9081-1
110. Li Y-C, Tzeng C-C, Song JH et al. (2006) Genomic alterations in human malignant glioma cells associate with the cell resistance to the combination treatment with tumor necrosis factor-related apoptosis-inducing ligand and chemotherapy. Clin Cancer Res 12:2716–2729. https://doi.org/10.1158/1078-0432.CCR-05-1980
111. Schneider P, Thome M, Burns K et al. (1997) TRAIL receptors 1 (DR4) and 2 (DR5) signal FADD-dependent apoptosis and activate NF-kappaB. Immunity 7:831–836. https://doi.org/10.1016/s1074-7613(00)80401-x
112. Degli-Esposti MA, Dougall WC, Smolak PJ et al. (1997) The novel receptor TRAIL-R4 induces NF-kappaB and protects against TRAIL-mediated apoptosis, yet retains an incomplete death domain. Immunity 7:813–820. https://doi.org/10.1016/s1074-7613(00)80399-4
113. Secchiero P, Gonelli A, Carnevale E et al. (2003) TRAIL promotes the survival and proliferation of primary human vascular endothelial cells by activating the Akt and ERK pathways. Circulation 107:2250–2256. https://doi.org/10.1161/01.CIR.0000062702.60708.C4
114. Tran SE, Holmstrom TH, Ahonen M et al. (2001) MAPK/ERK overrides the apoptotic signaling from Fas, TNF, and TRAIL receptors. The Journal of Biological Chemistry 276:16484–16490. https://doi.org/10.1074/jbc.M010384200
115. Söderström TS, Poukkula M, Holmström TH et al. (2002) Mitogen-activated protein kinase/extracellular signal-regulated kinase signaling in activated T cells abrogates TRAIL-induced apoptosis upstream of the mitochondrial amplification loop and caspase-8. J Immunol 169:2851–2860. https://doi.org/10.4049/jimmunol.169.6.2851
116. Eramo A, Pallini R, Lotti F et al. (2005) Inhibition of DNA methylation sensitizes glioblastoma for tumor necrosis factor-related apoptosis-inducing ligand-mediated destruction. Cancer Res 65:11469–11477. https://doi.org/10.1158/0008-5472.CAN-05-1724
117. Skiriute D, Vaitkiene P, Saferis V et al. (2012) MGMT, GATA6, CD81, DR4, and CASP8 gene promoter methylation in glioblastoma. BMC Cancer 12:218. https://doi.org/10.1186/1471-2407-12-218
118. Qi L, Bellail AC, Rossi MR et al. (2011) Heterogeneity of primary glioblastoma cells in the expression of caspase-8 and the response to TRAIL-induced apoptosis. Apoptosis 16:1150–1164. https://doi.org/10.1007/s10495-011-0645-6
119. Fianco G, Cenci C, Barilà D (2016) Caspase-8 expression and its Src-dependent phosphorylation on Tyr380 promote cancer cell neoplastic transformation and resistance to anoikis. Exp Cell Res 347:114–122. https://doi.org/10.1016/j.yexcr.2016.07.013
120. Contadini C, Ferri A, Di Martile M et al. (2023) Caspase-8 as a novel mediator linking Src kinase signaling to enhanced glioblastoma malignancy. Cell Death Differ 30:417–428. https://doi.org/10.1038/s41418-022-01093-x

121. Fianco G, Mongiardi MP, Levi A et al. (2017) Caspase-8 contributes to angiogenesis and chemotherapy resistance in glioblastoma. Elife 6. https://doi.org/10.7554/eLife.22593
122. Panner A, James CD, Berger MS et al. (2005) mTOR controls FLIPS translation and TRAIL sensitivity in glioblastoma multiforme cells. Mol Cell Biol 25:8809–8823. https://doi.org/10.1128/MCB.25.20.8809-8823.2005
123. Koessinger AL, Cloix C, Koessinger D et al. (2022) Increased apoptotic sensitivity of glioblastoma enables therapeutic targeting by BH3-mimetics. Cell Death Differ 29:2089–2104. https://doi.org/10.1038/s41418-022-01001-3
124. Qiu B, Wang Y, Tao J et al. (2012) Expression and correlation of Bcl-2 with pathological grades in human glioma stem cells. Oncol Rep 28:155–160. https://doi.org/10.3892/or.2012.1800
125. Fels C, Schäfer C, Hüppe B et al. (2000) Bcl-2 expression in higher-grade human glioma: a clinical and experimental study. J Neurooncol 48:207–216. https://doi.org/10.1023/a:1006484801654
126. Deshmukh R, Allega MF, Tardito S (2021) A map of the altered glioma metabolism. Trends Mol Med 27:1045–1059. https://doi.org/10.1016/j.molmed.2021.07.011
127. Bernhard C, Reita D, Martin S et al. (2023) Glioblastoma Metabolism: Insights and Therapeutic Strategies. Int J Mol Sci 24. https://doi.org/10.3390/ijms24119137
128. Hoxhaj G, Manning BD (2020) The PI3K-AKT network at the interface of oncogenic signalling and cancer metabolism. Nat Rev Cancer 20:74–88. https://doi.org/10.1038/s41568-019-0216-7
129. Dong Y, Tu R, Liu H et al. (2020) Regulation of cancer cell metabolism: oncogenic MYC in the driver's seat. Signal Transduct Target Ther 5:124. https://doi.org/10.1038/s41392-020-00235-2
130. Lacroix M, Riscal R, Arena G et al. (2020) Metabolic functions of the tumor suppressor p53: Implications in normal physiology, metabolic disorders, and cancer. Mol Metab 33:2–22. https://doi.org/10.1016/j.molmet.2019.10.002
131. Markl J, Sadava D, Hillis DM et al. (2019) Stoffwechselwege zur Gewinnung chemischer Energie. In: Sadava D, Hillis DM, Heller HC et al. (eds) PURVES BIOLOGIE. SPRINGER SPEKTRUM, [S.l.], pp 245–274
132. Warburg O, Minami S (1923) Versuche an Überlebendem Carcinom-gewebe. Klin Wochenschr 2:776–777. https://doi.org/10.1007/BF01712130
133. Lunt SY, Vander Heiden MG (2011) Aerobic glycolysis: meeting the metabolic requirements of cell proliferation. Annu Rev Cell Dev Biol 27:441–464. https://doi.org/10.1146/annurev-cellbio-092910-154237
134. Wang Z, Dai Z, Zhang H et al. (2023) Tumor-secreted lactate contributes to an immunosuppressive microenvironment and affects CD8 T-cell infiltration in glioblastoma. Front Immunol 14:894853. https://doi.org/10.3389/fimmu.2023.894853
135. Watson MJ, Vignali PDA, Mullett SJ et al. (2021) Metabolic support of tumour-infiltrating regulatory T cells by lactic acid. Nature 591:645–651. https://doi.org/10.1038/s41586-020-03045-2
136. Comito G, Iscaro A, Bacci M et al. (2019) Lactate modulates CD4+ T-cell polarization and induces an immunosuppressive environment, which sustains prostate carcinoma progression via TLR8/miR21 axis. Oncogene 38:3681–3695. https://doi.org/10.1038/s41388-019-0688-7
137. DeBerardinis RJ, Chandel NS (2020) We need to talk about the Warburg effect. Nat Metab 2:127–129. https://doi.org/10.1038/s42255-020-0172-2
138. Vlashi E, Lagadec C, Vergnes L et al. (2011) Metabolic state of glioma stem cells and nontumorigenic cells. Proc Natl Acad Sci U S A 108:16062–16067. https://doi.org/10.1073/pnas.1106704108
139. Marin-Valencia I, Yang C, Mashimo T et al. (2012) Analysis of Tumor Metabolism Reveals Mitochondrial Glucose Oxidation in Genetically Diverse Human Glioblastomas in the Mouse Brain In Vivo. Cell Metabolism 16:686. https://doi.org/10.1016/j.cmet.2012.10.010

140. Cheung EC, Vousden KH (2022) The role of ROS in tumour development and progression. Nat Rev Cancer 22:280–297. https://doi.org/10.1038/s41568-021-00435-0
141. Oppermann H, Ding Y, Sharma J et al. (2016) Metabolic response of glioblastoma cells associated with glucose withdrawal and pyruvate substitution as revealed by GC-MS. Nutr Metab (Lond) 13:70. https://doi.org/10.1186/s12986-016-0131-9
142. Oizel K, Chauvin C, Oliver L et al. (2017) Efficient Mitochondrial Glutamine Targeting Prevails Over Glioblastoma Metabolic Plasticity. Clin Cancer Res 23:6292–6304. https://doi.org/10.1158/1078-0432.CCR-16-3102
143. Braestrup C, Albrechtsen R, Squires RF (1977) High densities of benzodiazepine receptors in human cortical areas. Nature 269:702–704. https://doi.org/10.1038/269702a0
144. Papadopoulos V, Baraldi M, Guilarte TR et al. (2006) Translocator protein (18kDa): new nomenclature for the peripheral-type benzodiazepine receptor based on its structure and molecular function. Trends Pharmacol Sci 27:402–409. https://doi.org/10.1016/j.tips.2006.06.005
145. Fan J, Lindemann P, Feuilloley MGJ et al. (2012) Structural and functional evolution of the translocator protein (18 kDa). Curr Mol Med 12:369–386. https://doi.org/10.2174/1566524011207040369
146. Papadopoulos V, Amri H, Boujrad N et al. (1997) Peripheral benzodiazepine receptor in cholesterol transport and steroidogenesis. Steroids 62:21–28. https://doi.org/10.1016/s0039-128x(96)00154-7
147. Fan J, Campioli E, Midzak A et al. (2015) Conditional steroidogenic cell-targeted deletion of TSPO unveils a crucial role in viability and hormone-dependent steroid formation. Proc Natl Acad Sci U S A 112:7261–7266. https://doi.org/10.1073/pnas.1502670112
148. Mukhin AG, Papadopoulos V, Costa E et al. (1989) Mitochondrial benzodiazepine receptors regulate steroid biosynthesis. Proc Natl Acad Sci U S A 86:9813–9816. https://doi.org/10.1073/pnas.86.24.9813
149. Papadopoulos V, Berkovich A, Krueger KE et al. (1991) Diazepam binding inhibitor and its processing products stimulate mitochondrial steroid biosynthesis via an interaction with mitochondrial benzodiazepine receptors. Endocrinology 129:1481–1488. https://doi.org/10.1210/endo-129-3-1481
150. Brown RC, Degenhardt B, Kotoula M et al. (2000) Location-dependent role of the human glioma cell peripheral-type benzodiazepine receptor in proliferation and steroid biosynthesis. Cancer Letters 156:125–132. https://doi.org/10.1016/s0304-3835(00)00451-1
151. Zeno S, Zaaroor M, Leschiner S et al. (2009) CoCl(2) induces apoptosis via the 18 kDa translocator protein in U118MG human glioblastoma cells. Biochemistry 48:4652–4661. https://doi.org/10.1021/bi900064t
152. Chelli B, Falleni A, Salvetti F et al. (2001) Peripheral-type benzodiazepine receptor ligands: mitochondrial permeability transition induction in rat cardiac tissue. Biochem Pharmacol 61:695–705. https://doi.org/10.1016/s0006-2952(00)00588-8
153. Lejri I, Grimm A, Hallé F et al. (2019) TSPO Ligands Boost Mitochondrial Function and Pregnenolone Synthesis. J Alzheimers Dis 72:1045–1058. https://doi.org/10.3233/JAD-190127
154. Tu LN, Morohaku K, Manna PR et al. (2014) Peripheral benzodiazepine receptor/translocator protein global knock-out mice are viable with no effects on steroid hormone biosynthesis. Journal of Biological Chemistry 289:27444–27454. https://doi.org/10.1074/jbc.M114.578286
155. Zhao AH, Tu LN, Mukai C et al. (2016) Mitochondrial Translocator Protein (TSPO) Function Is Not Essential for Heme Biosynthesis. Journal of Biological Chemistry 291:1591–1603. https://doi.org/10.1074/jbc.M115.686360
156. Šileikytė J, Blachly-Dyson E, Sewell R et al. (2014) Regulation of the mitochondrial permeability transition pore by the outer membrane does not involve the peripheral benzodiazepine receptor (Translocator Protein of 18 kDa (TSPO)). Journal of Biological Chemistry 289:13769–13781. https://doi.org/10.1074/jbc.M114.549634

157. Morohaku K, Pelton SH, Daugherty DJ et al. (2014) Translocator protein/peripheral benzodiazepine receptor is not required for steroid hormone biosynthesis. Endocrinology 155:89–97. https://doi.org/10.1210/en.2013-1556
158. Gavish M, Bachman I, Shoukrun R et al. (1999) Enigma of the peripheral benzodiazepine receptor. Pharmacol Rev 51:629–650
159. Cosenza-Nashat M, Zhao M-L, Suh H-S et al. (2009) Expression of the translocator protein of 18 kDa by microglia, macrophages and astrocytes based on immunohistochemical localization in abnormal human brain. Neuropathol Appl Neurobiol 35:306–328. https://doi.org/10.1111/j.1365-2990.2008.01006.x
160. Beckers L, Ory D, Geric I et al. (2018) Increased Expression of Translocator Protein (TSPO) Marks Pro-inflammatory Microglia but Does Not Predict Neurodegeneration. Mol Imaging Biol 20:94–102. https://doi.org/10.1007/s11307-017-1099-1
161. Cai L, Kirchleitner SV, Zhao D et al. (2020) Glioblastoma Exhibits Inter-Individual Heterogeneity of TSPO and LAT1 Expression in Neoplastic and Parenchymal Cells. Int J Mol Sci 21. https://doi.org/10.3390/ijms21020612
162. Zhang L, Hu K, Shao T et al. (2021) Recent developments on PET radiotracers for TSPO and their applications in neuroimaging. Acta Pharm Sin B 11:373–393. https://doi.org/10.1016/j.apsb.2020.08.006
163. Albert NL, Unterrainer M, Fleischmann DF et al. (2017) TSPO PET for glioma imaging using the novel ligand 18F-GE-180: first results in patients with glioblastoma. Eur J Nucl Med Mol Imaging 44:2230–2238. https://doi.org/10.1007/s00259-017-3799-9
164. Batarseh A, Barlow KD, Martinez-Arguelles DB et al. (2012) Functional characterization of the human translocator protein (18kDa) gene promoter in human breast cancer cell lines. Biochim Biophys Acta 1819:38–56. https://doi.org/10.1016/j.bbagrm.2011.09.001
165. Rashid K, Geissl L, Wolf A et al. (2018) Transcriptional regulation of Translocator protein (18 kDa) (TSPO) in microglia requires Pu.1, Ap1 and Sp factors. Biochim Biophys Acta Gene Regul Mech 1861:1119–1133. https://doi.org/10.1016/j.bbagrm.2018.10.018
166. Batarseh A, Li J, Papadopoulos V (2010) Protein kinase C epsilon regulation of translocator protein (18 kDa) Tspo gene expression is mediated through a MAPK pathway targeting STAT3 and c-Jun transcription factors. Biochemistry 49:4766–4778. https://doi.org/10.1021/bi100020e
167. Weidner L, Lorenz J, Quach S et al. (2023) Translocator protein (18kDA) (TSPO) marks mesenchymal glioblastoma cell populations characterized by elevated numbers of tumor-associated macrophages. Acta Neuropathologica Communications 11:147. https://doi.org/10.1186/s40478-023-01651-5
168. Jaremko L, Jaremko M, Giller K et al. (2014) Structure of the mitochondrial translocator protein in complex with a diagnostic ligand. Science 343:1363–1366. https://doi.org/10.1126/science.1248725
169. Lacapère JJ, Delavoie F, Li H et al. (2001) Structural and functional study of reconstituted peripheral benzodiazepine receptor. Biochem Biophys Res Commun 284:536–541. https://doi.org/10.1006/bbrc.2001.4975
170. Rone MB, Liu J, Blonder J et al. (2009) Targeting and insertion of the cholesterol-binding translocator protein into the outer mitochondrial membrane. Biochemistry 48:6909–6920. https://doi.org/10.1021/bi900854z
171. Issop L, Ostuni MA, Lee S et al. (2016) Translocator Protein-Mediated Stabilization of Mitochondrial Architecture during Inflammation Stress in Colonic Cells. PLoS One 11:e0152919. https://doi.org/10.1371/journal.pone.0152919
172. Zeng J, Guareschi R, Damre M et al. (2018) Structural Prediction of the Dimeric Form of the Mammalian Translocator Membrane Protein TSPO: A Key Target for Brain Diagnostics. Int J Mol Sci 19. https://doi.org/10.3390/ijms19092588
173. McEnery MW, Snowman AM, Trifiletti RR et al. (1992) Isolation of the mitochondrial benzodiazepine receptor: association with the voltage-dependent anion channel and the adenine nucleotide carrier. Proc Natl Acad Sci U S A 89:3170–3174. https://doi.org/10.1073/pnas.89.8.3170

174. Liu J, Rone MB, Papadopoulos V (2006) Protein-protein interactions mediate mitochondrial cholesterol transport and steroid biosynthesis. The Journal of Biological Chemistry 281:38879–38893. https://doi.org/10.1074/jbc.M608820200
175. Rone MB, Midzak AS, Issop L et al. (2012) Identification of a dynamic mitochondrial protein complex driving cholesterol import, trafficking, and metabolism to steroid hormones. Mol Endocrinol 26:1868–1882. https://doi.org/10.1210/me.2012-1159
176. Verma A, Nye JS, Snyder SH (1987) Porphyrins are endogenous ligands for the mitochondrial (peripheral-type) benzodiazepine receptor. Proc Natl Acad Sci U S A 84:2256–2260. https://doi.org/10.1073/pnas.84.8.2256
177. Guidotti A, Forchetti CM, Corda MG et al. (1983) Isolation, characterization, and purification to homogeneity of an endogenous polypeptide with agonistic action on benzodiazepine receptors. Proc Natl Acad Sci U S A 80:3531–3535. https://doi.org/10.1073/pnas.80.11.3531
178. Rupprecht R, Papadopoulos V, Rammes G et al. (2010) Translocator protein (18 kDa) (TSPO) as a therapeutic target for neurological and psychiatric disorders. Nat Rev Drug Discov 9:971–988. https://doi.org/10.1038/nrd3295
179. Werry EL, Bright FM, Piguet O et al. (2019) Recent Developments in TSPO PET Imaging as A Biomarker of Neuroinflammation in Neurodegenerative Disorders. Int J Mol Sci 20. https://doi.org/10.3390/ijms20133161
180. Veenman L, Levin E, Weisinger G et al. (2004) Peripheral-type benzodiazepine receptor density and in vitro tumorigenicity of glioma cell lines. Biochem Pharmacol 68:689–698. https://doi.org/10.1016/j.bcp.2004.05.011
181. Cleary J, Johnson KM, Opipari AW et al. (2007) Inhibition of the mitochondrial F1F0-ATPase by ligands of the peripheral benzodiazepine receptor. Bioorg Med Chem Lett 17:1667–1670. https://doi.org/10.1016/j.bmcl.2006.12.102
182. Krestinina OV, Grachev DE, Odinokova IV et al. (2009) Effect of peripheral benzodiazepine receptor (PBR/TSPO) ligands on opening of Ca2+-induced pore and phosphorylation of 3.5-kDa polypeptide in rat brain mitochondria. Biochemistry (Mosc) 74:421–429. https://doi.org/10.1134/s0006297909040105
183. Mattei C, Taly A, Soualah Z et al. (2019) Involvement of the GABAA receptor α subunit in the mode of action of etifoxine. Pharmacol Res 145:104250. https://doi.org/10.1016/j.phrs.2019.04.034
184. Ammer L-M, Vollmann-Zwerenz A, Ruf V et al. (2020) The Role of Translocator Protein TSPO in Hallmarks of Glioblastoma. Cancers (Basel) 12. https://doi.org/10.3390/cancers12102973
185. Pannell M, Economopoulos V, Wilson TC et al. (2020) Imaging of translocator protein upregulation is selective for pro-inflammatory polarized astrocytes and microglia. Glia 68:280–297. https://doi.org/10.1002/glia.23716
186. Da Pozzo E, Tremolanti C, Costa B et al. (2019) Microglial Pro-Inflammatory and Anti-Inflammatory Phenotypes Are Modulated by Translocator Protein Activation. Int J Mol Sci 20. https://doi.org/10.3390/ijms20184467
187. Owen DR, Narayan N, Wells L et al. (2017) Pro-inflammatory activation of primary microglia and macrophages increases 18 kDa translocator protein expression in rodents but not humans. J Cereb Blood Flow Metab 37:2679–2690. https://doi.org/10.1177/0271678X17710182
188. Guilarte TR, Loth MK, Guariglia SR (2016) TSPO Finds NOX2 in Microglia for Redox Homeostasis. Trends Pharmacol Sci 37:334–343. https://doi.org/10.1016/j.tips.2016.02.008
189. Wolf A, Herb M, Schramm M et al. (2020) The TSPO-NOX1 axis controls phagocyte-triggered pathological angiogenesis in the eye. Nat Commun 11:2709. https://doi.org/10.1038/s41467-020-16400-8
190. Kuo C-L, Chou H-Y, Chiu Y-C et al. (2020) Mitochondrial oxidative stress by Lon-PYCR1 maintains an immunosuppressive tumor microenvironment that promotes cancer progression and metastasis. Cancer Letters 474:138–150. https://doi.org/10.1016/j.canlet.2020.01.019

191. Park J, Min J-S, Kim B et al. (2015) Mitochondrial ROS govern the LPS-induced pro-inflammatory response in microglia cells by regulating MAPK and NF-κB pathways. Neurosci Lett 584:191–196. https://doi.org/10.1016/j.neulet.2014.10.016
192. Maj T, Wang W, Crespo J et al. (2017) Oxidative stress controls regulatory T cell apoptosis and suppressor activity and PD-L1-blockade resistance in tumor. Nat Immunol 18:1332–1341. https://doi.org/10.1038/ni.3868
193. Zhang J, Li H, Wu Q et al. (2019) Tumoral NOX4 recruits M2 tumor-associated macrophages via ROS/PI3K signaling-dependent various cytokine production to promote NSCLC growth. Redox Biol 22:101116. https://doi.org/10.1016/j.redox.2019.101116
194. Cemerski S, Cantagrel A, van Meerwijk JPM et al. (2002) Reactive oxygen species differentially affect T cell receptor-signaling pathways. The Journal of Biological Chemistry 277:19585–19593. https://doi.org/10.1074/jbc.M111451200
195. Levin E, Premkumar A, Veenman L et al. (2005) The peripheral-type benzodiazepine receptor and tumorigenicity: isoquinoline binding protein (IBP) antisense knockdown in the C6 glioma cell line. Biochemistry 44:9924–9935. https://doi.org/10.1021/bi050150s
196. Maaser K, Höpfner M, Jansen A et al. (2001) Specific ligands of the peripheral benzodiazepine receptor induce apoptosis and cell cycle arrest in human colorectal cancer cells. Br J Cancer 85:1771–1780. https://doi.org/10.1054/bjoc.2001.2181
197. Chelli B, Salvetti A, Da Pozzo E et al. (2008) PK 11195 differentially affects cell survival in human wild-type and 18 kDa translocator protein-silenced ADF astrocytoma cells. J Cell Biochem 105:712–723. https://doi.org/10.1002/jcb.21865
198. Castellano S, Taliani S, Viviano M et al. (2014) Structure-activity relationship refinement and further assessment of 4-phenylquinazoline-2-carboxamide translocator protein ligands as antiproliferative agents in human glioblastoma tumors. J Med Chem 57:2413–2428. https://doi.org/10.1021/jm401721h
199. Kugler W, Veenman L, Shandalov Y et al. (2008) Ligands of the mitochondrial 18 kDa translocator protein attenuate apoptosis of human glioblastoma cells exposed to erucylphosphohomocholine. Cell Oncol 30:435–450. https://doi.org/10.3233/clo-2008-0431
200. Veenman L, Shandalov Y, Gavish M (2008) VDAC activation by the 18 kDa translocator protein (TSPO), implications for apoptosis. J Bioenerg Biomembr 40:199–205. https://doi.org/10.1007/s10863-008-9142-1
201. Li J, Wang J, Zeng Y (2007) Peripheral benzodiazepine receptor ligand, PK11195 induces mitochondria cytochrome c release and dissipation of mitochondria potential via induction of mitochondria permeability transition. Eur J Pharmacol 560:117–122. https://doi.org/10.1016/j.ejphar.2006.12.027
202. Azarashvili T, Grachev D, Krestinina O et al. (2007) The peripheral-type benzodiazepine receptor is involved in control of Ca2+-induced permeability transition pore opening in rat brain mitochondria. Cell Calcium 42:27–39. https://doi.org/10.1016/j.ceca.2006.11.004
203. Fan J, Wang K, Zirkin B et al. (2018) CRISPR/Cas9–Mediated Tspo Gene Mutations Lead to Reduced Mitochondrial Membrane Potential and Steroid Formation in MA-10 Mouse Tumor Leydig Cells. Endocrinology 159:1130–1146. https://doi.org/10.1210/en.2017-03065
204. Yao R, Pan R, Shang C et al. (2020) Translocator Protein 18 kDa (TSPO) Deficiency Inhibits Microglial Activation and Impairs Mitochondrial Function. Front Pharmacol 11:986. https://doi.org/10.3389/fphar.2020.00986
205. Milenkovic VM, Slim D, Bader S et al. (2019) CRISPR-Cas9 Mediated TSPO Gene Knockout alters Respiration and Cellular Metabolism in Human Primary Microglia Cells. Int J Mol Sci 20. https://doi.org/10.3390/ijms20133359
206. Banati RB, Middleton RJ, Chan R et al. (2014) Positron emission tomography and functional characterization of a complete PBR/TSPO knockout. Nat Commun 5:5452. https://doi.org/10.1038/ncomms6452

207. Liu G-J, Middleton RJ, Kam WW-Y et al. (2017) Functional gains in energy and cell metabolism after TSPO gene insertion. Cell Cycle 16:436–447. https://doi.org/10.1080/15384101.2017.1281477
208. Fu Y, Wang D, Wang H et al. (2020) TSPO deficiency induces mitochondrial dysfunction, leading to hypoxia, angiogenesis, and a growth-promoting metabolic shift toward glycolysis in glioblastoma. Neuro Oncol 22:240–252. https://doi.org/10.1093/neuonc/noz183
209. Veenman L, Alten J, Linnemannstöns K et al. (2010) Potential involvement of F0F1-ATP(synth)ase and reactive oxygen species in apoptosis induction by the antineoplastic agent erucylphosphohomocholine in glioblastoma cell lines : a mechanism for induction of apoptosis via the 18 kDa mitochondrial translocator protein. Apoptosis 15:753–768. https://doi.org/10.1007/s10495-010-0460-5
210. Miettinen H, Kononen J, Haapasalo H et al. (1995) Expression of peripheral-type benzodiazepine receptor and diazepam binding inhibitor in human astrocytomas: relationship to cell proliferation. Cancer Res 55:2691–2695
211. Vlodavsky E, Soustiel JF (2007) Immunohistochemical expression of peripheral benzodiazepine receptors in human astrocytomas and its correlation with grade of malignancy, proliferation, apoptosis and survival. J Neurooncol 81:1–7. https://doi.org/10.1007/s11060-006-9199-9
212. Hanahan D, Weinberg RA (2011) Hallmarks of cancer: the next generation. Cell 144:646–674. https://doi.org/10.1016/j.cell.2011.02.013
213. Stewart SA, Dykxhoorn DM, Palliser D et al. (2003) Lentivirus-delivered stable gene silencing by RNAi in primary cells. RNA 9:493–501. https://doi.org/10.1261/rna.2192803
214. Sancak Y, Peterson TR, Shaul YD et al. (2008) The Rag GTPases bind raptor and mediate amino acid signaling to mTORC1. Science 320:1496–1501. https://doi.org/10.1126/science.1157535
215. Ran FA, Hsu PD, Wright J et al. (2013) Genome engineering using the CRISPR-Cas9 system. Nat Protoc 8:2281–2308. https://doi.org/10.1038/nprot.2013.143
216. Dehairs J, Talebi A, Cherifi Y et al. (2016) CRISP-ID: decoding CRISPR mediated indels by Sanger sequencing. Sci Rep 6:28973. https://doi.org/10.1038/srep28973
217. Moeckel S, Meyer K, Leukel P et al. (2014) Response-predictive gene expression profiling of glioma progenitor cells in vitro. PLoS One 9:e108632. https://doi.org/10.1371/journal.pone.0108632
218. Cusulin C, Chesnelong C, Bose P et al. (2015) Precursor States of Brain Tumor Initiating Cell Lines Are Predictive of Survival in Xenografts and Associated with Glioblastoma Subtypes. Stem Cell Reports 5:1–9. https://doi.org/10.1016/j.stemcr.2015.05.010
219. Davis B, Shen Y, Poon CC et al. (2016) Comparative genomic and genetic analysis of glioblastoma-derived brain tumor-initiating cells and their parent tumors. Neuro Oncol 18:350–360. https://doi.org/10.1093/neuonc/nov143
220. Seliger C, Meyer A-L, Leidgens V et al. (2022) Metabolic Heterogeneity of Brain Tumor Cells of Proneural and Mesenchymal Origin. Int J Mol Sci 23. https://doi.org/10.3390/ijms231911629
221. Seliger C, Rauer L, Wüster A-L et al. (2023) Heterogeneity of Amino Acid Profiles of Proneural and Mesenchymal Brain-Tumor Initiating Cells. Int J Mol Sci 24. https://doi.org/10.3390/ijms24043199
222. Menevse AN, Ammer L-M, Vollmann-Zwerenz A et al. (2023) TSPO acts as an immune resistance gene involved in the T cell mediated immune control of glioblastoma. Acta Neuropathologica Communications 11:75. https://doi.org/10.1186/s40478-023-01550-9
223. Castro F, Cardoso AP, Gonçalves RM et al. (2018) Interferon-Gamma at the Crossroads of Tumor Immune Surveillance or Evasion. Front Immunol 9:847. https://doi.org/10.3389/fimmu.2018.00847
224. Holbrook J, Lara-Reyna S, Jarosz-Griffiths H et al. (2019) Tumour necrosis factor signalling in health and disease. F1000Res 8. https://doi.org/10.12688/f1000research.17023.1

225. Naval J, Miguel D de, Gallego-Lleyda A et al. (2019) Importance of TRAIL Molecular Anatomy in Receptor Oligomerization and Signaling. Implications for Cancer Therapy. Cancers (Basel) 11. https://doi.org/10.3390/cancers11040444
226. Hotfilder M, Knupfer H, Mohlenkamp G et al. (2000) Interferon-gamma increases IL-6 production in human glioblastoma cell lines. Anticancer Res 20:4445–4450
227. Tanabe K, Matsushima-Nishiwaki R, Yamaguchi S et al. (2010) Mechanisms of tumor necrosis factor-alpha-induced interleukin-6 synthesis in glioma cells. J Neuroinflammation 7:16. https://doi.org/10.1186/1742-2094-7-16
228. Munoz L, Yeung YT, Grewal T (2016) Oncogenic Ras modulates p38 MAPK-mediated inflammatory cytokine production in glioblastoma cells. Cancer Biol Ther 17:355–363. https://doi.org/10.1080/15384047.2016.1139249
229. Hasan T, Caragher SP, Shireman JM et al. (2019) Interleukin-8/CXCR2 signaling regulates therapy-induced plasticity and enhances tumorigenicity in glioblastoma. Cell Death Dis 10:292. https://doi.org/10.1038/s41419-019-1387-6
230. Lamano JB, Lamano JB, Li YD et al. (2019) Glioblastoma-Derived IL6 Induces Immunosuppressive Peripheral Myeloid Cell PD-L1 and Promotes Tumor Growth. Clin Cancer Res 25:3643–3657. https://doi.org/10.1158/1078-0432.CCR-18-2402
231. Owen MR, Doran E, Halestrap AP (2000) Evidence that metformin exerts its anti-diabetic effects through inhibition of complex 1 of the mitochondrial respiratory chain. Biochemical Journal 348:607–614. https://doi.org/10.1042/bj3480607
232. LaMoia TE, Shulman GI (2021) Cellular and Molecular Mechanisms of Metformin Action. Endocr Rev 42:77–96. https://doi.org/10.1210/endrev/bnaa023
233. Albert NL, Nelwan DV, Fleischmann DF et al. (2023) Prognostic Value of TSPO PET Before Radiotherapy in Newly Diagnosed IDH-Wild-Type Glioblastoma. J Nucl Med. https://doi.org/10.2967/jnumed.122.265247
234. Zinnhardt B, Roncaroli F, Foray C et al. (2021) Imaging of the glioma microenvironment by TSPO PET. Eur J Nucl Med Mol Imaging 49:174–185. https://doi.org/10.1007/s00259-021-05276-5
235. Singh SK, Hawkins C, Clarke ID et al. (2004) Identification of human brain tumour initiating cells. Nature 432:396–401. https://doi.org/10.1038/nature03128
236. Galli R, Binda E, Orfanelli U et al. (2004) Isolation and characterization of tumorigenic, stem-like neural precursors from human glioblastoma. Cancer Res 64:7011–7021. https://doi.org/10.1158/0008-5472.CAN-04-1364
237. Bode J, Veenman L, Caballero B et al. (2012) The 18 kDa translocator protein influences angiogenesis, as well as aggressiveness, adhesion, migration, and proliferation of glioblastoma cells. Pharmacogenet Genomics 22:538–550. https://doi.org/10.1097/FPC.0b013e3283539cdc
238. Rechichi M, Salvetti A, Chelli B et al. (2008) TSPO over-expression increases motility, transmigration and proliferation properties of C6 rat glioma cells. Biochim Biophys Acta 1782:118–125. https://doi.org/10.1016/j.bbadis.2007.12.001
239. Giuliano CJ, Lin A, Girish V et al. (2019) Generating Single Cell-Derived Knockout Clones in Mammalian Cells with CRISPR/Cas9. Curr Protoc Mol Biol 128:e100. https://doi.org/10.1002/cpmb.100
240. Linkous A, Balamatsias D, Snuderl M et al. (2019) Modeling Patient-Derived Glioblastoma with Cerebral Organoids. Cell Reports 26:3203-3211.e5. https://doi.org/10.1016/j.celrep.2019.02.063
241. Nutma E, Ceyzériat K, Amor S et al. (2021) Cellular sources of TSPO expression in healthy and diseased brain. Eur J Nucl Med Mol Imaging 49:146–163. https://doi.org/10.1007/s00259-020-05166-2

242. Hara T, Chanoch-Myers R, Mathewson ND et al. (2021) Interactions between cancer cells and immune cells drive transitions to mesenchymal-like states in glioblastoma. Cancer Cell 39:779-792.e11. https://doi.org/10.1016/j.ccell.2021.05.002
243. Zinnhardt B, Müther M, Roll W et al. (2020) TSPO imaging-guided characterization of the immunosuppressive myeloid tumor microenvironment in patients with malignant glioma. Neuro Oncol 22:1030–1043. https://doi.org/10.1093/neuonc/noaa023
244. Zhang X, Zeng Y, Qu Q et al. (2017) PD-L1 induced by IFN-γ from tumor-associated macrophages via the JAK/STAT3 and PI3K/AKT signaling pathways promoted progression of lung cancer. Int J Clin Oncol 22:1026–1033. https://doi.org/10.1007/s10147-017-1161-7
245. Bhat MY, Solanki HS, Advani J et al. (2018) Comprehensive network map of interferon gamma signaling. J Cell Commun Signal 12:745–751. https://doi.org/10.1007/s12079-018-0486-y
246. Qing Y, Stark GR (2004) Alternative activation of STAT1 and STAT3 in response to interferon-gamma. The Journal of Biological Chemistry 279:41679–41685. https://doi.org/10.1074/jbc.M406413200
247. Yu H, Lee H, Herrmann A et al. (2014) Revisiting STAT3 signalling in cancer: new and unexpected biological functions. Nat Rev Cancer 14:736–746. https://doi.org/10.1038/nrc3818
248. Meng Q, Xia Y (2011) c-Jun, at the crossroad of the signaling network. Protein Cell 2:889–898. https://doi.org/10.1007/s13238-011-1113-3
249. Li N, Wang J, Zhang N et al. (2018) Cross-talk between TNF-α and IFN-γ signaling in induction of B7-H1 expression in hepatocellular carcinoma cells. Cancer Immunol Immunother 67:271–283. https://doi.org/10.1007/s00262-017-2086-8
250. Hardwick M, Cavalli LR, Barlow KD et al. (2002) Peripheral-type benzodiazepine receptor (PBR) gene amplification in MDA-MB-231 aggressive breast cancer cells. Cancer Genet Cytogenet 139:48–51. https://doi.org/10.1016/s0165-4608(02)00604-0
251. Khabibov M, Garifullin A, Boumber Y et al. (2022) Signaling pathways and therapeutic approaches in glioblastoma multiforme (Review). Int J Oncol 60. https://doi.org/10.3892/ijo.2022.5359
252. Knight MJ, Riffkin CD, Muscat AM et al. (2001) Analysis of FasL and TRAIL induced apoptosis pathways in glioma cells. Oncogene 20:5789–5798. https://doi.org/10.1038/sj.onc.1204810
253. Tourneur L, Delluc S, Lévy V et al. (2004) Absence or low expression of fas-associated protein with death domain in acute myeloid leukemia cells predicts resistance to chemotherapy and poor outcome. Cancer Res 64:8101–8108. https://doi.org/10.1158/0008-5472.CAN-04-2361
254. Ashley DM, Riffkin CD, Muscat AM et al. (2005) Caspase 8 is absent or low in many ex vivo gliomas. Cancer 104:1487–1496. https://doi.org/10.1002/cncr.21323
255. Lee SH, Shin MS, Park WS et al. (1999) Alterations of Fas (APO-1/CD95) Gene in Transitional Cell Carcinomas of Urinary Bladder1. Cancer Res 59:3068–3072
256. Yao H, Song E, Chen J et al. (2004) Expression of FAP-1 by human colon adenocarcinoma: implication for resistance against Fas-mediated apoptosis in cancer. Br J Cancer 91:1718–1725. https://doi.org/10.1038/sj.bjc.6602136
257. Foehr ED, Lorente G, Vincent V et al. (2005) FAS associated phosphatase (FAP-1) blocks apoptosis of astrocytomas through dephosphorylation of FAS. J Neurooncol 74:241–248. https://doi.org/10.1007/s11060-004-7202-x
258. Scaffidi C, Fulda S, Srinivasan A et al. (1998) Two CD95 (APO-1/Fas) signaling pathways. EMBO J 17:1675–1687. https://doi.org/10.1093/emboj/17.6.1675
259. Rudner J, Jendrossek V, Lauber K et al. (2005) Type I and type II reactions in TRAIL-induced apoptosis -- results from dose-response studies. Oncogene 24:130–140. https://doi.org/10.1038/sj.onc.1208191

260. Cingöz A, Ozyerli-Goknar E, Morova T et al. (2021) Generation of TRAIL-resistant cell line models reveals distinct adaptive mechanisms for acquired resistance and re-sensitization. Oncogene 40:3201–3216. https://doi.org/10.1038/s41388-021-01697-6
261. Je H, Nam G-H, Kim GB et al. (2021) Overcoming therapeutic efficiency limitations against TRAIL-resistant tumors using re-sensitizing agent-loaded trimeric TRAIL-presenting nanocages. J Control Release 331:7–18. https://doi.org/10.1016/j.jconrel.2021.01.016
262. Sanlioglu AD, Dirice E, Aydin C et al. (2005) Surface TRAIL decoy receptor-4 expression is correlated with TRAIL resistance in MCF7 breast cancer cells. BMC Cancer 5:54. https://doi.org/10.1186/1471-2407-5-54
263. Mühlenbeck F, Schneider P, Bodmer JL et al. (2000) The tumor necrosis factor-related apoptosis-inducing ligand receptors TRAIL-R1 and TRAIL-R2 have distinct cross-linking requirements for initiation of apoptosis and are non-redundant in JNK activation. The Journal of Biological Chemistry 275:32208–32213. https://doi.org/10.1074/jbc.M000482200
264. Ichikawa K, Liu W, Zhao L et al. (2001) Tumoricidal activity of a novel anti-human DR5 monoclonal antibody without hepatocyte cytotoxicity. Nat Med 7:954–960. https://doi.org/10.1038/91000
265. van der Sloot AM, Tur V, Szegezdi E et al. (2006) Designed tumor necrosis factor-related apoptosis-inducing ligand variants initiating apoptosis exclusively via the DR5 receptor. Proc Natl Acad Sci U S A 103:8634–8639. https://doi.org/10.1073/pnas.0510187103
266. Bernardi P, Gerle C, Halestrap AP et al. (2023) Identity, structure, and function of the mitochondrial permeability transition pore: controversies, consensus, recent advances, and future directions. Cell Death Differ 30:1869–1885. https://doi.org/10.1038/s41418-023-01187-0
267. Desai R, East DA, Hardy L et al. (2020) Mitochondria form contact sites with the nucleus to couple prosurvival retrograde response. Sci Adv 6. https://doi.org/10.1126/sciadv.abc9955
268. Yasin N, Veenman L, Singh S et al. (2017) Classical and Novel TSPO Ligands for the Mitochondrial TSPO Can Modulate Nuclear Gene Expression: Implications for Mitochondrial Retrograde Signaling. Int J Mol Sci 18. https://doi.org/10.3390/ijms18040786
269. Tewari R, Sharma V, Koul N et al. (2009) Ebselen abrogates TNFalpha induced pro-inflammatory response in glioblastoma. Mol Oncol 3:77–83. https://doi.org/10.1016/j.molonc.2008.10.004
270. McFarland BC, Hong SW, Rajbhandari R et al. (2013) NF-κB-induced IL-6 ensures STAT3 activation and tumor aggressiveness in glioblastoma. PLoS One 8:e78728. https://doi.org/10.1371/journal.pone.0078728
271. Jones SA, Jenkins BJ (2018) Recent insights into targeting the IL-6 cytokine family in inflammatory diseases and cancer. Nat Rev Immunol 18:773–789. https://doi.org/10.1038/s41577-018-0066-7
272. Fousek K, Horn LA, Palena C (2021) Interleukin-8: A chemokine at the intersection of cancer plasticity, angiogenesis, and immune suppression. Pharmacol Ther 219:107692. https://doi.org/10.1016/j.pharmthera.2020.107692
273. Wu J, Gao F-X, Wang C et al. (2019) IL-6 and IL-8 secreted by tumour cells impair the function of NK cells via the STAT3 pathway in oesophageal squamous cell carcinoma. J Exp Clin Cancer Res 38:321. https://doi.org/10.1186/s13046-019-1310-0
274. Tsukamoto H, Nishikata R, Senju S et al. (2013) Myeloid-derived suppressor cells attenuate TH1 development through IL-6 production to promote tumor progression. Cancer Immunol Res 1:64–76. https://doi.org/10.1158/2326-6066.CIR-13-0030
275. Liu H, Zhao Q, Tan L et al. (2023) Neutralizing IL-8 potentiates immune checkpoint blockade efficacy for glioma. Cancer Cell 41:693-710.e8. https://doi.org/10.1016/j.ccell.2023.03.004
276. Mao F-Y, Zhao Y-L, Lv Y-P et al. (2018) CD45+CD33lowCD11bdim myeloid-derived suppressor cells suppress CD8+ T cell activity via the IL-6/IL-8-arginase I axis in human gastric cancer. Cell Death Dis 9:763. https://doi.org/10.1038/s41419-018-0803-7

277. Conroy S, Kruyt FAE, Wagemakers M et al. (2018) IL-8 associates with a pro-angiogenic and mesenchymal subtype in glioblastoma. Oncotarget 9:15721–15731. https://doi.org/10.18632/oncotarget.24595
278. Holst CB, Christensen IJ, Vitting-Seerup K et al. (2021) Plasma IL-8 and ICOSLG as prognostic biomarkers in glioblastoma. Neurooncol Adv 3:vdab072. https://doi.org/10.1093/noajnl/vdab072
279. Bader S, Würfel T, Jahner T et al. (2023) Impact of Translocator Protein 18 kDa (TSPO) Deficiency on Mitochondrial Function and the Inflammatory State of Human C20 Microglia Cells. Cells 12. https://doi.org/10.3390/cells12060954
280. Wang Q, He Z, Huang M et al. (2018) Vascular niche IL-6 induces alternative macrophage activation in glioblastoma through HIF-2α. Nat Commun 9:559. https://doi.org/10.1038/s41467-018-03050-0
281. Wang Z-Y, Bjorling DE (2011) Tumor necrosis factor-α induces expression and release of interleukin-6 by human urothelial cells. Inflamm Res 60:525–532. https://doi.org/10.1007/s00011-010-0298-x
282. Bunevicius A, Radziunas A, Tamasauskas S et al. (2018) Prognostic role of high sensitivity C-reactive protein and interleukin-6 in glioma and meningioma patients. J Neurooncol 138:351–358. https://doi.org/10.1007/s11060-018-2803-y
283. Jelluma N, Yang X, Stokoe D et al. (2006) Glucose withdrawal induces oxidative stress followed by apoptosis in glioblastoma cells but not in normal human astrocytes. Mol Cancer Res 4:319–330. https://doi.org/10.1158/1541-7786.MCR-05-0061
284. Jiang Z, Liu Z, Li M et al. (2019) Increased glycolysis correlates with elevated immune activity in tumor immune microenvironment. EBioMedicine 42:431–442. https://doi.org/10.1016/j.ebiom.2019.03.068
285. Beckermann KE, Dudzinski SO, Rathmell JC (2017) Dysfunctional T cell metabolism in the tumor microenvironment. Cytokine Growth Factor Rev 35:7–14. https://doi.org/10.1016/j.cytogfr.2017.04.003
286. Schmidt CA, Fisher-Wellman KH, Neufer PD (2021) From OCR and ECAR to energy: Perspectives on the design and interpretation of bioenergetics studies. Journal of Biological Chemistry 297:101140. https://doi.org/10.1016/j.jbc.2021.101140
287. Divakaruni AS, Paradyse A, Ferrick DA et al. (2014) Chapter Sixteen - Analysis and Interpretation of Microplate-Based Oxygen Consumption and pH Data. In: Murphy AN, Chan DC (eds) Methods in Enzymology : Mitochondrial Function, vol 547. Academic Press, pp 309–354
288. Tu LN, Zhao AH, Hussein M et al. (2016) Translocator Protein (TSPO) Affects Mitochondrial Fatty Acid Oxidation in Steroidogenic Cells. Endocrinology 157:1110–1121. https://doi.org/10.1210/en.2015-1795
289. Bader S, Wolf L, Milenkovic VM et al. (2019) Differential effects of TSPO ligands on mitochondrial function in mouse microglia cells. Psychoneuroendocrinology 106:65–76. https://doi.org/10.1016/j.psyneuen.2019.03.029
290. Frison M, Faccenda D, Abeti R et al. (2021) The translocator protein (TSPO) is prodromal to mitophagy loss in neurotoxicity. Mol Psychiatry 26:2721–2739. https://doi.org/10.1038/s41380-021-01050-z
291. Gatliff J, East DA, Singh A et al. (2017) A role for TSPO in mitochondrial Ca2+ homeostasis and redox stress signaling. Cell Death Dis 8:e2896. https://doi.org/10.1038/cddis.2017.186
292. Mailloux RJ (2020) An Update on Mitochondrial Reactive Oxygen Species Production. Antioxidants (Basel) 9. https://doi.org/10.3390/antiox9060472
293. Ludwig K, Le Belle JE, Muthukrishnan SD et al. (2023) NADPH oxidase promotes glioblastoma radiation resistance in a PTEN-dependent manner. Antioxid Redox Signal. https://doi.org/10.1089/ars.2022.0086
294. Su X, Yang Y, Guo C et al. (2021) NOX4-Derived ROS Mediates TGF-β1-Induced Metabolic Reprogramming during Epithelial-Mesenchymal Transition through the PI3K/AKT/HIF-1α Pathway in Glioblastoma. Oxid Med Cell Longev 2021:5549047. https://doi.org/10.1155/2021/5549047

295. Hsieh C-H, Shyu W-C, Chiang C-Y et al. (2011) NADPH oxidase subunit 4-mediated reactive oxygen species contribute to cycling hypoxia-promoted tumor progression in glioblastoma multiforme. PLoS One 6:e23945. https://doi.org/10.1371/journal.pone.0023945
296. Sesen J, Dahan P, Scotland SJ et al. (2015) Metformin inhibits growth of human glioblastoma cells and enhances therapeutic response. PLoS One 10:e0123721. https://doi.org/10.1371/journal.pone.0123721

Publications

Menevse, Ayse N.*, **Ammer, Laura-Marie***, Vollmann-Zwerenz, Arabel, Kupczyk, Marcell, Lorenz, Julia, Weidner, Lorraine, Hussein, Abir, Sax, Julian, Mühlbauer, Jasmin, Heuschneider, Nicole, Rohrmus, Celine, Mai, Laura S., Jachnik, Birgitt, Stamova, Slava, Volpin, Valentina, Durst, Franziska C., Sorrentino, Antonio, Xydia, Maria, Milenkovic, Vladimir M., Bader, Stefanie, Braun, Frank K., Wetzel, Christian H., Albert, Nathalie L., Tonn, Joerg-Christian, Bartenstein, Peter, Proescholdt, Martin, Schmidt, Nils O., Linker, Ralf A., Riemenschneider, Markus J., Beckhove, Philipp*, and Hau, Peter* (2023): *TSPO acts as an immune resistance gene involved in the T cell mediated immune control of glioblastoma.* Acta Neuropathologica Communications 11 (1). * Authors contributed equally

Ammer, Laura-Marie, Vollmann-Zwerenz, Arabel, Ruf, Viktoria, Wetzel, Christian H., Riemenschneider, Markus J., Albert, Nathalie L., Beckhove, Philipp, and Hau, Peter (2020): *The Role of Translocator Protein TSPO in Hallmarks of Glioblastoma.* Cancers 12 (10), S. 2973.

Weidner, Lorraine, Lorenz, Julia, Quach, Stefanie, Braun, Frank K., Rothhammer-Hampl, Tanja, **Ammer, Laura-Marie**, Vollmann-Zwerenz, Arabel, Bartos, Laura M., Dekorsy, Franziska J., Holzgreve, Adrien, Kirchleitner, Sabrina V., Thon, Niklas, Greve, Tobias, Ruf, Viktoria, Herms, Jochen, Bader, Stefanie, Milenkovic, Vladimir M., von Baumgarten, Louisa, Menevse, Ayse N., Hussein, Abir, Sax, Julian, Wetzel, Christian H., Rupprecht, Rainer, Proescholdt, Martin A., Schmidt, Nils O., Beckhove, Philipp, Hau, Peter, Tonn, Joerg-Christian, Bartenstein, Peter, Brendel, Matthias, Albert, Nathalie L., and Riemenschneider, Markus J. (2023): *Translocator protein (18kDA) (TSPO) marks mesenchymal glioblastoma cell populations characterized by elevated numbers of tumor-associated macrophages.* Acta Neuropathologica Communications 11 (1).

Seliger, Corinna, Rauer, Lisa, Wüster, Anne-Louise, Moeckel, Sylvia, Leidgens, Verena, Jachnik, Birgit, **Ammer, Laura-Marie**, Heckscher, Simon, Dettmer, Katja, Riemenschneider, Markus J., Oefner, Peter J., Proescholdt, Martin A., Vollmann-Zwerenz, Arabel, and Hau, Peter (2023) *Heterogeneity of Amino Acid Profiles of Proneural and Mesenchymal Brain-Tumor Initiating Cells.* International journal of molecular sciences 24 (4).

Acknowledgement

Like any other significant achievements in life, this PhD was not something I could have accomplished alone. In this regard, I consider myself incredibly fortunate to be surrounded by so many inspiring and supportive colleagues, family members and friends.

First and foremost, I want to deeply thank my PhD supervisor Prof. Dr. Peter Hau for giving me the opportunity to complete my PhD in his laboratory. Your guidance and encouragement have been invaluable to me throughout this project. Thank you for all your time reading and correcting my manuscripts and for your commitment in pushing the finalization of the paper forward. I also want to specifically thank you for your continued efforts in securing the financial support that allowed me to complete this thesis properly.

I would also like to express my gratitude to my PhD thesis mentors, Prof. Dr. Christian Wetzel, Prof. Dr. Dr. Corinna Seliger-Behme and Prof. Dr. Philipp Beckhove. Thank you for your time and effort providing valuable feedback and thought-provoking questions.

I would like to thank Prof. Dr. Christian Wetzel, Prof. Dr. Oliver Bosch and Prof. Dr. Philipp Beckhove for their participation in my examination committee. I´d also like to extend my thanks to Prof. Dr. Markus Riemenschneider for his willingness to serve as a substitute examiner.

A special thanks goes to Dr. Arabel Vollmann-Zwerenz and Birgit Jachnik, the heart of the lab, who made the last four years so enjoyable:

Arabel did an outstanding job, always taking the time to answer my questions and guiding me through the challenging times of this thesis. Sitting back-to-back in the office, our discussions about the enigmatic functions of TSPO and our shared love for fantasy romance novels were always fun and easy, and they will be greatly missed! Thank you also for proofreading basically everything I have ever written and offering your experienced advice.

Thank you, Birgit, for always cheering me up when things did not go my way and for all your clever ideas to overcome countless challenges. I deeply appreciate your patience in teaching me practically everything and all your help in the never-ending CRISPR/Cas cell culture. The long hours in the cell culture were so much more enjoyable when you were sitting in the next hood. I will sincerely miss our coffee mornings talks and our Mensa Fridays.

I would also like to thank Eva, who joined the lab last year. Thank you for your excellent support in completing the missing qPCRs, which gave me the time to finally start writing my thesis.

I want to express my deep gratitude to Dr. Tobias Welz, who evolved from the helpful Postdoc at the other side of the floor to my running buddy, to one of my closest friends. Thank you for your endurance in not only running but also listening to my concerns, always offering helpful

ideas and support, and our hourless discussions about work-related and not so much work-related topics.

A special appreciation goes to all my colleagues and former colleagues in D4: Jasmin, Annette, Silvia, Lohmi, Anna, and Eva-Maria. Thank you for all your valuable scientific insights, for generously allowing me to use your equipment, for sharing your methods, and for providing me with countless materials whenever I needed them. I'm also grateful for all the lunch breaks, cake-eating sessions, and birthdays we celebrated together.

Many thanks to Dr. Vladimir Milenkovic and Stefanie Bader for their generosity in providing me with plasmids and antibodies and for always taking the time to help me whenever I had questions about CRISPR/Cas or Seahorse assays.

I also want to thank Ayse and Lorraine for our collaboration, science talks and shared ideas. Together we have navigated through all sorts of challenges, and I wish you alle the best in the future.

My thanks also go out to all the medical, master and bachelor students who made the four years so diverse and enjoyable: Franzi, Bettina, Sina, Melissa, Celine, Simon, Adelina. Special thanks to Laura - you were a breath of fresh air, and it was always fun working together!

My most heartfelt thanks go to my family, my parents Hubertus and Doris and my brother Marco. Your support and belief in me have been a source of strength and motivation. Finally, I want to thank Andreas, for always standing by my side, patiently listening to my complaints and ideas, and celebrating my successes with me. Your support means the world to me.

Selbstständigkeitserklärung

Ich, Laura-Marie Ammer geboren am 31.01.1995 in Wolfhagen, erkläre hiermit, dass ich die vorliegende Arbeit ohne unzulässige Hilfe Dritter und ohne Benutzung anderer als der angegebenen Hilfsmittel angefertigt habe.

Die aus anderen Quellen direkt oder indirekt übernommenen Daten und Konzepte sind unter Angabe der Quelle gekennzeichnet. Insbesondere habe ich nicht die entgeltliche Hilfe von Vermittlungs- bzw. Beratungsdiensten (Promotionsberater*innen oder andere Personen) in Anspruch genommen.

Die Arbeit wurde bisher weder im In- noch im Ausland in gleicher oder ähnlicher Form einer anderen Prüfungsbehörde vorgelegt.

Ort, Datum Unterschrift